CONE PENETRATION TEST IN A VIRTUAL CALIBRATION CHAMBER

JOANNA BUTLANSKA

A thesis submitted in partial fulfillment of the requirements for the degree of Doctor of Philosophy

Departament de Enginyeria del Terreny, Cartogràfica i Geofísica
L'Escola Tècnica Superior d'Enginyers de Camins, Canals i Ports
Universitat Politècnica de Catalunya
BARCELONATECH

SUPERVISORS:
Prof. Antonio Gens Solé
Dr. Marcos Arroyo Alvarez de Toledo

LOCATION:
Barcelona
May 13, 2014

To *My Family*

ABSTRACT

Cone penetration test (CPT) is a fast and reliable site investigation tool for exploring soils and soft ground. While the interpretation of the test results in clay has advanced considerably from a theoretical and numerical viewpoint that of tests in sands still relies largely on empirical correlations. A major source of such correlations comes from tests done in calibration chambers (CC), where soil state and properties might be tightly controlled.

Calibration chambers are relatively large pieces of equipment, and calibration chamber testing is expensive and time consuming. Moreover, CC tests are performed on freshly reconstituted sands whose fabric may vary from that of natural sand deposits. Hence, correlations developed for one type of sand might not be suitable for another sand deposit. Numerical DEM-based calibration chambers might offer an interesting alternative to the more cumbersome physical tests.

This study is the first attempt to perform a three-dimensional DEM-based simulations of the cone penetration test. The three-dimensional commercial DEM code (PFC_{3D}) is used to develop Virtual Calibration Chamber CPT (VCC CPT) model. This commercial code has the advantage of incorporating a robust, well verified DEM algorithm implementation. Therefore this work could focus directly on the issue of validation. Validation was performed by systematic comparison with experimental results taken from the one of the largest CC CPT testing campaigns ever performed: that carried out at the geotechnical laboratories of ENEL-CRIS, Milan and ISMES, Bergamo, Italy on Ticino sand.

To achieve that objective, several steps were necessary. First, calibration of an analogue discrete material to represent Ticino sand was performed using single-element tests. By trial-and-error, contact DEM parameters were adjusted to fit the results to a single isotropically compressed drained triaxial test. Afterwards, the mechanical response of the discrete material was further validated by performing additional triaxial tests with different initial conditions. The VCC CPT model was then constructed. Comprehensive dimensional analysis showed that the best option to balance computational efficiency and realism was to fill the chamber with a scaled-up calibrated discrete material, so that average grain size was 50 times that of Ticino sand. Cone size was doubled to increase the cone to particle ratio and chamber height shortened by factor of 2.

Scaled-up grain size resulted in noisy penetration curves. An original filtering technique was proposed to extract steady state cone resistances. A basic series of simulations was performed to explore the effect of initial stress and relative density in cone resistance. The results obtained from the simulations did fit closely the trends that had been previously established using physical chambers. That result was taken as a general validation of the proposed simulation approach.

From the micromechanical point of view, the granular material is highly discontinuous and inhomogeneous. Obtaining a homogeneous initial state (especially in the zone of the penetrating cone) is crucial to obtain easily interpretable results. Specific procedures to assess initial state inhomogeneities were developed. They revealed

the important role of model boundaries (rigid walls), both passive and active (servo-controlled), during specimen formation.

DEM-based models can provide results at various level of resolution i.e. the micro-scale, the meso-scale and the macro-scale. The macro-scale is the scale of most interest from an engineering viewpoint, because it deals with system responses such as cone tip resistance. Meso-scale results, such as stresses or strains, are required to compare results with those obtained using other approaches (e.g. continuum models). Micro-scale results provide insight on behavior observed at larger scales. To apply multi-scale analysis to the VCC simulations specific post processing methods were developed and applied.

A large series of VCC CPT has been performed. Simulations were performed for models with different horizontal servo-control walls, various sizes of chamber (by enforcing model symmetry), cone and particles and two boundary conditions (BC1: σ_v=constant and σ_h=constant and BC3: σ_v=constant and ϵ_h=0). The results were analyzed, focusing on aspects such as chamber size, particle size and boundary condition effects on steady state cone resistance values. A smaller number of tests have also been examined from the point of view of shaft resistance. Most trends and results obtained are shown to be in agreement with previous physical tests. When disagreements appear, the causes are identified: the most severe disagreements result from initial inhomogeneities in the discrete model. The work described in this thesis showed ease the burden of future CPT calibrations in granular materials.

KEYWORDS: cone penetration test, CPT, distinct element method, DEM, cone resistance, chamber size effect, homogeneity, model symmetry, micro–behavior

RESUMEN

Los ensayos de penetración estática de cono (CPT) son una de las herramientas más importantes en el reconocimiento geotécnico. La interpretación de los resultados de ensayo en arcilla ha avanzado considerablemente desde un punto de vista teórico y numérico. Sin embargo la interpretación de los resultados en los materiales granulares (por ejemplo arena) todavía está basada en correlaciones empíricas provenientes de las pruebas realizadas en cámaras de calibración (CC), donde el estado del suelo y sus propiedades pueden ser controlados.

Las cámaras de calibración son equipos relativamente grandes, y los ensayos en ellas son bastante costosos en tiempo y recursos. Por otra parte, las pruebas se realizan en muestras de arenas reconstituidas cuyas propiedades varían respecto de los depósitos naturales de donde provienen. Por lo tanto, las correlaciones desarrolladas en un tipo de arena podrían no ser adecuadas para otro depósito distinto. Cámaras de calibración numéricas (virtuales) basadas en el método de elementos discretos (DEM) podrían ofrecer una alternativa interesante a los ensayos físicos.

Este estudio es el primer intento de realizar una simulación basadas en el método de los elementos discretos tridimensionales de ensayos de penetración de cono. El código comercial tridimensional (PFC3D) ha sido usado para desarrollar el modelo de CPT de Cámara de Calibración Virtual (CPT VCC). Este código comercial incorpora un algoritmo DEM robusto y bien contrastado. Por lo tanto, este trabajo podía centrarse directamente en el tema de la validación. La validación fue realizada mediante una comparación sistemática con los resultados experimentales obtenidos en una de las mayores campañas de CPT CC jamás realizadas: la que se llevó a cabo en los laboratorios geotécnicos de ENEL-CRIS, Milán y ISMES, Bergamo, Italia en arena de Ticino.

Para alcanzar este objetivo fueron necesarios varios pasos. En primer lugar, se llevó a cabo la calibración de un material discreto análogo a arena de Ticino mediante ensayos elementales. Por prueba-y-error, los parámetros de contacto DEM fueron ajustados para adaptarse a los resultados de un ensayo de compresión triaxial drenado sobre una muestra isótropa. Más tarde la simulación de ensayos triaxiales adicionales permitió validar la respuesta mecánica del material discreto. A continuación se construyó el modelo CPT VCC. Un análisis dimensional exhaustivo mostró que la mejor opción para crear un modelo eficiente y real era llenar la cámara con un material con el tamaño de grano 50 veces mayor que el de la arena de Ticino. El tamaño del cono se duplicó para aumentar la relación entre el diámetro del cono y el diámetro de las partículas. La altura de la cámara fue acortada por un factor de 2.

El tamaño de grano ampliado resultó en curvas de penetración con mucho ruido. Se propuso una técnica original de filtrado para extraer la resistencia de punta estacionaria. Se realizó una serie básica de simulaciones para explorar el efecto de la tensión inicial y la densidad relativa sobre la resistencia de cono. Los resultados obtenidos de las simulaciones se ajustan estrechamente a las tendencias establecidas previamente en cámaras físicas. Este resultado fue tomado como una validación general del programa de simulación propuesto.

Desde el punto de vista de la micro-mecánica, el material granular es muy discontinuo y no homogéneo. La obtención de un estado inicial homogéneo (especialmente en la zona de penetración del cono) es crucial para obtener resultados fácilmente interpretables. Por lo tanto se han desarrollado procedimientos específicos para evaluar heterogeneidades del estado inicial. Los resultados manifestaron el papel clave del contorno de modelo (paredes rígidas), tanto pasivo como activo (servo-controlados), durante la formación del modelo.

Los modelos basados en el DEM puede proporcionar resultados a varios niveles de la resolución, es decir del micro-, meso- y macro escala. Desde el punto de vista de ingeniería la macro-escala es la escala de mayor interés, porque tiene que ver con las respuestas del sistema, tales como la resistencia de punta. Resultados de meso-escala (tensiones y deformaciones), se requieren para comparar dichos resultados con los de otros métodos (por ejemplo, modelos continuos). Los resultados de micro-escala proporcionan una visión sobre el comportamiento observado a escalas más grandes. Métodos específicos de post-procesamiento fueron desarrollados y aplicados a las simulaciones de CPT en VCC para su análisis multi-escala.

Se ha realizado una gran serie de VCC CPT. Las simulaciones se realizaron para modelos con diferentes posiciones en las paredes horizontales de servo-control, varios tamaños de cámara (mediante la aplicación de simetría), varios tamaños del cono y de las partículas y dos condiciones de contorno (BC1: σ_v=constant and σ_h=constant and BC3: σ_v=constant and ϵ_h=0). Los resultados se analizaron centrándose en varios aspectos como el tamaño de la cámara, el tamaño de las partículas y los efectos de condiciones de contorno sobre el valor de la resistencia de punta. Un número limitado de los CPT fue examinado desde el punto de vista de la resistencia del fuste del cono. Se observó que la mayoría de las tendencias y los resultados obtenidos estaban de acuerdo con resultados previos obtenidos en ensayos físicos. Cuando aparecen desacuerdos se han identificado las causas; los desacuerdos más graves son consecuencia de la falta de homogeneidad inicial en el modelo discreto. El trabajo presentado en esta tesis debería facilitar futuras calibraciones CPT en materiales granulares.

Palabras clave: penetración de cono, CPT, método de los elementos discretos, DEM, resistencia de cono, efecto de tamaño de cámara de calibración, homogeneidad, simetría del modelo, comportamiento micro

PUBLICATIONS

This thesis is a monograph, which contains some unpublished material and is based on the following publications wherein some ideas and figures have appeared previously.

Publications in the journals:

1 M. Arroyo, J. Butlanska, A. Gens, F. Calvetti and M. Jamiolkowski (2011). Technical Note: Cone penetration tests in a virtual calibration chamber. **Géotechnique** 61(6), pp: 525–531 [doi: 10.1680/geot.9.P.067]

2 J. Butlanska, M. Arroyo, A. Gens, C. O'Sullivan (2014). Multi-scale analysis of cone penetration test (CPT) in a virtual calibration chamber. **Canadian Geotechnical Journal**, 51(1), pp: 51-66, [doi:10.1139/cgj-2012-0476]

3 J. Butlanska, M. Arroyo and A. Gens (2014). Steady state of solid-grain interfaces during simulated CPT. **Studia Geotechnica et Mechanica**, 35(4), [doi: 10.2478/sgem-2013-0034]

4 J. Butlanska, M. Arroyo (2014,accepted for publications). Discussion to 'Stresses Development around Displacement Piles Penetration in Sand'. **Journal of Geotechnical and Geoenvironmental Engineering**.

Publications in the conference proceedings:

1 M. Arroyo, N. González, J. Butlanska, A. Gens and J.C.P. Dalton (2008). SBPM testing in Bothkennar clay: structure effects. Geotechnical and Geophysical Site Characterization–Huang & Mayne (eds). pp. 257–263

2 J. Butlanska, M. Arroyo and A. Gens (2009). Homogeneity and symmetry in DEM models of cone penetration. 6th International Conference on the Micromechanics of Granular Media. Golden CO: American Institute of Physics (AIP), pp. 425–428.

3 M. Arroyo and J.Butlanska (2009). Simulación numérica de ensayos de penetración estática. Jornada técnica: Ensayos de penetración estàtica en el proyecto geotécnico. CEDEX. Madrid.

4 J. Butlanska, M. Arroyo and A. Gens (2010). Virtual Calibration Chamber CPT tests on Ticino sand. 2nd International Symposium on Cone Penetration Testing, CPT'10, Huntington Beach, California, pp. 217–224

5 J. Butlanska, M. Arroyo and A. Gens (2010). Size effects on a virtual calibration chamber. 7th European Conference on Numerical Methods in Geotechnical Engineering, NUMGE 2010, Trondheim, pp. 225–230

6 J. Butlanska, C. O'Sullivan, M. Arroyo and A. Gens (2010). Mapping Deformation during CPT in Virtual Calibration Chamber. International Symposium on Geomechanics and Geotechnics: From Micro to Macro (IS-Shanghai 2010), Shanghai, vol.1, pp. 559–564

7 C. O'Sullivan, J. Butlanska and G. Cheung (2010). Calculating Strain in 3D DEM Simulations. IOP Conference Series: Materials Science and Engineering, 10 (1) [doi:10.1088/1757-899X/10/1/012076]

8 N. Climent, J. Butlanska, M. Arroyo and A. Gens (2011). Triaxial and cone penetration tests in a discrete analogue of Toyoura sand. Continuum and Distinct Element Numerical Modeling in Geomechanics. Proceedings of the 2nd International FLAC/DEM Symposium. February 14-16, 2011, Melbourne, Australia

9 J. Butlanska, M. Arroyo and A. Gens (2013). 3D DEM simulation of CPT in sand. Proceedings of the 4th International Conference on Site Characterization ISC-4, 17–21 September 2012, Porto de Galinhas–Pernambuco, Brasil

10 M. Arroyo, J. Butlanska, A. Gens and C. O'Sullivan (2013). Effect of radial walls on CPT in DEM–based Virtual Calibration Chamber. Proceedings of the 3rd International Symposium on Computational Geomechanics (COMGEO III), Krakow, Poland, 21-23 August, 2013

11 J. Butlanska, M. Arroyo and A. Gens (2014). Shaft capacity observed in numerical simulation of multi-sleeve CPT. Proceedings of 3rd International Symposium on Cone Penetration Testing, May 12-14, 2014–Las Vegas, Nevada

12 M.O. Ciantia, M. Arroyo, Butlanska and A. Gens (2014). DEM modelling of a double-porosity crushable granular material. ubmitted to IS-Cambridge 2014: International Symposium on Geomechanics from Micro to Macro (1-3 September 2014 Cambridge, UK.)

13 J. Butlanska, M. Arroyo and A. Gens (2014). Probing DEM specimen heterogeneity by simulated CPT. Submitted to IS-Cambridge 2014: International Symposium on Geomechanics from Micro to Macro (1-3 September 2014 Cambridge, UK.)

Experience is what you get when you didn't get what you wanted

— Dan Stanford

ACKNOWLEDGMENTS

This thesis would not have been possible without the support of many people. Foremost, I would like to express my sincere gratitude to my supervisors–Prof. Antonio Gens and Dr Marcos Arroyo–for making my PhD possible at the UPC. I am thankful for their faith in my abilities and for giving me the freedom to explore on my own. Further, I thank Marcos for his continuous support of my PhD study and research, for his patience, motivation, enthusiasm, and immense knowledge. His guidance helped me in all the time of research and writing of this thesis.

Besides my advisors, I would like to acknowledge the inputs from Prof. Francesco Calvetti (Politecnico di Milano), Prof. Michele Jamiolkowski (Politecnico di Torino) and Dr. Catherine O'Sullivan (Imperial College of London). Francesco, thank you for your guidance and engagement in DEM, especially, for the introduction to PFC^{3D}. Michele, thank you for sharing the largest data set of triaxial, CPT, DMT, etc. carried out at the geotechnical laboratories of ENEL–CRIS, Milan and ISMES, Bergamo, Italy. Catherine, thank you for your guidance and engagement in the numerical experiments, especially, in post–process analysis. I appreciate that you were always willing to help in solving my dilemmas. I thank you all for sharing your knowledge with me. It was an honor to meet and work with you all.

The financial support to complete this project and received from UPC through doctoral grant (BES–2006–12168) from the Ministry of Sciences and Innovation is gratefully acknowledge.

Many thanks go to my friends who accompanied me during these years with their friendship. Without you all my stay in Barcelona would not be so awesome. Special thanks go to all people that I have met during my short stays in Milan, Torino and London. I also thank my 'old' and 'new' officemates for a friendly work environment.

Last but not least, thanks to my family for the support they have given me all these years. I owe my deepest gratitude to Prashanth–my husband and my baby-girl Emma, for making me laugh every day. Thank you for your endless love and support during this difficult Thesis years.

CONTENTS

LIST OF FIGURES

LIST OF TABLES

1 INTRODUCTION

Brick walls are there for a reason: they let us prove how badly we want things

— Randy Pausch

1.1 INTRODUCTION

Cone penetration tests are one of the basic tools of geotechnical soil characterization. They are particularly valuable for granular soils, where intact sample retrieval is very difficult. Interpretation of the test results relies largely on empirical correlations (e.g. Mayne [2007]). A major source of such correlations is done in calibration chambers (CC), where soil state and properties can be strictly controlled (Huang et al. [2004]). Results from CC tests are used to establish relationships between the observed outcomes like cone resistance (q_c) and material descriptors like (i) relative density, D_R (Schmertmann [1976], Houlsby and Hitchman [1988], Jamiolkowski et al. [1988], Hsu and Huang [1999]), (ii) friction angle, ϕ (Houlsby and Hitchman [1988]), (iii) state parameter ξ, (Been et al. [1987], Yu et al. [1996]), (iv) stress history, OCR (Mayne [2005]) and (v) effective stress state (vertical, horizontal or mean), σ'. However, CC are relatively large pieces of equipment, and calibration chamber testing is expensive and time consuming. Hence, the idea of complementing the physical tests with numerical equivalents seems therefore attractive. These numerical models allow internal parameters that are difficult to measure in-situ to be monitored and the additional insight that they provide into CPT-soil interaction can improve interpretation techniques.

There have been several partially successful attempts to model CPT tests in sands using finite elements Susila and Hryciw [2003], Huang et al. [2004], Ahmadi et al. [2005]. However boundary value problems involving large strain contact problems in dilatant materials remain difficult to model with continuum–based approaches Bienen et al. [2011]. One of these difficulties is the need for a relatively advanced soil constitutive models which typically requires a relatively complex calibration process. It is therefore worth exploring the potential of alternative approaches such as the discrete element method.

The distinct element method, DEM, can be a promising alternative to conventional continuum approaches for investigating the behaviour of soils and key aspects of soil material (e.g. Wang and Leung [2008]) as well to solve larger–scale engineering problems Cundall [2001], Maynar and Rodríguez [2005], Bertrand et al. [2008].

In DEM the granular material (e.g. sand) is modeled with individual particles that interact only at the contacts that may be lost or gained during penetration. The overall resistance of the artificial soil system depends on the changes in contacts between (a) device–particles and/or (b) particle–particle. Moreover, one essential feature of DEM–based models is that they can be examined at various levels of resolution, i.e. the micro–scale (derived from the basic modelling unit, i.e. contact and particle) and the meso-scale (continuum inspired variables: stress, strain). The ability to switch from

one level of resolution to another makes use of DEM–based models very attractive (Butlanska et al. [2013b]).

The first attempts to apply DEM to model cone penetration tests were performed using 2D elements, or disks Huang and Ma [1994], Calvetti and Nova [2005b], Jiang et al. [2006b]. This dimensional restriction was imposed on the modelers because of the high computational cost of 3D DEM modelling. Many interesting results were obtained, but, for the most part, the comparison with tests on real soils remained qualitative rather than quantitative. Only recently Butlanska et al. [2010b] more realistic 3D simulations of the CPT problem have been achieved. Arroyo et al. [2011] showed that a CPT performed in a virtual calibration chamber (VCC) filled with a discrete analogue of Ticino sand resulted on steady state penetration values that were in close quantitative agreement with predictions based on correlations previously established in physical chambers. Such correlations between tip resistance, initial mean stress and density Jamiolkowski et al. [2003] are still the cornerstone of much practical field work interpretation and the agreement noted was therefore encouraging. Similar work, but with a somewhat different emphasis, was recently presented by Mcdowell et al. [2012], Lin and Wu [2012].

In this thesis a numerical technique is adopted to simulate granular material as a three dimensional assembly. The particles are design as spherical (with inhibited rotation) and granular assembly modeled as a linear elastic perfectly plastic material. The cone penetration mechanism is simulated using DEM implemented in the PFC^{3D} code of ITASCA Group. The DEM allows (i) generating various numerical models with different initial conditions, geometries and boundary conditions and hence (ii) to investigate many aspects of penetration process in granular material (micro–and macro–behavior) with a relative low cost. Moreover, calibration of PFC^{3D} model is straightforward and easy to perform. Only four micro–parameters need to be adjusted, viz. the normal and tangential stiffnesses (k_n and k_s), the interparticle friction (ϕ_μ) and damping (δ), to fit the numerical results to the experimental ones (e.g. triaxial compression tests).

The numerical modeling of calibration chamber and cone device allows for the extension and extrapolation of a physical test series. It allows qualitative comparison with macro–scale observations on physical tests in sands: the observed macro–scale effects of soil initial density, of the vertical stress applied, of the radial boundary condition and of particle shape on cone penetration can be captured in the models. Hence, the connection between scales might sometimes be made directly from micro–scale observation to macro–scale response.

1.2 AIM & OBJECTIVES

The motivation for the current was to discover if 3D DEM–based virtual calibration chambers for in–situ tests are feasible on current desktop computers and can in future partially replace physical testing. The research is aimed to perform a series of numerical simulations of the cone penetration tests in discrete 3D system in order to assess a mechanism of penetration process. The basic objectives of this work are: The research is aimed to perform a series of numerical simulations of the cone penetration tests in discrete 3D system in order to assess a mechanism of penetration process. The basic objectives of this work are:

1. Study of the existing methods used to analyze CPT, especially calibration chamber testing and numerical methods;
2. Constructing a DEM model that can reproduce physical calibration chamber results;
3. Account for the model inhomogeneities and explore model symmetry;
4. Determine the influence of initial conditions on penetration mechanism and macro results;
5. Examine the stress–strain response of the model induced by the penetration process;
6. Evaluate effects of boundary conditions, chamber/cone geometries and relative particle sizes on the macro/micro response.

1.3 OUTLINE OF THE THESIS

The material presented in this thesis is contained within ten chapters, from which the first and the last one are the introduction and conclusions, respectively. Many of the aspects raised in thesis are already published in the conference proceedings and journals listed in the Publications list.

The point of departure for this thesis was the revision of already existing methods used for CPT analysis in sand. Hence, in *Chapter 2* the current interpretation procedures and results are described including analytical and semi-analytical methods (bearing capacity method, cavity expansion method and strain path method) empirical methods (calibration chamber method) and numerical methods (finite element and distinct element methods). In *Chapter 3* we focus on calibration chamber testing (empirical method) performed in sand. Therein, one of the largest CC CPT testing campaign performed at the geotechnical laboratories of ENEL-CRIS, Milan and ISMES, Bergamo, Italy is recalled. The basic information about apparatus, used materials and main results are presented. *Chapter 4* contains the fundamentals of distinct element method (DEM) as implemented in $\mathrm{PFC}_{3\mathrm{D}}$, features of $\mathrm{PFC}_{3\mathrm{D}}$ and also the method of 'translating' micro-to-macro behavior. In *Chapter 5* we present the approach used to construct the virtual calibration chamber (VCC CPT) models. In addition, the calibration of the micro-parameters (DEM parameters) is explained as an essential step for realistic simulations of material behavior. Next, the validation of the model based on triaxial compression tests is also performed. The last two sections explain the need for introducing model simplifications (chamber and cone dimensions, grain size). Finally, the VCC CPT model is set up. The homogeneity and symmetry of the model are investigated in *Chapter 6*. *Chapter 7* deals with the macro-response of the VCC CPT model via. penetration curves for different initial model settings. The micro-response of the model, for different initial inputs, is explored in *Chapter 8*. *Chapter 9* investigates the problems and limitations observed in the CC testing viz. types of servo-controls, cone/chamber size and boundary condition effects and relative particle size effects (at macro and micro-level). Conclusions and recommendations for future work are placed in *Chapter 10*.

2

CPT TESTING IN SAND

2.1 INTRODUCTION

Due to difficulties in extracting undisturbed sand samples for laboratory testing, in–situ testing techniques are widely used to characterize the engineering properties of granular soils. One of the fastest and more reliable devices used in geotechnical engineering for site investigation, to explore soil profiles and to measure *in situ* soil properties is the cone penetration test (Figure 1). The CPT soundings can be used either as a replacement of or as a complement to conventional rotary drilling and sampling methods. During cone penetration, a steel rod equipped with the cone probe (Figure 2) is hydraulically pushed into the ground at a constant rate and continuous or intermittent measurements are taken via electronic readings of cone tip resistance, q_c, and sleeve friction, f_s. Additional sensors can be provided to increase the number and type of measurements taken: pore water pressure, resistivity, inclination, and shear wave velocity, as well as a number of environmental measurements (gamma, pH, salinity, temperature, etc.). The continuous nature of CPT readings permits clear delineation of various soil strata, their depths, thicknesses, and extent. Cone penetration tests can be advanced into most soil types ranging from soft clays and firm silts to dense sands and hard overconsolidated clays. During field CPT, the sleeve friction is used to calculate friction ratio ($FR = R_f = \frac{f_s}{q_t} * 100\%$) that is used as a simple index to identify soil type (Mayne [2007]). In clean quartz or siliceous sands (comparable parts of quartz and feldspar), it is observed that friction ratios are low: $R_f < 1\%$, while in clays and clayey silts of low sensitivity, $Rf > 4\%$. However, in soft sensitive to quick clays, the friction ratio can be quite low, approaching zero in many instances. The results can be interpreted within different theoretical frameworks or using empirical methods, or both. At least 20 different CPT soil classification methods have been developed, including well–known methods in Begemann [1965], Schmertmann [1978], Robertson [1986], Robertson and Campanella [1983] and Robertson [1990].

In this chapter we describe a set of methods which are normally used to analyze cone penetration test results. Emphasis is given to those methods applied for granular material (sand). In that kind of material, the penetration is generally drained with no excess pore pressure generated during the test (Lunne et al. [1997]). We also provide the basic ideas behind each method. At the end we summarize previously performed numerical simulations of CPT using as a tool FEM as well as DEM. Some parts of this chapter are published in article [3] from the publications list (page ix).

2.2 CURRENT INTERPRETATION PROCEDURES

The cone penetration process has been modeled by a number of different approaches, which can be divided in three main categories: (i) analytical and semi–analytical methods, (ii) numerical methods and (iii) empirical methods. The most widely used theories are (see Yu and Mitchell [1998]):

1. Analytical and semi–analytical methods
    - Bearing Capacity Method (BCM)
    - Cavity Expansion Method (CEM)
    - Strain Path Method (SPM)
2. Numerical Methods
    - Finite Element Method (FEM)
    - Distinct Element Methods (DEM)
3. Empirical Methods
    - Calibration Chamber Method (CC)

While each of these methods may be used alone for cone penetration analysis (Yu and Mitchell [1998]), better prediction of the cone penetration mechanism might be obtained by some combination of these methods. Successful analyses were performed combining CEM+SPM and CEM+BCM (Salgado et al. [1997]), SPM+FEM (Teh and Houlsby [1991]), CEM+FEM (Abu-Farsakh et al. [2003]). This section deals with the general ideas laying behind these approaches and their capabilities and limitations.

2.2.1 *Analytical and semi–analytical Methods*

2.2.1.1 *Bearing Capacity Method (BCM)*

Bearing Capacity was one of the first methods applied to analyze CPT. In it, the cone resistance, q_c, is assumed to be equal to the collapse load of a deep circular foundation in soil. Two analytical approaches can be recognized, viz. (i) limit equilibrium and (ii) slip–line analysis respectively. The former method assumes a failure mechanism at first (Figure 3) and then global equilibrium of the soil mass is analyzed to determined the failure load (see for e.g. Meyerhof [1961], Durgunoglu and Mitchell [1975]). However, this method ignores effect of soil stress–strain behavior and requires the use of shape factors to convert from wedge to cone penetration (from plain strain to axisymmetric solution). The latter method combines yield criterion with the equations of equilibrium to give a set of differential equations of plastic equilibrium in the soil mass. From these basic slip–line differential equilibrium equations, a slip–line network (Figure 4) can be constructed and the collapse load determined. Example of this approach can be found in Sokolovskiĭ, V.V. [1965], Simone and De Golia [1988], Houlsby and Wroth [1982], Janbu and Senneset [1974].

The main limitation of BCM (see Yu and Mitchell [1998]) are: (i) deformations of the soil are neglected and hence the relation of soil stiffness and compressibility with cone resistance cannot be established, (ii) analysis ignores the influence of the cone penetration process on the initial stress state around the shaft, (iii) the slip–line analysis is more rigorous than limit equilibrium method in the sense that the latter method only satisfies the global equilibrium inside the slip line network region, while the stress distribution outside this region is not defined. To overcome these limitations, other methods have been investigated. Examples of some bearing capacity solutions for both cohesive and cohesionless materials can be found in Table 1.

2.2.1.2 *Cavity Expansion Method (CEM)*

The similarity between *Cavity Expansion* and cone penetration was first pointed by Bishop et al. [1945] after series of experimental tests on the indentation of ductile materials by cylindrical punches with conical heads. The authors observed that the pressure required to produce a deep hole in elastic–plastic medium is proportional to that necessary to expand a cavity of the same volume under the same conditions. The use of cavity expansion method to predict cone resistance requires two 'ingredients': (i) a theoretical (analytical or numerical) limit pressure solution for cavity expansion in soils and (ii) a relation between cavity limit pressure and cone resistance (Figure 5). The advantages of CEM is that it allows both elastic and plastic deformations of the soil during penetration to be taken into account and is able to consider (in an approximate manner) both the influence of the cone penetration process on the initial stress state and the effect of stress rotation that occurs around the cone tip. Some semi–empirical relationships proposed to relate the cone resistance to the cavity expansion limit pressure are collected in Table 2.

2.2.1.3 *Strain Path Method (SPM)*

The *Strain Path Method* known as the *Steady State Theory* is an approximate analytic technique to predict soil disturbance caused by piles or penetrometers in the ground and to define the cone resistance. The soil is treated as a viscous fluid and the flow field is establish from potential function. The assumption of SPM is that the deformations and strain fields caused during penetration process are kinematically constrained and can be estimated independently from the actual constitutive properties of the surrounding soil by differentiating the velocity flow. The soil deformations and strains are independent of the shearing resistance of the soil. Due to that the penetration process became essentially strain–controlled. The steady state solution procedures can be found in following papers Baligh [1985], Houlsby et al. [1985], Teh [1987], Whittle [1992] and Yu [2000]. Some examples of steady state solutions for cone resistance in cohesive soils can be found in Table 3.

The SPM can be considered to be superior to the CEM, since it accounts for the two dimensional nature of the penetration process. However, the SPM assumes no volume change in the soil during penetration. Therefore, all applications of the methods have been to the case of undrained penetration, which is out of the scope of this thesis.

2.2.2 *Empirical Methods*

A large number of CPT interpretation methods (already presented above) are available, however, none of them fully account for the complexity of the problem. The interpretation of the CPT depends largely on empirical correlations based on experience. That is why, over the years there has been a high demand for validated correlation between cone tip resistance and engineering soil properties.

For cohesive soils, where penetration is undrained, the tip resistance is often correlated with vane shear strength or undrained shear strength obtained from laboratory testing on undisturbed undrained clay sample. Some examples of these correlations are collected in Table 1 to Table 3.

Undisturbed sampling of clean sands is now possible using special one–dimensional freezing methods (Mayne [2006]), but at great expense associated with time and special costly equipment. Thus, it is quite difficult to obtain undisturbed sand sample and hence, similar correlations are not possible. Instead, the CPT measurements are performed in laboratory calibration chamber (CC) under strictly controlled conditions. This method allows many parameters to be controlled and accounted for, including sand density (D_R), state parameter (ξ), drained shear strength of sand (C'), constrained modulus (M), Young's modulus (E), the small strain shear modulus (G) and stress state (K_0). The CC offers an experimental or empirical way to interpret results of CPT. These empirical correlations may be divided in the following categories (after Yu and Mitchell [1998]):

I correlations in terms of relative density ($D_R - \sigma'$)–Schmertmann [1976], Houlsby and Hitchman [1988], Jamiolkowski et al. [1988], Hsu and Huang [1999]

II correlations in terms of friction angle ($\phi - \sigma'$)–Houlsby and Hitchman [1988]

III correlations in term of state parameter (ξ)–Been et al. [1987], Yu et al. [1996]

IV correlations in terms of stress history (OCR-ϕ)–Mayne [2005]

In the first category (**I**) the q_c was assumed to be primarily dependent on relative density and stresses: (i) vertical–Schmertmann [1976], (ii) horizontal–Houlsby and Hitchman [1988] and (iii) mean–Jamiolkowski et al. [1988], Hsu and Huang [1999]. In the second category (**II**) the q_c was assumed to be primarily dependent on the horizontal stress and friction angle. In third category (**III**), the q_c was assumed to be dependent, to both state parameter and (i) mean stress–Been et al. [1987], (ii) cylindrical cavity limit pressure–Yu et al. [1996]. In the fourth category, the q_c was assumed to be dependent to overconsolidation ratio and friction angle. The summary of correlation for cone tip resistance based on calibration chamber test results can be viewed in Table 6.

Although calibration chamber testing has been widely used to establish correlations between cone tip resistance and soil properties, there are some issues which make the q_c differ from that measured in the field. This difference is mainly caused by (i) limited size of chamber, (ii) boundary conditions imposed in the chamber, (iii) uniqueness of the correlation (correlation obtained for one sand cannot be generally applied to another soil). These and others problems/limitations of calibration chamber testing as well as the main results can be found in the next chapter (Chapter 3).

2.2.3 *Numerical Methods*

The cone penetration test (CPT) is a boundary value problem, which is difficult to model since it involves moving boundary conditions, large deformations, non–linear material behavior and interface behavior. An accurate analysis is essential if a correct interpretation of the test results is to be obtained.

In this summary we include results of two different approaches: (i) Finite Element Method (continuum based approach) and (ii) Discrete Element Method (Discrete particle based approach). It is expected that these methods will play an increasingly important role for analyzing penetration tests, because they have many advantages such as:

- the initial stress states can be prescribed;
- the soil stiffness and compressibility can be easily modeled;
- an increase in stress during the penetration can be easily assessed;
- the failure modes need not be assumed;
- both equilibrium equations and yield criterion are satisfied;
- the discrete behavior of granular media is modeled (DEM);
- micro–mechanics is investigated (DEM).

2.2.3.1 *Continuum based approaches*

Since the early 80's the cone penetration test in soils has been analyzed using the *Finite Element Method* (FEM). Two alternatives can be recalled:

- small strain analyses, in which the cone is introduced into a pre–bored hole, with the surrounding soil still at its in situ stress state. Next, an incremental plastic collapse calculation is carried out and the collapse load is assumed to be equal to the cone resistance. The first such analysis was performed by de Borst and Vermeer [1982] for cohesive soils. A similar analysis was later performed by Griffiths [1982].
- large strain analysis include the effects of cone penetration on initial stress condition since the cone must be pushed into ground with a vertical displacement of several times the diameter of the cone penetrometer. The examples of large strain analyses can be found in the following papers Budhu and Wu [1992], Cividini and Gioda [1988] and van Den Berg [1994].

Some times the FEM has been used in combination with other approaches like Strain Path Method (Teh and Houlsby [1991]) or Cavity Expansion Method (Abu-Farsakh et al. [2003]). However, they do not always give correlation between the cone factors and soil type but they do provide a check of the factors affecting the cone resistance and the verification of empirical relations and what is more important, a better understanding of the penetration process. Because cone penetration involves finite deformation of the soil and large scale sliding at the penetrometer –soil interface, numerical modeling of it is quite difficult and various approximations are adopted. For instance, de Borst and Vermeer [1982] performed finite element analysis of cone penetration assuming small strains which exclude mentioned numerical difficulties. However, as was pointed out by Houlsby et al. [1985], in the conventional small strain finite element analyses (de Borst and Vermeer [1982]), the cone shaped object is placed in pre–bored hole and the fact that the cone is continuously penetrating is ignored and in consequence effects of displacement, strain and material rotation are also ignored. Moreover, this method is unable to generate the necessary residual stress field around the cone and therefore the ultimate cone resistance is achieved inappropriately. In order to simulate sufficient displacement, a large deformation model is essential (Kiousis et al. [1988], Teh and Houlsby [1991], van Den Berg [1994], Yu et al. [2000], Susila and Hryciw [2003], Abu-Farsakh et al. [2003], Huang et al. [2004], Lu [2004], Lu et al. [2004]), Wei et al. [2005].

From the papers presented in Table 4 we can read that some of the analyses present numerical simulation tests of fully drained tests (in sand) in terms of effective stresses and some–fully undrained (in clay) in terms of total stresses. In the CPT numerical investigations soil stress–strain behavior has been described using constitutive models based on classical and critical state soil mechanics and conventional plasticity theory. Elastic behavior was assumed to be either linear or non–linear and the plastic zone was modeled as perfect plasticity with Tresca, Mohr–Coulomb, von Mises, Drucker–Prager yield functions.

To avoid frequent re–meshing in the large strain finite element calculations, two techniques have been adopted: (i) a conventional Updated Lagrangian method (see Yu et al. [2000], Abu-Farsakh et al. [2003], Wei et al. [2005]) and (ii) Arbitrary Lagrangian Eulerian formulation (ALE) (e.i. van Den Berg [1994], Susila and Hryciw [2003], Lu [2004], Lu et al. [2004]). The first technique uses a Lagrangian formulation and when the mesh distorts it is adapted using special re–meshing techniques. In ALE, the evolution of the mesh and material particles are uncoupled and the mesh evolution is constrained so that excessive mesh distortion is avoided (Hamel [2000]).

In the first numerical investigations the initial stress states were assumed isotropic (see Kiousis et al. [1988], van Den Berg [1994], Yu et al. [2000]), while we know that this is not the case for most of the naturally consolidated soils. To investigate the effect of initial stress anisotropy on *in situ* soil stresses and its effect on the cone factor, some investigations were performed (Teh and Houlsby [1991], Susila and Hryciw [2003], Abu-Farsakh et al. [2003], Wei et al. [2005], Huang et al. [2004], Lu [2004]). Moreover, some of the authors adopted a special models which include soil anisotropy; Wei et al. [2005] used an anisotropic modified Cam Clay model (Defalias [1987]) that consider both the initial stress anisotropy and the induced anisotropy (hardening anisotropy). Based on that, it was concluded that the cone resistance is controlled more by the horizontal stresses than the vertical stresses (i.e. Ahmadi [2000], Teh and Houlsby [1991]).

For numerical purposes, in some analyses the penetrometer was assumed to be initially pre–bored (Kiousis et al. [1988], van Den Berg [1994], Abu-Farsakh et al. [2003], Lu [2004], Lu et al. [2004], Wei et al. [2005]) while others the penetrometer started penetration from the top of the layer (Susila and Hryciw [2003], Huang et al. [2004], Ahmadi [2000]).

For the soil–device interface behavior (tip–soil and shaft–soil), some researches proposed either smooth (Kiousis et al. [1988], Teh and Houlsby [1991], van Den Berg [1994])–test in clay (Lu [2004], Lu et al. [2004]) or frictional contact (de Borst and Vermeer [1982], Van Den Berg et al. [1996])–test in sand (Yu et al. [2000], Susila and Hryciw [2003], Wei et al. [2005], Huang et al. [2004], Lu et al. [2004]) while the other have employed a special interface model (Abu-Farsakh et al. [2003]). In Ahmadi [2000] the penetrometer itself was not modeled. The studies showed that the interface friction have a significant effect on the computed cone resistance. In most analyses the cone steel was modeled as a rigid body.

In following paragraph we describe in more detail the results obtained by numerical simulations of CPT in sands.

NUMERICAL RESULTS OVERVIEW: SAND

Numerical analysis of CPT in sands have focused on several aspects of the problem:

- identification of the steady state;
- the evolution of the stress distribution around the cone;
- extent of the plastic zone;
- the cone factor (N_k) evaluation;
- effect of the in situ stress;
- effect of the cone (shaft) roughness;
- effect of the soil rigidity index

Van Den Berg et al. [1996] adopted a large strain Eulerian finite element method to simulate static soil penetration in a two–layered system:

A) clay on sand

B) sand on clay.

The soil was obeying a non–associated Drucker–Prager criterion. The penetration process was initiated by applying incremental material displacement at the lower boundary of mesh while the cone was modeled as a fixed boundary and soil material was moved upward through the mesh (Figure 6). Special interface elements were used with the Coulomb model describing the friction mechanism.

The authors performed two series of simulations. The first studied cone penetration from (soft) clay into a (stiffer) sand layer and the second system studied penetration from a sand layer into a clay layer. The first simulations (clay on sand) showed that 15 cm penetration into the sand layer were needed to reach a new steady state cone resistance ($\sim 4d_c$) while in the second group of simulations (sand on clay) it was observed that around 20 cm of penetration was needed to reach steady state in clay. Moreover, for this particular case (case b), the cone resistance started to drop at a distance of about 10 cm above the clay boundary. Authors examined influence of stiffness ratio between the sand–clay and clay–sand and it was found to play an important role on the results (cone resistance). However, the authors emphasized that their study was of a qualitative nature and no attempt was made to compare with physical results.

Susila and Hryciw [2003] employed a finite element model based on a large strain formulation to study cone penetration in normally consolidated sand. A non–associated Drucker–Prager model was employed to represent sand behavior. To handle the large distortion of sand surrounding the cone an auto–adaptive remeshing technique (applied only to the soil close to the cone) was adopted and was found to maintain a high–quality mesh and avoid numerical problems. The cone–soil and the shaft–soil interfaces were modeled as frictional. The cone (d_c = 18 mm) was modeled using elastic elements (not rigid body) and was introduced at the top of the soil mesh (not to a pre–bored hole). Penetration was achieved by vertical movement of the cone with a constant velocity of 2 cm/s. The finite element model for the analysis can be seen in Figure 7. The authors performed a parametric study to examine the effects of the internal friction angle (ϕ) and the initial effective overburden stress (σ'_o) on

the cone tip resistance (q_c). They presented the following results: (i) evolution of the tip resistance with penetration, (ii) typical sleeve friction versus penetration plot, (iii) distribution of sleeve friction along cone and shaft and (iv) typical soil stress contours. The authors noticed that for different ϕ and σ'_{vo} the steady–state penetration depth varied from 90–350 mm. The conclusion was that dense sand required greater penetration distance to reach steady state than loose sand (hence confirming a result from Van Den Berg et al. [1996]). The reason of this phenomena was that the volumetric strain near the cone was greater for loose sand, therefore the radial displacements decreased much sooner with distance for loose sand. Hence, in dense sand, tip resistance was affected by the soil within a 600–800 mm (16–22 d_c, d_c–cone diameter) zone above and below the cone tip while in loose sand the zone was approximately 180–260 mm (5–7d_c).

The typical friction resistance, f_s, at the center of the sleeve and a distribution of resistance along its length were found to follow the non–uniform distribution pointed previously by Kiousis et al. [1988]. Moreover, a thin separation between soil and cone shaft interface (at the cone shoulder) was also observed. This finding supported a recommendation to move the location of the cone sleeve further from the cone tip. The contours of normalized effective vertical stresses and normalized effective horizontal stresses surrounding the cone tip increased greatly due to penetration. Moreover, it was observed that immediately above the cone tip there was an area of slightly lower horizontal stress, which partly explained the lower sleeve friction resistance measured on the sleeve friction elements just above the cone.

The finite element model presented by the authors was compared with previous models (bearing capacity, cavity expansion and calibration chamber). Figure 8 shows that numerical results compare very well with other methods, especially with the experimental chamber test results for normally consolidated Ticino sand (Ghionna [1984]).

Huang et al. [2004] performed a finite element analysis of cone penetration tests in cohesionless soils. The penetrometer (d_c = 35.7 mm) was idealized as a rigid body and the soil as an elastic perfectly plastic material obeying Mohr–Coulomb yield criterion. The authors used commercial finite element program ABAQUS for FE calculations. This software uses a concept of a *master surface* and a *slave surface*, with the former being able to penetrate the latter. Hence, the surface of rigid body was defined as the master surface, while the potential contact surface in the soil body was deemed to be the slave surface. The elastic deformation was described by the elastic modulus E (or the shear modulus–G) and Poisson's ratio υ, while the plastic deformation was characterized by the friction angle ϕ and dilation angle ψ. A non–associated flow rule was used to simulate the dilatant behavior of the soil. The penetration process was modeled realistically through a frictional element which allows sliding. The penetration process was simulated by applying incremental pressure force to the nodes representing the cone boundary (left side of the mesh). The finite element mesh for the analysis can be seen in Figure 9.

A parametric study was performed to illustrate the influence of various factors, including soil stress state, shear modulus, friction angle and dilation angle on the cone resistance at the steady state. It was observed that the steady state was reached sooner at higher stress level (p_0) and the cone resistance increased linearly with p_0.

The FEM results were compared with twov previous solutions based on: (i) a bearing capacity approach (Robertson and Campanella [1983]) and (ii) a theory of cavity expansion (Salgado et al. [1997], Vesic [1977], Yu and Houlsby [1991]). The comparison can be viewed in figures 10, 11 and 12. It was shown that numerical result was more similar to those obtained by cavity expansion problem than a bearing capacity problem. The deformation mode of the soil around the cone, as well as the plastic zone were found to be similar to that caused by cavity expansion. The modulus G was found to play a significant role on cone resistance values. Further studies showed also the dependence of the cone resistance on the ϕ and the ψ. It was found that an increase in ψ gave a higher increase in q_c than that of ϕ.

Ahmadi [2000], Ahmadi et al. [2005] proposed a numerical modeling procedure to evaluate cone tip resistance in sand. The procedure involved a moving boundary simulating cone penetration. The Mohr–Coulomb elastic–plastic model was chosen as a material model. The parameters needed for the model were: shear and bulk modulus (G and B) or constrain modulus and Poisson's ratio (M and ν) and friction and dilation angle (ϕ and ψ). In contrast to previously described analysis, this procedure is displacement controlled (not stress–controlled). The penetration process is defined by imposing vertical and horizontal displacement to the nodal points of inner boundary (Figure 13). In that sense the cone device was not modeled as such.

The procedure was verified by comparing predicted numerical values of cone tip resistance with experimental database of cone tip resistance measured in calibration chamber on Ticino sand (ENEL–CRIS) (Lunne et al. [1997]) for different boundary conditions (BC1 and BC3). The error band between predicted and measured results was $\pm$ 25%. The comparison between predicted and measured cone tip resistance can be viewd in Figure 14. The analysis showed that the in situ horizontal stress is a major factor in tip resistance; for different vertical stresses and same horizontal stress the cone resistance resulted with similar cone resistance value. This finding was in agreement with calibration chamber results. The author conclude that the cone resistance was mostly a measure of the soil modulus and the dilation angle and this finding was in a agreement with the work performed by Huang et al. [2004]. Moreover, the analysis showed that cone resistance marginally increases with a change (increase) in friction angle.

Although the model parameters selected were generally realistic, the authors state that the results obtained in their study required further verification.

2.2.3.2 *Discrete based approaches*

The *Discrete Element Method* (DEM) is a promising alternative to conventional continuum approaches (FEM) for analyzing boundary value problems involving large deformations. DEM was developed by Cundall and Strack [1979] as a novel method based on the mechanical interaction of discontinuous bodies. The behavior of the soil is modeled as the outcome of the particle and contact properties. In this method no mesh is required and so no special approach to define cone–soil interactions is needed. An intrinsic feature of DEM is their ability to make and break contacts. Therefore, they are well suited to modeling problems involving large displacements or localizations. However, the limitation of DEM is its high computational cost which is directly linked to the number of particles.

In this section, only the results from a previously performed DEM–CPT analyses will be recalled. The fundamentals of the DEM can be found in Chapter 4. Few studies have been carried out on DEM analyses of CPTs on granular materials. Huang and Ma [1994] were among the first to apply DEM to simulate CPT in sand in 2D. Most recent works modeling penetration test using DEM are of Calvetti and Nova [2005a], Jiang et al. [2006b] and thoes published in Powders & Grains conference proceedings (Breul et al. [2009]). The summary of the DEM–CPT analyses can be seen in Table 5.

NUMERICAL OVERVIEW OF PREVIOUS RESULTS

Huang and Ma [1994] proposed a numerical technique coupling the DEM and boundary element method (BEM) to simulate a granular soil deposit as a two –dimensional, circular disk assembly. Only half on the penetrometer and soil mass were simulated. In the BEM region the material was modeled as a linear elastic solid that extends outwards to infinity. Properties of DEM disks were described with normal and shear contact stiffness and interparticle friction with values mentioned in Table 5. The disk assembly was generated by simulating a pluviation process. After pluviation, the assembly was consolidated under K_o conditions. The cone penetrometer with 60^o apex. and radius of 5 mm was inserted into soil mass with penetration rate of 20cm/sec. The friction sleeve had a length of 133.8 mm ($3.75d_c$)

The authors performed three simulations for different lateral dimensions of DEM regions ($4d_c$, $8d_c$ and $12d_c$,) and one test for overconsolidated sample with OCR equal 10 and under different boundary conditions, whether the stresses or strains are kept constant (named as BC1, BC3 (Figure 21) and BC5). Boundary condition BC5 is referred to the simulated field conditions, where the soil extends laterally to infinity and is achieved by coupling DEM/BEM. Macro–and micro–analyses were performed. Due to limited computational resources, the authors obtained evolution (in time) of (i) deformation, (ii) velocity, (iii) stresses, (iv) displacement fields and (v) stress path only for one penetration depth (=$4d_c$).

The q_c profiles showed a rather 'noisy' response with the coefficient of variation exceeding 8.9%. The results for the lowest number of particles (3000) showed the trend of increasing q_c with depth (boundary proximity effect: lateral wall is positioned $4d_c$ from the axis). The horizontal stress measurement (taken for the entire embedded cone) showed stress reduction just behind the cone base. As a consequence the FR [1] started low and then increased with depth. The same horizontal stress reduction was observed in FEM analysis performed by Susila and Hryciw [2003]. The authors did not observe a significant difference (only 6%) in measured horizontal stress evolution for NC and OC tests.

Examination of the micromechanics showed that the contact forces (CF) were concentrated in the vertical direction below and around the face of the penetrometer tip and that the CF were slightly more laterally widespread in the OC than in the NC assembly. Moreover, for NC, the disk movement followed a pattern that was similar to the failure mechanism shown in Figure 3c with large disk movements concentrated in areas below the cone base. The magnitude of disk movements for OC assembly was less than for NC. The disk movements were confined in a smaller area, but extended

1 FR - friction ratio defined as a ratio of shaft resistance to cone resistance in % ($\left(\frac{f_s}{q_s}\right)100\%$)

above the cone base. The failure mechanism was between those of Figure 3b and Figure 3d. The average contact stress in two measurement zones (Figure 15) indicated that the increase in coordination number was more significant for smaller disks.

Typically in geomechanics we interpret soil response within a continuum mechanics framework (i.e. in terms of stress and strain). To be able to "translate" DEM results (forces and displacements) into continuum variables a homogenization algorithm is required. The authors used a linear approach for strain calculation proposed by Ting et al. [1993]. The average strain tensor was computed from the derivative of particulate displacements, via solving system of equations (equations 5.2 and 5.3 in Huang and Ma [1994]). The DEM assembly was divided into 200 small 'computing zones' ($0.75d_c$ x $0.75d_c$) which contained approximately 100 disks each. The strain was averaged over these 'computing zones' and contours of strain were plotted (ϵ_{yy}, ϵ_v and γ_{oct}). In all assemblies, the material dilated in front of the cone tip. The maximum dilation in term of volumetric strain occurred at $\approx 1.5d_c$ ahead of the cone tip and its value increased with increasing OCR value. A vertical strain (ϵ_{yy}) below 2% was found along the DEM boundary for BC1 cases in OC assemblies which confirmed the suggestion (Parkin [1988]) that q_c values in OC sands are less sensitive to the lateral boundary condition in NC sands.

Stress analysis showed that in both cases (NC, OC), vertical stresses (σ_v) reduced along the face of the cone, while above the cone they stabilized at values slightly below their initial one. The peak value occurred at approximately $1r_c$ below the cone tip. The horizontal stress (σ_h) contours showed that the peak value occurred in areas adjacent to cone face and that peak value was 40% higher for OC assembly. As well as in σ_v contours, the horizontal stresses attenuated rapidly along the face of the cone. However, reduction of σ_h is faster for OC case. Moreover, the simulations have indicated that neither σ_v nor σ_h above the cone base were sensitive to the soil loading history. The FR was expected to be affected by loading history, but was too low to be a useful index for the soil in situ lateral stress. The authors made unsuccessful attempts to compare DEM results with continuum approaches, like cavity expansion and bearing capacity methods to establish correlations between soil mass properties and CPT results.

More advanced DEM analysis to study deep penetration mechanism in granular material was performed by **Jiang et al. [2006b]**. The authors focused on the effect of soil–penetrometer interface friction (frictionless/frictional or smooth/rough), by choosing different frictional coefficient μ between the tip (sleeve) and particles (i.e. μ = 0–frictionless and μ = tan(ϕ)–frictional). The 2D DEM code was used to carry out simulations on granular soil mass under amplified gravity with a K_o lateral stress boundary conditions. As well as in Huang and Ma [1994] only half of the penetrometer and soil mass was considered (Figure 16). The material used in the ground was composed of 20 disk types with the size and properties mentioned in Table 5. The multi–layer under–compaction method (Jiang et al. [2003]) was used to generate target soil assembly which consisted of 10000 particles. Two DEM penetration tests have been carried out and penetration mechanism was continuously investigated by tip resistance, deformation pattern, displacement paths, velocity vector distributions and stress field. The stresses were calculated as an average values computed over a given volume (Cundall and Strack [1979]).

The q_c profiles showed a response similar to that obtained by Huang and Ma [1994]– a rather 'noisy' q_c increasing with depth for both smooth and rough cases. The normalized q_c values by the initial vertical stresses (σ_{v0}) with the penetration depth curves showed the trend similar to that observed in centrifuge modeling (Bolton et al. [1999]). The q_c/σ_{v0} initially increased ((0 ~ 0.85)d_c), then decreased ((0.85 ~ 3.5) d_c) and finally approached a constant values ((7 ~ 12) d_c). No attempts were made to compare the obtained results with physical tests.

The analysis showed that tip–soil friction has a great influence on deformation pattern, specially near the penetrometer during all penetration levels. During shallow penetration for frictional case, the top grid section nearest to the penetrometer was dragged downward under the ground surface, while half of its top neighbor grid was pushed sideward and upward. In contrast, for frictionless case, halves of the two top grids near the penetrometer were pushed sideward and upward. In deep penetration-1, the penetration had more influence on the grids next to the sleeve than on those below the tip points. The closest grids to the tip were pushed downward and sideward, while the rest grids were pushed upward and sideward. An evident difference between smooth and rough cases was that, in the rough case, several particles in each grid being in the contact with the frictional tip (sleeve) were greatly dragged down by the device, and hence these grids were peculiarly extended and twisted. In smooth case, no such pattern was observed. During deep penetration-2, the penetration had a more influence on the grids below the tip point than those being in contact with the sleeve. Moreover, in the PR case, fewer particles in the grid close to the frictional tip (sleeve) were dragged down compared to deep penetration-1. However, the shapes of these grids were also very extended and distorted.

Displacement paths showed that penetration led to complex soil movement. Generally, increasing with the distance from the penetrometer, the distribution of horizontal displacement changed from 'penetrometer' shape to 'pear' shape. During the penetration process, the soil mass underwent several failure mechanisms (Figure 3a to Figure 3d).

Velocity analysis showed that the particle velocity increased with penetration depth during shallow penetration in the smooth and rough cases. In deep penetrations, it increased slightly in the frictional case but decreased slightly in frictionless case with penetration depth. Generally, higher soil–tip friction led to smaller value of maximum velocity in the shallow penetration, but larger in the subsequent deep penetration as that in frictionless case. Maximum velocities occurred close to the tip in frictional case and close to the sleeve in frictionless case.

As it might be expected, the penetration process had a great effect on the stress distribution in the area close to the penetrometer. The soil mass was continuously undergoing loading and unloading process and experienced a large rotation of principal stresses (180°). The stresses (vertical, horizontal) of soil close to the penetrometer increased from their initial value to a large peak stress and then decreased to constant value (slightly larger than the initial one). Generally, the frictional case led to a slightly smaller peak value but larger rotation of the stresses than frictionless case. Moreover, the authors noticed that the maximum major principal stresses occurred near the tip with the direction perpendicular to the tip. Far from the cone the stresses were controlled by the initial conditions of the ground. Large tip–soil friction led to larger stresses beneath the cone tip.

Calvetti and Nova [2005a] performed simulation of static penetration test to validate a friction angle and secant modulus (Φ–E_{50}) correlation obtained from simulation of series of biaxial tests using discrete element code PFC^{2D}. The cross–section of the simulated cone was standard (10 cm2), with cone diameter equal to 100 mm. The penetration tests were performed for various interparticle friction angles (Φ) and confining stresses (S_0). From each penetration curve, a steady–state cone tip resistance was extracted. Unfortunately, the authors did not mention the method of choosing the steady state q_c.

For a given set of contact parameters collected in Table 5, q_c was found to be larger for the denser specimen, and it increased non linearly with confining pressure. Moreover, q_c increased with increasing interparticle friction. On the contrary the stiffness of contacts had no influence on cone resistance (verified by performing a parallel series of simulations with k_N and k_S ten times larger than default). These results were in sharp contradiction with those shown by Huang et al. [2004]using FEM simulations. The authors proposed a relationship between q_c and s_0 (Figure 18a):

$$q_c = q_{c0}\left(\frac{s}{s_0}\right)^{0.8\div0.85} \tag{2.1}$$

Results obtained from biaxial compression and CPT were then used to build DEM–based correlations of q_c–Φ (Figure 18b) and q_c–E_{50} (Figure 18c). All the correlations are qualitatively similar to those proposed by various authors to interpret CPT data (i.e. Robertson and Campanella [1983]).

Breul et al. [2009] performed three–dimensional simulations of CPT in a coarse granular material. The analysis was performed to validate numerically the correlation (obtained experimentally) between cone resistance and material density (q_c–γ_d). The granular soil was modeled by spherical particles that imitated a basaltic material. The contact law between particles (and particles–cone) was defined with an interparticle friction of 0.85. The walls of the model were rigid and frictionless. The sample was created by radius expansion method (REM) and consisted of 1800 to 2200 particles. The void ratio varied from 0.72 to 0.54. The cone penetrometer was modeled by an infinitely stiff rod of 14 mm in diameter and a head apex of 90^o (Figure 19) and was driven at a constant velocity of 100 mm/sec.

During the penetrometer insertion a cone resistance as a function of depth was calculated every 2 mm. The penetrograms were similar to those obtained during a penetration test in real granular material. Moreover, the penetration curves were quite noisy and stayed in agreement with other DEM–CPT analyses (Huang and Ma [1994], Jiang et al. [2006b]). The comparison between numerical and experimental average cone resistance and density was found to be in good agreement (Figure 20). However, the numerical q_c was slightly lower than the value obtained during the experimental tests. This difference was explained by the choice of contact properties and boundary conditions.

2.3 SUMMARY

In this chapter a number of different approaches for modeling cone penetration test (CPT) were discussed. These methods were divided in three main groups (i) analytical and semi–analytical (bearing capacity, cavity expansion and strain path methods), (ii) numerical methods (continuum and discrete methods) and (iii) empirical methods (calibration chamber testing). The following remarks can be drawn:

1. Bearing capacity does not represent actual conditions because it ignores soil compressibility, stiffness and the influence of stress state around the shaft of cone penetrometer.

2. Cavity expansion takes into account soil deformations during penetration process, changes in initial stress state and the effect of stress rotation that occur around cone tip. This method can be used for both clay and sand.

3. Strain path has also been used with some success to analyze cone penetration process performed in clay.

4. Finite element method can take into account many factors affecting cone penetration process (initial stress states, soil compressibility and stiffness, increase in stress during the penetration).

5. Discrete approaches can eliminate problems concerning large mesh deformations and significant errors caused by that. DEM are using relatively simple models of the real situations. Only two journal publications are available till now. Both of them focuses on penetration mechanism and factors influencing it. However, the DEM results has not been compared quantitatively to field CPT. Moreover, the analyses were performed in 2D. It is important to recognize that real granular material is three dimensional. The effort should be put to on relating 2D models to real 3D problems.

6. Calibration chamber testing plays an important role in both verifying and establishing correlations between cone tip resistance and soil properties. This is the object of the following chapter.

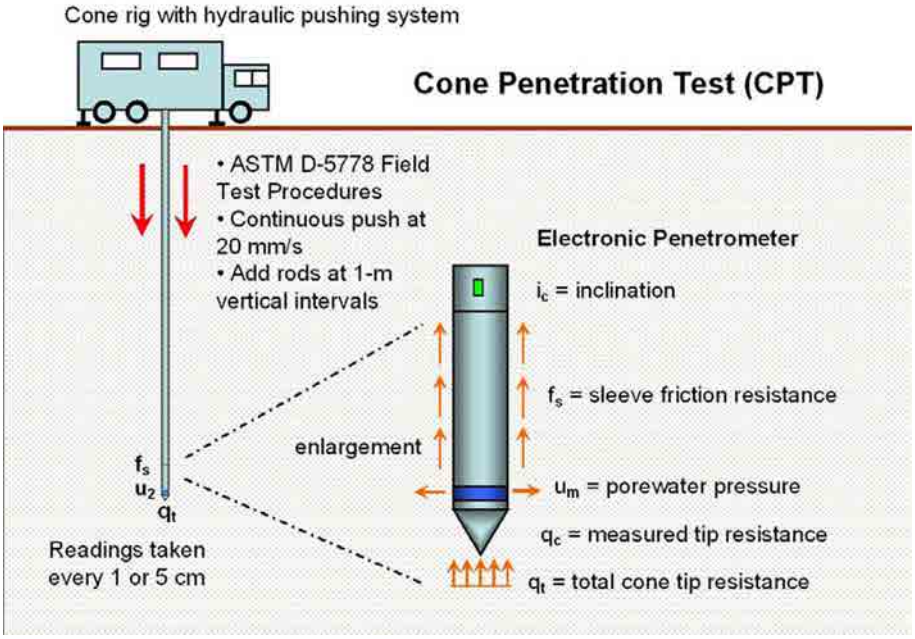

Figure 1: Overview of the Cone Penetration Test (CPT) Per ASTM D 5778 Procedure (Mayne [2007]

(a) (b)

(c)

Figure 2: Selection of Penetrometers from (a) van den Berg series; (b) Fugro series; (c) Georgia Tech collection (Mayne [2007])

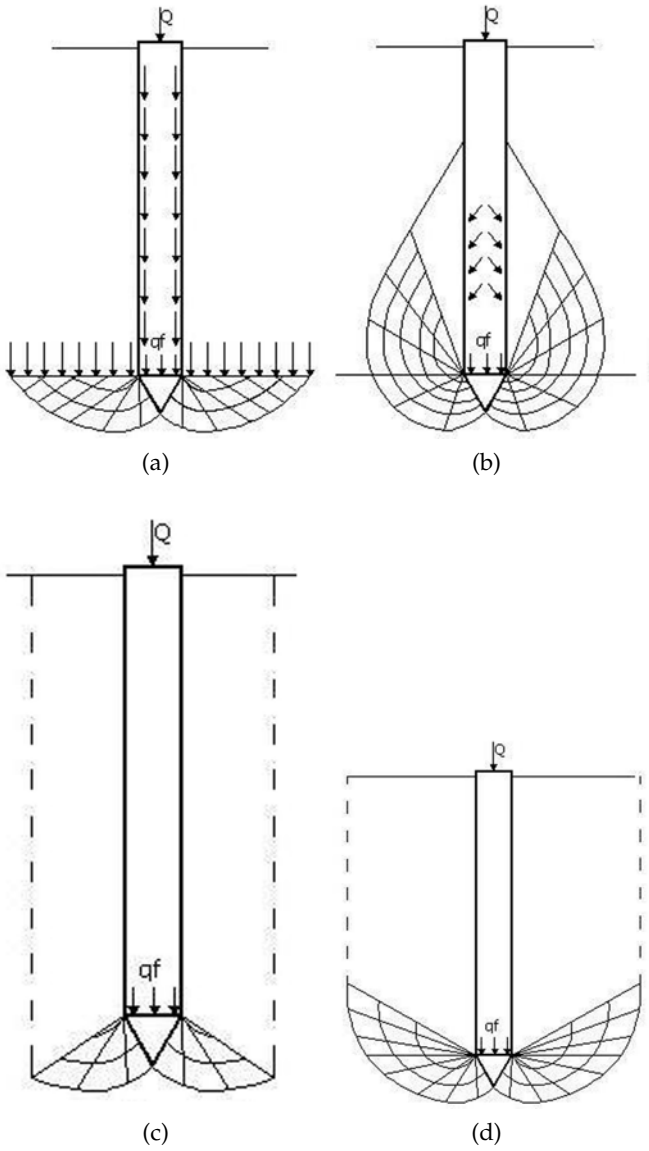

Figure 3: Assumed failure mechanisms for deep penetration (a) Terzaghi [1943]; (b) De Beer [1948],Hu [1965], Meyerhof [1951]; (c)Berezantev and Golubkov [1961],Vesic [1963]; (d) Biarez et al. [1961], Hu [1965]

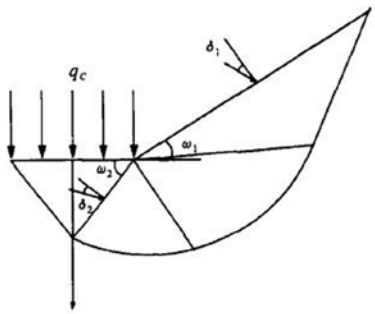

Figure 4: Slip line network for wedge and cone penetration analysis (Yu and Mitchell [1998])

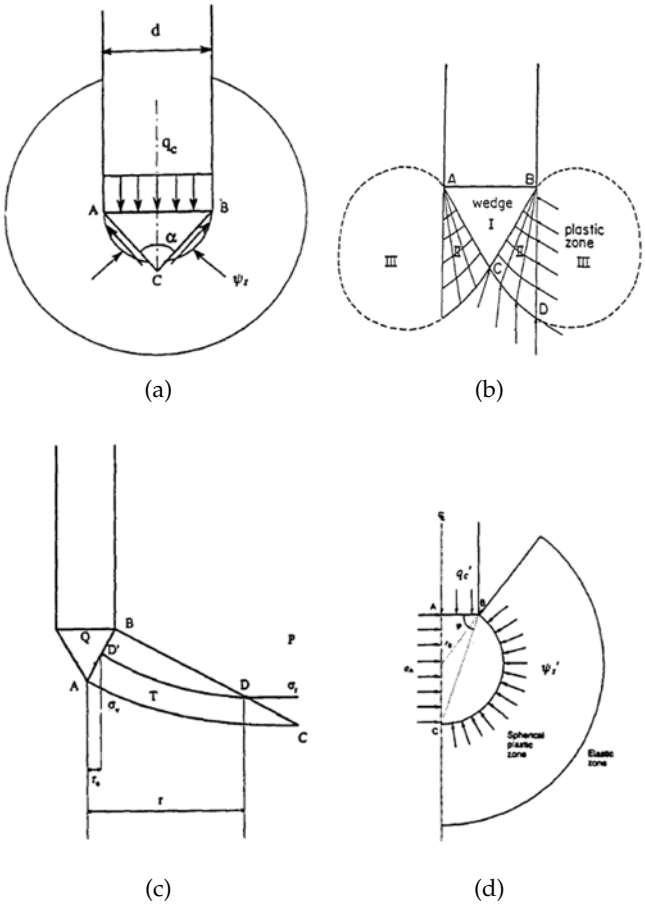

Figure 5: Assumed relationship between cone resistance and cavity limit pressure Yu and Mitchell [1998] (a) Ladanyi and Johnston [1974]; (b) Vesic [1977]; (c) Salgado [1993]; (d) Yasufuku and Hyde [1995]

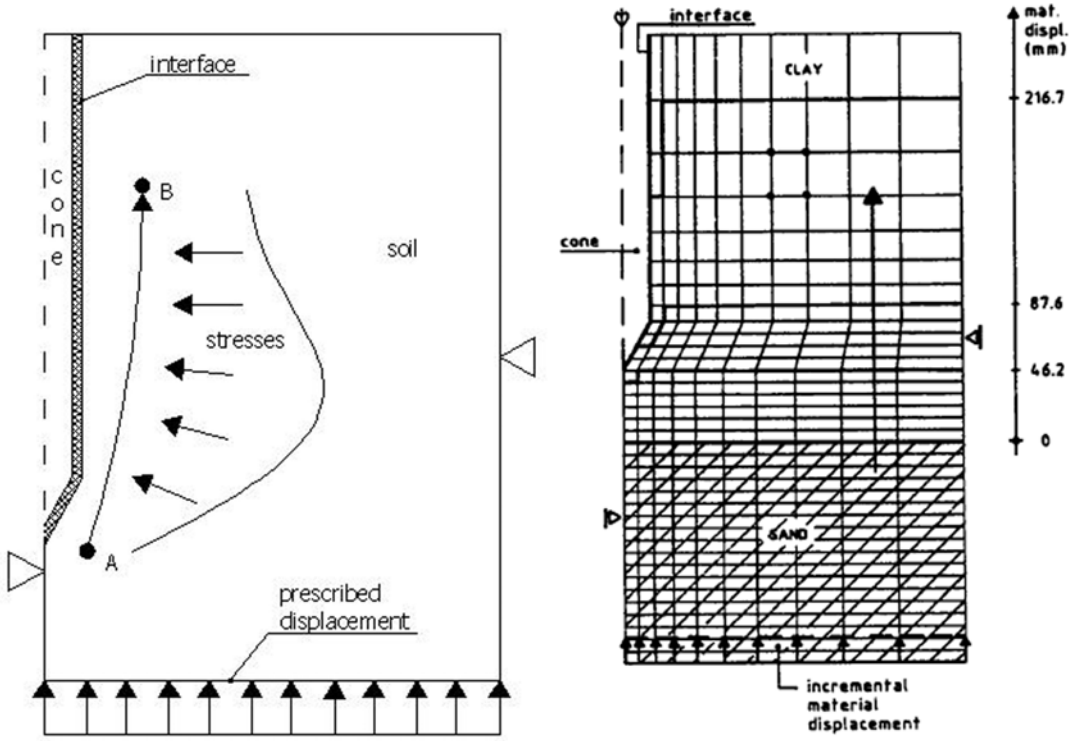

(a) (b)

Figure 6: Cone penetration problem (a) Schematic view of approach; (b) finite element mesh and localization of clay–sand boundary during penetration (Van Den Berg et al. [1996])

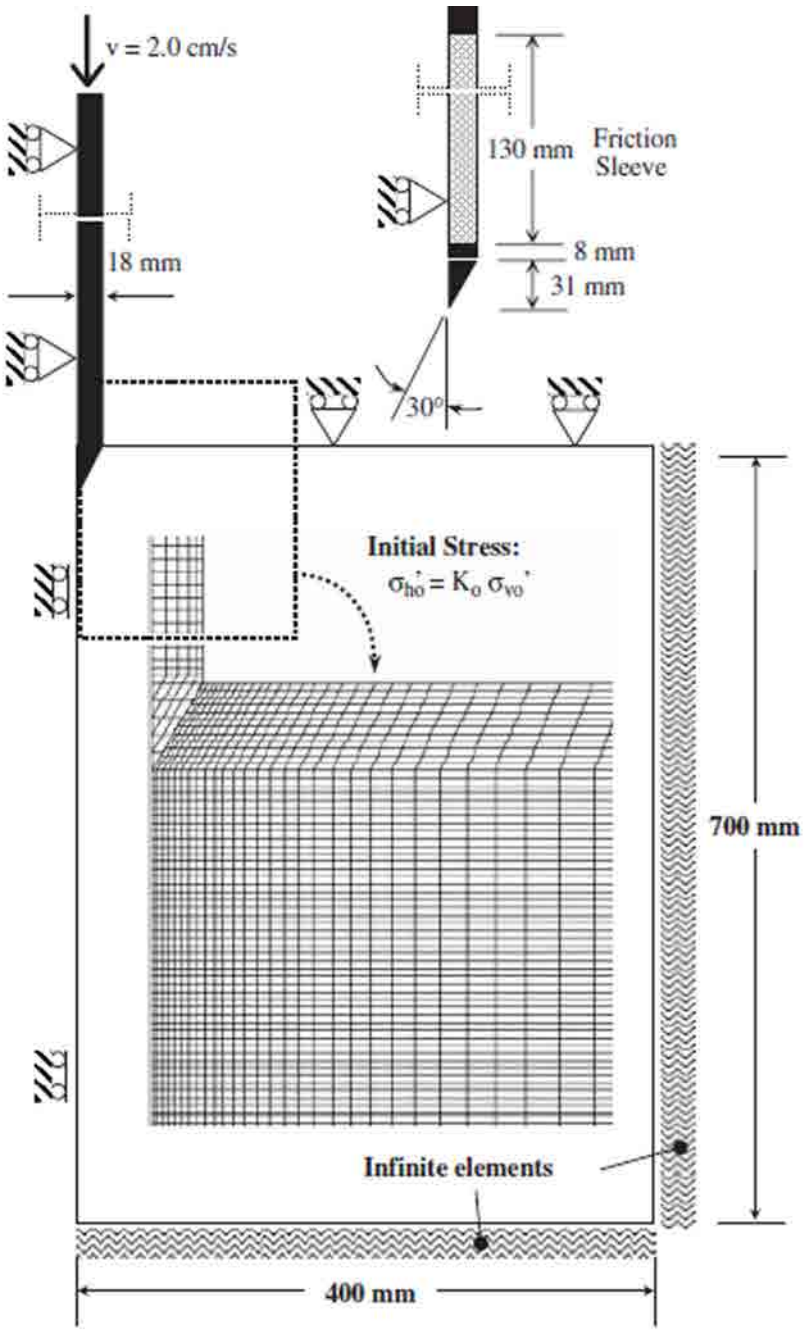

Figure 7: Finite element mesh, geometry, initial positions and boundary conditions (Susila and Hryciw [2003])

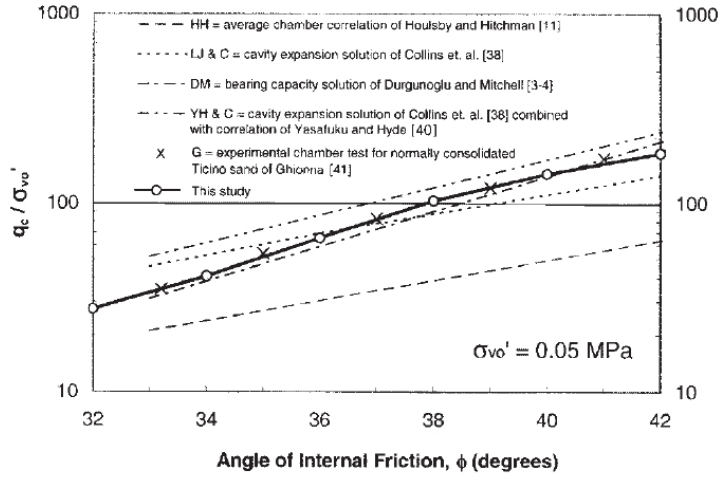

(a)

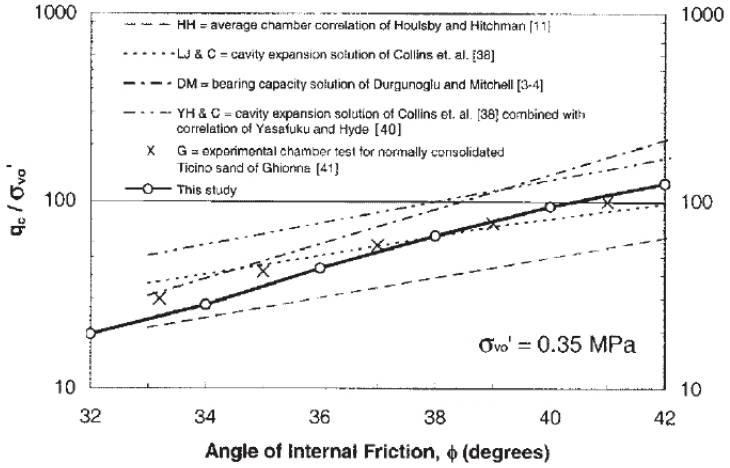

(b)

Figure 8: Comparison between FEM results with previous model (after Yu and Mitchell [1998]): (a) σ_{v0} = 0.05 MPa, (b) σ_{v0} = 0.35 MPa

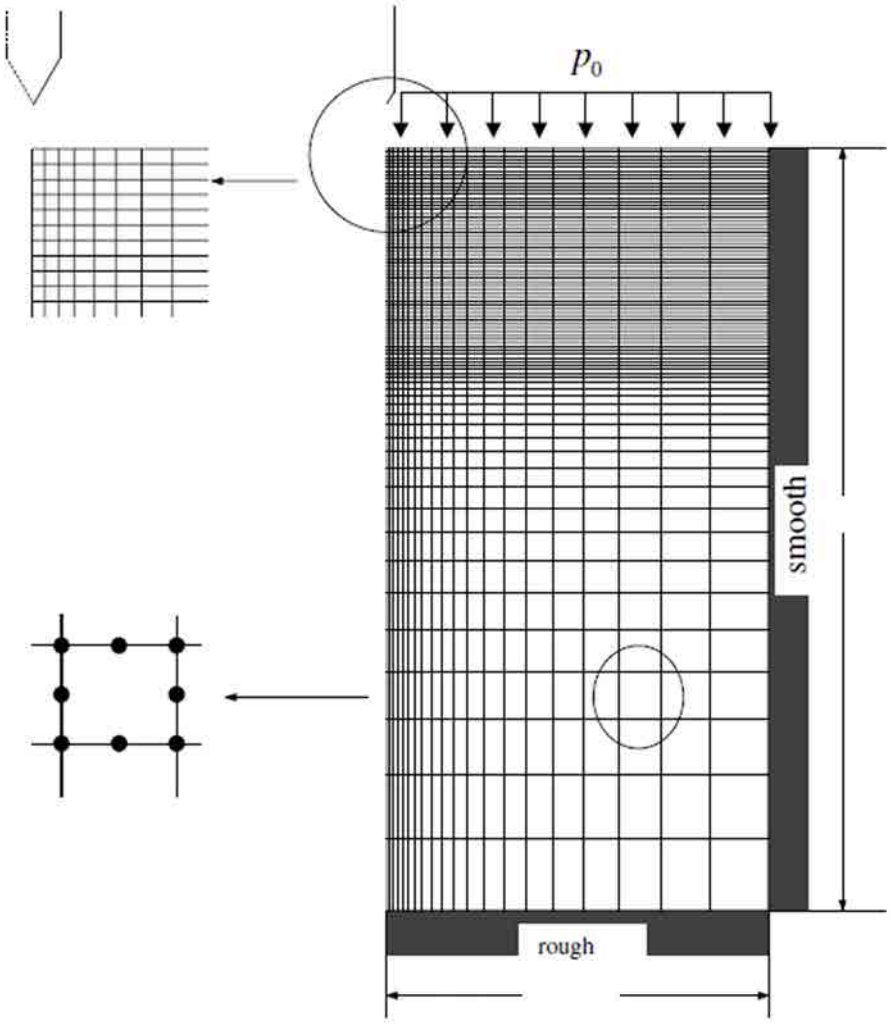

Figure 9: Finite element mesh for analysis (Huang et al. [2004])

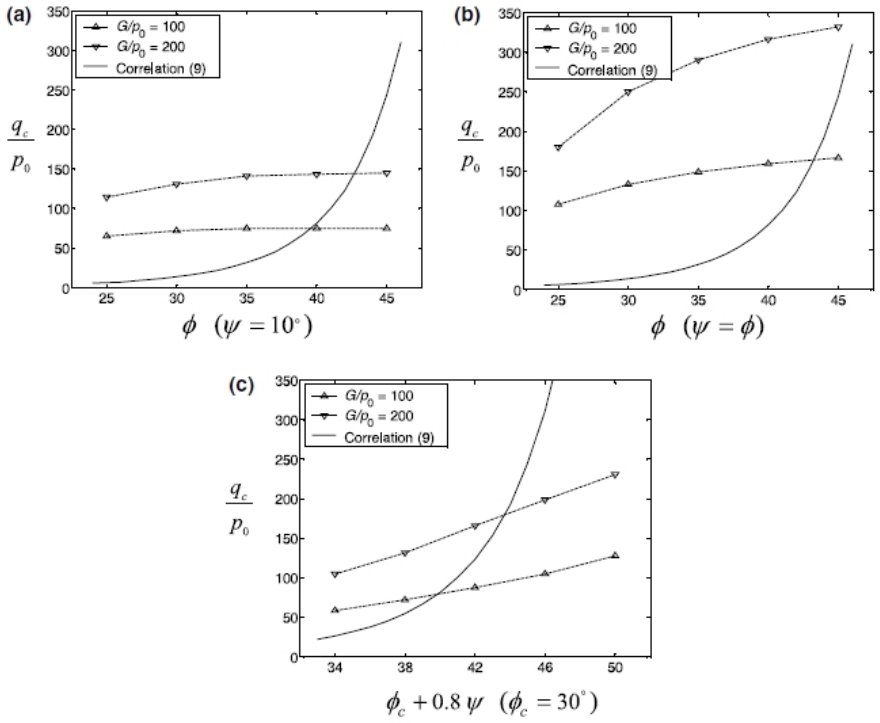

Figure 10: Comparison of correlation proposed by Robertson and Campanella [1983] (solid curves) with numerical results of Huang et al. [2004] (dashed curves) for: (a) various friction angles with dilation angle $\psi = 10^o$; (b) various friction angles with associated flow and (c) various peak friction and dilatancy angles given through Bolton's relation (Bolton [1986])

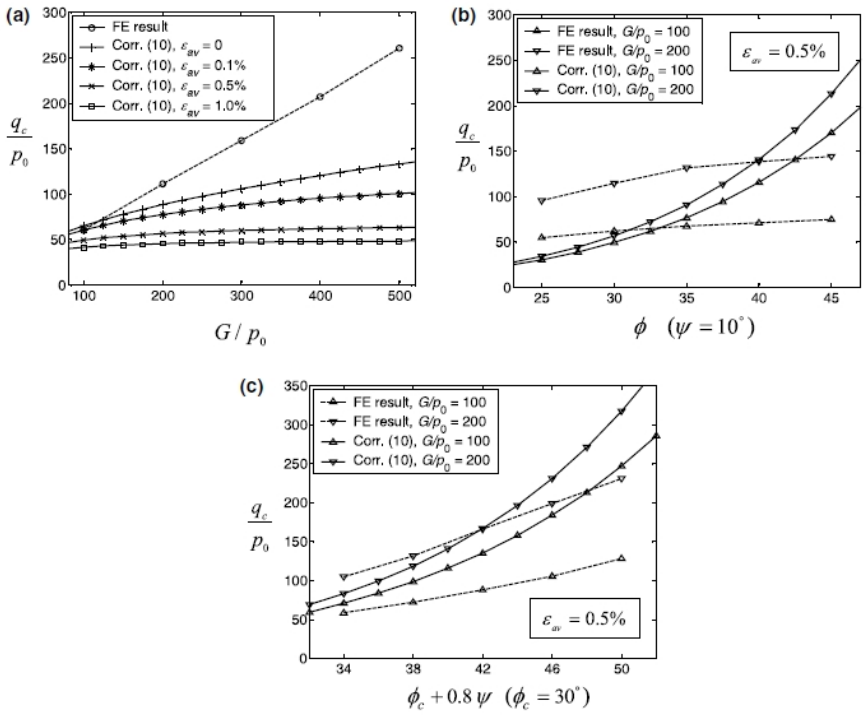

Figure 11: Comparison of correlation proposed by Vesic [1972] (solid curves) with numerical results of Huang et al. [2004] (dashed curves) for: (a) various friction angles with dilation angle $\psi = 10^o$; (b) various friction angles with associated flow and (c) various peak friction and dilatancy angles given through Bolton's relation (Bolton [1986])

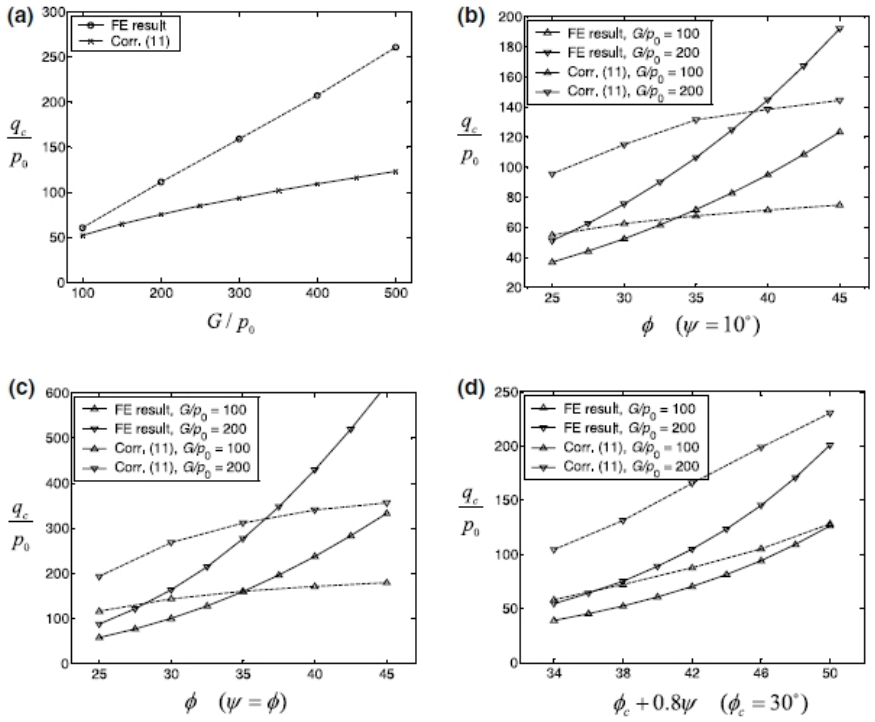

Figure 12: Comparison of correlation proposed by Yu et al. [1996] (solid curves) with numerical results of Huang et al. [2004] (dashed curves) for: (a) various ratios of shear modulus to stress; (b) various friction angles with constant dilation angle (c)various friction angles with associated flow and (d) various peak friction and dilation angles given through Bolton's relation (Bolton [1986])

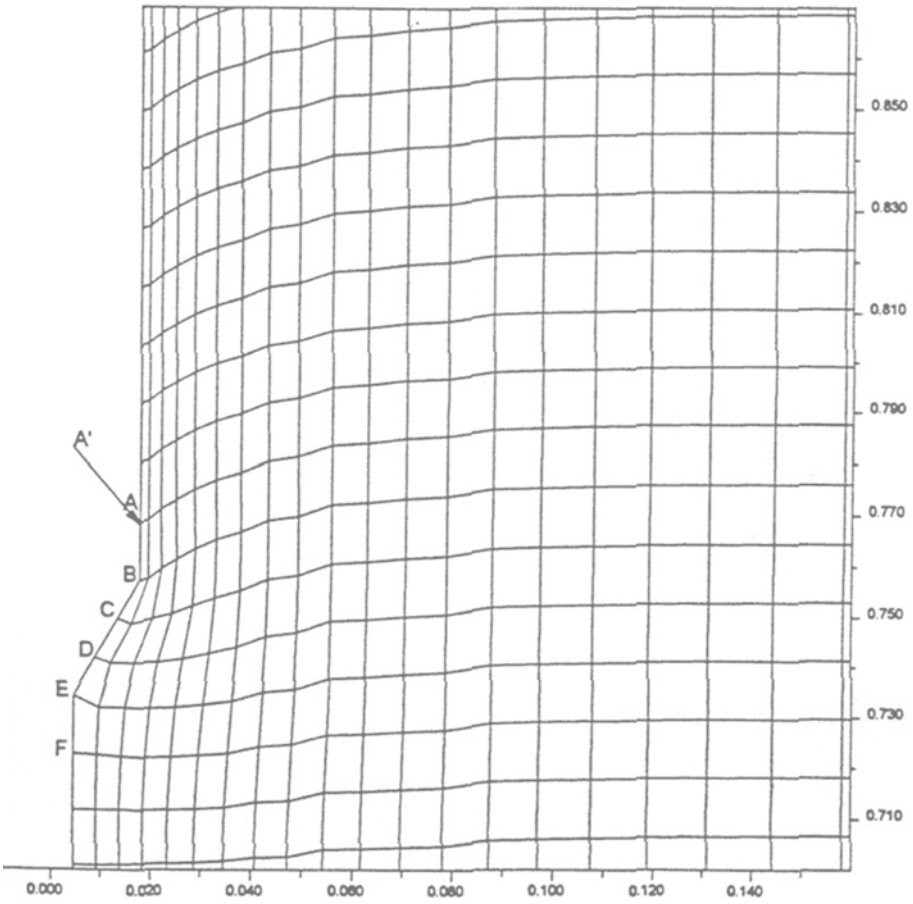

Figure 13: Finite element mesh for analysis and deformation pattern around cone tip (Ahmadi [2000], Ahmadi et al. [2005])

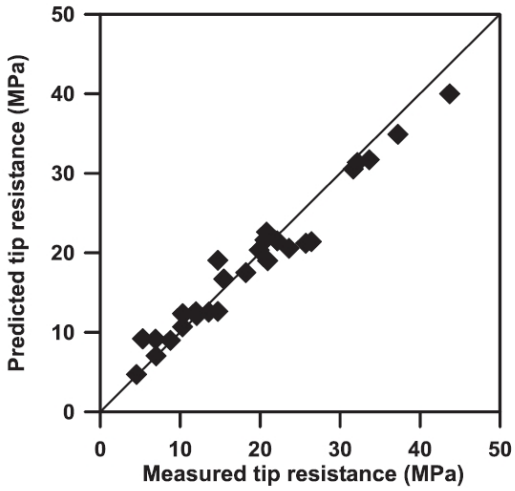

(a)

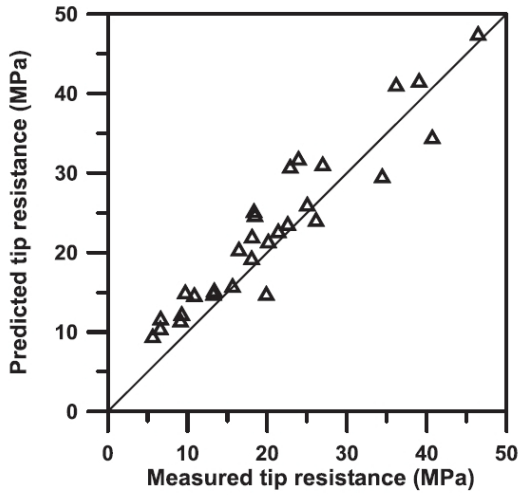

(b)

Figure 14: Comparison between predicted and measured tip resistance for: (a) BC1, D_R = 53.2–92.8%, σ_{v0} = 61.8–715.1 kPa, OCR = 1.00–14.67, K_0 = 0.370–1.296; (b) BC3, D_R = 46.2–94.4%, σ_{v0} = 62.8–716.1 kPa, OCR = 1.00–14.41, K_0 = 0.390–1.356

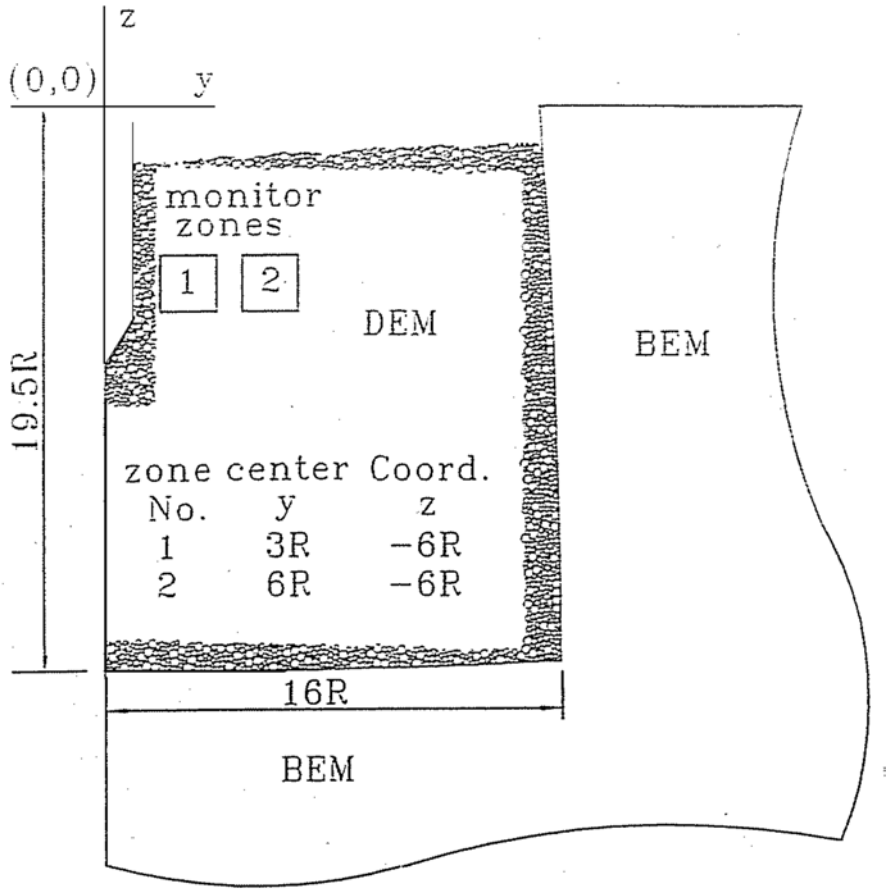

Figure 15: Boundary conditions in DEM–BEM analysis (Huang and Ma [1994])

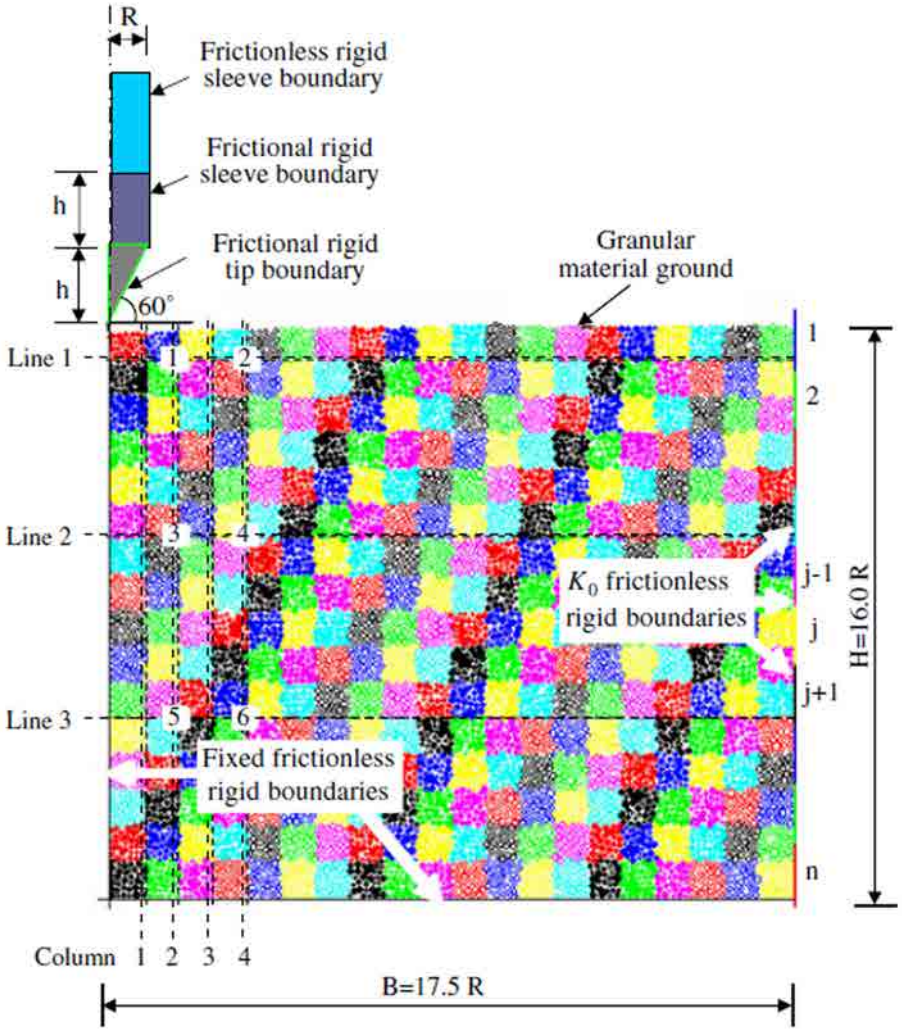

Figure 16: Boundary conditions in DEM analysis (Jiang et al. [2006b])

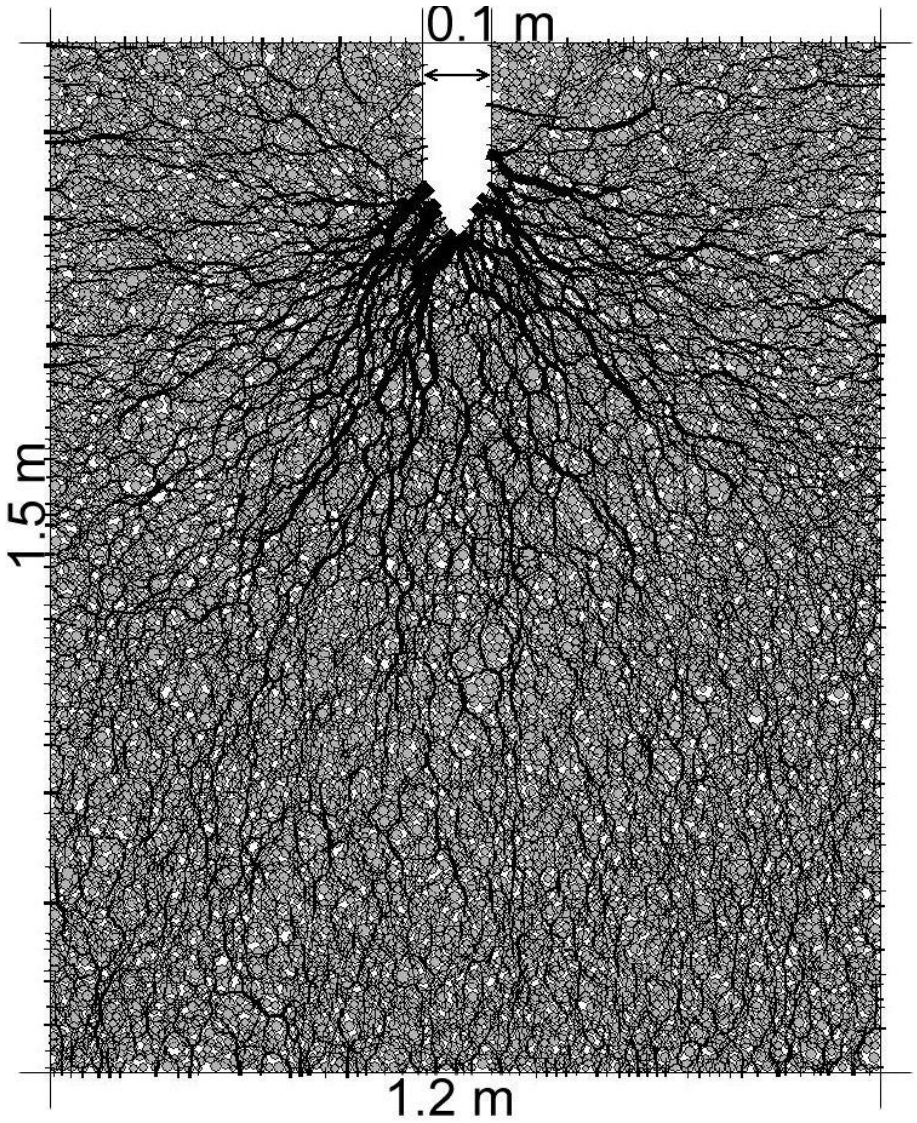

Figure 17: Boundary conditions in DEM analysis (Calvetti and Nova [2005a])

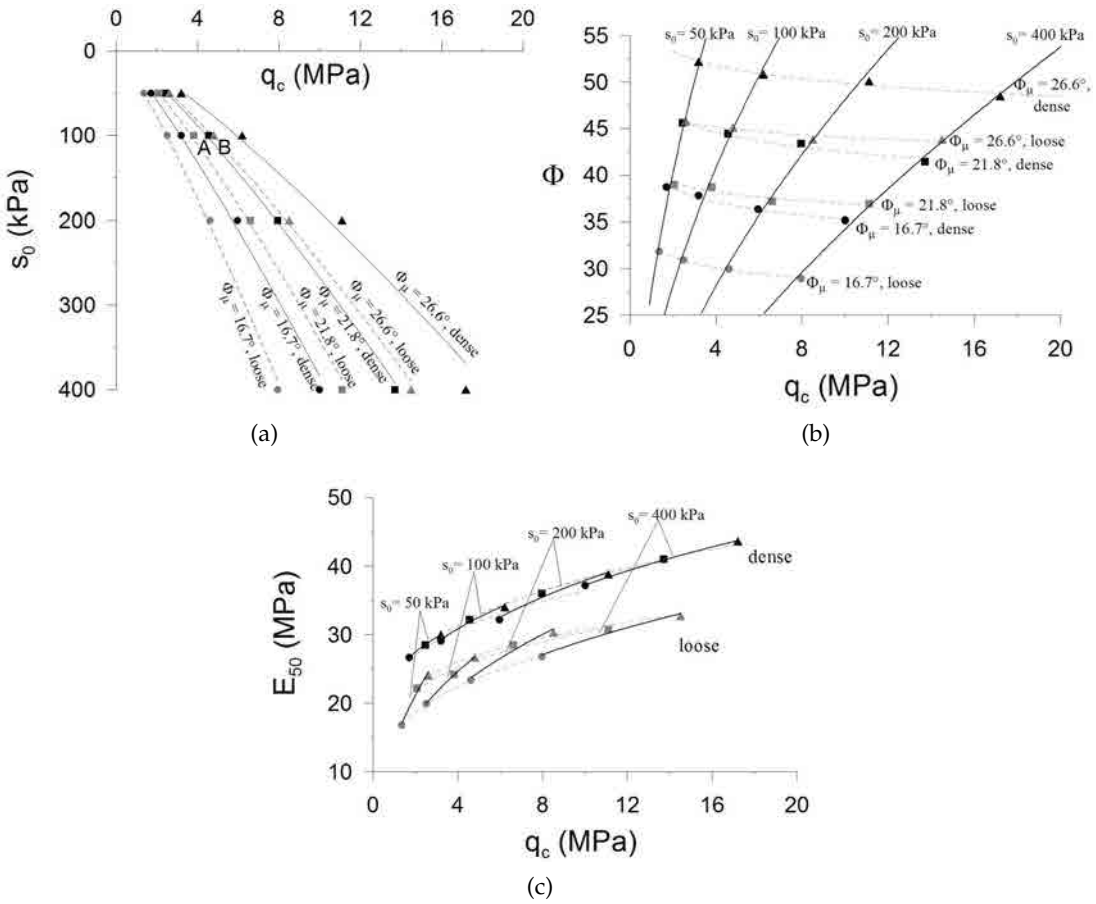

Figure 18: Correlations between steady–state cone tip resistance and (a) confining pressure, s_0; (b) interparticle friction, Φ; (c) secant modulus, E_{50}

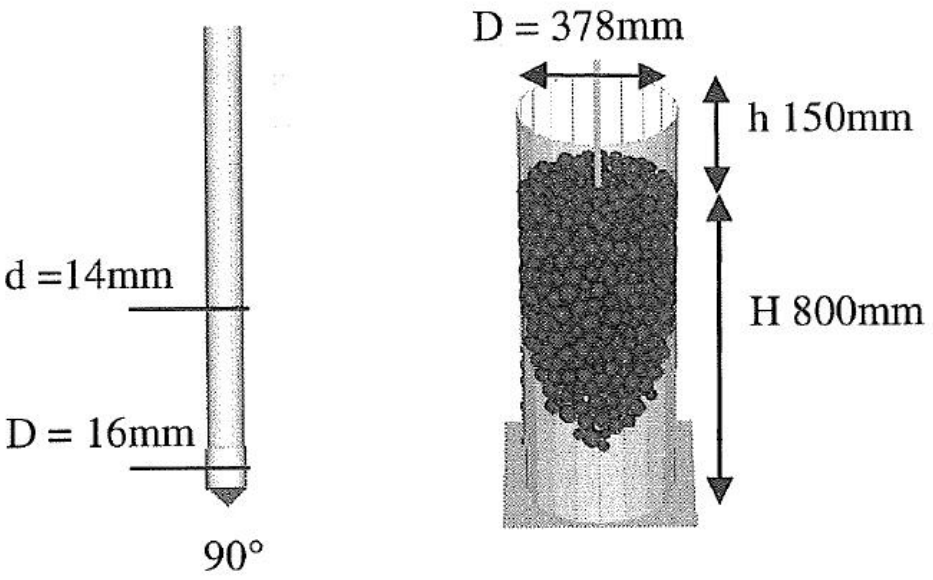

Figure 19: Geometrical characteristics of the DEM model (Breul et al. [2009])

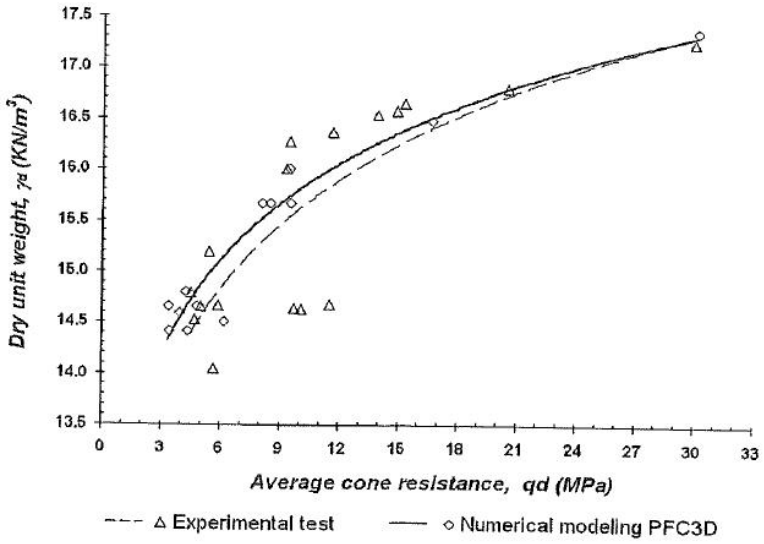

Figure 20: Comparison between experimental and numerical average cone tip resistance and density (Breul et al. [2009])

Table 1: Examples of Bearing Capacity Solutions for Cone Penetration Resistance

Reference	Method	Cone factor or main conclusions
Cohesive Soil		
Meyerhof [1961]	limit equilibrium analysis: Figure 3b	$N_c=1.15\cdot(6.28+a+\cot\frac{a}{2})$
Durgunoglu and Mitchell [1975]	limit equilibrium analysis; Figure 3d	$N_c=1.2\cdot(2.442+3.303\,\lambda+\sin[(1-\lambda)\frac{\pi}{2}])$
Houlsby and Wroth [1982]	Slip line analysis with 60° cone	cone resistance increases indefinitely with penetration depth
Cohesionless Soil		
Durgunoglu and Mitchell [1975]	limit equilibrium analysi: Figure 3d	$N_c=0.194\exp(7.629\tan\phi)$
Sokolovskiĭ, V.V. [1965]	Slip line analysis: Figure 4	$N_c=K\frac{\cos\delta_1\cos(\omega_2+\delta_2)(1+\sin\phi\cos(\Delta_2+\delta_2))}{\cos\delta_2\omega_2(1-\sin\phi\cos(\Delta_1-\delta_1))}$; $\Delta_{1,2}=\frac{\sin\delta_{1,2}}{\sin\phi}$, $K=e^{[\pi-2\omega_2-(\Delta_2+\delta_2)-2\omega_1-(\Delta_1-\delta_1)]\tan\phi}$
Simone and De Golia [1988]	Slip line analysis: Figure 4	$N_c=\frac{1+\sin\phi}{1-\sin\phi}\cdot\exp[(\pi-2\beta)\tan\phi]$
Janbu and Senneset [1974]	Limit equilibrium analysis: Figure 3c	cone factors for plane strain cases are much less than those for axisymmetric cases, cone roughness has a significant effect on the cone factor value

Table 2: Examples of Cavity Expansion Solutions for Cone Penetration Resistance

Authors	Method	Cone factor or main conclusions
Cohesive Soil		
Ladanyi and Johnston [1974]	Figure 5a	N_c=3.06+1.33ln $\frac{G}{S_u}$
Vesic [1972, 1977]	Figure 5b	N_c=3.90+1.33ln $\frac{G}{S_u}$
Yu [1993]	limit pressure+rigorous plasticity solution	N_c=4.18+1.155ln $\frac{\sqrt{3}G}{2S_u}$–smooth cone; N_c=9.4+1.155ln $\frac{\sqrt{3}G}{2S_u}$–rough cone
Cohesionless Soil		
Ladanyi and Johnston [1974]	Figure 5a	$N_c=\frac{(1+2K_o)A}{3}[1+\sqrt{3}\tan(\lambda\phi)]$
Vesic [1972, 1977]	Figure 5b	$N_c=\frac{1+2K_o}{3-\sin\phi}\exp[(\frac{\pi}{2}-\phi)\tan\phi]\cdot\tan^2(45^\circ+\frac{\phi}{2})(I_{rr})^n$
Salgado et al. [1997]	Figure 5c	the cone factor can not be expressed analytically a numerical procedure needs to be used
Yasufuku and Hyde [1995]	Figure 5d	$N_c=\frac{1+2K_oA}{3(1-\sin\phi)}$

Table 3: Examples of Steady State Solutions for Cone Penetration Resistance

Reference	Cone factor or main conclusions
Cohesive Soil	
Baligh [1985] Whittle [1992]	$N_c = 1.51 + 2\ln\frac{G}{S_u}$
Teh and Houlsby [1991]	$N_c = 1.25 + 1.84\ln\frac{G}{S_u} + 2\alpha_c - 2\Delta$
Yu [2000]	N_c quite sensitive to the OCR

Table 4: The summary of existing numerical analysis of the cone penetration test

Reference	**Applied Method**	**Soil type**	**Soil interface**	**shaft/cone-soil process**	**Installation process**	**Cone Factor,** N_k/N_c	d_c**, appex.**
de Borst and Vermeer [1982]	FEM	clay	linear elastic-perfectly plastic model with Mohr-Coulomb yield criterion	s–s [2]–0.5 C_u [3], c–s [4]–0.8 C_u	pre-bored	18	–
Kiousis et al. [1988]	FEM	clay	elasto–plastic with cap model [92?]	negligible	pre-bored	8.5	-

Continued on next page

2 s-s–shaft–soil interaction
3 c_u–undrained shear strength
4 c–s–cone–soil interaction

Reference	Applied Method	Soil type	Soil interface	shaft/cone-soil process	Installation process	Cone Factor, N_k/N_c	d_c; appex.
Teh and Houlsby [1991]	FEM+SPM [5]	clay	linear elastic-perfectly plastic with von Mises yield criterion	smooth	pre-bored	13.08	-
Van Den Berg et al. [1996]	FEM	sand/clay	Drucker–Prager model and von Mises yield criterion	δ=0°–clay, δ=14°–sand	pre-bored	-	60°

Continued on next page

5 FEM+SPM–Finite Element Method + Strain Path Method

Reference	Applied Method	Soil type	Soil interface	shaft/cone-soil process	Installation process	Cone Factor, N_k/N_c	d_c; appex.
Yu et al. [2000]	FEM	clay	Modified Cam Clay model	$\delta = 0$; $0.25\phi_{cs}$; $0.5\phi_{cs}$; $0.75\phi_{cs}$; ϕ_{cs}; $\phi_{cs} = 30°$, δ-interace friction	-	-	60°
Susila and Hryciw [2003]	FEM	sand	non–associated Drucker-Prager model	δ=0.50ϕ, ϕ=32; 34; 36; 38; 40; 42 [°], δ-interface friction	from the top	-	18; 60°
Abu-Farsakh et al. [2003]	FEM+CEM [6]	clay	modified Cam Clay model	Katona model [87]	pre-bored	10.74-14.13	5.6, 6.3; 60°

Continued on next page

6 FEM+CEM–Finite Element Analysis + Cavity Expansion Method

Reference	Applied Method	Soil type	Soil interface	shaft/cone-soil process	Installation process	Cone Factor, N_k/N_c	d_c; appex.
Wei et al. [2005]	FEM	clay	anisotropic modified Cam Clay model	δ=14°	pre-bored	-	5.6; 60°
Huang et al. [2004]	FEM	sand	elastic–perfectly plastic with Mohr Coulomb yield criterion	ϕ_{sc}=0; 5; 10; 15; 20 [°], ϕ_{sc}–interface friction	from the top	-	35.7; 60°
Lu [2004], Lu et al. [2004]	FEM	clay	elastic–perfectly plastic with Tresca yield criterion	f=0 (smooth shaft), f=1 (rough shaft)	from the top	9.6-14.5	-; 60°
Ahmadi [2000]	FEM	sand	elastic–perfectly plastic Mohr Coulomb	-	from the top	-	35.7; 60°

end of Table

Table 5: Summary of DEM–CPT analyses

	Huang and Ma [1994]	Jiang et al. [2006b]	Calvetti and Nova [2005a]	Breul et al. [2009]
Analysis	2D axisymmetric			3D
Particles	circular disks			spherical particles
number	3000, 12000, 18000	10000		1800–2200
d_{max} [mm]	1.5	3.525	18	50
d_{50} [mm]	0.8	2.925	13	–
d_{min} [mm]	0.3	2.25	9	25
C_u	1.28	1.25	–	-
e(n)	0.22	0.24	(0.16, 0.2)	0.72–0.54
particle rotation	50/50%	–	No	–
Interparticle friction ϕ_μ	25°	26.5°	16.7°, 21.8°, 26.6°	40.36°
damping δ	0.04	–	0.05	0.05
Contact stiffness, k_n, k_s [MN/m]	300, 210	1500, 1000	100, 100	–
Method of generated assembly	pluviation, K_o consolidation	multi–layer under–compaction, K_o consolidation	REM* [7], isotropic compression	REM
boundary walls dimensions	rigid, frictionless, Figure 15	rigid, frictionless, free top wall, Figure 16	Figure 17	rigid frictionless, Figure 19
Cone				
d_c [mm]	10	36	100	16
appex. α	60°	60°	60°	90°
d_c/D_{max}, d_c/D_{50}, d_c/D_{min}	6.66; 12.5; 33.34	10.20; 12.30; 16.0	55.5;7.69;11.1	0.32;-;0.64
penetration rate	20 cm/sec.	0.2 cm/sec	–	10 cm/sec

Continued on next page

7 REM–RADIUS EXPANSION METHOD

	Huang and Ma [1994]	Jiang et al. [2006b]	Calvetti and Nova [2005a]	Breul et al. [2009]
cone–soil interaction	frictional	frictional; frictionless	frictional	frictional

end of Table

Table 6: Summary of correlation for cone tip resistance based on calibration chamber test results

Authors	Category	cone resistance or cone factor
Schmertmann [1976]	I(i)	$q_c = C_o(\sigma_{v0})^{C_1}\exp(C_2 D_R)$
Houlsby and Hitchman [1988]	I(ii)	$q_c = C_o(\sigma_{h0})^{C_1}\exp(C_2 D_R)$
Jamiolkowski et al. [1988]	I(iii)	$q_c = C_o(p_0)^{C_1}\exp(C_2 D_R)$
Hsu and Huang [1999]		$q_c = 492 p_{atm}\left(\frac{p_0}{p_{atm}}\right)^{0.46}\exp(2.33 D_R)$
Houlsby and Hitchman [1988]	II	$q_c = \sigma_{h0}\exp[0.16(\phi - 9^o)]$
Been et al. [1987]	III(i)	$N_q = \frac{1+2K_o}{3}[1 + k\exp(-m\xi)]$
Yu et al. [1996]	III(ii)	$\frac{q_c}{\psi_1} = \exp(1.542 - 3.37\xi)$
Mayne [2005]	IV	$OCR = \left[\frac{0.192\left(\frac{q_c}{p_{atm}}\right)^{0.22}}{(1-\sin(\phi))\left(\frac{\sigma_{v0}}{p_{atm}}\right)^{0.31}}\right]^{\left[\frac{1}{\sin(\phi)-0.27}\right]}$

3

CALIBRATION CHAMBER TESTING

3.1 INTRODUCTION

Calibration chamber testing (CC) provides an effective way to study cone penetration test (CPT) in sands under strictly controlled conditions (material, density, stress state and boundary). Results from CC CPT are then used to verify as well as establish correlations between cone tip resistance and engineering soil properties. Typically, shaft friction is also measured during penetration, however no relationship between f_s (obtained from CC) and soil properties have been proposed.

The history of large calibration chambers (CC) started in 1969 at the Materials Research Division, Country Roads Board (CRB), Melbourne, Victoria, Australia (Holden [1991]). The original CRB chamber (design by R. Lilley and J.C. Holden) housed a sand sample of 0.76 m in diameter and 0.91 m in height prepared by pluvial deposition under K_o conditions. The radial wall was designed as flexible, the top wall as rigid and the bottom wall as a cushion to apply stresses.

The calibration chamber used after that differed in number of ways, including (i) dimensions, (ii) wall stiffness, (iii) nature of lateral, top and bottom boundaries (rigid or flexible), (iv) sample deposition procedures, (v) capability to handle saturated specimen and (vi) form of control of boundary conditions (strain or stress control). An extensive list of most calibration chambers in use around the world was provide by Ghionna and Jamiolkowski [1991]. Hsu and Huang [1999] updated this list by adding two calibration chambers being currently used at the National Chiao–Tung University in Taiwan. Calibration chamber testing has also been applied to other types of in situ tests including Marchetti dilatometer (Borden [1991], Baldi et al. [1986a], Jamiolkowski et al. [2003]), pressuremeter (Huang et al. [1991]), cone pressuremeter (Yu et al. [1996]), hydraulic fracture (Been and Kosar [1991]) and calibration of pile foundations (Kulhawy [1991], O'Neil [1991]).

Most of the CCs were designed as a cylinder with dimensions given by its radius and height. The smallest CC had 0.51 m in diameter and 0.76 m in height and was used at University of Clarkson in USA, while the largest CC had 2.1 m in diameter and 2.9 m in height and was built at Cornell University, USA. A cubical CC with side of 2.1 m was created at the University of Texas at Austin, USA.

Holden, while designing the first CC, pointed out that a flexible lateral boundary subjected to constant pressure would have a smaller effect on cone penetration and frictional resistance than a rigid one. Hence, the lateral walls were designed as flexible in all CCs, while top and bottom varied between being flexible, rigid or cushion–like. The sand specimen, was generally prepared by pluvial deposition in air or vacuum, using gravity mass or traveling spreaders. That king of preparation gives highly repeatable results and of good, or at least acceptable, uniformity (Bellotti et al. [1982]).

CC research has been largely dominated by uniform, predominantly silica sands, with a limited number of experiments on uncemented carbonate sands and a few tests on Belgium glauconitic sand (Bellotti and Jamiolkowski [1990]). An attempt to

use more realistic material (silty sand) was made at the Virginia Polytechnic Institute (Brandon et al. [1990]), whereas Wesley [2007] tested pumice sand. Some CC offered also the possibility of saturating the specimens. The boundary conditions could be controlled in four ways (Figure 21), depending on whether stress or strain boundary conditions were imposed on the top, bottom or radial surfaces of the sample.

In this chapter both the main results obtained in CC and problems/limitations of CC testing will be recalled. A detailed description of one of the largest CC CPT testing campaign performed to this day will be given, including characteristics of the material, general set–up of the CC apparatus, conditions of the tests and main results.

3.2 MAIN RESULTS OBTAINED IN PHYSICAL CALIBRATION CHAMBER

As was mentioned above, CC testing provides an effective way to study cone penetration resistance in sands under strictly controlled conditions. Generally, most of the CC work performed in this area was aimed at:

(I) establishing correlations between cone tip resistance and soil properties;

(II) validating already existing correlations;

(III) clarifying chamber size effect;

(IV) examining boundary condition effects.

In this section only the two first points ((i) and (ii)) above will be examined in detail while the last two points ((iii) and (iv))will be discussed in the section dealing with problems & limitations of CC testing.

Knowledge of the relationship between cone tip resistance (q_c) and relative density (D_R), and stress state (σ') is important in interpreting the CPT in sand. The concept of relative density is still extensively used in geotechnical engineering as an index of the mechanical properties of coarse grained soils. Therefore, one basic motivation of CC testing has been to obtain correlations between tip point resistance and relative density, so that the latter can be estimated from field q_c.

The first comprehensive correlation between the cone tip resistance and D_R (on the basis of CPTs performed in CC on six different sands) was given by (Schmertmann [1976]–unpublished Report) and subsequently mentioned in a number of later publications (i.e. Jamiolkowski et al. [1988]). The penetration test was assumed to be primarily dependent on relative density and vertical stress. Hence, such correlation relates D_R to the effective overburden stress, σ'_{v0}, and is applicable to normally consolidated (NC) fine to medium unaged clean sands (Figure 22). Tests were performed under BC1/BC3 boundary conditions.

Jamiolkowski et al. [1988] based on 484 CC CPTs performed in three silica sands (Ticino, Toyoura and Hokksund) have attempted to present correlations ($q_c - D_R$), similar to that of Schmertmann, considering the effect of CC size on the measured q_c and giving appropriate consideration to mechanically overconsolidated (OC) sands. The proposed expressions involved the effective overburden stress in case of NC but required the estimation of mean geostatic stress for OC deposit (Figure 23). More details about this work are presented in Section 3.4.

Hsu and Huang [1999] performed a series of CC CPT tests in the new simulator system developed at National Chiao–Tung University in Taiwan. The CC had 790

mm in diameter and 1600 mm in height. The lateral boundary consisted of a stack of rings connected with each other by an inflatable silicone rubber membrane on the inside. This was the main difference between conventional CC and this one. The vertical boundary was stress controlled only, while lateral boundary was stress and/or strain controlled. The CC CPTs were performed in Da Nang sand at different relative densities and stress states. The proposed a $q_c - D_R$ relationship similar to that of Schmertmann and Jamiolkowski (Jamiolkowski et al. [1988]) but with different coefficients: C_0, C_1, C_2. Moreover, they found that the initial mean normal stress had the most consistent relationship with q_c. The boundary effect was substantially reduced using this new system. For a first time, q_c obtained from CC CPT in the new simulator had been used without boundary effect correction factor (Figure 24).

Houlsby and Hitchman [1988] did not follow Schmertmann, and concluded that q_c in sand depended primarily on the horizontal stress (not vertical stress) and the angle of friction. The authors proposed two new expressions to correlate cone tip resistance to horizontal stress and to interparticle friction. The interparticle friction (peak friction angle in triaxial test) was calculated using semi–empirical expression proposed by Bolton [1986]. The ϕ_{crit} at the critical state was taken as 33° for the quartz of Leighton Buzzard sand. The relationship was fitted by a power expression to a series of CC CPT results on Leighton Buzzard sand at three different densities and a range of stress states. The results can be seen in Figure 25. Moreover, the relationship proposed by authors was also validated with results from previous work in CC on Ticino and Hokksund sands (Jamiolkowski et al. [1988]). Tests were performed under BC1 boundary conditions.

Been et al. [1987] proposed an alternative approach for characterizing sand behavior called 'state parameter' concept (Been and Jefferies [1985]). The definition of state parameter ($\psi = \xi$) is illustrated in Figure 26. The state parameter is a quantitative measure of the state of a sand that combines the effects of void ratio and effective stress in a unique way, irrespective of the median grain size, silt content, mineralogy and stress level for the broad class of sub–angular to sub–rounded sands (Been et al. [1986]). The state parameter combines the influence of void ratio and stress level in a unique way for all sands by reference to an ultimate (steady) state. The ψ, is simply the void ratio difference between the current void ratio (e_λ) and the steady state void ratio (e_{ss}) at the same stress level. However, a practical application of the relationships between state parameter and behavioral properties is dependent on the ability to measure ξ in situ. Hence, Been et al. [1987] used data from large chamber test on six sands (~ 400 tests) and related cone resistance, stress level and density together with knowledge of the SSL (steady state line) to obtain cone tip resistance–state parameter relationship. The results can be seen in Figure 27. Tests were pefromed under BC1/BC3 boundary conditions.

Yu et al. [1996] proposed an interpretation method for determining sand properties from the cone tip resistance (q_c) and the pressuremeter limit pressure (Ψ_L) measured with the cone pressuremeter. The method could be used to deduce the angle of internal soil friction (ϕ_{ps}) and in situ sand state (ξ_0) from the ratio of measured q_c and Ψ_L which was found to be largely independent of the CC size.

All these CC–based correlations between the cone tip resistance and the soil properties have been presented before in Table 6.

3.3 PROBLEMS & LIMITATIONS OF CC CPT TESTING

Although calibration chamber testing has been widely used to obtain correlations between cone resistance and soil properties, it has some limitations which make the results difficult to extrapolate to the field. Ghionna and Jamiolkowski [1991] have summarized a number of problems associated with the calibration chamber testing.

- Aging & cementation,
- sand type, and
- chamber size & boundary type effect

are among the important issues to be discussed.

3.3.1 *Aging & cementation*

CC tests are performed on freshly reconstituted sands whose fabric may vary from that of natural sand deposits. The natural soil may have a highly developed structure, built up in geological time by phenomena such as drained creep, early diagenesis, cementation, etc. Schmertmann [1991] has shown that these effects have a significant influence on measured cone tip resistance, soil strength and stiffness. The author demonstrated that soil aging over engineering times can cause a general 50 to 100 % improvement effect in many key soil properties. Moreover, most engineering–time age–strengthening effects result from increased basic soil friction, including dilatancy and not from increased cohesion.

Drnevich et al. [1986] conducted a laboratory study to investigate the effect of cementation on the cone penetration resistance of sand. Their results indicated that cementation had a moderate effect on the penetration resistance of sand. For very lightly cemented soils, the magnitude of cohesion (c′) is relatively small and generally did not exceed 20 to 40 kPa. Also Ghionna and Jamiolkowski [1991] concluded that cementation give soils some value of c′ with an almost negligible influence on the peak angle of shearing resistance (ϕ'_p). However, even very light cementation has an important influence on the stiffness, especially at the small and intermediate strain level. An increase in q_c would result from an increase in the stiffness.

Jamiolkowski et al. [2003] stated that there might be an influence of aging & cementation on CPT results. However, lack of information able to estimate and quantify their influence make these issues difficult to account for.

3.3.2 *Sand type*

Most of the CC tests have so far been performed on uniform, clean, predominantly silica sand, what is called an 'academic' soil. In the nature, deposit of sands is rarely as uniform, and almost always contain a non negligible percentage of fines which may significantly change engineering behavior and soil properties. Ghionna and Jamiolkowski [1991] pointed that many relevant engineering problems are linked to more crushable and compressible and slightly cemented material, such as carbonate and glauconitic sands. Pender et al. [2006] and Wesley [2007] performed CC CPT tests on both hard grained quartz sand and a crushable pumice sand, which was four times

more compressible. Behavior of pumice sand was found to be similar to that of other soft grained sands (carbonate sand), but the CC q_c did not fit with previous correlations developed for quartz sand.

3.3.3 *Chamber size & boundary type effects*

The use of calibration chamber results to predict field performance needs to take into account the effect of limited chamber dimensions. Size effects are observed when the test outcomes vary for constant sand properties and conditions as a function of equipment dimensions. Size effect is usually explored using the parameter R_d, a chamber–to–cone diameter ratio ($\frac{D_{cc}}{d_c}$). A related aspect is the influence of variable testing boundary conditions and how these may result in different size effects.

Since the early 80's, these issues have been examined by various researchers. Parkin and Lunne [1982] summarized work performed in two different calibration chambers with two differently sized penetrometers. They did not observe a significant size effect for loose sand, whereas for dense sand there was a clear influence of chamber size up to $R_d > 50$. Cone tip resistance (q_c) increased with R_d for both BC1 and BC3 conditions, although somewhat faster in the former case. In later work, Parkin [1988] suggested that the R_d value required to eliminate chamber size effects might be greater then 70.

Jamiolkowski et al. [1985] proposed the following formula to correct q_c measured in the CC for the chamber size effect:

$$q_{c,field} = q_{c,CC}\left(1 + \frac{0.2(D_R(\%) - 30)}{60}\right) \tag{3.1}$$

where $q_{c,CC}$ is the experimental value of tip resistance measured in CC, D_R is a relative density and $q_{c,field}$ is the corrected tip resistance expected to be measured in the field for the same sand with the same density and stress state as that in the CC. The above formula was valid for a standard cone penetrometer (d_c = 36 mm) and chamber with 1.2 m in radius and BC1 boundary conditions. Moreover, the formula implies that loose ($D_R \leqslant 30\%$) are not affected by the CC size. In later work Jamiolkowski et al. [2003] adopted a more general correction formula (Tanizawa [1992]), depending on both relative density and chamber–to–cone diameter ratio (R_d). The formula for stress controlled boundary (BC1) had the following expression:

$$q_{c,field} = q_{c,CC} \cdot CF \tag{3.2}$$

where CF is a correction factor calculated as follows:

$$CF = a \cdot (D_R)^b \tag{3.3}$$

The lower bound of D_R below which CF is equal 1 varies depending on R_d factor. The variables a and b are empirical functions of R_d inferred from CC performed in Ticino Sand (Figure 30a and Figure 30b).

Schnaid and Houlsby [1991], using only BC1 tests, confirmed that for all sand densities the chamber size could affect the results and that the effect was more significant for dense sand. They also showed that cone resistance and pressuremeter limit pressure were similarly affected.

Mayne and Kulhawy [1991] after examining six data sets from CC CPT's for different ranges of R_d proposed the following correction factor for size effects:

$$q_{c,corrected} = q_{c,measured}\left(\frac{R_d - 1}{70}\right)^{\frac{D_R(\%)}{200}} \tag{3.4}$$

where $q_{c,corrected}$ is the corrected cone tip resistance, $q_{c,measured}$ is cone tip resistance measured in CC. The above equation assumes that a 'free field' condition is achieved for $R_d > 70$ and was meant to apply equally for both BC1 and BC3 conditions.

Salgado et al. [1998] applied a mixture of cavity expansion and slip line theory to quantify chamber size effect. The theory predicts that the difference between 'free field' and chamber q_c values increases for decreasing Rd and that q_c measured under BC1 or BC4 conditions is always smaller than the corresponding 'free field' values. The difference (or correction factor) is not only dependent on density, but also on ambient stress and material parameters. The opposite held for q_c measured under BC3 or BC2 conditions; the q_c value predicted decreased with increasing R_d, and thus CC results should lie above "free field" values. That result was contrary to some available experimental evidence, but the discrepancy was attributed to experimental imperfections in the enforcement of the no lateral strain condition.

Taking a different approach to all mentioned researchers Hsu and Huang [1999] did not propose a new correction factor to eliminate boundary effect. The authors developed a calibration chamber system in which CPT could be performed under simulated field conditions. The main difference between standard CC and the new simulator was a design of lateral boundary, that consisted of a stack of rings lined with an inflatable silicone rubber membrane on the inside. This innovation facilitated boundary displacement measurements and stress control. The lateral boundary conditions could vary with depth. The authors compared their results (without correction) with empirical correlations ($D_R - \sigma$) proposed by Baldi et al. [1986b] and Jamiolkowski et al. [1988]. The results showed a similar trend to that of Jamiolkowski et al. [1988] at relative density 65 and 84%.

Wesley [2002] noticed that in analyzing CC results it was normally assumed that σ_v (overburden stress, stress above the cone tip) was the same as the applied vertical stress. However, after examination of the mechanics of CC testing, the author showed that this assumption was not valid and the stress state in CC was quite different from that in the field. In CC the vertical stress is applied using loading piston at the base of the sample and during test the stresses in front of the cone are limited by the applied pressure at the base or the rigidity of the base and the vertical stress above the cone is reduced (Figure 31b) as follows:

$$\sigma_v = \sigma_b - \frac{q_c}{{R_d}^2} \tag{3.5}$$

where σ_b is a vertical stress applied to the base of sample and R_d is a chamber to cone diameter ratio. For the field (Figure 31a) situation, in contrast to this, the vertical stress above the cone remains constant (equal to the overburden pressure), while that below the cone increases by an amount dependent on the cone force and the properties of the soil and can be calculated as follow:

$$\sigma_v = \sigma_{v(t)} + \frac{q_c}{{R_d}^2} \tag{3.6}$$

where $\sigma_{v(t)}$ is a vertical stress applied to the top of sample. The cone tip resistance calculated using eqn. 3.6 for different vertical stresses and R_D ratios showed a similar trend to the experimental graph presented by Parkin [1988]. The observed reduction of q_c was caused by decrease in R_D. The author suggested that this reduction is caused by changed stress state and the correction should be applied on σ_v rather than on q_c.

3.3.4 *Other*

Other issues concerning CC testing are sample inhomogeneities and cost. The sand specimen, is generally prepared by pluvial deposition in air or vacuum, using gravity mass or traveling spreaders. That king of preparation was giving results (q_c) highly repeatable and of good, or at least acceptable, uniformity (stresses at the cone base). However Ghionna and Jamiolkowski [1991] pointed out that sample preparation problem is more acute when moving into the preparation of CC specimens of non uniformly graded and silty sands. They believed, that for such materials, new techniques assuring preparation of uniform and repeatable large size specimens are needed.

The cost of CC testing need to be understood in terms of time and money. Testing in large size calibration chambers is time–consuming and expensive. Bellotti et al. [1982] pointed that to perform one CPT test in one week, four people are needed (two specialized technicians).

To completely resolve the issue of calibration chamber size effect, more experimental researches are needed, especially for higher R_d ratios. Moreover, to reduce cost of CC CPT testing, several researches have also carried out testing programmes on smaller triaxially loaded samples using miniature cones (Puppala et al. [1991], Peterson [1991]. Ghionna and Jamiolkowski [1991], Bolton et al. [1999] also proposed that centrifuge tests may be used to check some of the CC effects.

3.4 ENEL/ISMES CC DATABASE

One of the largest CC CPT testing campaigns ever performed was that carried out at the geotechnical laboratories of ENEL–CRIS, Milan and ISMES, Bergamo, Italy. ENEL–CRIS was the research laboratory of the Italian Electricity Company, with geotechnical, structural and hydraulic divisions. ISMES was a mixed–capital research company. Both organizations had calibration chambers similar to that of CRB.

3.4.1 *Apparatus employed*

The complete ENEL–CRIS calibration chamber apparatus is shown schematically in Figure 32. The equipment consists of a flexible wall chamber, a loading frame, a mass sand spreader for sand deposition and a saturation system. The chamber can impose four types of boundary conditions: BC1, BC2, BC3 and BC4 as referred in Figure 21. The height of the CC is 1.5 m, and the diameter is 1.2 m. The vertical stresses are applied to the specimen via a piston raised by pressurized water and lateral stresses are applied by the pressure of water surrounding the specimen. The sand specimen is enclosed at the sides and base by a membrane. The side membrane is sealed around

an aluminum plate which forms the top boundary of the specimen and transfers the thrust of the chamber piston from the sand to a very rigid lid. The hole in the center of the lid allows the penetration of the cone into the sand specimen by pushing.

The specimen is prepared by a technique of pluvial deposition through air. Normally consolidated and overconsolidated sand specimens can be obtained at K_o conditions by increasing or decreasing the vertical stress and keeping lateral strain equal to zero. It is also possible to saturate the sand specimen. This is done with de–aired water after the chamber has been closed. Penetration is performed after the specimen is left for 30 minutes at constant stress and after the chamber valves are operated to reproduce the described boundary conditions, BC.

3.4.2 *Materials tested*

The ENEL/ISMES CC CPTs were done in three well–known silica sands: fine to medium Ticino sand (TS), Toyoura sand (TOS) and Hokksund sand (HS) and in two calcareous sands: Quiou and Kenya sands.

3.4.2.1 *Ticino sand*

The particle size distribution of Ticino sand is shown in Figure 33. Index properties are summarized in Table 7 and Table 8. Two micro–graphs of grain shape of Ticino sand with diameter 0.33 mm and glass beads (~ DEM particle) with diameter 0.32 mm can be viewed in Figure 34.

The material contains quartz (28%), feldspar (30%), mica (5%). Ticino Sand is a poorly graded granular material with angular to sub–rounded grains, a coefficient of uniformity, C_u ($= D_{60}/D_{10}$), approximately equal to 1.61 and a mean particle diameter, D_{50}, of 0.53 mm. The minimum, e_{min}, and maximum e_{min}, void ratios of Ticino Sand are 0.578 and 0.924, which correspond to maximum, $n_{max} = 0.489$, and minimum, $n_{min} = 0.366$, respectively (Table 8)). The specific gravity of Ticino sand is 2.69. The sphericity [1] of particles lays between 0.7 to 0.8.

3.4.2.2 *Other sands*

Figure 35 shows particle size distribution of other sand investigated in ENEL/ISMES CC CPT testing. The properties of those sands can be viewed in Table 9. Together with Ticino sand, Hokksund and Toyoura sands were used to establish and validate correlations between cone resistance and soil properties.

3.4.3 *Main results*

The ENEL/ISMES campaigns were one of the most comprehensive and reliable CPT CC test series aimed for establishing correlations between cone tip resistance and soil properties, clarifying boundary conditions and chamber size effect. These tests included five penetrometer diameters (35.7, 25.4, 20, 11 and 10 mm) and one calibration chamber diameter (1.2 m). All CPT's were performed using the cylindrical

1 Sphericity indicates whether one, two, or three of the particle dimensions are of the same order of magnitude, and it is defined as the diameter of the largest inscribed sphere relative to the diameter of the smallest circumscribed sphere. It varies from 0.5 (less spherical) to 1 (spherical)

Fugro–type electrical cone tips. The test series covered the full range of relative densities from loose ($D_R \sim 22$) to very dense ($D_R \sim 98$), and of vertical stresses from 50 to 700 kPa, with overconsolidated ratio varying from 1 to 15. A large number of cone penetration tests were carried out, however only 484 CPTs were used in the analysis; 66% under BC1, 11% under BC2, 20% under BC3 and 3% under BC4. Moreover, the number of tests for given set of initial conditions (D_R and σ') and different cone sizes was limited and did not cover full range of diameter ratios. The q_c readings at 0.75 m depth were taken as those representative of the test ('steady state cone tip resistance').

Three aspects related to the use of CPT results were examined, including evaluation of relative density (D_R), angle of internal friction (ϕ') and deformation parameters. The CC CPTs resulted in following information: γ_d, D_R, σ_v, K_o, OCR, M_o, q_c, f_s and d_c. Typical examples of cone and shaft resistance evolution with penetration depth can be seen in Figure 36.

3.4.3.1 D_R–q_c *correlation*

The writers adopted a Schmertmann–type equations to fit the experimental data and to evaluate D_R:

$$q_c = C_0 \cdot p_a \left(\frac{\sigma}{p_a}\right)^{C_1} \exp(C_2 D_R) \tag{3.7}$$

$$D_R = \frac{1}{C_0} \ln\left(\frac{\frac{q_c}{p_a}}{C_0(\frac{\sigma'}{p_a})^{C_1}}\right) \tag{3.8}$$

where q_c is a measured (steady state) cone tip resistance, p_a is an atmospheric pressure ($\approx$ 100 kPa), σ' is an initial effective stress component and C_0, C_1 and C_2 are non–dimensional experimental coefficients. The authors observed that when the above equations referred to NC sands only, it was possible to assume $\sigma' = \sigma_v$ (Figure 37a). But when OC sands were examined, it was necessary to adopt $\sigma' = \sigma_h$ or σ_{mo} (mean stress) (Figure 37b). The values of experimental coefficients (C_0, C_1 and C_2) are listed in Table 10. The authors explained that a unique relation between q_c and D_R through σ_v cannot exists because q_c in OC deposit is completely controlled by the initial effective horizontal stress (σ_h).

All above mentioned correlations have been developed after q_c measured in CC was corrected for chamber size effect (as explained in Section 3.3.3).

3.5 SUMMARY

This chapter introduced one of the largest CC CPT testing campaign performed at two geotechnical laboratories ENEL-CRIS (Milan) and ISMES (Bergamo). The following conclusions can be drawn:

1. The CC CPT test are performed under strictly controlled conditions: material, stress state and boundary conditions

2. CPT CC testing allow to verify and establish new correlations between cone tip resistance and testing conditions. The $f(q_c, \mathrm{soilproperties})$ function is unique for given sand or group sands with similar mineralogy

3. Although more than 30 years of comprehensive research on CC has increased ability to interpret CPT, there are still significant uncertainties that should be reduced in future work including:
   - more realistic soils (not only 'academic' sands)
   - performing more tests with larger R_d ratio for a better definition of the boundary effect
   - new techniques to prepare homogeneous specimens, as well as new procedures to verify homogeneity
   - new procedure to quantify effect of aging fabric and cementation on CPT results (i.e. include artificial aging in the laboratory)

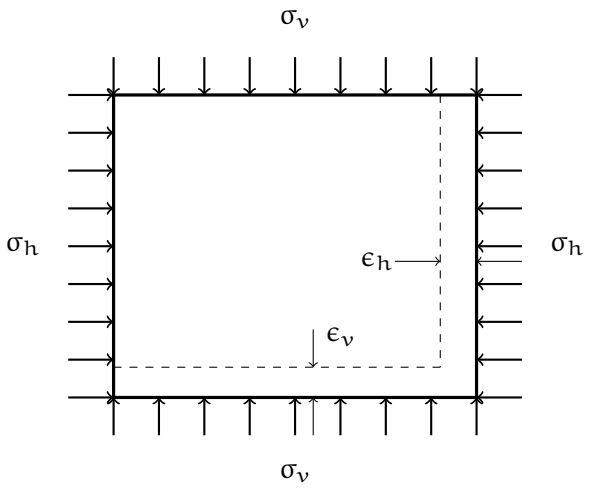

	top and bottom boundary		lateral boundary	
	stress	strain	stress	strain
BC1	constant	-	constant	-
BC2	-	0	-	0
BC3	constant	-	-	0
BC4	-	0	constant	-

Figure 21: Types of boundary conditions in calibration chamber testing.

Table 7: Grain size distribution of TS4

Diameter [mm]	0.9	0.62	0.50	0.40	0.30	0.20	0.15	0.1	0.09

% finer by weight [%]	100	69.9	39	15	5	2	1	1	0

Table 8: TS properties: minimum, maximum and mean grain particle diameters; minimum and maximum density and roundness

Sand gradation	D_{min}	D_{max}	D_{50}	γ_{min}	γ_{max}	e_{min}	e_{max}	R
	[mm]	[mm]	[mm]	$[kN/m^3]$	$[kN/cm^3]$	[-]	[-]	[-]
TS4	0.3	0.9	0.53	13.64	17.24	0.578	0.924	0.40

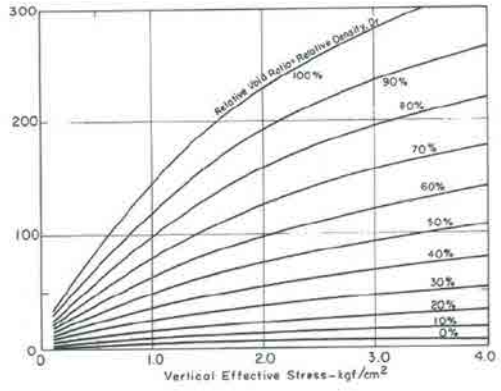

Figure 22: Q–CPT bearing capacity to estimate relative density in normally consolidated silty fine to uniform medium sand (after Schmertmann [1976])

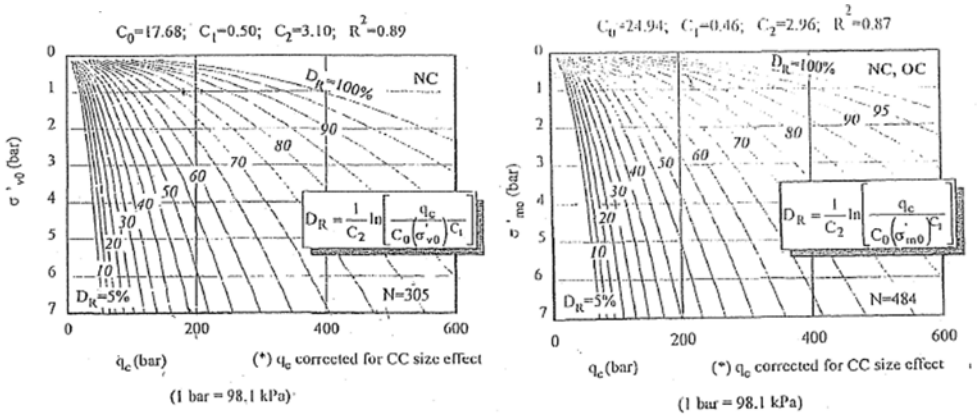

(a) (b)

Figure 23: Relationship between cone tip resistance and relative density for (a) normally consolidated; (b) normally consolidated and overconsolidated siliceous sands (after Jamiolkowski et al. [2003])

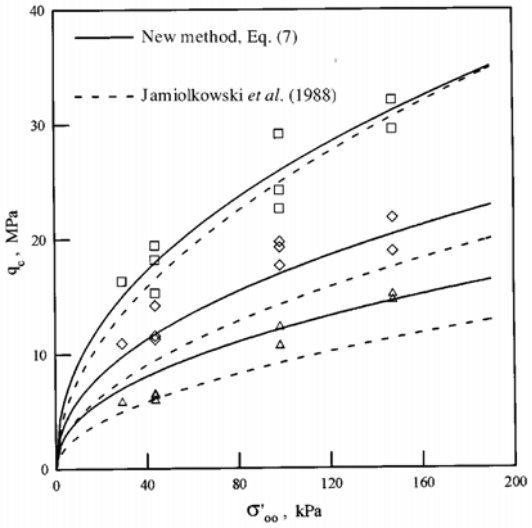

Figure 24: Relationship between cone tip resistance and mean stress (after Hsu and Huang [1999])

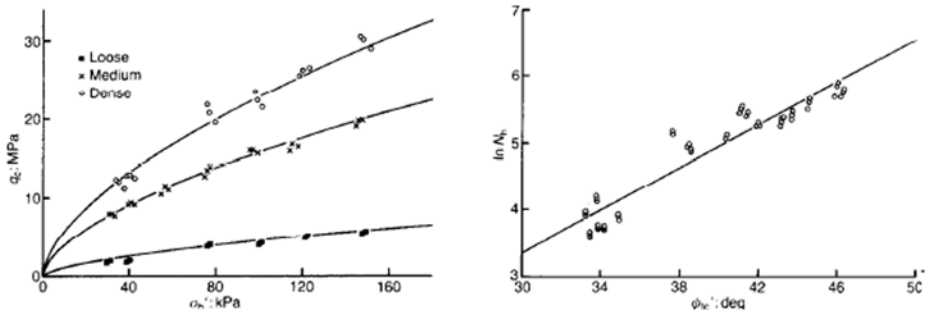

(a) (b)

Figure 25: Relationship between cone tip resistance (q_c or $N_h = \frac{q_c}{\sigma_{h0}}$) and (a) horizontal stress; (b) friction angle for Leighton Buzzard sand (after Houlsby and Hitchman [1988])

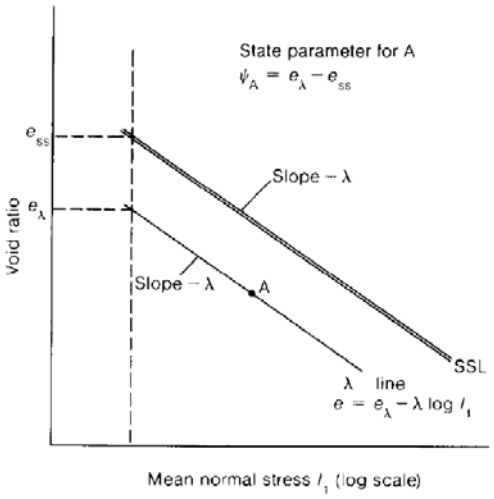

Figure 26: Definition of state parameter (after Been and Jefferies [1985])

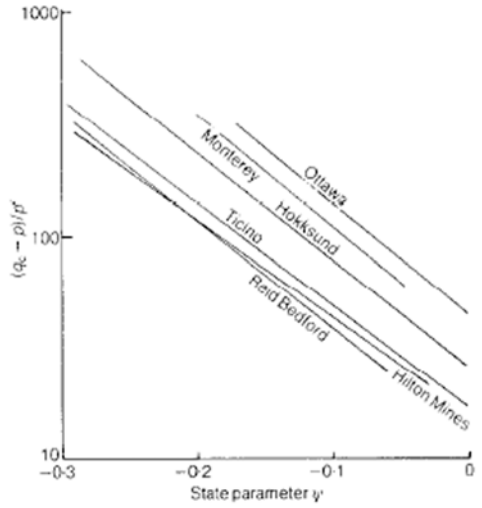

Figure 27: Summary of normalized cone resistance and state parameter for normally consolidated sands (after Been et al. [1987])

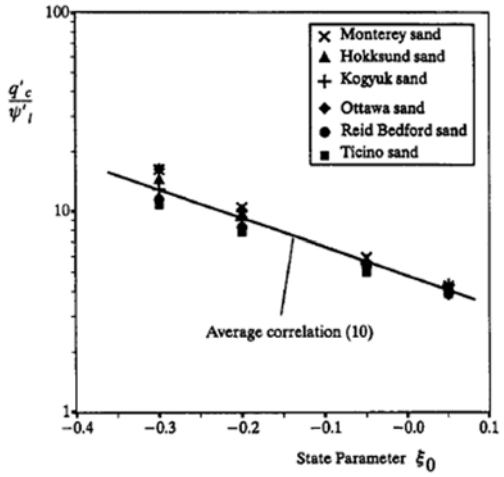

Figure 28: Theoretical correlation between $\frac{q_c}{\psi_L}$ and ξ_0 for six different sands (after Yu et al. [1996])

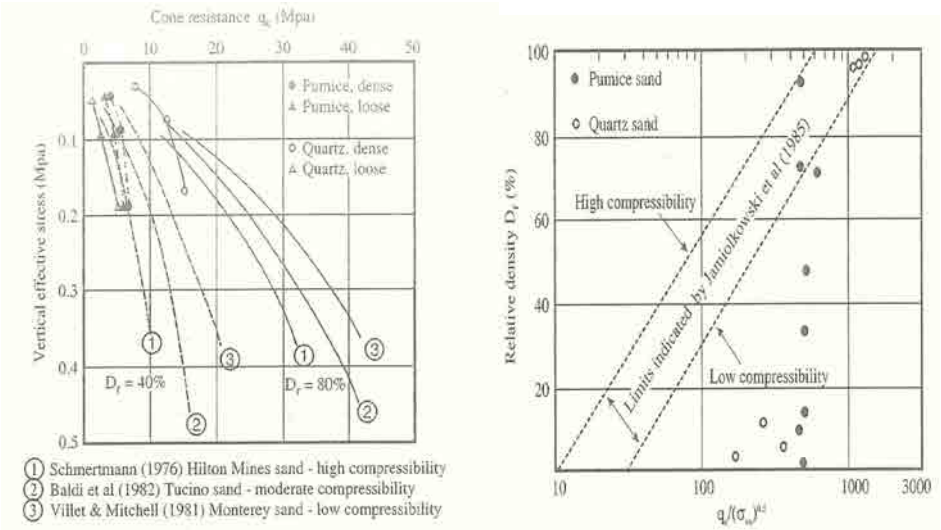

(a) (b)

Figure 29: Comparison of results with other sands of varying compressibility(a) after Robertson and Campanella [1983] and (b) after Jamiolkowski et al. [1985]

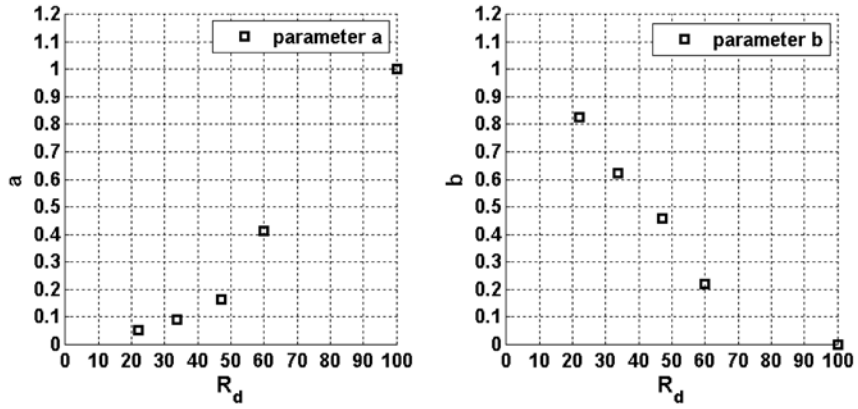

(a) (b)

Figure 30: Coefficient (a) a and (b) inferred from the CC performed in TS and TOS

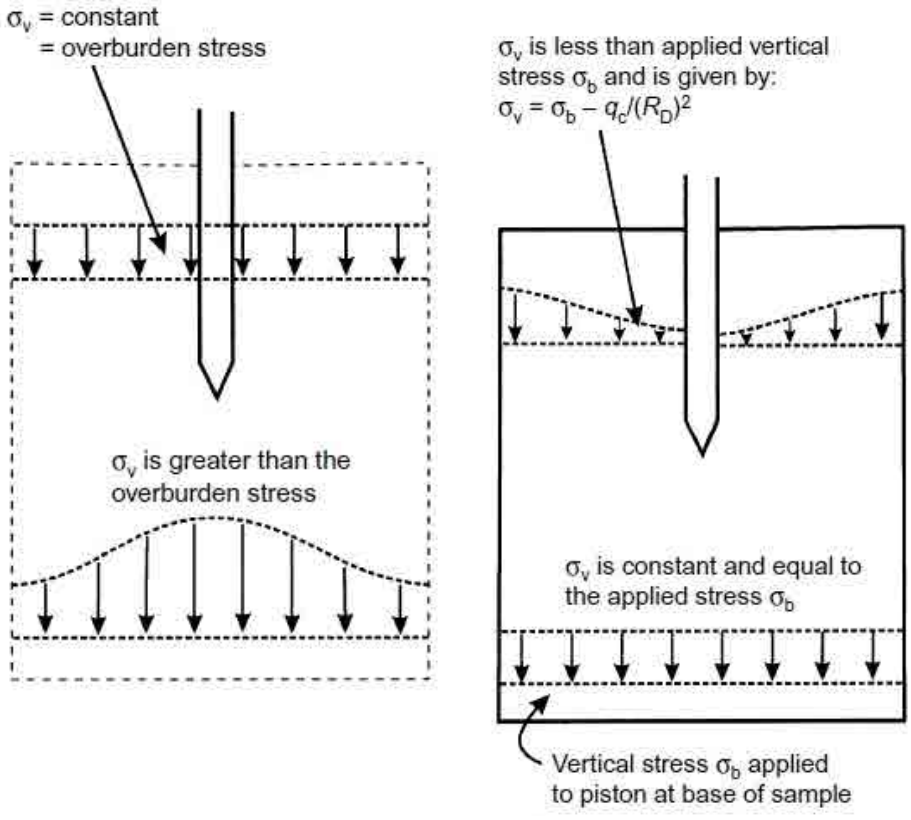

(a) (b)

Figure 31: Stress state in (a) field and (b) chamber (after Wesley [2002])

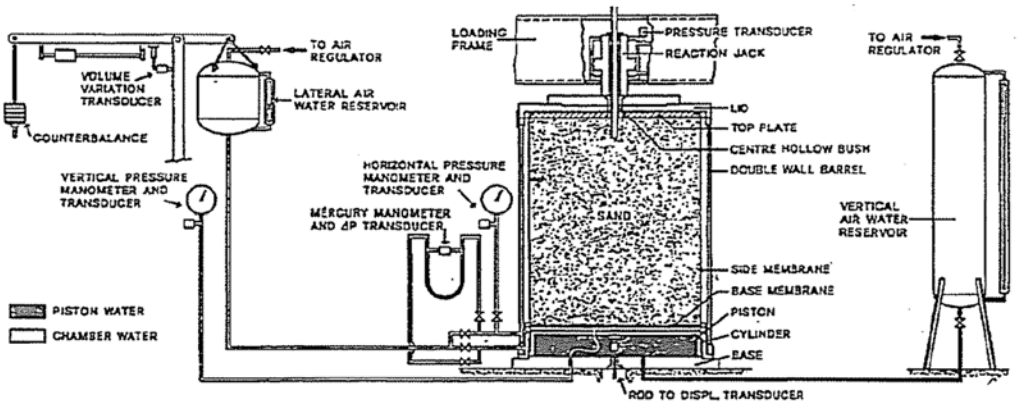

Figure 32: The cross–section, the arrangement and the instrumentation of the CC in ENEL–CRIS (after Bellotti et al. [1982])

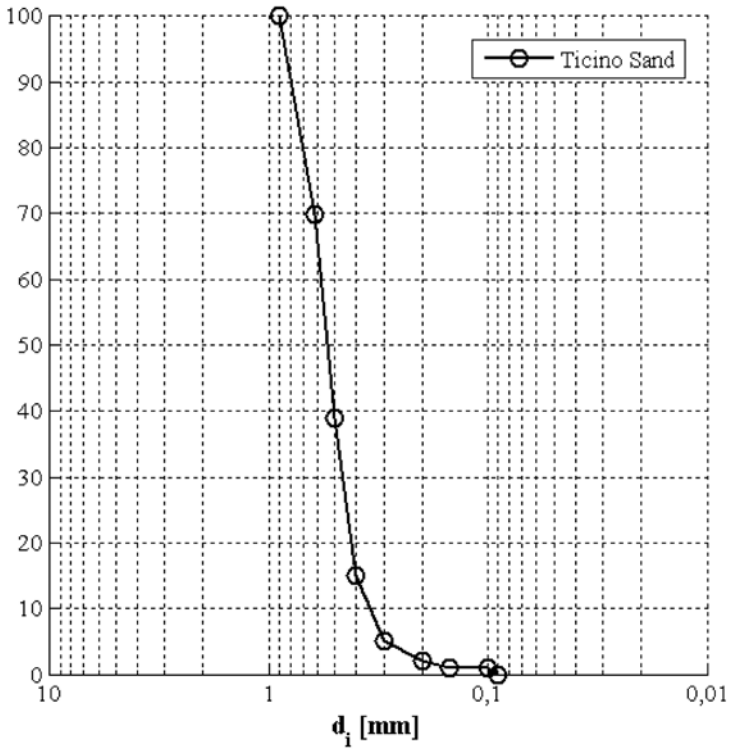

Figure 33: Particle size distribution of Ticino Sand

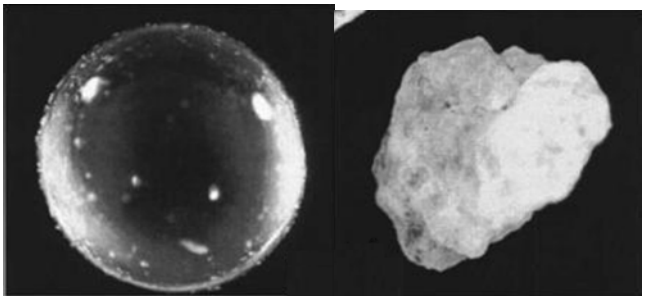

(a) (b)

Figure 34: Micro–graphs showing grain shape of (a) glass beads of 32 mm in diamter; (b) Ticino sand of 33 mm in diameter

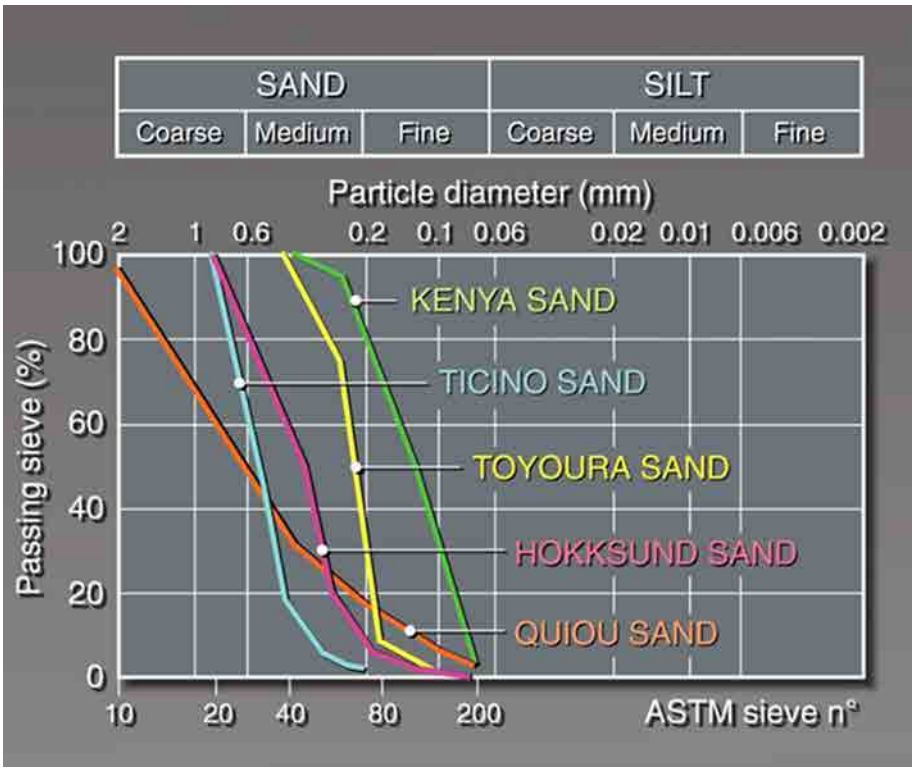

Figure 35: Particle size distribution of other sand used in CC tests at ISMES/ENEL: Toyoura, Hokksund, Quiou. Kenya sands) (M. Jamiolkowski lecture G–166–S. Pietroburgo–CPTU–NM)

Table 9: Index of properties of other sand used in CC tests at ISMES/ENEL

Sand gradation	D_{50}	C_u	γ_{min}	γ_{max}	e_{min}	e_{max}	G_s
	[mm]	[-]	[kN/m^3]	[kN/m^3]	[-]	[-]	[-]
Toyoura	0.22	1.35	13.09	16.13	0.611	0.985	2.65
Hokksund	0.45	1.91	11.10	17.24	0.578	0.929	2.72
Quiou	0.71	4.47	12.92	15.29	0.838	1.282	2.72
Kenya	0.13	1.85	9.85	11.97	1.277	1.769	2.78

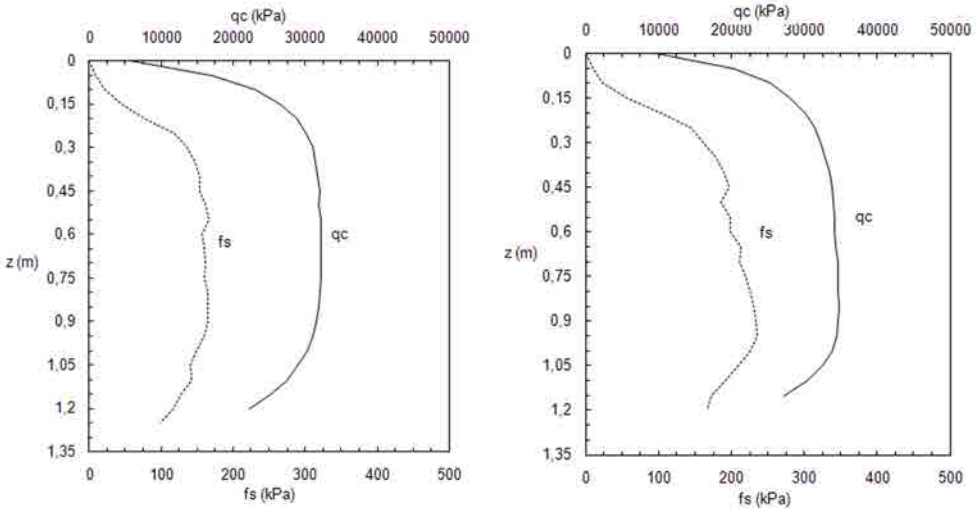

Figure 36: Influence of boundary type conditions on cone and shaft resistance under (a) BC1 and (b) BC3. Tests are performed on Ticino sand with $\sigma_v = 313$ kPa and $\sigma_h = 133$ kPa, $D_R = 95\%$ and OCR=1.0

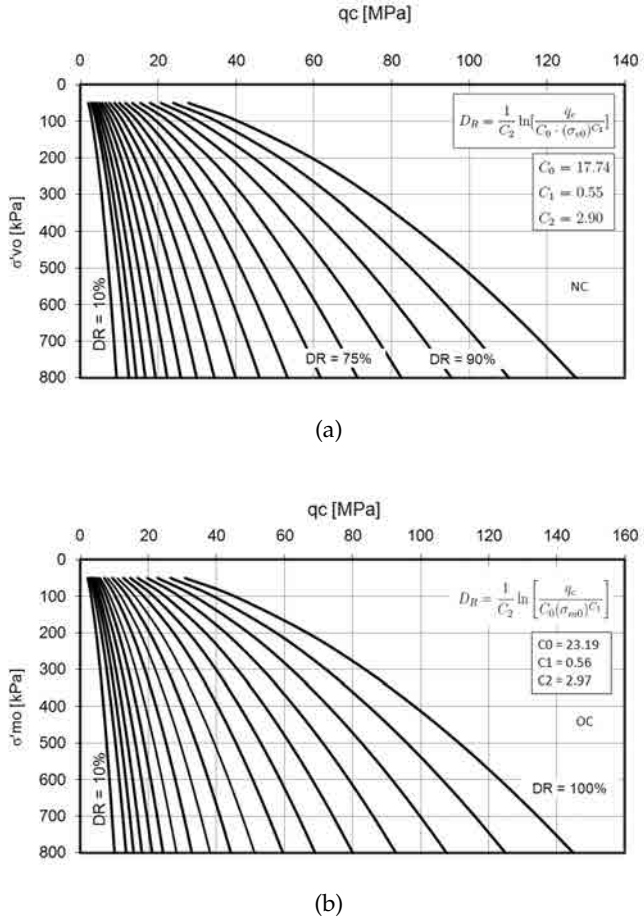

Figure 37: Relative density of (a) normally consolidated (NC) and (b) overconsolidated (OC) Ticino sand

Table 10: Coefficients C_0, C_1, C_2 from Eg. 3.7; (TS–Ticino Sand, TOS–Toyoura Sand, HK–Hokksund Sand)

$\sigma' = \sigma'_{v0}$	TS	TS + TOS + HS
C_0	17.74	17.68
C_1	0.55	0.50
C_2	2.90	3.10
R	0.90	0.89
$\overline{\sigma}$	0.12	0.10
N	305	180
$\sigma' = \sigma'_{m0}$	TS	TS + TOS + HS
C_0	23.19	24.94
C_1	0.56	0.46
C_2	2.97	2.96
R	0.87	0.87
$\overline{\sigma}$	0.10	0.10
N	299	484

4

DISCRETE ELEMENT METHOD

4.1 INTRODUCTION

The *Discrete Element Method* also known as the *Distinct Element Method* (**DEM**) is a numerical technique suitable to investigate the mechanical behaviour of assemblies of discrete particles. It can be used to simulate efficiently quasi–static and dynamical behavior of large granular assemblies. The DEM was introduced by Cundall [1971] for the analysis of rock–mechanics problems. Later, DEM analysis was expanded and applied also to soils (Cundall and Strack [1979]). A full description of the method can be found in following references: Cundall [1988], Hart et al. [1988] and O'Sullivan [2011b]. In the last few decades, many researchers have worked on the developments of DEM, aiming to (i) obtain information that can be used to formulate and/or validate more realistic continuum constitutive models, (ii) model populations of particles that conform with the specifications of a real granular material. Efforts are also been made to enhance the capabilities of the DEM by (i) implementing more efficient algorithms for contact detection, updating, and determination of the interaction at contact, (iv) including particle–fluid interaction and (v) combining DEM–FEM.

In this work a simplified version of the 'classical' DEM, proposed by Cundall and Strack [1979], Cundall [1988] is used. This version is implemented in PFC^{3D}, a three–dimensional commercial DEM code developed by Itasca Consulting Group, Inc.

Generally, PFC^{3D} allows to generate spherical particles that displace independent of one another and interact only at contacts or interfaces between particles. In DEM models two characteristics need to be defined at the onset: (i) representation of the contacts which may break and form while the system moves and (ii) representation of the particles (material) which can move relative to each other and rotate. The inter–particle contact (acting at a point) may be represented as a (i) soft contact (Figure 38b) or (ii) hard contact (Figure 38a). In hard contact (= event driven method), the inter–penetration or deformation during impact are disregarded and the collision is infinitely brief, instantaneous. A hard sphere approach is suitable for those analysis involving rapid granular flow, where the granular material is completely or partially fluidized, i.e. avalanches, rapid flow through conduits in manufacturing process. This approach is not commonly considered in current geotechnical engineering research or practice.

PFC^{3D} adopts a soft contact approach (time–driven method), where particles are rigid, but may overlap at the contact point. The magnitude of interaction depend on the inter–particle penetration depth (overlap size). The contact between particles is generally modeled as a spring–dashpot system (Figure 39). In that kind of system, the divider is incorporated in order to not allow any contact forces between particles which are separated and the slider represents Mohr–Coulomb friction law and allows to determine the shear forces between two particles along tangential direction. Most of the approaches used in the field of geomechanics fall into the soft–sphere category.

The solid material consists of a number of particles that may be assumed to be rigid

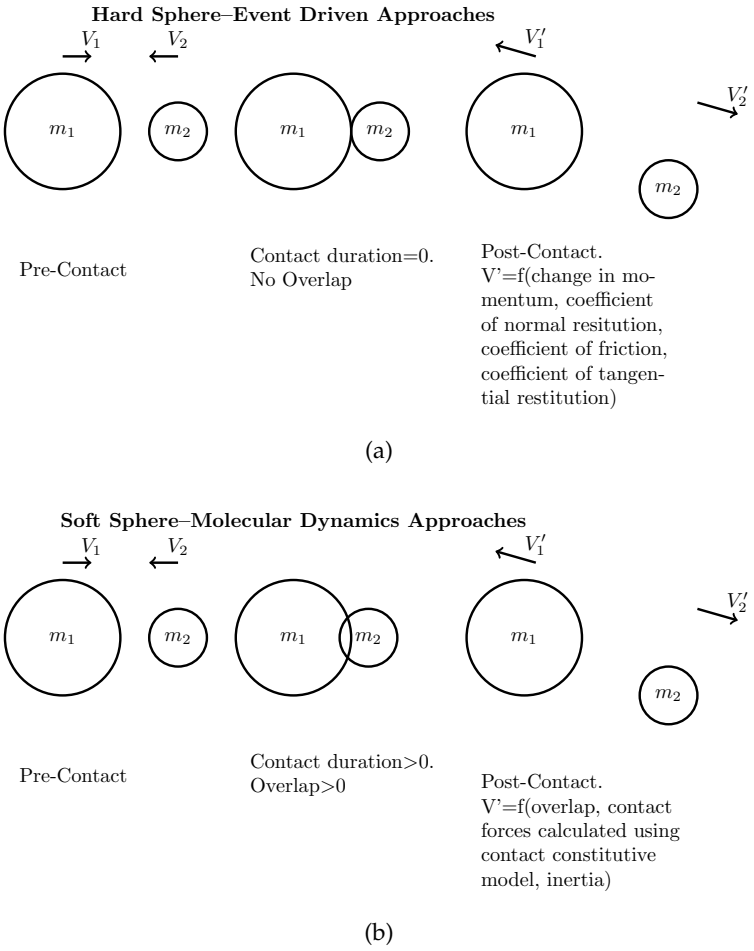

Figure 38: (a) Hard and (b) soft sphere approaches in DEM (after O'Sullivan [2011a])

or deformable. DEM modeling is typically restricted to cohesionless or granular materials. In that kind of materials, deformation results primarily from the sliding and rotation of particles as rigid bodies and the opening and interlocking at interfaces, and not from individual particle deformation. Hence, precise modeling of particle deformation is not necessary to obtain a good approximation of the mechanical behavior for such systems (Itasca Consulting Group, Inc [2008]).

In this chapter the fundamentals of DEM (PFC^{3D}) will be recalled. We will show that all calculations performed in DEM alternate between the application of Newton's second law to the particles and a force–displacement law at the contact. Next, the constitutive contact models will be described. We will also look at dynamic nature of the model. Later some insight into PFC^{3D} programming and implementation will be given to understand the operation of the Code. Finally, the tools employed to describe DEM results at both micro and macro levels will be presented.

4.2 FUNDAMENTALS OF DEM AS IMPLEMENTED IN PFC3D

The *Distinct element method* (DEM) is based on the use of an explicit numerical scheme in which the interaction of the particles is monitored contact by contact and the motion of the particles is modeled particle by particle (Cundall and Strack [1979]). Mod-

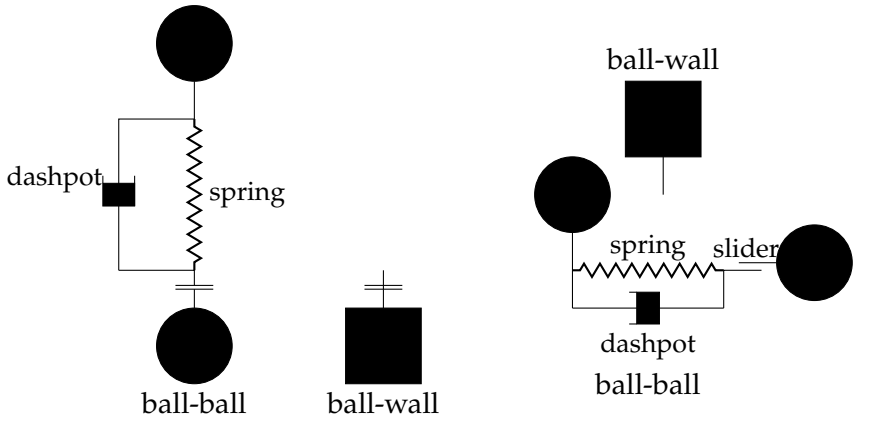

(a) normal direction (b) shear direction

Figure 39: Contact models: ball–ball and ball–wall in the normal and tangential direction.

eling with DEM involves the execution of many thousands of time steps, in which two laws are applied: (i) Newton's second law to the particles and (ii) force–displacement law at the contact. The former law (law of motion=Newton's second law) is used to determine the motion of each particle arising from the contact and body forces acting upon it, while the latter (force–displacement law) is used to update the contact forces arising from the relative motion (overlap) at each contact. At each time step the position of each particle is identified and updated.

For a well–defined problem simulated by DEM, a few fundamental steps need to be followed (after O'Sullivan [2011a]):

- specify initial geometry (including boundary conditions)
- identification of particles being in contact
- calculation of resultant forces on particles (= contact , body and applied forces) $\rightarrow$ force–displacement law
- calculation of accelerations and velocities of particles $\rightarrow$ Newton's second law
- calculation of current displacements
- update system geometry

The basic structure of the DEM algorithm consists of a loop that contains all these points. It should be noted that in quasi–static DEM simulation, physical time is of no importance and the goal is to achieve the equilibrium or steady flow with minimum computer effort and in a way that is numerically stable.

4.2.1 *Dynamic equilibrium*

In DEM, the interaction of the particles is treated as a dynamic process with states of equilibrium developing whenever the internal forces balance. The equilibrium contact forces and displacements of stressed assembly of particles are found by series of

calculations tracing the movements of the individual particles. These movements are the result of the propagation through the medium of disturbances originating at the boundaries. It is a dynamic process and the speed of propagation is a function of the physical properties of the discrete medium (Cundall and Strack [1979]).

4.2.2 *Calculation cycle*

The calculations performed in the DEM alternate between the application of Newton's second law to the particles and a force–displacement law at the contact (Figure 40)

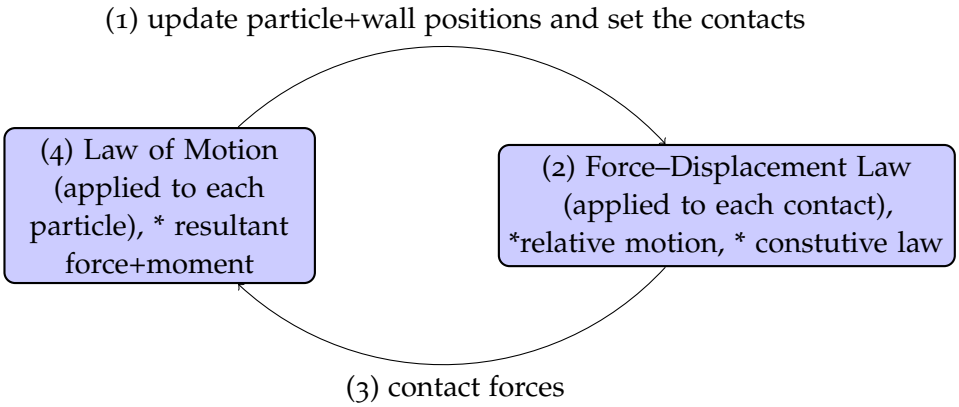

Figure 40: Calculation cycle in PFC^{3D}

4.2.2.1 *Force–displacement law*

The force–displacement law operates at contact and relates the relative displacement between two entities at a contact (ball–ball and ball–wall) to the contact force acting on the entities. This law is defined in term of contact point, ${x_i}^c$ (Eq. 4.1), lying on a contact plane defined by a unit vector, n_i and expressed as:

$$ {x_i}^c = \begin{cases} {x_i}^{[A]} + (R^A - \frac{1}{2} \cdot U^n) \cdot n_i & ball - ball \\ {x_i}^{[B]} + (R^B - \frac{1}{2} \cdot U^n) \cdot n_i & ball - wall \end{cases} \tag{4.1} $$

where U^n is an overlap, defined to be the relative contact displacement in the normal direction:

$$ U^n = \begin{cases} R^A + R^B - d & ball - ball \\ R^B - d & ball - wall \end{cases} \tag{4.2} $$

where d is a distance between the ball centers or between the ball center and the wall (Figure 43). For ball–wall contact, n_i is directed along the line defining the shortest distance (d) between the ball center and the wall. This direction is found by mapping the ball center into relevant portion of space defined by wall. For ball–ball contact, the unit normal, n_i, that defined the contact plane is given by:

$$ n_i = \frac{{x_i}^{[B]} - {x_i}^{[A]}}{d} \tag{4.3} $$

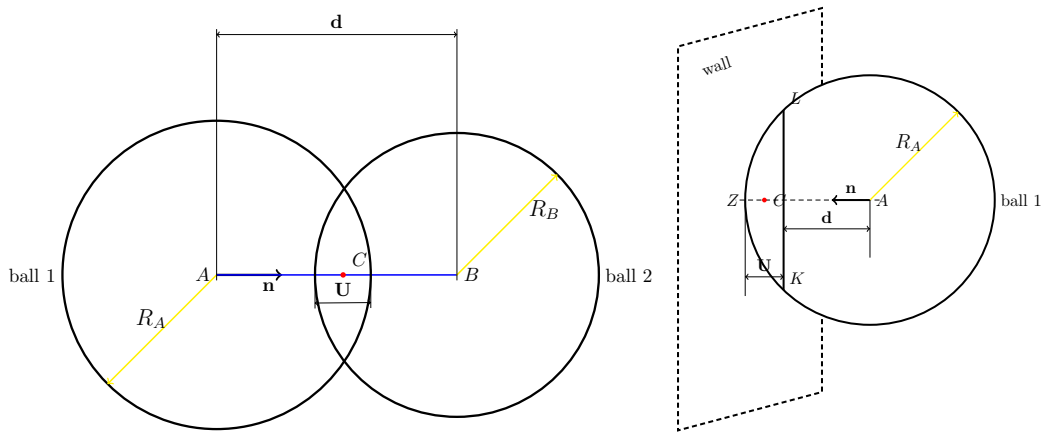

(a) ball-ball (b) ball-wall

Figure 41: Contact description

The graphical description of n_i, d as well as location of contact point can be seen in Figure 41a for a ball–ball contact and Figure 41b for a ball–wall contact.

The contact force vector, F_i, can be decomposed into normal and shear components (Figure 42) with respect to the contact plane as follow:

$$F_i = {F_i}^n + {F_i}^s \tag{4.4}$$

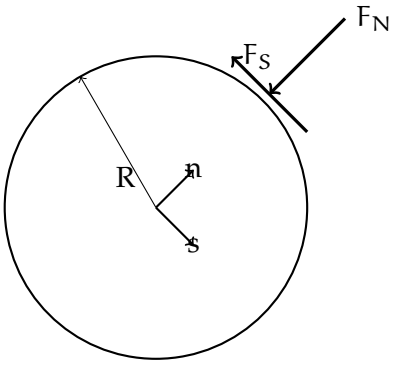

Figure 42: Decomposition of the contact force

Moreover, the contact forces are related to a corresponding displacements via normal and shear stiffness. The normal and shear contact force vectors are calculated as:

$$\begin{aligned} {F_i}^n &= K^n \cdot U^n \cdot n_i && (4.5)\\ {F_i}^s &= {F_{i,old}}^s + \Delta {F_i}^s && (4.6) \end{aligned}$$

where K^n is the normal stiffness at the contact (secant modulus), ${F_{i,old}}^s$ is an old shear vector existing at the start of the time step (after it has been rotated to account

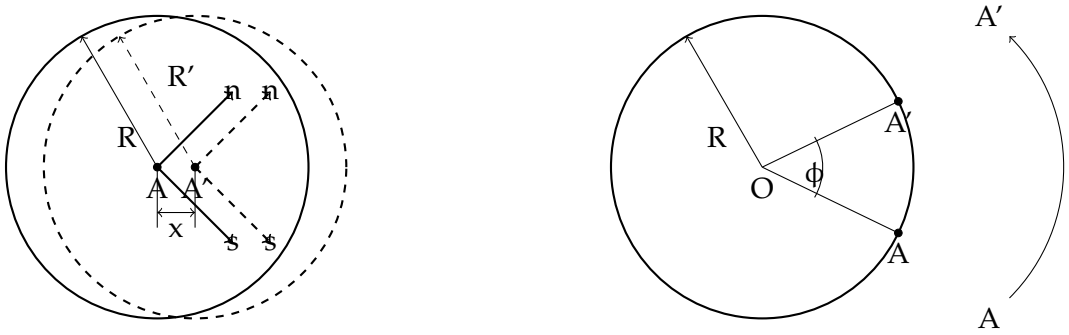

(a) translational motion (b) rotational motion

Figure 43: Types of motion of a single particle

for the motion of the contact plane) and $\Delta F_i{}^s$ is a shear elastic force–increment vector calculated as:

$$\Delta F_i{}^s = -k^s \cdot \Delta U_i{}^s \tag{4.7}$$

where K^s is the shear stiffness at the contact (secant modulus). Both values of the stiffnesses are determined by the current contact–stiffness model (for instance, the linear contact model or Hertz–Mindlin (nonlinear) contact model).
Finally, after satisfying the constitutive relations, the contribution of contact force to the resultant forces and moment on the two entities in contact are used to update the motion of each rigid particle. This is done by applying the Law of Motion.

4.2.2.2 *Law of motion*

> **The rate of change of momentum of a body is proportional to the resultant force acting on the body and is in the same direction.**

The motion of a single rigid particle is determined by the resultant force and moment vectors acting upon it and determined using force–displacement law. Moreover, this motion is described in terms of the translational motion of a point in the particle (Figure 43(a)) and the rotational motion of the particle (Figure 43(b)).

The translational motion of a center of the mass (Eq.4.8) is described in terms of its position (x_i), velocity ($\dot{x}_i$) and acceleration ($\ddot{x}_i$), while rotational motion (Eqn. 4.9) is described in terms of its angular velocity (ω_i) and angular acceleration ($\dot{\omega}_i$).

$$F_i = m \cdot (\ddot{x}_i - g_i) \tag{4.8}$$

$$M_i = H_i = I \cdot \omega_i \tag{4.9}$$

In eqns. 4.8 and 4.9 F_i is the resultant force, m is a total mass of the particle, g_i is the body force acceleration vector (e.g. gravity vector), M_i is a resultant moment

acting on the particle and H_i is the angular momentum of the particle. Moreover, these equations are integrated using a centered difference procedure involving a timestep of Δt. The quantities $\dot{x}_i$ and ω_i are computed at the mid–intervals of $(t \pm n\frac{\Delta t}{2})$, while the quantities x_i, F_i and M_i are computed at the primary intervals of $(t \pm n\Delta t)$. Finally, the velocities are expressed by:

$$\dot{x}_i^{(t+\frac{\Delta t}{2})} = \dot{x}_i^{(t-\frac{\Delta t}{2})} + (\frac{F_i{}^{(t)}}{m} + g_i) \cdot \Delta t \tag{4.10}$$
$$\omega_i{}^{(t+\frac{\Delta t}{2})} = \omega_i{}^{(t-\frac{\Delta t}{2})} + (\frac{M_i{}^{(t)}}{I}) \cdot \Delta t$$

In the final step the position of each particle center is updated using following formula:

$$x_i{}^{(t+\Delta t)} = x_i{}^{(t)} + \dot{x}_i^{(t+\frac{\Delta t}{2})} \cdot \Delta t \tag{4.11}$$

The calculation cycle for the law of motion are summarized in Table 11.

Table 11: Calculation cycle for the Law of Motion

Step	$t - \frac{\Delta t}{2}$	t	$t + \frac{\Delta t}{2}$	$t + \Delta t$
Quantities	F_i, M_i, x_i	$\dot{x}_i, \omega_i$	$\dot{x}_i, \omega_i$	F_i, M_i, x_i

The values $F_i{}^{(t+\Delta t)}, M_i{}^{(t+\Delta t)}$ are obtained by application of the force–displacement law and $x_i{}^{(t+\Delta t)}$ is found using eqn. 4.11.

4.2.3 *Contact constitutive model*

The constitutive behavior of material is given at contact level. The contact model is described by three components:

- contact stiffnesses which relate the contact forces and relative displacements in the normal and shear directions
- slip behavior which enforces a relation between shear and normal contact forces such that the two contacting entities may slip relative to one another
- bonding behavior (contact and/or parallel bonds) which acts as a kind of glue joining the two particles

PFC^{3D} also allows the implementation of user–defined contact models. In our study a simple linear stiffness functional contact model is always used. The model parameters are (i) the normal stiffness (k_n), (ii) the ratio between normal to tangential stiffness ($\frac{k_n}{k_s}$) and (iii) the interparticle friction (μ). The slip occurs when the absolute value of shear force at any contact exceeds the limit ($|F^s{}_{(i)}| > F^s{}_{(max)}$). No bonding exists between particles.

4.2.4 *Damping*

In order to dissipate energy stored into the system and in consequence to reduce the computational time (= number of steps) needed by the system of particles to reach its steady (equilibrium) state, PFC^{3D} offers the possibility of using frictional sliding or/and numerical damping. Friction occurs during sliding when the absolute value of shear force at any contact exceeds the limit. However, frictional sliding may not be active in a given model, or may not be sufficient to arrive at a steady state solution in a reasonable number of steps. Hence, local damping (acting on each ball) and viscous damping (acting at each contact) are available in PFC^{3D} to dissipate supplied energy. Local damping applies a damping force, with magnitude proportional to unbalanced force, to each ball. Viscous damping adds normal and shear dashpots (at each contact) which act parallel with the existing contact model and provide forces that are proportional to the relative velocity difference between two elements (ball–ball or ball–wall). In PFC^{3D}, by default local damping is active and viscous damping is inactive.

For compact assemblies, local damping is the most suitable to establish equilibrium and to conduct quasi–static analysis. A damping–force term is added to the equation of motion eqns. 4.8 and 4.9, such that the damped equations of motion can be written as:

$$\begin{aligned} F_{(i)} + {F^d}_{(i)} &= M_{(i)} \cdot A_{(i)}, \text{for i=1...6} && (4.12)\\ M_{(i)} \cdot A_{(i)} &= m \cdot \ddot{x}_{(i)}, \text{for i=1...3} && (4.13)\\ &= I \cdot \dot{\omega}_{(i)}, \text{for i=4...6} \end{aligned}$$

where $F_{(i)}$, $M_{(i)}$ and $A_{(i)}$ are the generalized force, mass and acceleration components, respectively. ${F^d}_{(i)}$ is a damping force.

$${F^d}_{(i)} = -\alpha |F_{(i)}| \mathrm{sign}(v_{(i)})^1, \text{for i=1...6} \quad (4.14)$$

expressed in terms of the generalized velocity:

$$\begin{aligned} v_{(i)} &= \dot{x}_{(i)}, \text{for i=1...3} && (4.15)\\ &= \omega_{(i-3)}, \text{for i=4...6} \end{aligned}$$

The damping force is controlled by the damping constant α.
This form of damping has the following advantages:

- only accelerating motion is damped
- α is non–dimensional
- damping is frequency–independent (regions with different natural periods are damped equally, using the same α)

Use of damping does not affect the equilibrium value of the forces (Itasca Consulting Group, Inc [2008]), but it does reduce the number of calculation cycles needed to achieve convergence to the steady–state solution (either equilibrium or steady–state failure–collapse).

4.2.5 *Integration procedure*

The solution scheme of DEM model is identical to that used by the explicit finite–difference method for continuum analysis. The use of the explicit numerical scheme makes it possible to simulate the nonlinear interaction of a large number of particles without excessive memory requirements or the need for an iterative procedure. The equations of motion are integrated using a centered finite–difference scheme expressed by equations 4.10 above. The computed solution produced by these equations will remain stable only if the chosen time step will be so small that, during a single time step, disturbances will not propagate from any particle further than to its immediate neighbors. Then, at all times the resultant forces on any particle are determined exclusively by its interaction with the contacting particles.

In PFC^{3D}, the time step (Δt) is taken as a fraction less than one of the critical time step, which is applied separately to each degree of freedom (assumption: degrees of freedom are uncoupled). The final critical time step is taken to be the minimum of all critical time steps computed for all degrees of freedom of all bodies.

$$t_{crit} = \min\left(\sqrt{\frac{m}{k^{tran}}}, \sqrt{\frac{I}{k^{rot}}}\right) \tag{4.16}$$

where k^{tran} and k^{rot} are the translational and rotational stiffness, respectively; I is the moment of inertia of particle. The stiffnesses are estimated by summing the contribution from all contacts, using only the diagonal terms of the contact stiffness matrix and are expressed as follow:

$$\begin{aligned} {k_{(i)}}^{tran} &\approx \tilde{k}_{(ii)} = \left[(k^n - k^s){n_{(i)}}^2 + k^s\right] \\ {k_{(i)}}^{rot} &\approx \hat{k}_{(ii)} = \left[R^2 k^s (1 - n^2_{(i)})\right] \end{aligned} \tag{4.17}$$

where k^n, k^s are the normal and tangential stiffnesses, $n_{(i)}$ is the contact normal vector and R is the particle radius. In these equations the subscripts are enclosed by braces to indicate that this is not a vector and that the Einstein summation convention does not apply to the repeated indices. It should be recorded that for more complex contact laws (viscosity or creep) the choice of time step should be reconsidered and checked by trial and error.

4.3 FEATURES OF PFC3D

4.3.1 *Built-in programming language: FISH*

The PFC^{3D} allows for personalization through an in–house programming language named FISH. All subroutines described later in this study have been written using this language. FISH enables the user to define new variables, functions and features, however, some useful functions come already with the program.

Apart form FISH, a user written C++ code space allows to create private PFC^{3D} executables from which that code can be executed. User–written C++ functions may be executed from the PFC^{3D} command line, or various places in the code. A new constitutive contact model can be added to PFC^{3D} by writing the model in C++ language,

compiling it as a DLL (dynamic link library) file and loading the DLL into PFC^{3D} whenever needed.

4.3.2 *Main entities*

The particle–flow model (PFC^{3D}) defines particles called 'BALLS'. Any surfaces are called 'WALLS' and are used to apply boundary conditions such as wall velocity or stresses. Walls can be generated using the WALL command:

WALL ...

..., **id** =, **face**(x1, y1, z1)(x2, y2, z2)(x3, y3, z3)(x4, y4, z4)

..., **id** =, **origin**(x0, y0, z0)**normal**(x1, y1, z1)

..., **typecylinder**, **id** =, **end1**(x1, y1, z1), **end2kn**(x2, y2, z2), **rad** = rad1, rad2

These commands create a wall with unique identification number (ID). **Face** creates a wall, that is defined by four vertices given by; x–, y–, and z–coordinates, has finite dimensions and only one active side which can interact with balls. Finite walls consume more time and memory, but do appear on graphic output. They are necessary when, for example, balls may come into contact with convex edges or vertices.

Infinite walls are created by specifying **origin** and **normal** and are useful to provide boundary conditions for a simple geometrical form. They can be also used to limit the region in which particles are generated and then discarded. Infinite walls do not appear in graphic output. Moreover, they are more efficient computationally than finite walls because no checking of the edge conditions is necessary during cycling.

WALL type cylinder creates cylinder–or cone–shaped walls. These walls are plotted as a wire–frames, consisting multiple flat plates. To define cylinder/cone the two end position of the axis as well as the radii at those positions are specified.

Walls can be fixed in space or not. They can be given translational and/or rotational velocity via the WALL command:

w_xvel,	**w_yvel**,	**w_zvel**,	**w_radvel**
w_rxvel,	**w_ryvel**,	**w_rzvel**,	

which assigns velocity components in the x–, y–, and z–and radial directions. These commands are used to define compression, loading and penetration processes. The reaction forces acting on the walls can be measured (though in–built FISH functions) and monitored (i.e. history variable). The reaction forces are:

w_xfob,	**w_yfob**,	**w_zfob**,	**w_radfob**

defined as unbalanced forces acting in x–, y–, z–, and r–direction, respectively. Normal and shear stiffnesses (for linear contact model) as well as friction coefficient for a wall with given identification number are set up using the following physical property functions:

w_kn, w_ks, w_fric

Particles can be generated using the commands GENERATE and/or BALL. The GENERATE command creates a specified number of particles limited by the walls and with positions influenced by other objects (no overlap allowed) with radii drawn at random either from a uniform statistical distribution or from a Gaussian distribution (using the keyword *gauss*). The BALL command allows the user to create spheres (one at given time) that can eventually overlap each other.

BALL, id =, x =, y =, z =, rad =

GENERATE, id = i, j, x = xi, xn, y = yi, yn, z = zi, zn, (gauss)rad = r1, r2

To represent a granular material with disordered internal structure, particles are generated in a irregular manner, having also to attain a specified porosity. If the target porosity is unrealistically low, a truncated generation will occur and decrease in particle radii and/or increase the space available are required. If the requested number of particles should fit into given space, then the keyword **tries** may be added to the **GENERATE** command line to increase the number of attempts (default value is 20000). As is was mentioned, **GENERATE** will not place a new particle if it overlaps another particle or wall. Hence, a population of particles with artificially small radii is created within the specified volume. The particles are then expanded until desired porosity is obtained. It is possible to do that by multiplying the initial radius to attain the desired one:

ini rad mul *multiplier*

Rotation of particles can be inhibited by fixing an angular motion in x–, y–, and z–direction.

FIX zs ys xs

Properties of the particles, including density and normal and tangential stiffnesses are assigned with the **PROPERTY** command, :

PROPERTY density = kn = ks =

4.3.3 *Implementation of BC in this study*

In the case of a cubical specimen, three plates (one for each axis) are fixed (ABCD, ABEF, ACEG), the remaining three plates are used to apply loading conditions while in the cylindrical specimen only the bottom plate remains fixed (Figure 44). The lateral plates (BDFH and CDGH) and cylinder–wall are servo–controlled to apply the desired confining stress. Four different control schemes (Figure 21) were implemented in order to simulate different tests conditions, as follows:

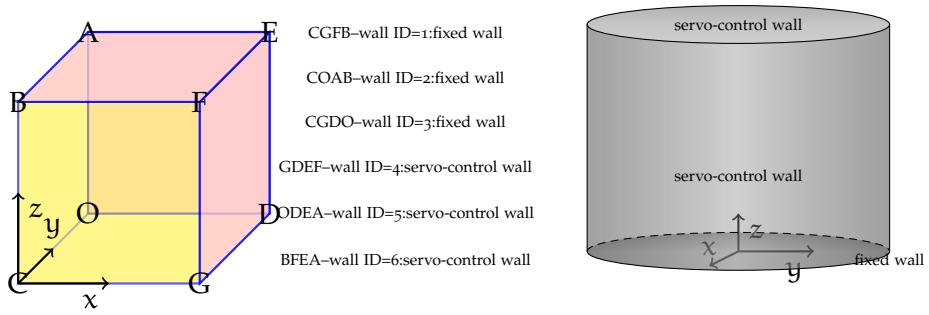

Figure 44: Geometry of the samples: fixed and servo–controlled walls

1. SIGMA–SIGMA –all stresses are controlled (to apply isotropic/anisotropic stresses to triaxial specimens and to apply a BC1 boundary condition (σ_v=constant and σ_h=constant)) in a CC.

2. VEL–SIG –horizontal stresses and velocity of the top plate are controlled (to perform strain controlled triaxial test and to apply a BC4 boundary condition ($\Delta\epsilon_v = 0$ and σ_h=constant) in a CC.

3. VEL–VEL –horizontal and vertical strains are controlled (to apply boundary condition BC2 ($\Delta\epsilon_v = 0 = \Delta\epsilon_h = 0$)) in a CC.

4. SIG–VEL – vertical stress and horizontal strains are controlled (to apply BC3 condition in a CC ($\Delta\epsilon_H = 0$ and σ_V=constant) or to perform one–dimensional compression through top plate–EDO)

The FISH implementation routines for these schemes can be found in Appendix A.

4.3.4 *Specimen generation in this study*

The PFC^{3D} code allows to generate only spherical particles with either a uniform distribution between maximum and minimum particles diameter or a Gauss distribution. To achieve a better fit to the experimental grain size distribution, it was then necessary to develop a different technique to generate the DEM specimen.

4.3.4.1 *Exact experimental PSD*

From the experimental grain size curve we extracted the following diameters d_0, d_{10}, d_{20}, d_{30}, d_{40}, d_{50}, d_{60}, d_{70}, d_{80}, d_{90}, d_{100} (numbers correspond to the percentage finer by weight). 10 classes are thus established[2](Figure 45) and for each of them a representative, average radius (i.e. r_{25} on Figure 45) is assigned to each class. Hence,

$$\begin{aligned} r_{k5} &= 0.5(r_i + r_j) \\ i &= 0, 10, 20, ..., 100 \\ j &= 10, 20, 30, ..., 100 \\ k &= 5, 15, 25, ..., 95 \\ i &< j \end{aligned} \tag{4.18}$$

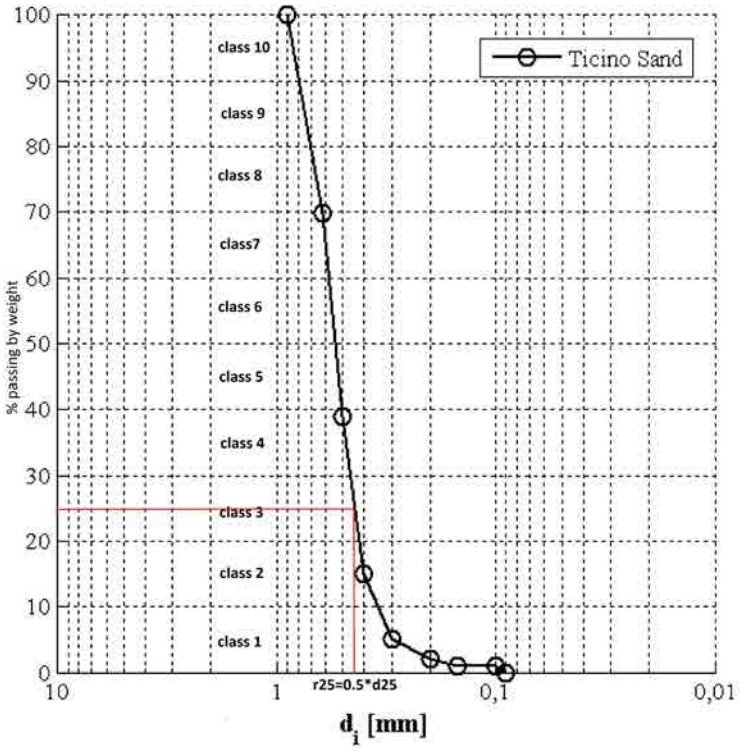

Figure 45: Grain size curve of Ticino Sand TS4 generated using method I

To build a specimen with given initial porosity (n) we adopted the following expression:

$$n = 1 - \frac{V_{(p)}}{V} \tag{4.19}$$

where $V_{(p)}$ is the volume of all particles in the specimen, and V is the total specimen volume. The volume of the solid part of the specimen can be calculated as follows:

$$\begin{cases} V_{(p)} = V(1-n) \\ V_{(p)} = \sum N_i \cdot \frac{4}{3}\pi {R_i}^3 \end{cases} \tag{4.20}$$

where N_i is a number of particles with given radius $R_i = R_{k5}$ and assuming the same density for all particles can be expressed by:

$$N_i = \frac{3}{4\pi} \cdot \frac{0.1 V_{(p)}}{R_{k5}^3} \tag{4.21}$$

Next, we sum number of particles within the given radius ranges (N_i) to obtain limit values (lower and upper limit) for each bin.

$$\begin{aligned} n1 &= N_i \\ n2 &= n1 + N_{i+1} \\ &\dots \\ n10 &= n9 + N_{i+1} \end{aligned} \tag{4.22}$$

2 * depending on the form of PSD distribution more or less classes might be selected

Finally, using the particle generation command we create uniformly distributed particles within each bin.

GENERATE, id = n1, n2, x = xi, xn, y = yi, yn, z = zi, zn, rad = r1, r2

The implementation procedure can be seen in file *count_diameter_radial.fis*. in Appendix A. This particle generation procedure can be used to reproduce even complicated (not regular) experimental grain size curves.

4.4 INTERPRETATION TOOLS: FROM MICRO–TO–MACRO BEHAVIOR

The results of DEM simulations can be described at various levels of resolution, using variables that have different origins and purposes. The variables that are employed can be categorized as either discrete or continuum-inspired. As for the levels of resolution it is convenient to distinguish between the microscopic level, the mesoscopic level and the macroscopic level of description.

Discrete variables are those directly derived from the basic modelling units, i.e. particles and contacts i.e. contact points, contact forces, particle displacements, etc. Continuum–inspired variables are those that can be also employed in continuum-mechanics: stress and strain tensors are the most common, but a fabric tensor might be another relevant example.

The microscopic level of resolution describes variables at the highest possible resolution, that is, at the particle or contact level: the variables described at this level are usually discrete, but they might be also continuum inspired (e.g. particle stress). In this section we will describe the microscopic variables examined in this thesis.

In this section we will describe also the criteria and procedures that have been employed in this thesis for analyzing the simulation results at the mesoscopic level. The mesoscopic level of resolution uses a representative volume element (RVE) to obtain averaged values of the relevant variables: both discrete and continuum-inspired variables can be represented at this level. How the RVE is defined (which size and geometry is specified, what averaging procedure is applied) is crucial for the outcome. These criteria have to be specified bearing in mind the purpose of the exercise. Sometimes the purpose might be is the justification/proposal of a micro basis for a continuum constitutive law (e.g. Jiang et al. [2006a]). In this case a coherent definition of the RVE with that underlying the continuum model is necessary. On the other hand, sometimes the purpose of the mesoscopic analysis it is mainly that of gaining understanding on an engineering system. In that case the RVE choice might be more pragmatic. The different RVE that have been used in this work for averaging purposes and mesoscopic description are illustrated in Figure 47 . As illustrated measurement spheres (MS), cylindrical shells volumes (=RV) and horizontal bands (CB) have been used to define averaging volumes (V).

Finally, the macroscopic level of resolution makes reference to properties or responses of the whole system being described like cone tip resistance, sample boundary displacements, sand production in a well simulation, etc. They are usually observed at the external boundaries of the discrete material.

The macro-response of the system is usually of engineering interest. It can be used to specify the material properties. For a material with arbitrary packing, a micro-

property specification procedure is needed to establish micro-parameters such as particle stiffness (k_n and k_s), particle friction coefficient (ϕ_μ) and damping (δ). In this approach, the relationship between the micro–parameters and the macro–response can be established by fitting the input micro–parameters in a series of simulations. The micro–parameters of the particle assemblies can then be determined by matching its macro-property response to a particular physical material. This procedure is called micro-parameter calibration and is described in detail in Chapter 5.

4.4.1 *Discrete–inspired variables*

The discrete–inspired variables that are employed in this work are:

- total (or active) number of contact points or number of contact points per particle (coordination number);
- contact normal orientation;
- contact forces;
- particle displacement.

The graphical presentation of all these variables uses MATLAB as a post–processing tool.

4.4.1.1 *Coordination number*

The coordination number (C_n) is described at the mesoscopic level. It is then defined as average number of active contacts per particle in a given volume (V) and is computed as:

$$C_n = \frac{\Sigma_{N_p} n_c^{(p)}}{N_p} \tag{4.23}$$

The summations are taken over the N_p particles with centroids in the measured region (volume); $n_c^{(p)}$ is the number of active contacts (carrying a nonzero normal force) of particle (P). The C_n is investigated before and during the cone penetration process to capture inhomogeneities in the model (before) and changes caused by penetrating device (during).

4.4.1.2 *Contact forces*

Contact forces are examined at micro and mesoscopic level. At the microscopic level we represent the contact force network, drawing a line between the centroids of particles in contact, with the line thickness proportional to the contact force magnitude. Contact forces tend to develop force chains (strong or weak) that are important for understanding of particulate material response and also allow to observe any inhomogeneities in the material. However, plots of contact force network allow only qualitative analysis of the contact forces. A mesoscopic approach for analyzing the contact distribution is to look at polar histograms or rose plots that indicate the number of contacts forces oriented in a given direction within a given volume.

4.4.1.3 *Particle displacement*

Particle displacement is described at the micro (for individual particle) and meso (for group of particles) level. The graphical presentation of particle displacement will be present in two ways: (i) plan view of spheres colored to indicate magnitude of displacement and (ii) plots of displacement paths of particles (group of particles within a REV) in zones spatially distributed all over the specimen with different vertical and radial distances from cone device.

4.4.2 *Continuum–inspired variables*

4.4.2.1 *Porosity*

Porosity can be calculated using following expression:

$$n = 1 - \frac{V^{(p)}}{V} \tag{4.24}$$

where V is a total measurement volume, and $V^{(p)}$ is the volume of particles. The volume occupied by particles needs to be accurately determined. The volume of particles that are completely within the measurement volume is straightforward and can be calculated by summing volumes of all spheres with given radius, R:

$$V^{(p)} = \sum_{N_p} \frac{4}{3}\pi R^3 \tag{4.25}$$

The problem comes when part of the particles intersect one or more measurement volume boundaries. A procedure to calculate partial volumes of a spheres was developed by Cheung [2010]. When consider the cylindrical bands (CB), the particle intersection with the inner or outer circumferential boundaries can be approximated as a two intersecting spheres or plane intersecting spherical particle. Thus, there are four possible scenarios depending on the position of the centroids of particles in the selected volume (Figure 46).

SCENARIO I Inner circumferential/bottom plate of measurement volume boundary intersects with the particle, and the centroid of particle is within the measurement volume:

SCENARIO II Inner circumferential/bottom plane measurement volume boundary intersects with the particle, and the centroid of particle is outside the measurement volume

SCENARIO III Outer circumferential/top plane measurement volume boundary intersects with the particle, and the centroid of particle is within the measurement volume

SCENARIO IV Outer circumferential/top plane measurement volume boundary intersects with the particle, and the centroid of particle is outside the measurement volume

The detailed calculation of particle volumes can be seen in Appendix C.

4.4.2.2 *Stresses*

A microscopic description of stress is obtained by representing the magnitude of average stresses for individual particles. The average stress in particle in equilibrium is calculated as:

$$\overline{\sigma}_{ij}^{(p)} = -\frac{1}{V^{(p)}} \sum_{N_c} |x_i^{(c)} - x_i^{(p)}| n_i^{(c,p)} F_j^{(c)} \tag{4.26}$$

where $V^{(p)}$ is the particle volume, $x_i^{(c)}$ is a location of force ($F_j^{(c)}$) acting at contact, $x_i^{(p)}$ is the location of the particle centroids and $n_i^{(c,p)}$ is the unit–normal vector directed from particle centroids to the contact location. It should be noted that, in general, the particle stress tensor, $\overline{\sigma}_{ij}^{(p)}$ thus computed, might be asymmetric (see Misra [1993], Oda and Iwashita [1999]). For simplicity, only the symmetric part of it is considered ($\hat{\sigma}_{ij}$). The particle stress tensor was always evaluated in a certain reference. To express it a transformation to a cylindrical coordination was sometimes necessary. The detailed procedure can be seen in Appendix B.

For a mesoscopic description the average stress $\overline{\sigma}_{ij}$ in a volume V is defined by:

$$\overline{\sigma}_{ij} = -\left(\frac{1-n}{\sum_{N_p} V^{(p)}}\right) \sum_{N_p} \overline{\hat{\sigma}}_{ij}^{(p)} V^p \tag{4.27}$$

where $\overline{\sigma}_{ij}$ is the stress tensor acting throughout the volume V, $\hat{\sigma}_{ij}^{(p)}$ is the average stress (symmetric part) in particle (p), $V^{(p)}$ is the volume of particles, whose centroids are included in volume V. Having calculated volumes of particles and in consequence porosity, we can than obtained average stress within the measurement volume by using eqn. 4.27.

The stress distribution in an assembly can be obtained by defining a number of MS ((Figure 47a)) at different locations in the assembly and calculating the average stress in each measurement sphere. This procedure was used to quantify homogeneity of the model prior to penetration process. Full analysis can be found in Chapter 6. The ring–type volumes (Figure 47c) and cylindrical bands (Figure 47b) are used to analyze changes in stresses while the penetration proceeds.

4.4.2.3 *Strains*

Calculation of stresses in DEM is rather straightforward and based on averaging approach. When calculating strains using DEM approach, the displacements and rotations (if not inhibited) are calculated for selected points and then a homogenization technique is applied as a post–processor to obtain an average displacement gradient value for a collection of particles. The strains are then calculated from the displacement gradients.

Several homogenization approaches for strain calculations are available (i.e. Bagi and Bojyar [2001], Dedecker et al. [2000], Cambou [2000], however, two significant limitations of these methods remain: (i) problems with incorporation of particle rotations and (ii) the problem of capturing and visualization of the strain localization. Hence, a new method proposed by O'Sullivan et al. [2003] using a domain discretization for strain calculation is adopted in this work. This method is capable of capturing

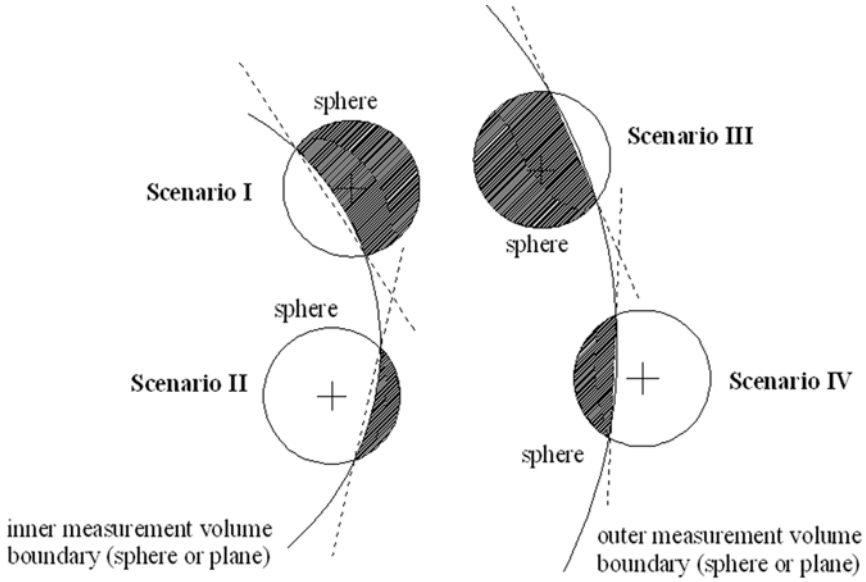

Figure 46: Intersection with circumferential RV boundary

particle rotations and employs a non–local meshfree interpolation procedure capable of smoothing the erratic displacements in strain localizations, to better define their evolution. In this section we only provide a general rules of meshfree homogenization approach for strain calculation. For more detailed description of the method refer to O'Sullivan et al. [2003].

A schematic diagram of this approach can be seen in Figure 48. Basically, in the meshfree approach, to each particle is assigned a region of influence ('circular' (2D) or 'spherical' (3D)) over which it contributes to the calculated strains. This contribution decrease as the distance from the particle centroid increase. That kind of response can be capture by wavelet type functions, which guarantee that the interpolation function describing the displacement field is continuous and differentiable over the region of influence also called compact support. The advantage of this method is that provides a smooth interpolation basis capable of capturing the high deformation gradient fields (and strain field), and can eliminate the high inter–element variation in strain values associated with the triangulation (or other cell based) homogenization approaches. Example of wavelet functions (1D, 2D and 3D) can be seen in Figure 49.

The displacements are known from the DEM simulations ($u(x_i)$). A grid is generated to serve as a referential continuum discretization over the volume of particles under consideration and the strains are calculated at these grid points. In the original code (O'Sullivan et al. [2003]), a rectangular grid was generated, while in our study a cylindrical grid was adopted. This alternative grid was implemented in the original MATLAB code and employed to calculate radial and circumferential strains (ϵ_Θ and ϵ_r). Figure 50 shows the top and side view of cylindrical grid. The cylindrical grid consists of 5160 grid points distributed in 10 horizontal layers (Δ_z=0.0624 m). Each horizontal layers consist of 516 grid points equally spaced (Δ_r=0.05 m).

The nodal displacements at the grid points can be expressed as follow:

$$u(x) \simeq N_p \sum_{i=1} K_\rho(x - x_i, x) u(x_i) \Delta V_i \tag{4.28}$$

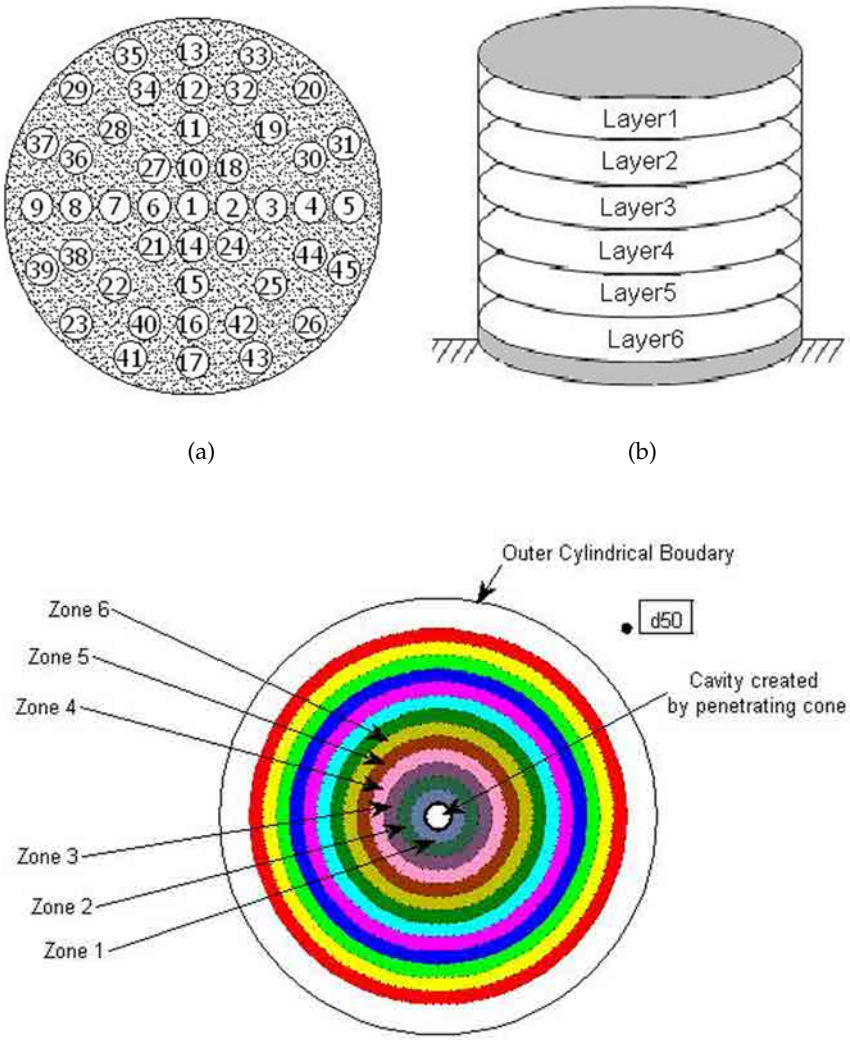

Figure 47: The averaging volumes (a) measurement spheres (MS), (b) horizontal layers and (c) cylindrical shells volumes

where N_p is the number of nodes, ΔV_i is the nodal weight, and the term $K_\rho(x - x_i, x)$ is given by:

$$K_\rho(x - x_i, x) = C_\rho(x - x_i, x)\Phi_\rho(x - x_i, x) \tag{4.29}$$

where $C_\rho(x - x_i, x)$ is a correction function to reduce the interpolation error, $\Phi_\rho(x - x_i, x)$ is the compact Kernel function, and ρ is a dilation parameter that defines the size of the window function (see Figure 48). The size of the window was equal to diameter of particles multiplied by factor 5. The compact kernel function is shown in Figure 49c. There are several ways to calculate the correction function. The simplest way is to use the condition of partition of unity,

$$\sum^{N_{p\,i=1}} C_\rho(x - x_i, x)\Phi_\rho(x)\Delta V_i \tag{4.30}$$

to determine $C_\rho(x - x_i, x)$ at an arbitrary point x. Each grid point is also associated with a weight, ΔV_i which is determined as:

$$\Delta V_i = \frac{1}{N_\nu} \cdot \sum_{k=1}^{N_T} \Delta\Omega_k \tag{4.31}$$

where $\Delta\Omega_k$ represents the volume of tetrahedron k with a vertex at point i, N_T is the total number of tetrahedra with vertices at point i, N_ν is the number of tetrahedron (=4 in 3D).

The calculated strains in Cartesian coordinates sometimes required a transformation to a polar coordinates. The transformation equations can be seen in Appendix D.

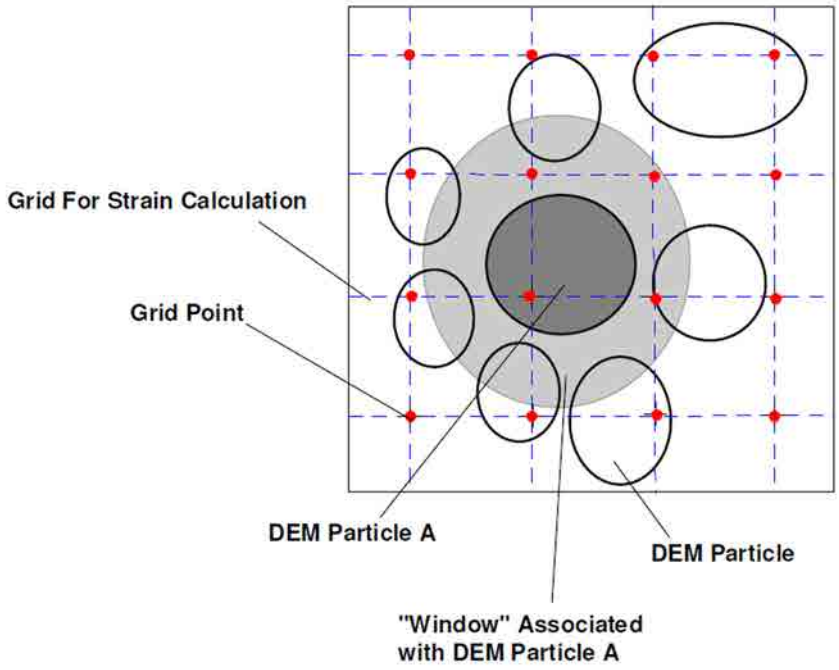

Figure 48: Schematic diagram of meshfree interpolation approach (after O'Sullivan et al. [2003])

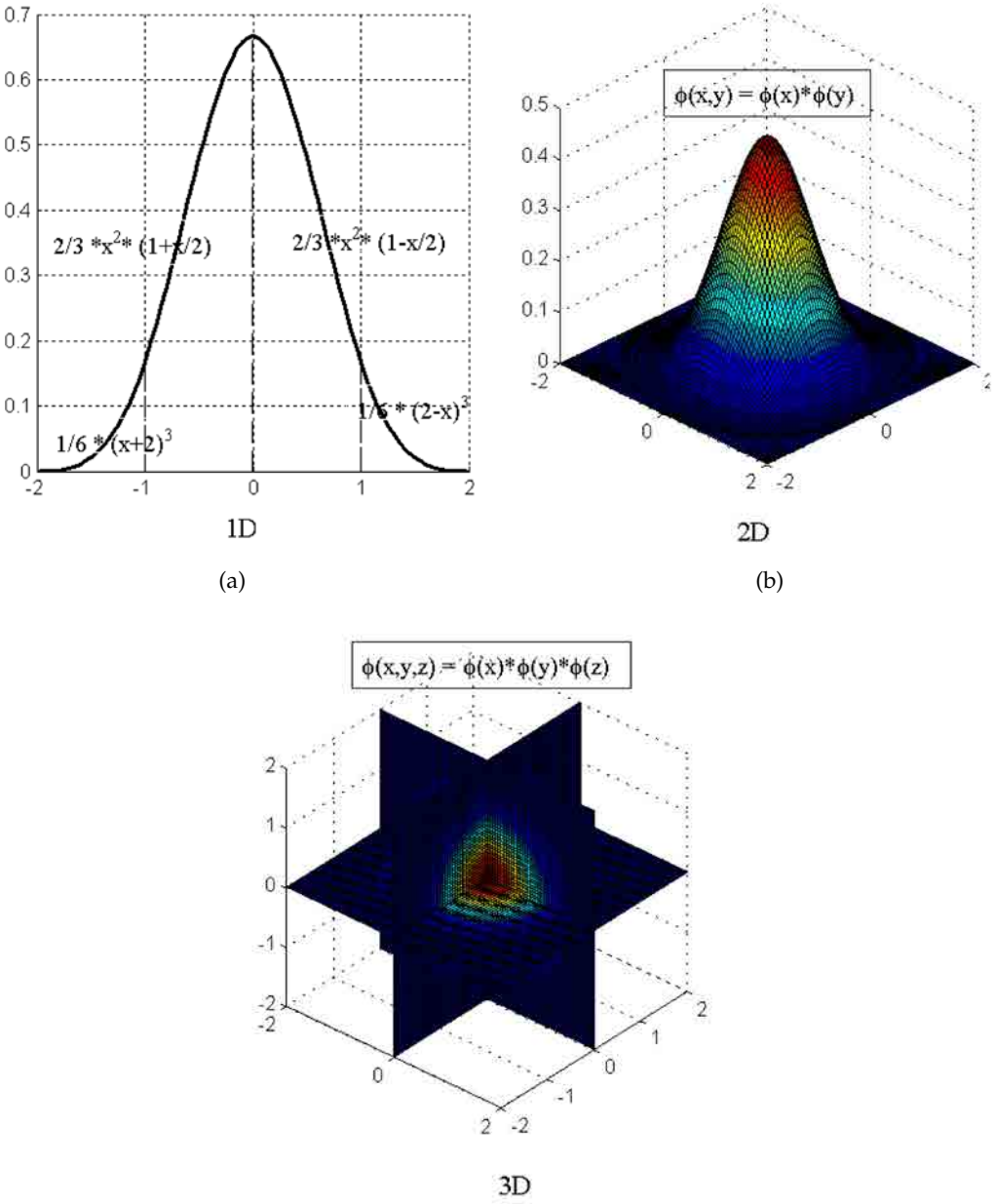

Figure 49: Diagram of wavelet functions in (a) 1D analysis, (b) 2D analysis and (c) 3D analysis (used in this work)

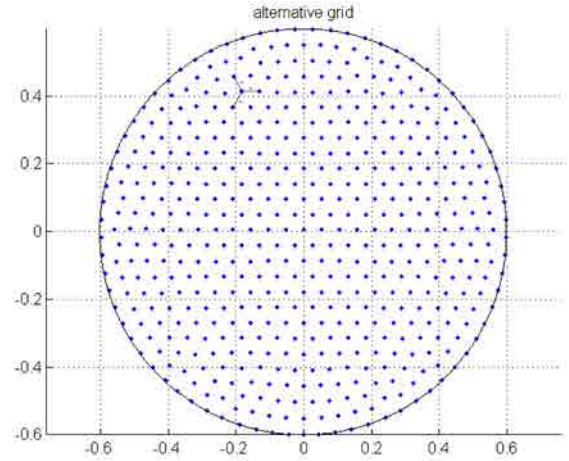

(a)

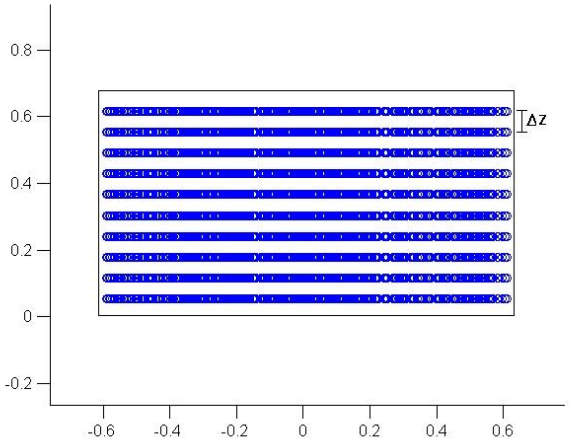

(b)

Figure 50: Cylindrical grid used in meshfree non–linear analysis (a) top view and (b) side view

4.5 SUMMARY

In this chapter a fundamentals of Discrete Element Method (DEM) are presented such as dynamic nature of the model, basic calculation scheme, the constitutive contact models, etc. Moreover, a main commands used in the programming language (FISH) are also mentioned and described.

The very important part of this chapter contained the description of microscopic (directly derived from the basic modelling units, i.e. contact, particle) and mesoscopic (averaged over a volume) variables for analyzing the simulation results. The averaging or homogenizing (but may include grid projection and interpolation as ancillary techniques) to obtain representative values of the relevant variables within a volume that contains several, possibly many elements were introduced. The representative element volume (RVE) such as spheres (MS), cylindrical shells volumes (=RV) and horizontal bands (=CB) was introduced and used to define averaging volumes (V).

Calculation of stresses in DEM was based on averaging approach of Cundall and Strack [1979], Cundall [1988] while calculation of strains was based on the novel meshfree method proposed by O'Sullivan et al. [2003].

5

BUILDING VCC CPT MODELS

5.1 INTRODUCTION

In this chapter a numerical model representing a virtual calibration chamber (VCC) trough the discrete element method is built. The material properties are selected to reproduce the macroscopic behavior of a granular material in drained triaxial compression test (TRXD). During a DEM TRXD test simultaneous values of axial strain (ϵ_a), volumetric strain (ϵ_{vol}), confining and deviatoric stress (p and q), changes in porosity/void ratio (n/e), coordination number (C_N) and others are registered. All these measurements are then used to examine the stress–strain behaviour of the numerical assembly.

The PFC^{3D} code (described in Chapter 4) is used to perform all numerical simulations presented in this thesis. The DEM model is composed of spherical particles with given particle distribution and built up to variable initial stress and density. Two types of DEM models are described herein. First, the single Element Test (ET), a small cubical sample used to calibrate micro–parameters, including k_n, α, K_{eff} and δ, that represent granular material behavior. Second–the Virtual Calibration Chamber (VCC), designed as a cylindrical chamber to reproduce, as far as possible, a physical calibration chamber (ENEL/ISMES–Chapter 3) in which to perform cone penetration tests.

In Section 5.2 the micro–parameter calibration procedure is described, including the specimen preparation procedure and the material properties to be calibrated. Different methods for DEM sample generation implemented in the PFC^{3D} code were explored, including (i) isotropic–compression method (**ICM**), (ii) multi–layer method (**MLM**) and (iii) radius expansion method (**REM**). A basic description of these as well as their implementation procedure is also given here.

Section 5.3 presents a series of DEM TRXD simulations performed to validate the DEM model at varies confining stresses and densities. Some insights on microscopic behavior via contact evolution are also given.

In Section 5.4 we present and discuss model constraints for the VCC related to model physical dimensions and grain size.

In the last section (Section 5.5) both the VCC and the cone device are described. The flow charts of each stage of the VCC CPT Code, including sample preparation, stress history application and cone penetration test can be inspected in Appendix F.

5.2 MICRO–PARAMETER CALIBRATION: DRAINED TRIAXIAL COMPRESSION ON TICINO SAND

To reduce the number of particles the DEM model was designed as a small sample but still able to reproduce the behavior of the real sand. To perform calibration analysis two types of samples were used: (i) cubical, defined by a side dimension a, and (ii) cylindrical (a small version of the VCC model, to be described later) with diameter D and height H. Both models can be seen in Figure 51. The boundaries of both speci-

mens are defined by smooth (frictionless) wall elements, through which either stresses or displacements can be imposed. In this respect, the principal directions of stresses and strains coincide with the coordinate axes x, y, z and their values are obtained from boundary forces, (as it is done in laboratory testing). Principal strains are calculated directly from the wall displacements and principal stresses are calculated from forces arising from all contacting balls acting on walls. Table 12 provide details of the particular physical tests and two DEM models used for micro–parameter calibration.

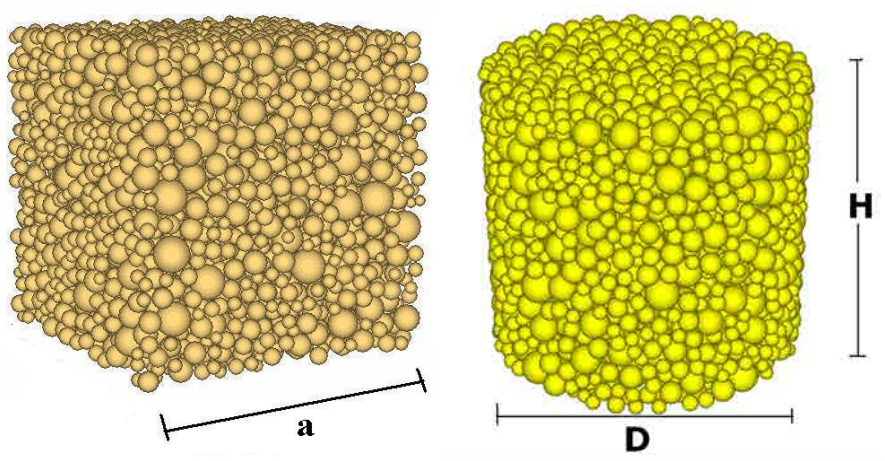

(a) (b)

Figure 51: (a) cubical and (b) cylindrical DEM model used for material calibration

Table 12: Parameters of the calibration specimens

Properties	Unit	Physical Test	Num–Cub	Num–Cyl
PSD	[-]	Figure 52(a)	Figure 52(b)	Figure 52(c)
D x H (a)	mm x mm (mm)	71 x 146	(8)	8 x 8
e	[-]	0.673	0.665	0.647
D_R	[%]	72.5	74.8	80
p_0	[kPa]	99.2	100	100

5.2.1 *Specimen generation procedure*

5.2.1.1 *Sampling a PSD*

Generally, for simplicity, in DEM simulations the particle size distribution (PSD) is taken as a uniform between two particular (extreme) values (R_{min} and R_{max}) (see Wang [2003], Potyondy and Cundall [2004], Holt et al. [2005] and Cho et al. [2007]). That kind of distribution does not reflect the real material used in experimental/laboratory testing. That is why, in our work, a new technique for fitting the numerical grain size distribution to the experimental one was proposed. The procedure used in

the current research to generate particles for a DEM specimen that follow the PSD of Ticino sand was detailed in Chapter 4 while describing *particle generation*. It must be noted that grain size curve of Ticino sand was truncated; particles with diameters smaller than d_{10} were eliminated. The resulting particle distribution is illustrated in Figure 52(b).

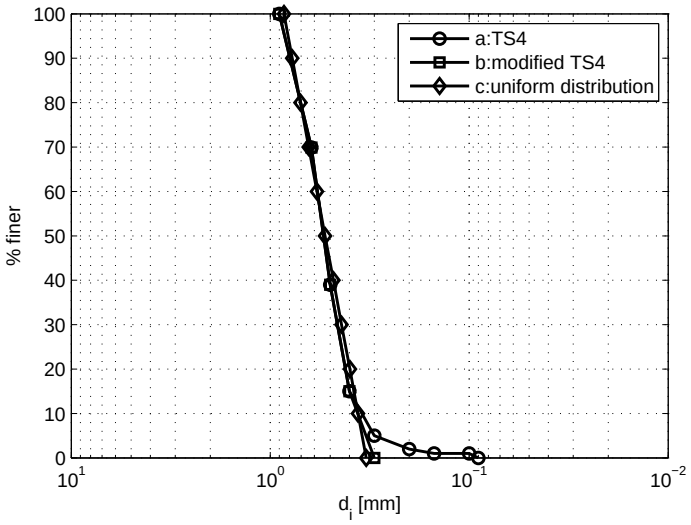

Figure 52: Grain size curve of Ticino Sand used in calibration procedure

5.2.1.2 *Filling a volume: REM*

Many different methods of specimen generation in DEM have been proposed (Jiang et al. [2003], Ng [2004]). The most common are:

(I) Fixed–Point Method, where particle and contact data are obtained from:

- visual observations and laboratory testing (photos, density, normal stiffness);
- theoretically derived data for regularly-packed ideal cases, such as simple cubic systems.

(II) Isotropic–Compression Method, where all particles are randomly positioned in a large area (volume) in such a manner that they do not overlap. Interparticle friction coefficient is set to very small values so that interparticle sliding is permitted. Boundary walls are then moved inward, or a consolidation pressure is applied on the boundaries. The process continues until a target void ratio or stress state is achieved at equilibrium. The interparticle friction coefficient is then reset to representative values in order to carry out the numerical simulation under any given loading conditions.

(III) Multi–Layer with Undercompaction Method (developed by Jiang et al. [2003]) is a method similar to that proposed by Selig and Ladd [1978]for physical specimens. The DEM specimen is divided into n layers. In each layer the particles are randomly generated. In the next step compression is carried out by moving down the top wall to the specific specimen height while the other three walls are kept fixed. This process is repeated until all layers are filled with particles

and compacted. The average void ratio of the n layers below the $(n+1)$ layer is initially compacted to a void ratio ($\bar{e}_n$) larger than the final target value $\bar{e}$. Applying this principle to each layer of soil until the average void ratio of whole specimen $\bar{e}_t$ is equal to the desired target value $\bar{e}$ when compacting the last layer of soil, requires that $\bar{e}_1 > \bar{e}_2 > ... > \bar{e}_n > ... > \bar{e}_t = \bar{e}$ ($\bar{e}_n$ is an average void ratio of all n layers below when compacting the nth layer, $\bar{e}_t$ is the void ratio of whole specimen after compacting the last layer).

(IV) Expansion Method, where all particles with reduced radii and reduced friction are randomly positioned in a specific volume, which is very close to actual desired specimen size, and no overlap/contact force is developed between any two particles. In the next step the radii of all particles are restored gradually while the consolidation pressure is kept constant on boundaries. The boundaries are allowed to move accordingly so that the target stress state is achieved at equilibrium. Once the desired radii are restored, interparticle friction coefficients are reset to their normal values.

Jiang et al. [2003] stated that method (i) is a simple method generally used to validate DEM codes. Method (ii) and (iv) generate essentially dense specimen. Method (iii) allows to reproduce both dense and loose samples.

In our work, the DEM TRXD specimen was generated using PFC^{3D} default generation method called *Radius Expansion Method* (**REM**)–method (iv). A schematic flow chart of REM can be seen in Figure 53.

It must be pointed out, that the low interparticle coefficient applied during placement of particles, results in a relatively dense specimen. Moreover, the feasible range of relative density using this numerical approach differs from that obtained in experiments. The maximum $D_{R,max}$ possible to reproduce is 90–95% (95%–physical CC) whereas the minimum, $D_{R,min}$ is 40–45% (22%–physical CC). The discrepancy between numerical and physical sample ranges might be due to particle shape, roundness, angularity and the fact that spherical particles cannot clamp and break (Sukumaran and Ashmawy [2001], Cho et al. [2006], Fannin et al. [2008]).

During the DEM model generation procedure, contact force networks developing between neighboring particles were observed. Figure 54 illustrate the force chains developing between particles after applying isotropic compression stress of 100 kPa ($D_R = 75\%$) in specimens created with three, mentioned above, methods (REM, ICM and MLM). Looking at the contact forces and contact chains we can notice that there is no much difference in contact forces between these three methods. Moreover, the magnitude of normal (Figure 56) and tangential forces (Figure 57) did not shown inportant difference. The maximum number of contacts (Figure 55) between particles is 10 for REM and ICM and 11 for MLM method. For MLM the higher number of contacts are oriented verticaly and this may be due to the way of sample generation (compression by moving down the top wall). The macro–response results can be seen in Figure 58. The apparent difference was observed.

On the other hand, REM was far less time–consuming (by a factor of 30 or more). More details about the other methods explored can be seen in Appendix E. Ng [2004] also observed a negligible difference between different methods of granular material preparation. Hence, the further investigation was perfrormed on samples generated

with REM. The *before* and *after* of REM while generating cubical sample are illustrated in Figure 59.

The homogeneity of the specimen was checked by using a variety of measurement spheres (Figure 60). Some of the MS are centered in the specimen and have variable radius (Reg-1 to Reg-6) while the others are of identical size but differ in location (Reg-7 to Reg-9). The values of porosity (Table 13) in Reg-7, Reg-8, Reg-9 show a certain degree of homogeneity. In Reg-9 we observe the smaller porosity value (more dense region) which might be caused by closeness to the moving, servo–controlled right walls during compression process. The larger value can be observed in Reg-8, farther away from the moving walls.

The variation of porosity as a function of the radius for the MS centered with the sample showed increase in porosity with decreasing size of MS (except Reg-1). Moreover, the loosest region was that of the smallest size of the MS (Reg-6). The position of the measurement regions as well as the porosity results can be viewed in Figure 60.

Table 13: Porosity in region increased radially Reg-1, Reg-2, Reg-3, Reg-4, Reg-5, Reg-6, Reg-7, Reg-8, Reg-9

Region	n_{actual} [-]	$n_{actual}/n_{required}$
Reg-1 (biggest)	0.368	0.920
Reg-2	0.364	0.910
Reg-3	0.366	0.915
Reg-4	0.371	0.927
Reg-5	0.383	0.957
Reg-6 (smallest)	0.415	1.040
Reg-7	0.375	0.937
Reg-8	0.381	0.952
Reg-9	0.365	0.912

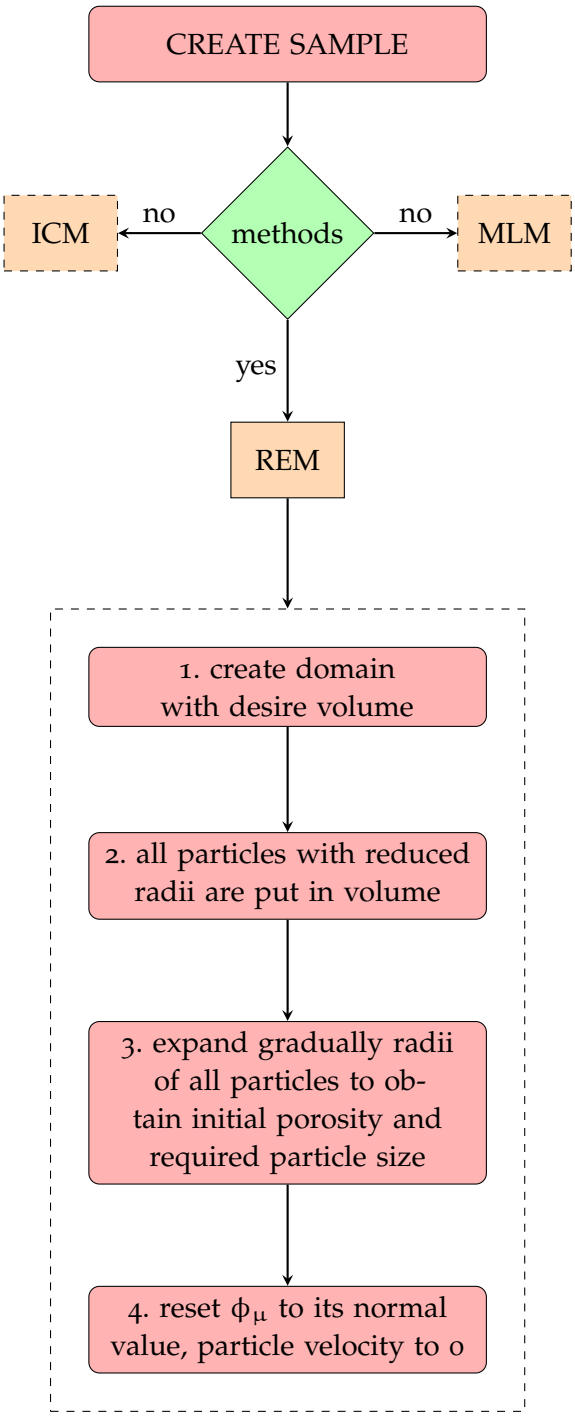

Figure 53: Flow chart of REM

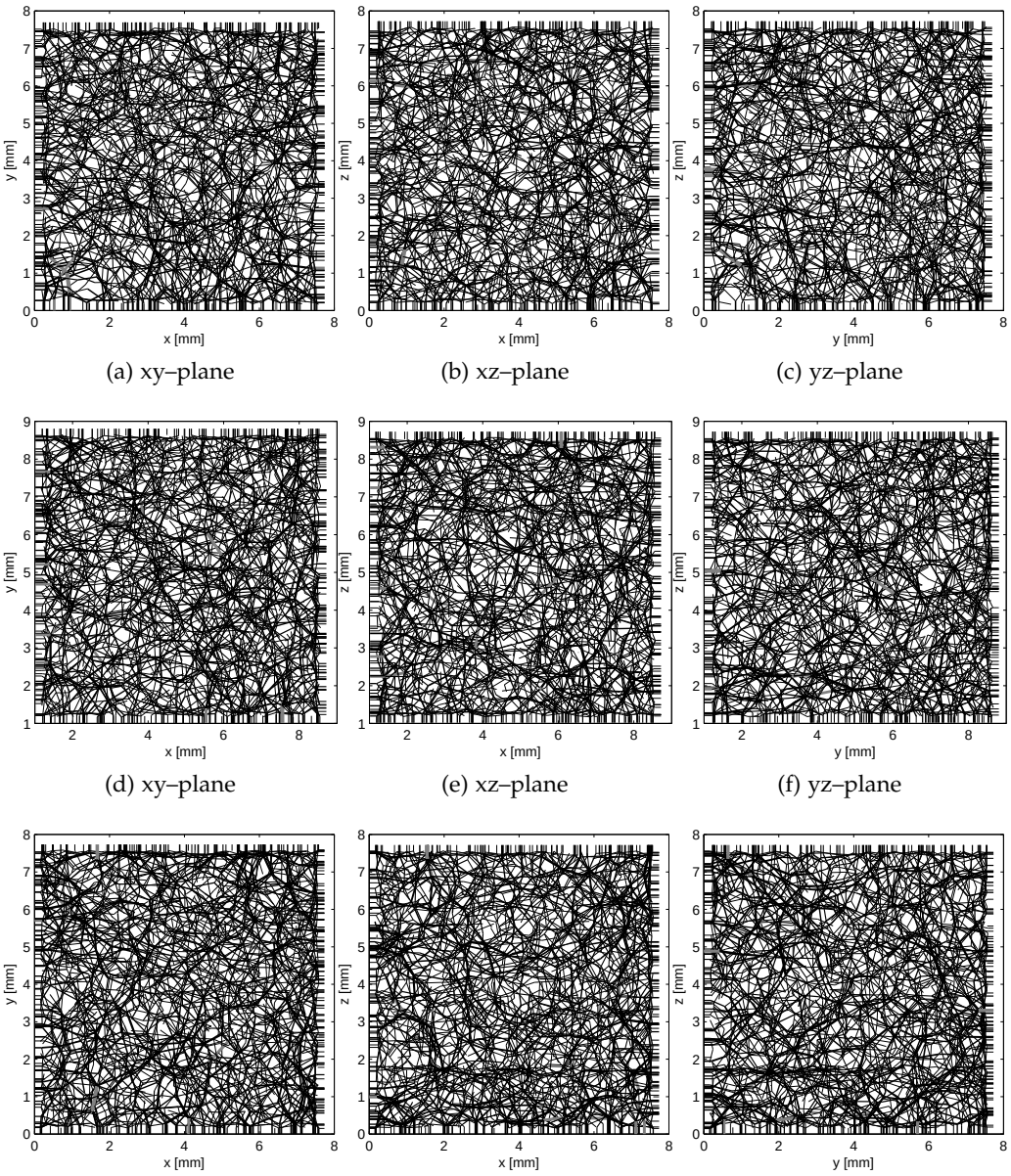

(a) xy–plane (b) xz–plane (c) yz–plane

(d) xy–plane (e) xz–plane (f) yz–plane

(g) xy–plane (h) xz–plane (i) yz–plane

Figure 54: Projections on a plane of all 3D vectors within specimens generated with (a)-(c) REM, (d)-(f) ICM and (g)-(i) MLM after application of isotropic stress of ~ 100 [kPa]

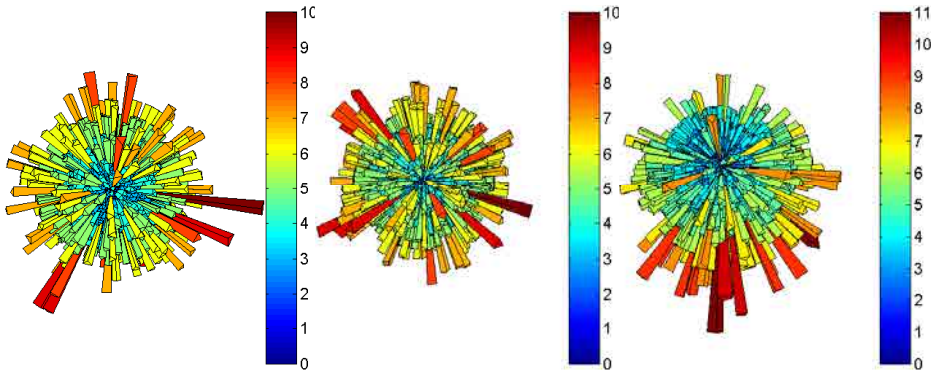

(a) REM (b) ICM (c) MLM

Figure 55: Contact normal orientation within specimens generated with (a) REM, (b) ICM and (c) MLM after application of isotropic stress of ~ 100 [kPa], $D_R = 75\%$

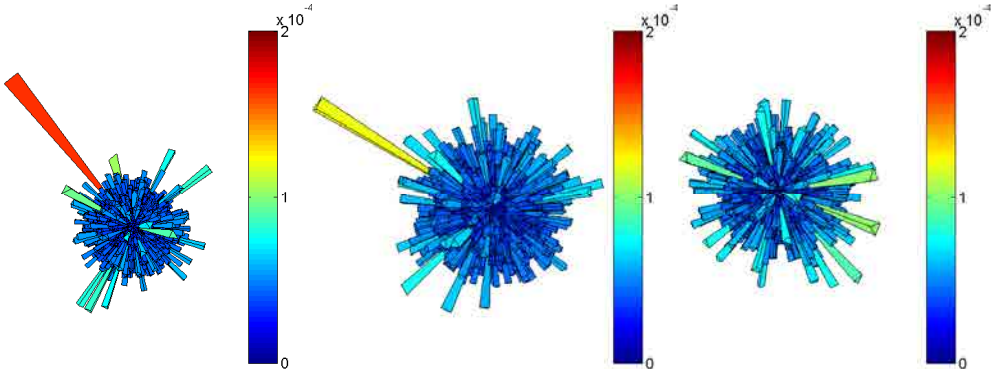

(a) REM (b) ICM (c) MLM

Figure 56: Histograms of the contact normal force magnitude within specimens generated with (a) REM, (b) ICM and (c) MLM after application of isotropic stress of ~ 100 [kPa], $D_R = 75\%$

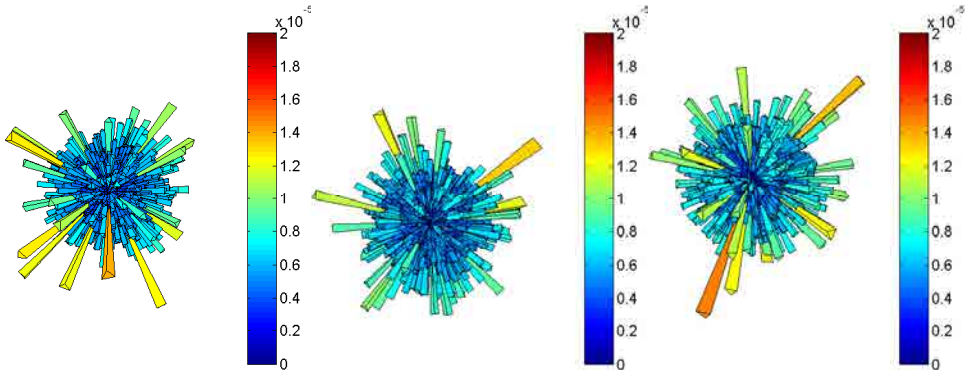

(a) REM (b) ICM (c) MLM

Figure 57: Histograms of the contact tangential force magnitude within specimens generated with (a) REM, (b) ICM and (c) MLM after application of isotropic stress of ~ 100 [kPa], $D_R = 75\%$

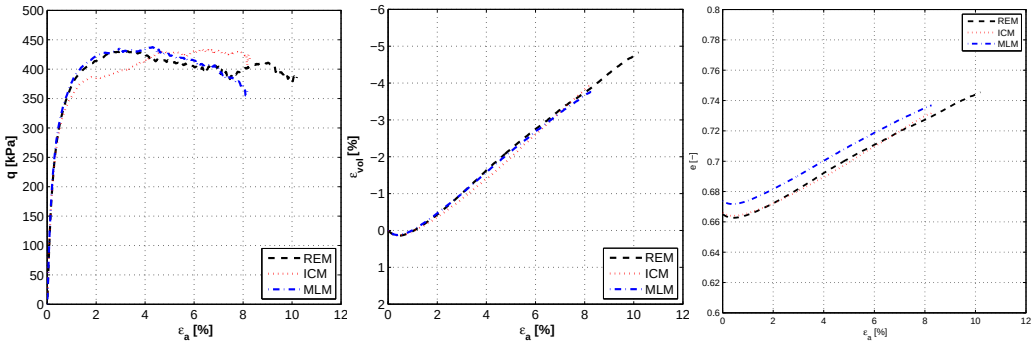

(a) (b) (c)

Figure 58: Comparison of the triaxial response of three specimens created with different generation methods for $D_R = 75\%$ and $p_0 = 100$ kPa: (a) ϵ_a vs. q, (b) ϵ_a vs. ϵ_{vol} and (c) ϵ_a vs. e

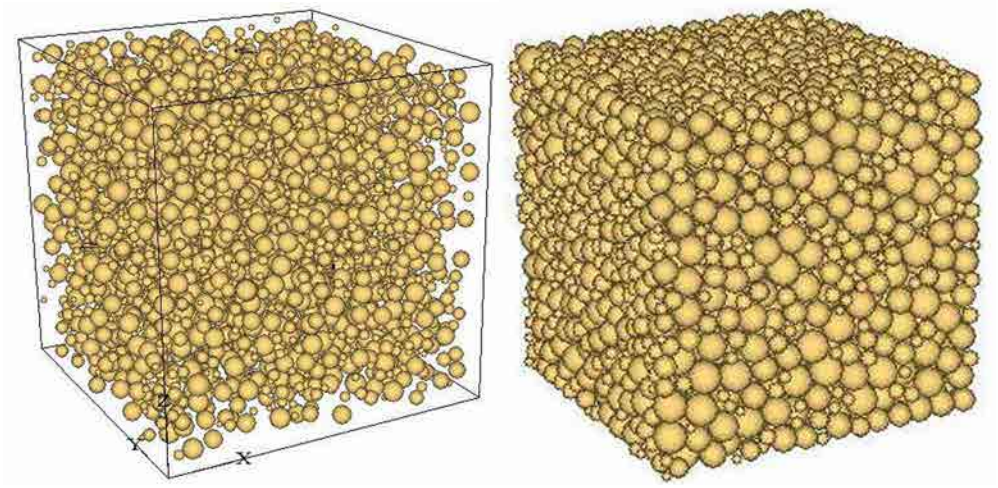

(a) (b)

Figure 59: Radius Expansion Method: view (a) after generation particles (*e*=6.55); (b) after expansion radius (*e*=0.85)

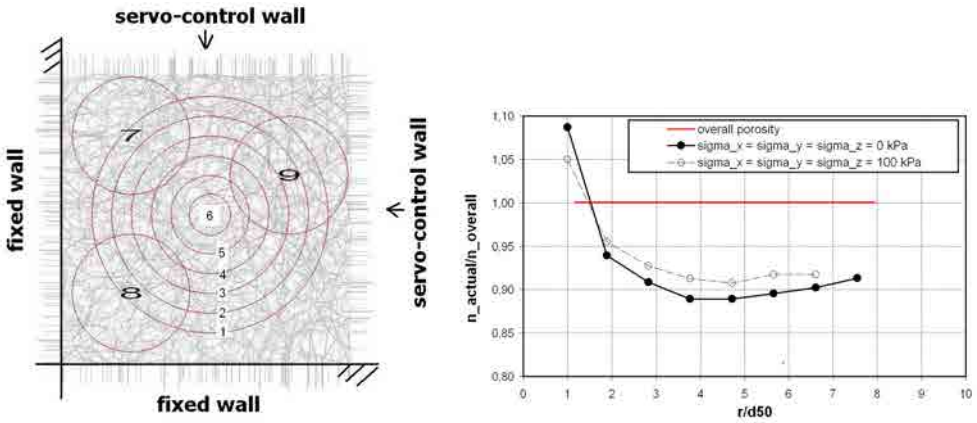

(a) (b)

Figure 60: Porosity measurements on MS of increasing radius for specimens with initial isotropic stress 0 0 and 100 kPa: (a) posotion of measurement spheres MS and (b) porosity vs. normalized radius of MS

5.2.2 *Material properties*

The material properties of DEM assembly are defined at contact and particle level and are required to capture macro–response of DEM models. These parameters are:

- normal contact stiffness (k_N)
- ratio between contact normal and tangential stiffness ($\alpha = \frac{k_N}{k_S}$)
- interparticle friction coefficient ($\tan(\phi_\mu)$)
- damping (δ)

All parameters were determined by trial–and–error method to provide a best fit to experimental data, namely a single drained triaxial compression test at a confining stress p_0 of 100 kPa and D_R = 75%. The parameters that were finally selected for subsequent analysis are collected in Table 14.

A linear elastic–perfectly plastic behavior with purely frictional limit conditions (no interparticle bonding) was assumed at the contacts. The contact stiffness was proportional to particle diameter through the expression:

$$k_N = K_{coeff} \cdot 2.0 \cdot \frac{D_1 \cdot D_2}{D_1 + D_2} \tag{5.1}$$

where D_1 and D_2 are the diameters of particles being in contact, K_{coeff} is a constant fitted to 300 $\frac{MN}{m}$. The parameter α was set to be equal 0.25. The interparticle friction coefficient ($\tan(\phi_\mu)$) was found to give the best fit for a value of 0.35.

Particle rotation was inhibited to be able to model the behavior of relatively hard and angular sand, such as Ticino. Oda and Iwashita [1999] suggested that in some cases particle rotation can be neglected without losing generality in the analysis of kinematics. This happens when either all particles rigidly rotate at the same rate or do not rotate at all (which approximates this case). Finally, it should be mentioned that our simulations employed numerical damping, of the non-viscous nature proposed by Cundall (Cundall [1988]). This is equivalent to suppress mechanical wave propagation in the system and is particularly useful to achieve rapid convergence in quasi-static problems. The definition and formulation of this damping (δ) was given in section 4.2.4: the parameter δ was assumed to be equal to 10%.

Figure 61 shows contact force networks developing between neighboring particles in cubical and cylindrical sample generated with REM and after application of isotropic stress ok 100 kPa. It can be observed, that cubical sample seems to be more homogeneous and generate more contacts between particles. Figure 62 confirms that maximum number of contacts between neighbouring particles is 10 while in cylindrical sample is only 6. However, the cylindrical sample

The stress–strain curve in a $q{:}\epsilon_a$ plane, the volumetric response of the material, loading path (p vs. q) and the void ratio evolution can be seen in Figure 66. Generally, the model reproduces the experimental deviatoric and volumetric response quite well. Dilatant behavior was observed before peak deviator stress for all tests. However, the numerical results overestimate somewhat the strength of the material. Also, low axial strains (ϵ_a<1%), the DEM model resulted in a more stiff initial response. This might be realted to the somewhat larger initial density (porosity, void ratio) of the numerical samples (see Figure 66d and Table 13).

In the next section a series of numerical analysis is presented to estimate the influence of these contact parameters on the DEM simulated sand response. Moreover, due to fact that the behaviour of cubical sample was more close to the experimental results, the validation of the DEM model was performed on it.

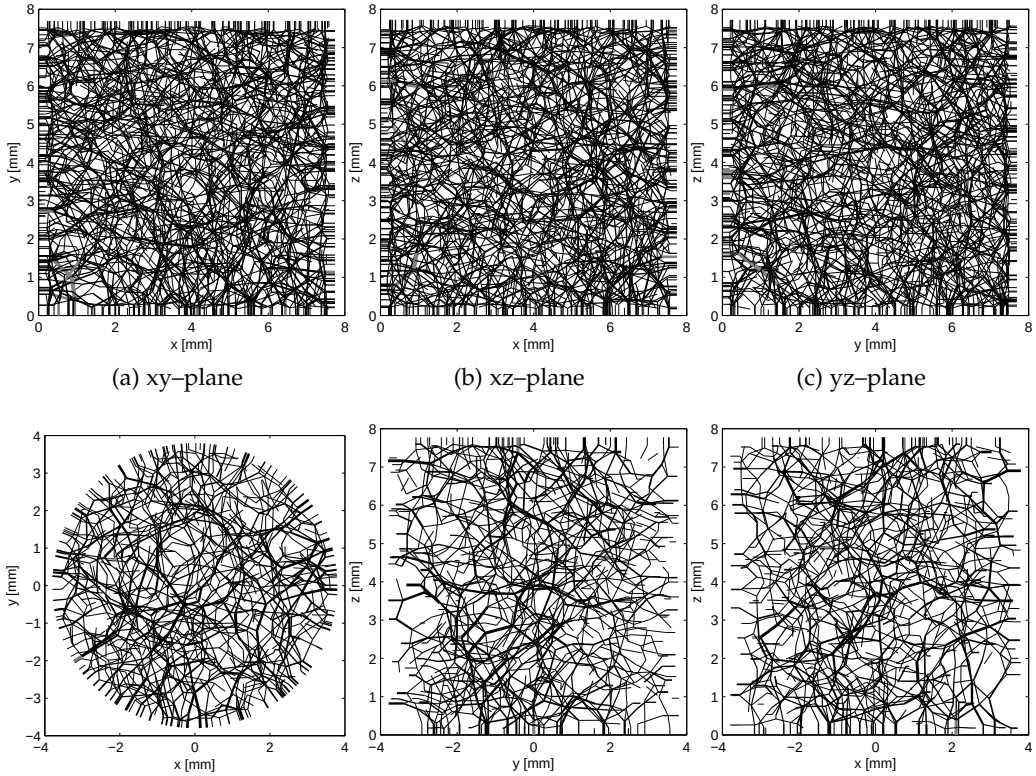

(a) xy–plane (b) xz–plane (c) yz–plane

(d) xy–plane (e) xz–plane (f) yz–plane

Figure 61: Projections on a plane of all 3D vectors within (a)-(c) cubical and (d)-(f) cylindrical specimens generated with REM and after application of isotropic stress of ~ 100 [kPa]

Table 14: Parameters used in the numerical simulations of Ticino sand

Normal contact stiffness	k_N	$K_{coeff}{}^1 \cdot 2.0 \cdot \frac{D1 \cdot D2}{D1+D2}$
Tangential contact stiffness	k_S	$0.25 \cdot k_N$
Interparticle friction angle	$(\tan\phi_\mu)/\phi_\mu$	0.35 /19.3°
Damping	δ	0.1

5.3 TRIAXIAL TESTING PROGRAM–DEM MODEL VALIDATION

After the initial micro–parameter calibration process, the mechanical response of the model was further validated by performing eight additional DEM TRXD. Those tests are summarized in Table 15. The previously calibrated parameters (Table 14)

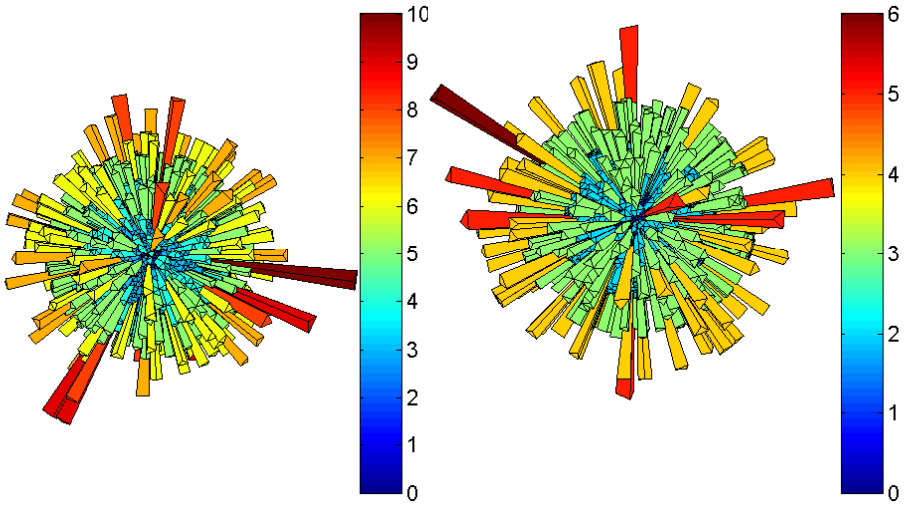

(a) cubical sample (b) cylindrical sample

Figure 62: Contact normal orientation within (a) cubical and (b) cylindrical specimen generated with REM and after application of isotropic stress of ~ 100 [kPa], $D_R = 75\%$

were used without any extra adjustment. The numerical specimens were confined at three different isotropic stresses and three relative densities corresponding to loose, medium and dense sand. The detailed information is listed in Table 15. The numerical results were then compared with experimental tests performed in similar conditions. The comparison was made in terms of (i) deviatoric behavior, (ii) volumetric behavior, (iii) loading path and (iv) void ratio changes. Although the laboratory tests were performed on cylindrical samples with 71 mm diameter and 141 mm height, all numerical tests (1 to 9) discussed in this section were performed on cubical samples with a side of 8 mm.

Tests 5 and 8 were performed at about the same relative density as the calibration test (test ID. 2) but at higher confining stresses. On the other hand, tests 1, 4 and 7 refer to a much looser material (D_R=45%) and tests 3, 6 and 9 refer to a very dense one (D_R=90%). The main tests results can be seen in figures 67 to 69.

In general, the numerical model reproduces the experimental deviatoric curves quite well, especially for low confining stress. The stress–strain curves (Figure 67a, 68a and 69a) for the drained triaxial simulations show that with an increase in confining pressure and in sample density (Figure 71a) there is an increase in peak deviatoric stress. However, for the higher confining stresses (200 and 300 kPa), the model overestimates the strength of the material. Also, the response of the numerical models at the beginning of shearing (pre–peak) was stiffer than the experimental one. The discrepancies between numerical and experimental results are more pronounced for loose material. Calvetti and Nova [2005a] related these differences to the difficulty of generating an initial homogeneous numerical specimen. This point will be further discussed in Chapter 6 while examining homogeneity of virtual calibration chamber (VCC) at initial stage (that is after applying stress path and before penetration test).

Figures 67b, 68b and 69b show the comparison between experimental tests and DEM simulations in terms of the volumetric response. The DEM models showed a later change from contraction to dilation than the experimental record, especially for

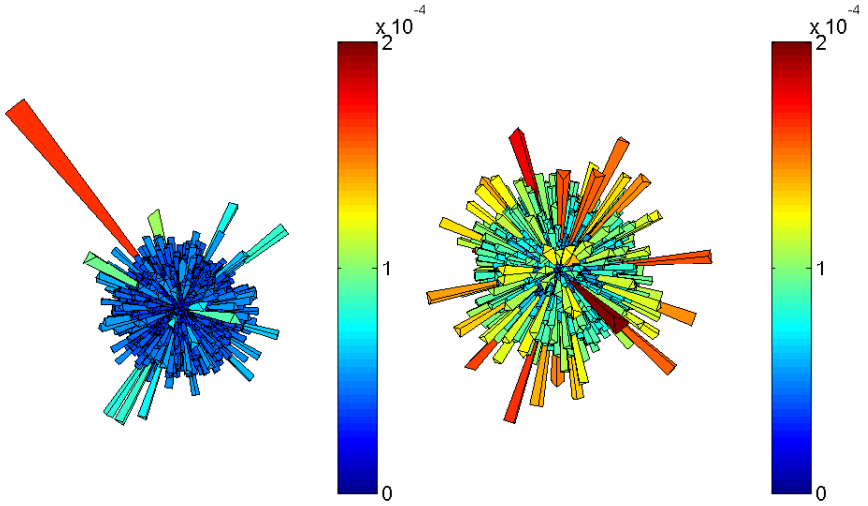

(a) cubical sample (b) cylindrical sample

Figure 63: Histograms of the contact normal force magnitude within (a) cubical and (b) cylindrical specimen generated with REM and after application of isotropic stress of ~ 100 [kPa], $D_R = 75\%$

loose sand ((Figure 67b). Matching for the medium and dense specimens was more successful (Figure 68b and Figure 69b). Numerical trials with the calibration tests showed that by better matching the volumetric behavior we might mismatch the deviatoric behavior. Consequently, it is more likely that the differences can be attributed to the fact that the particles experimentally tested are not completely spherical, therefore particle geometry effects may be responsible for part of the found difference. This issue was examined by many researches by performing DEM simulations on samples consisting particles of different shapes and sizes (Antony and Kuhn [2004], Ng [2009], Ng [2001], Mirghasemi et al. [2002]). For example, Gotteland et al. [2009] used non convex simple elements made up of interlocked, jointed or linked spheres which allow a high level of interlocking within the granular assembly to reproduce the mechanical behavior of a granular assembly (Ticino sand). The deviatoric and volumetric fitting was remarkably good.

Normally, DEM specimens are built to specified initial void ratio (porosity, relative density). At the beginning of the triaxial test the maximum error $\left(\left|\frac{(e_{exp}-e_{DEM})}{e_{exp}}\right| * 100\%\right)$ was around 2.8% (test 6). The comparison between numerical and experimental void ratio evolution is shown on following figures 67d, 68d and 69d. The evolution of void ratio with confining pressure (log scale) can be seen in Figure 71c.

Granular materials tend to reach the same void ratio during shear deformations and irrespective of the initial void ratio (Casagrande [1936]). This behavior can be seen in Figure 71d. Moreover, for the same confining stress (constant lateral stresses) all the specimens approach a common deviator stress at large strain levels (Figure 71a). This state is called critical state (= steady state) in which deformation continues without volume change. Dense granular materials reach the critical state as a results of dilation, while loose materials tend to reach the same state after volumetric contraction (Rothenburg [2004]). Moreover, peaks and steady state zones were defined and compare with the experimental ones. Figure 71b shows that these critical stages

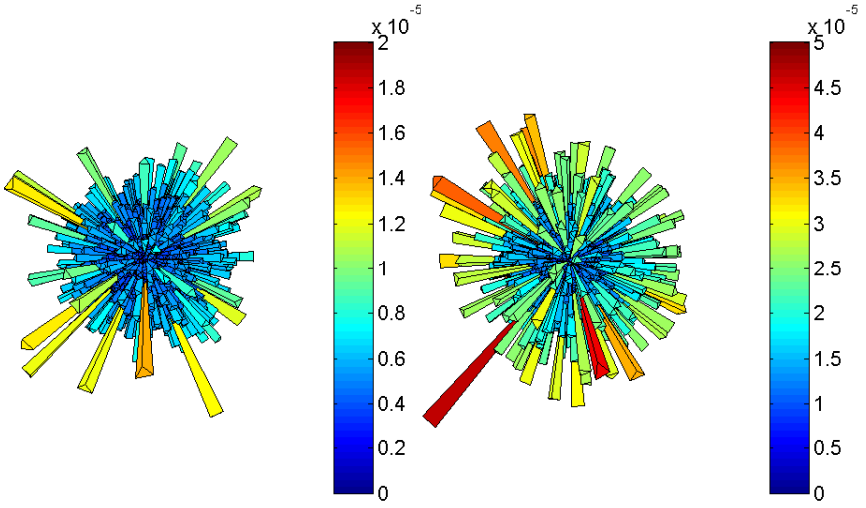

(a) cubical sample (b) cylindrical sample

Figure 64: Histograms of the contact tangential force magnitude within (a) cubical and (b) cylindrical specimen generated with REM and after application of isotropic stress of ~ 100 [kPa], $D_R = 75\%$

are in agreement with mechanical behavior of real Ticino sand. The definition of peak and critical states are illustrated in Figure 70. Figure 72 presents peaks and residual strength envelopes of the DEM material deduced from the triaxial compression tests.

An additional information obtained from DEM analysis is the information about contact evolution during shearing. Figure 73 present the changes of average coordination number C_N with axial strains for loose, medium and dense specimens. It can be observed that there is an increase in coordination number during very short initial stage for loose (Figure 73a) and medium (Figure 73b) sand, then a fast reduction in C_N until a constant value is reached (between 2.5 and 3) for all cases. Rothenburg [2004] developed a theory of critical state for the evolution of coordination number during quasi–static deformation of granular materials. The theory is based on the concept that shear deformations tend to destroy interparticle contacts and create locally unstable configurations that regain stability by forming new or restoring old interparticle contacts. The process is operating in such way that in dense state the rate of contact disintegration exceeds the rate of contact creation, while in the critical state both rates are equalized. In loose states more contacts are created than disintegrated until rates are equalized.

Figure 74 represents the evolution of the coordination number with void ratio during triaxial simulation. An important differences can be seen between loose, medium and dense samples. For DEM model with D_R = 45% (loose sample–Figure 71a) we observe an almost linear reduction in void ratio and increase in coordination number at initial stage follwed by a decrease in C_N (increase in e) till constant value is reached. The behaviour of medium (D_R=75%) and dense (D_R=90%) samples is shown in Figures 71b and 71c. In these cases, contacts are lost following an exponential decrease in C_N until a lower limit value of coordination number is reached (2.5–3).

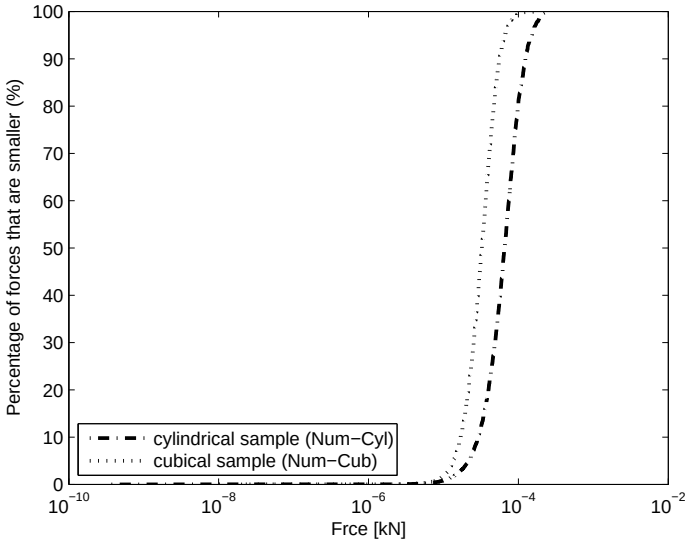

Figure 65: Cumulative force magnitude distribution within cubical and cylindrical specimen generated with REM and after application of isotropic stress of ~ 100 [kPa], D_R = 75%

5.4 SCALING UP GRAIN SIZE

It is well known (McKinney and Rice [1981], Bazant et al. [1991], Bazant and Planas [1998]) that sample size plays an important role in cemented granular materials and has a significant influence on the observed mechanical response. However, there is less experimental evidence about non–cemented, cohesionless granular material, such as sand and gravel. Kuhn and Bagi [2009] suggested that phenomena that cause a size effect in cemented materials may be also present in cohesionless materials. To investigate that, Kuhn and Bagi [2009] performed 2D discrete element method simulations of biaxial test on assemblies consisted of 256 to 66000 particles. The samples apart from being isotropically compressed where also prepared with two types of boundaries, such as rigid walls (similar to our analysis) and periodic walls. The DEM specimens were prepared using two different methods, however initial parameters for each specimen, like average coordination number, average porosity and average pressure were the same. The authors concluded that:

- peak strength decreases when assembly size increases ($\approx$ 4%)
- stiffness reduces slightly with wall boundaries ($\approx$ 0.8%) and with periodic boundaries ($\approx$ 0.3%)
- deformations are less uniform in large specimens, with deformations concentrated in a smaller fraction of the assembly area

Finally, the authors stated, that for realistic micro band patterning and to eliminate size effect at least a few thousand particles were needed.

To built our VCC CPT model, we had to keep in mind the last message of Kuhn and Bagi [2009] dealing with a minimum number of particles. To estimate optimal number of particles needed for our DEM model we had to consider four important dimensions of the problem, viz. (i) cone diameter (d_c), (ii) calibration chamber dimensions (diam-

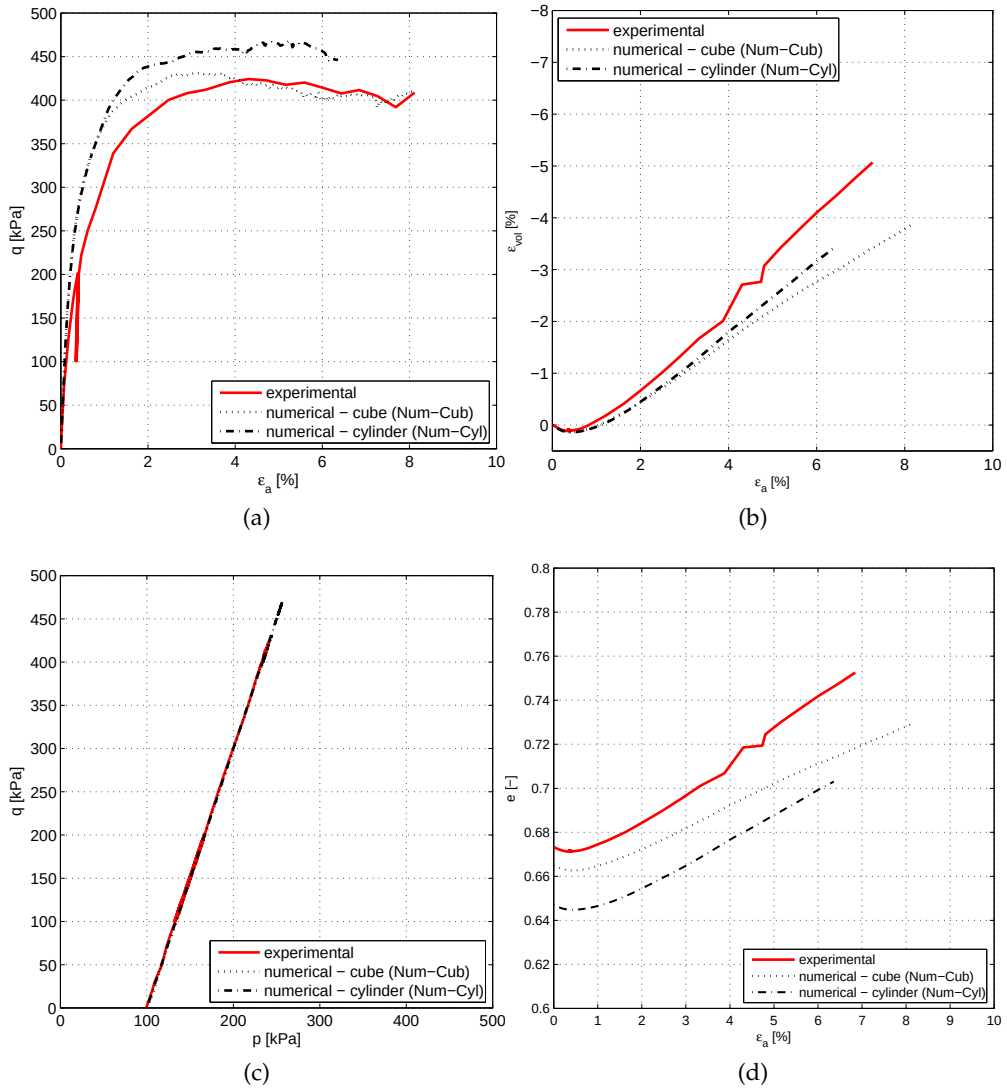

Figure 66: Stress–strain response of the numerical model with calibrated parameters for D_R = 75% and p_0 = 100 kPa (a) ϵ_a vs. q (b) ϵ_a vs. ϵ_{vol}, (c) p vs. q and (d) ϵ_a vs. n

eter, D_{CC}, and height, H_{CC}) and (iii) a measure of particle size (D_{50}). Considering all these dimensions, three non–dimensional ratios might then be defined:

$$\begin{aligned} n_p &= \frac{d_c}{D_{50}} \\ R_d &= \frac{D_{CC}}{d_c} \\ n_h &= \frac{H_{CC}}{d_c} \end{aligned} \tag{5.2}$$

The volume of particle (V_p) required to fill a given specimen volume (V) can be calculated from the following formula:

$$V_p = V(1-n) \tag{5.3}$$

Table 15: Ticino sand: drained triaxial compression simulations performed in this analysis

Test ID.	Isotropic stress p_0 [kPa]	Relative density D_R (D_{R0}) [%]	Porosity n [-]	Void ratio e [-]
1 (validation)	110	45.9 (45)	0.433	0.765
2 (calibration)	100	74.9 (75)	0.399	0.664
3 (validation)	100	88.9 (90)	0.381	0.616
4 (validation)	200	47.3 (45)	0.431	0.760
5 (validation)	200	75.5 (75)	0.398	0.662
6 (validation)	200	89.5 (90)	0.380	0.614
7 (validation)	300	48.7 (45)	0.430	0.755
8 (validation)	300	76.2 (75)	0.397	0.660
9 (validation)	300	93.7 (90)	0.374	0.599

where n is a required porosity and V is a total volume of specimen (cylindrical shape) and can be expressed using the ratios given by eqn. 5.2, as follow:

$$V = \pi \frac{D_{cc}^2}{4} H_{CC} = \frac{\pi}{4}(R_d \cdot d_c)^2 \cdot n_h \cdot d_c = \frac{\pi}{4} R_d^2 d_c^3 n_h \tag{5.4}$$

For a material with a perfectly uniform (monodisperse) grain size distribution the solid volume is given exactly by:

$$V_p = N\frac{4}{3}\pi r^3 = N\frac{1}{6}\pi D_{50}^3 \tag{5.5}$$

For a material with a non-uniform grain size distribution we might assume:

$$V_p = \sum_{i=1}^{N} \frac{4}{3}\pi r^3 \approx \frac{N}{f_G}\frac{1}{6}\pi D_{50}^3 = \frac{N}{f_G}\frac{\pi}{6}\left(\frac{d_c}{n_p}\right)^3 \tag{5.6}$$

Now, substituting eqns. 5.4 and 5.6 into eqn. 5.3 we obtain $N_{estimate}$[2]:

$$N_{estimate} = f_G \cdot \frac{3}{2} \cdot n_p^3 \cdot R_d^2 \cdot n_h \cdot (1 - n) \tag{5.7}$$

where n is the overall porosity and f_G is an empirical factor accounting for the grain size distribution of the material. The vale of f_G was chosen while comparing number of particles computed using the formula 5.7 and those actually generated in DEM specimens. For the truncated Ticino sand grain size distribution employed in our models, this factor was approximately equal to 1.3.

As Table 16 illustrates, a DEM model that maintained the experimental CC dimensions and mean grain size of Ticino sand would require more than 1E10 particles, even allowing for fine truncation. Such a number does not seem practicable and some

2 Note that in the table the calculation of $N_{estimate}$ was performed for porosity, n, equal to 0.38.

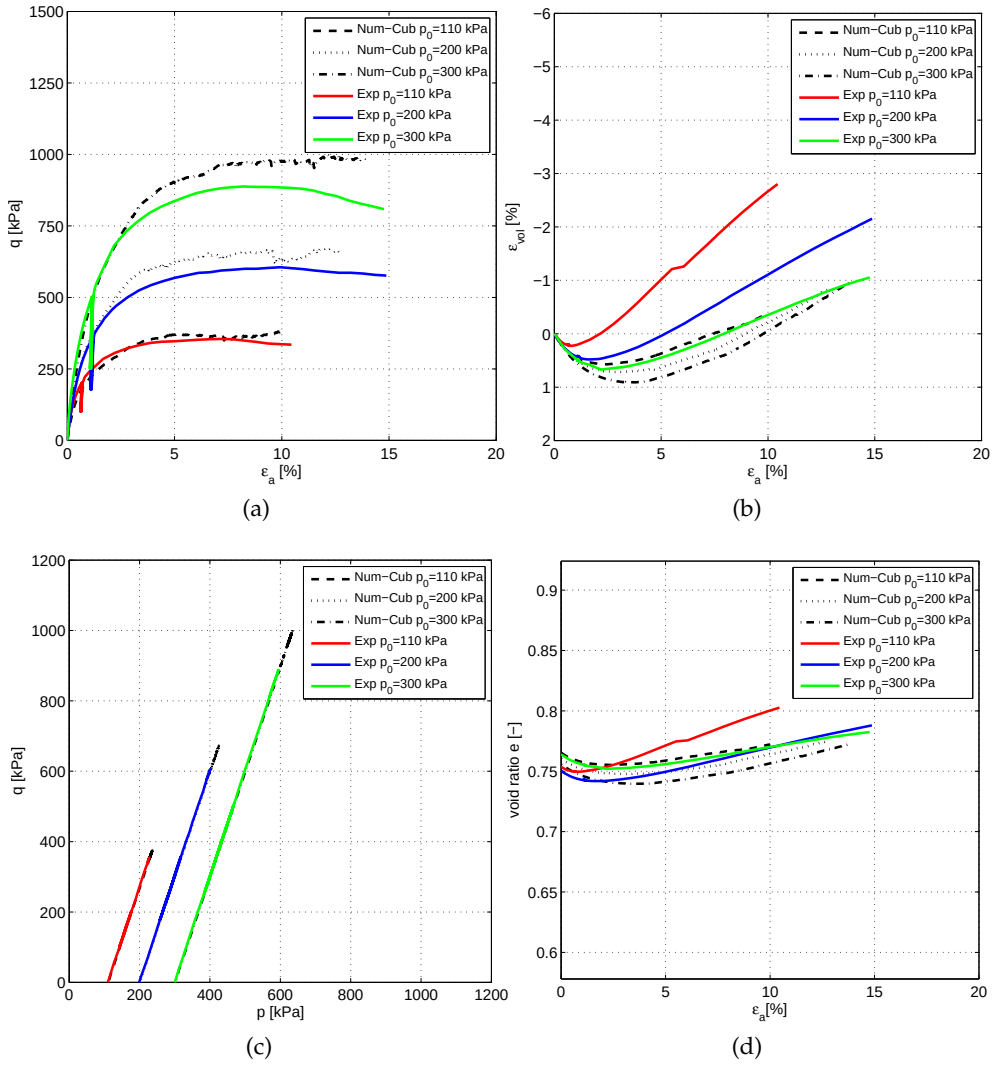

Figure 67: Comparison of experimental and numerical triaxial results for tests with $D_R = 45\%$ and $p_0 = 110$, 200 and 300 kPa (a) deviatoric stress: ϵ_a vs. q; (b) volume strains: ϵ_a vs. ϵ_{vol}; (c) stress path in p:q plane and (d) void ratio e vs. ϵ_a

trade–offs are necessary.

To achieve a manageable particle number, a uniform scaling factor of 50 was applied to the grain size distribution (Figure 75), the cone size was multiplied by 2 from that in the physical tests and the calibration chamber was shortened by another factor of 2. As might be seen in Table 2 this resulted in 65000 elements (N_{eff}) in the densest specimens, almost an order of magnitude more than the number employed in previous two–dimensional studies. Our models had similar cone to chamber dimensions ratios (R_d, n_h) than those previous studies, but strongly curtailed the very expensive cone to particle ratio, n_p to just 2.7, (compared with 67 in the physical chamber). This constraint, as discussed later, has a large bearing on the model results and their interpretation.

A series of three triaxial compression tests were performed to check if the scaling up of the grain size distribution had any effect on the macro response of the DEM model. The results can be viewed in Figure 76. It is clearly visible, that there is no problem

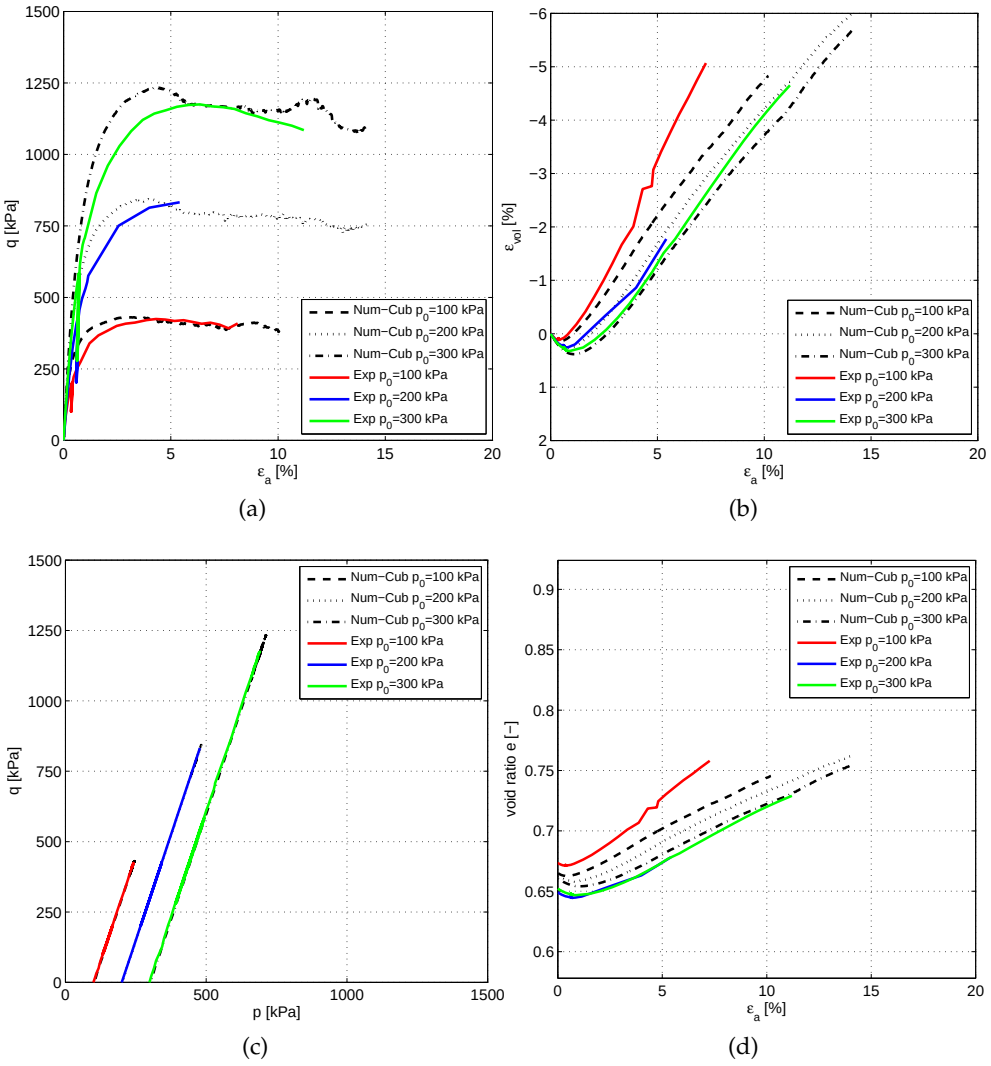

Figure 68: Comparison of experimental and numerical triaxial results for tests with $D_R = 75\%$ and $p_0 = 100$, 200 and 300 kPa (a) deviatoric stress: ϵ_a vs. q; (b) volume strains: ϵ_a vs. ϵ_{vol}; (c) stress path in p:q plane and (d) void ratio e vs. ϵ_a

in scaling up the material size and preserving frictional shear strength at the macro level. Sitharam and Nimbkar [2000] and Kuhn and Bagi [2009] offer extensive proof of this using 2D DEM models. Sitharam and Nimbkar [2000] even include detailed comparisons between parallel gradation materials, such as those resulting from the scaling proposed in this study, showing very minor differences in fabric parameters.

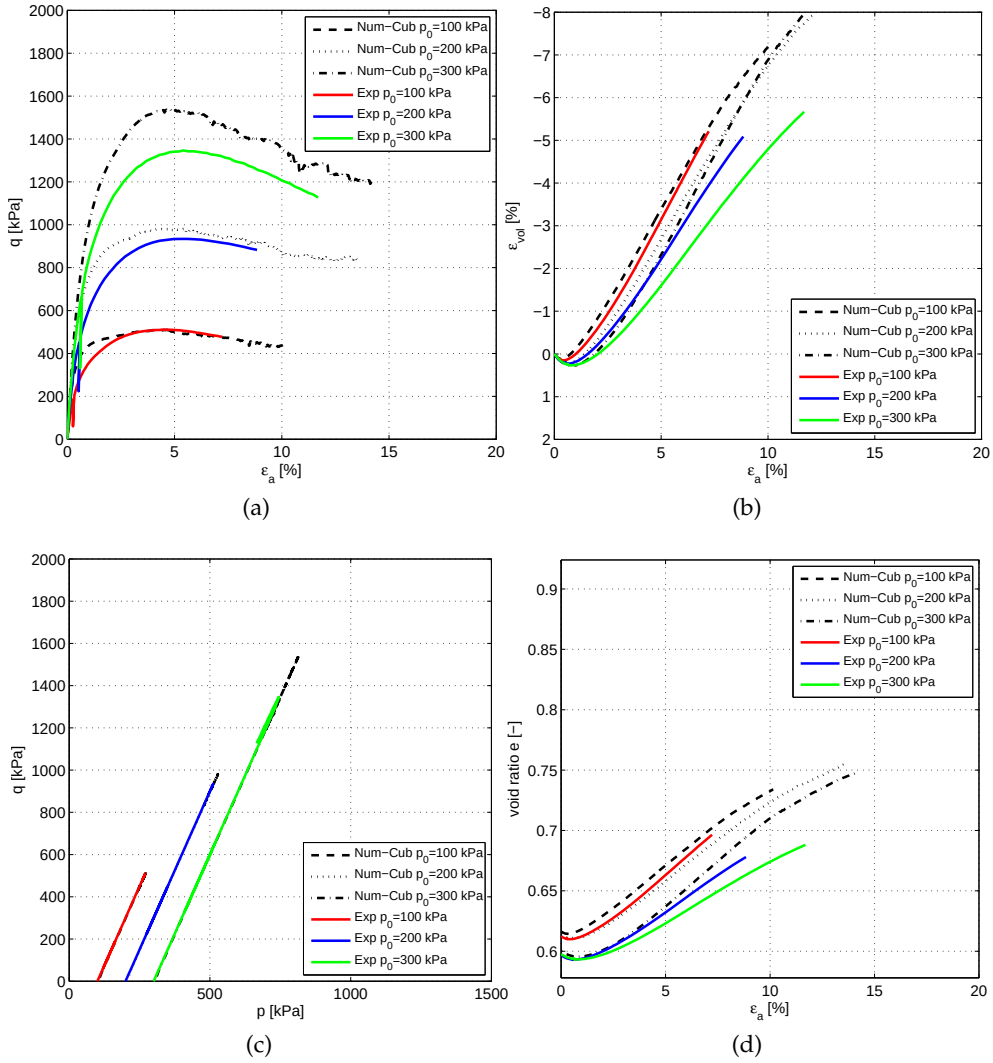

Figure 69: Comparison of experimental and numerical triaxial results for tests with D_R = 90% and p_0 = 100, 200 and 300 kPa (a) deviatoric stress: ϵ_a vs. q; (b) volume strains: ϵ_a vs. ϵ_{vol}; (c) stress path in p:q plane and (d) void ratio e vs. ϵ_a

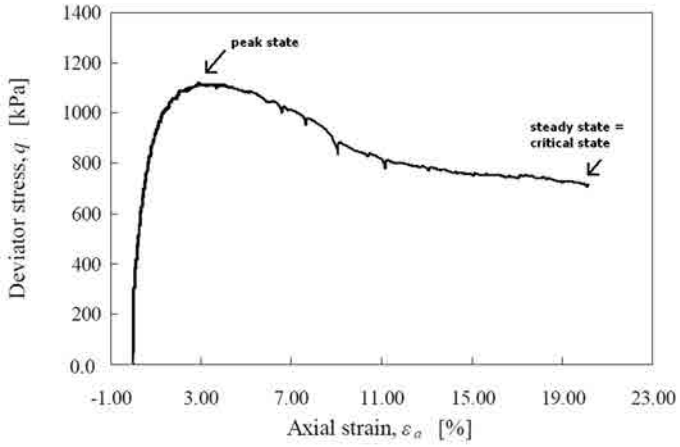

Figure 70: Definition of peak and steady (critical) states

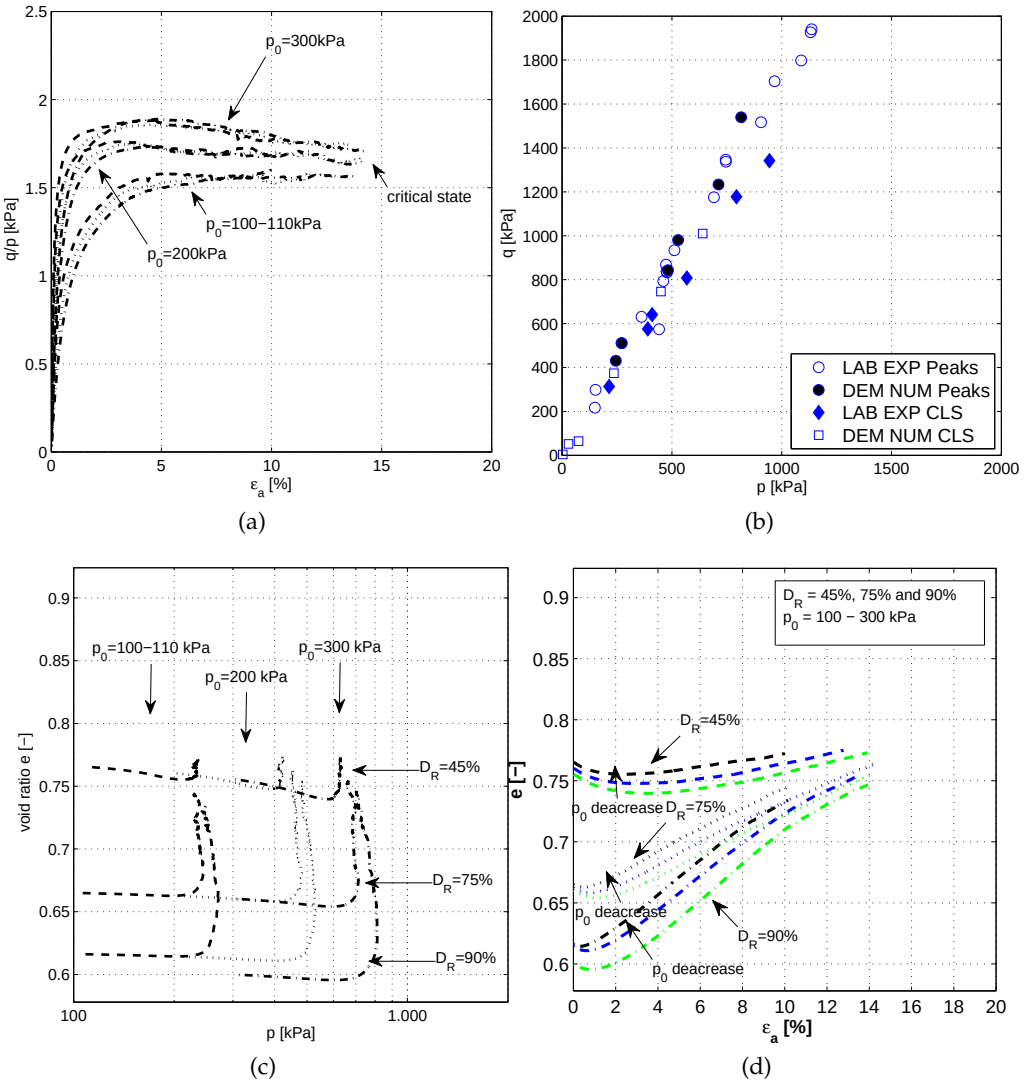

Figure 71: (a) Evolution of $\frac{q}{p}$ with ϵ_a for range of confining stresses and densities; (b) Stress paths of the triaxial tests carried out on the 3D DEM model in comparison with the yield and peak states for the Ticino sand; (c) Evolution of e with p for range of confining stresses and densities (d) Evolution of e with ϵ_a for range of confining stresses and densities

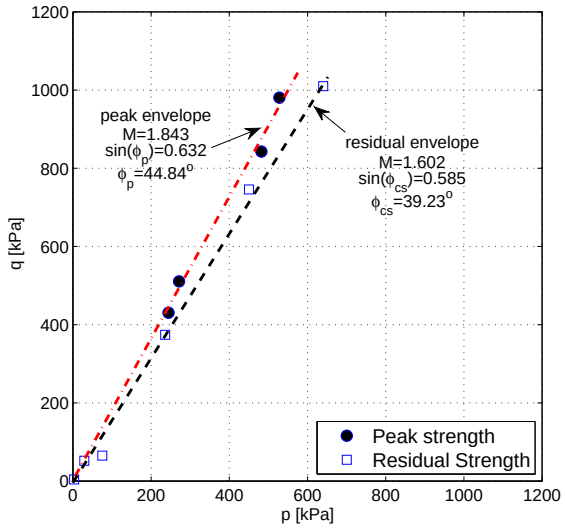

Figure 72: Peak and residual strength envelopes of the material deduced from DEM triaxial test

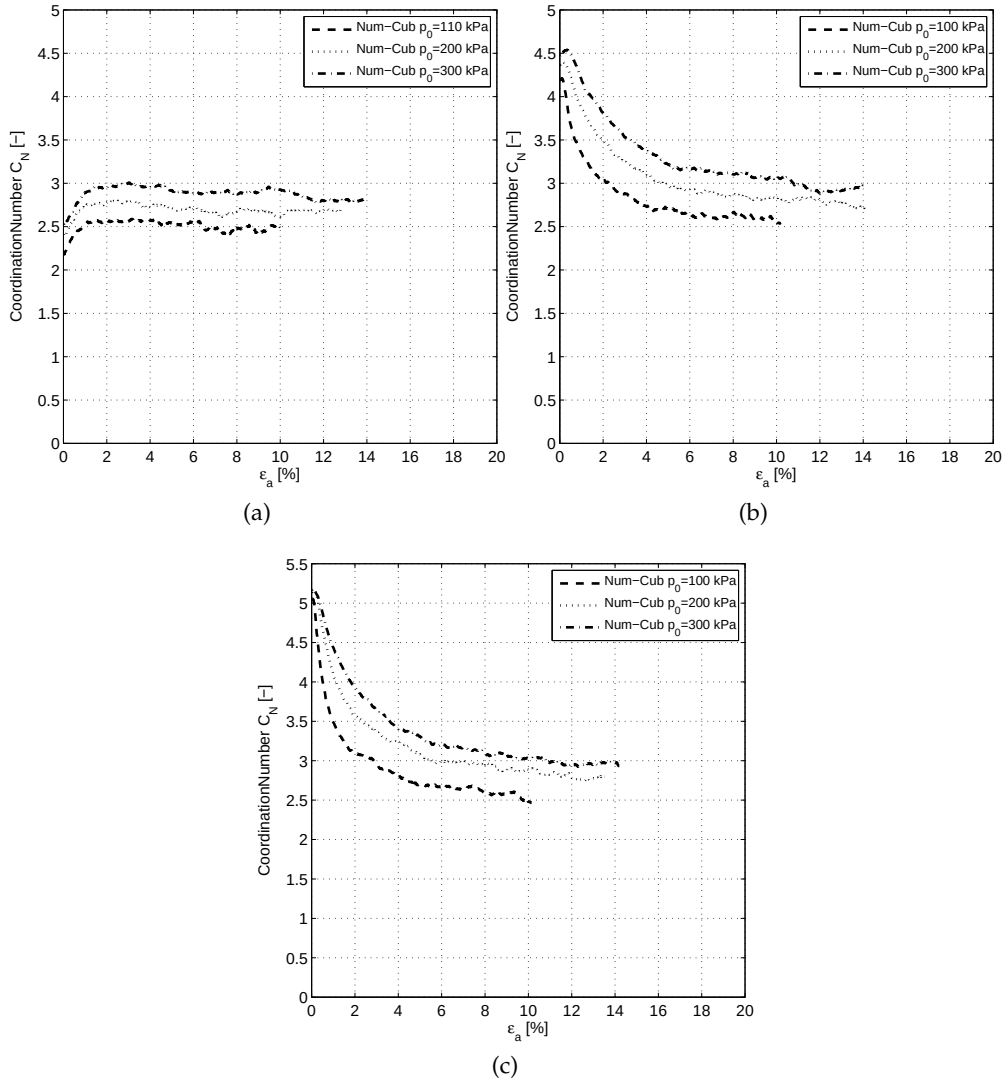

Figure 73: Evolution of coordination number with axial strain for tests with: (a) D_R = 45%; (b) D_R = 75% and (c) D_R = 90%

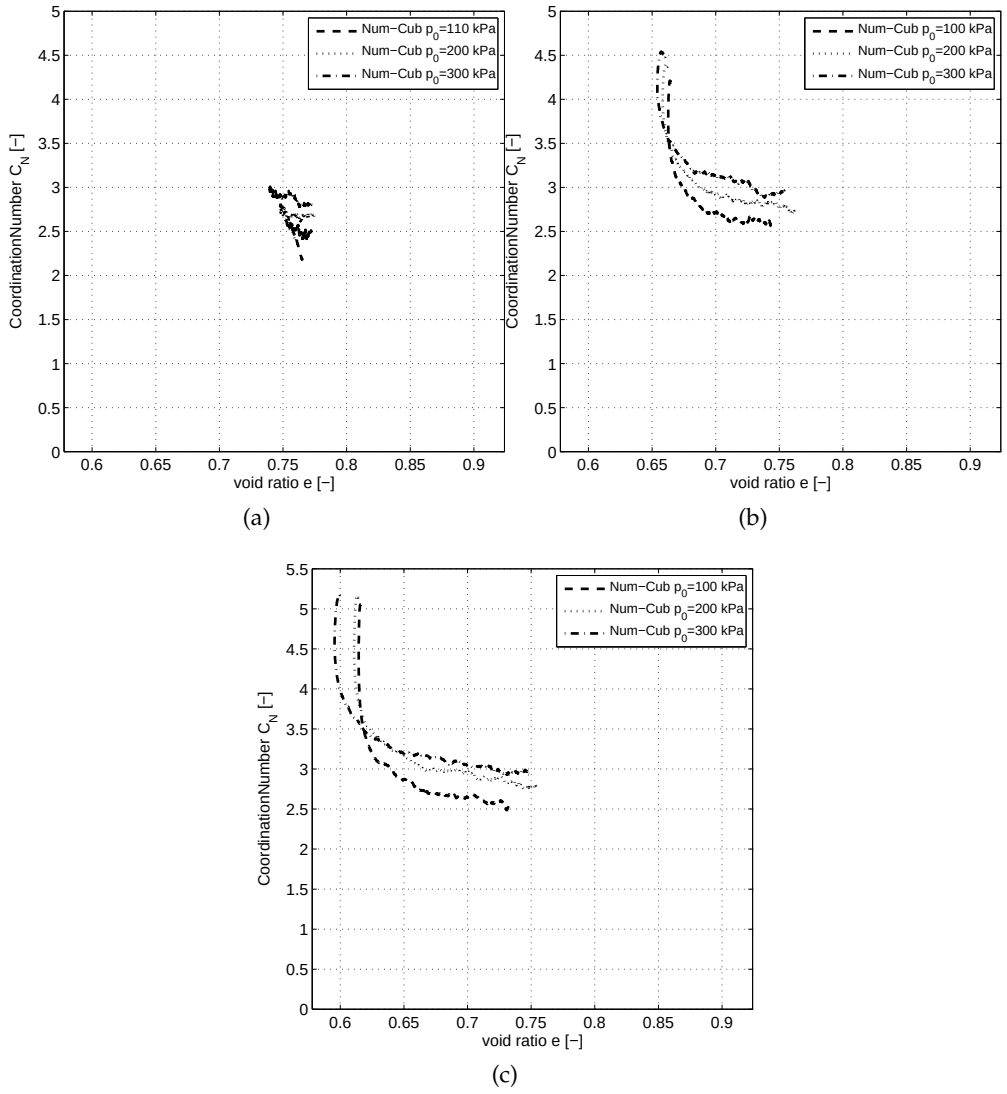

Figure 74: Evolution of coordination number with void ratio for tests with: (a) D_R = 45%; (b) D_R = 75% and (c) D_R = 90%

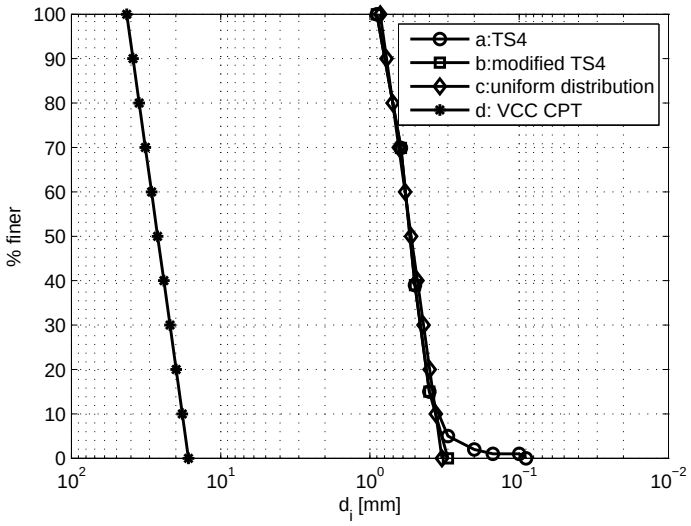

Figure 75: Grain size curve of Ticino Sand used in VCC CPT

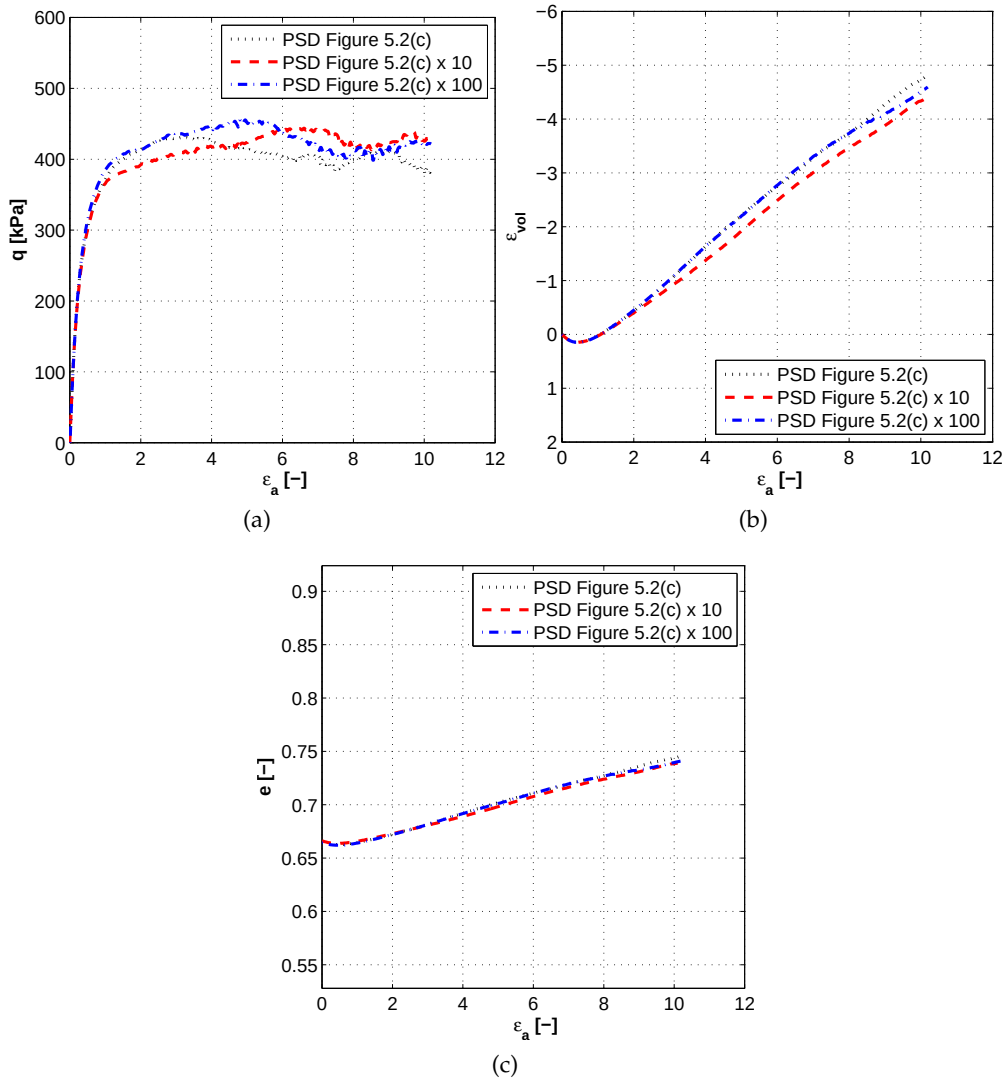

Figure 76: (a) ϵ_a versus q curves; (b) ϵ_a versus ϵ_{vol} and (c) ϵ_a versus e for different size of particles, D_R = 75 [%], p_0 = 100 [kPa]

Table 16: Summary of geometrical characteristics and estimate of model particle requirements in various cases

CASE	ENEL/ISMES CC	THIS STUDY	Huang and Ma [1994]	Calvetti and Nova [2005a]	Jiang et al. [2006b]
	-	3D	2D	2D	2D
d_c [mm]	35.6	71.2	10	100	36
D_{CC} [mm]	1200	1200	160	1200	630
H_{CC} [mm]	1500	700	97.5	1500	288
D_{50} [mm]	0.53	26.5	0.8	13.5	2.925
n_p [-]	67	2.7	12.5	7.4	12.6
R_d [-]	33.7	16.9	16	12	17.5
n_h [-]	16.9	9.8	9.8	15	8
$N_{estimate}$	$1.8E^{10}$	$6.5E^{4}$	$5.9E^{6}$	$1.1E^{6}$	$5.5E^{6}$
Neff	-	$6.5E^{4}$	$< 1.8E^{4}$	$1.0E^{4}$	$1.0E^{4}$

5.5 VCC CPT MODEL CONSTRUCTION

5.5.1 *Virtual Chamber description*

A schematic diagram of the virtual calibration chamber (VCC) used in this investigation is shown in Figure 77. As was mentioned above the height of VCC was shortened by a factor 2 with respect to that used in the ENEL/ISMES test campaign. Diameter remained equal to that of physical CC (Table 17). The virtual calibration chamber walls were modeled as rigid and frictionless while the physical CC consisted of a flexible, frictionless wall chamber. In VCC the axial and radial loads were applied through the top and cylindrical walls respectively, while the bottom platen remained fixed. In ENEL/ISMES the vertical stresses were applied to the specimen via a piston positioned in the base of CC. The lateral stresses were applied by the pressure of water surrounding the specimen and the top wall was designed as a rigid lid.

In VCC the specimens were created to a relative density slightly above the target value by the radius expansion method (discussed above) while in CC using a pluvial deposition technique through air. After DEM assembly generation, the model particle velocity was reset to zero. The VCC specimen was subjected to an isotropic compression stress of 10 kPa in which–by trial and error–interparticle friction might be relaxed to obtain a more accurate fit with the relative density target. The accuracy–$\frac{achieved-target}{target}$–on the target density achieved by this procedure was always better than 5%. In the next step the interparticle friction was reset to that adjusted in the calibration. In the next step either isotropic or one–dimensional compression loading was applied until the target value of stresses/void ratio was reached. After equilibration, a cone penetration process starts. In physical CC all specimens were submitted to one dimensional compression. The implemented routines of each stage of CPT, including either sample generation and preparation and penetration process can be found in Appendix A.

5.5.2 *Cone penetration test*

A schematic view of the cone device used in the simulations can be seen in Figure 77. The cone shaft is described with four rigid cylindrical walls, one frictionless (top one) and three frictional. The height of each shaft wall is 0.1 m. The physical penetrometer shaft is frictional with height of approximately 150 mm. The cone tip in both cases (experimental and numerical) had an angle of 60 degrees and was frictional. Perfect roughness was assumed in the contact between cone and particles, with particle–wall friction equal to the interparticle friction coefficient ($\tan(\phi_\mu)$=0.35). The diameter of the cone was set to 71.2 mm, which is a double that of the experimental cone (35.6 mm). The reason for that was to guarantee a minimum number of contacts ($\geqslant$ 10) between particle assembly and cone tip. The cone penetration process was performed at a constant rate of 10 cm/s, which is five times faster than the in situ test (2 cm/s). Both for the physical as well as for the simulated chamber a constant stress BC1 or non radial strain–BC3–boundary conditions was maintained during cone penetration by successive adjustments of chamber radius and height. Penetration was halted at 10–20 cm from the chamber bottom in DEM VCC CPT and 30 cm in physical CC.
Three types of CPTs were performed:

1. to validate D_R–σ' correlation obtained from physical CC (ENEL/ISMES)–Section 7.4.1
2. to examine chamber size and boundary condition effects–Chapter 9
3. to reproduce selected experimental tests from CC CPT database and compare them with DEM results–Section 7.4.2

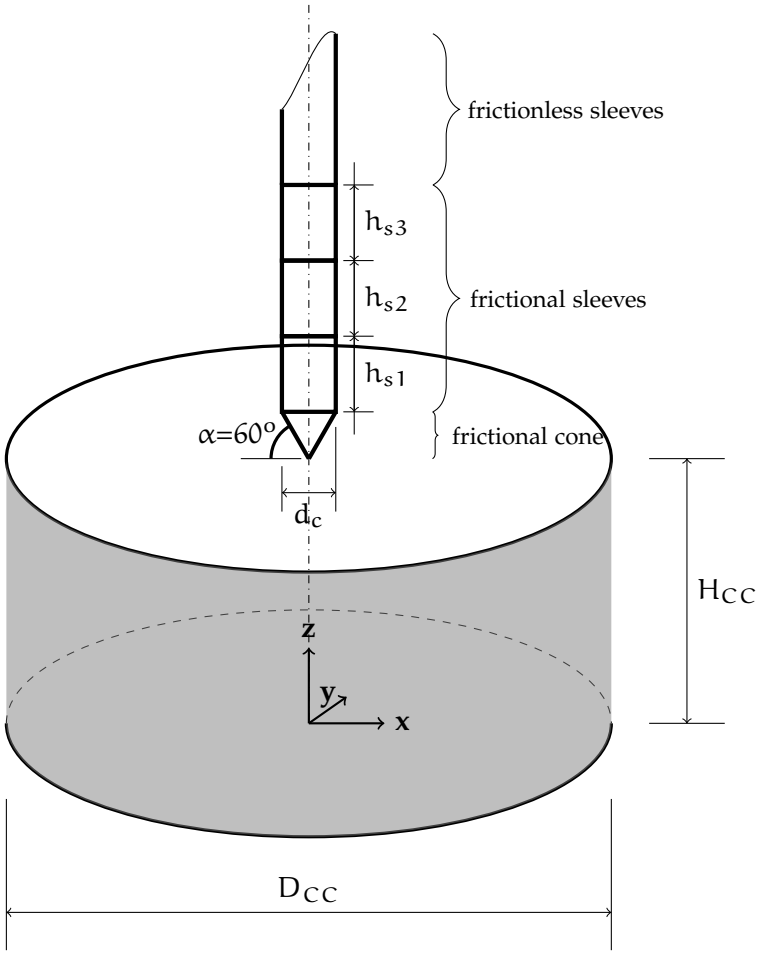

Figure 77: Schematic view of virtual calibration chamber, VCC, and cone device

Table 17: Dimensions of calibration chamber and cone device

Calibration Chamber	Units	Physical CC	Numerical VCC
D_{cc}	[m]	1.2	1.2
H_{cc}	[m]	1.5	0.7
Cone Device			
d_c	[mm]	35.6	71.2
Appex. angle	[°]	60	60
h_{s1}	[mm]	134	100
h_{s2}	[mm]	-	100
h_{s3}	[mm]		100

5.6 SUMMARY

A numerical model representing small cubical sample of 8 mm side of Ticino sand was used to calibrate the DEM material parameters. These parameters were determined by trial-and-error in order to provide a best fit to a single isotropically compressed drained triaxial test confined at 100 kPa and formed with D_R=75%. Adequacy of the calibration parameters was verified by simulating a variety of triaxial tests at differing confinements and initial densities. In general, the numerical model reproduced the experimental curves quite well.

Numerical specimens were built to specified porosity using the radius expansion method (REM). In this method all particles were initially created with radius smaller than their target, and then all radius are incrementally expanded until porosity is close to the objective. Other specimen formation methods, like multi–layer (MLM) or isotropic compaction (ICM) were also tried but, for the models described in this chapter, no apparent macro–response difference was observed. On the other hand, REM was far less time–consuming. Moreover, to fill large volume with discrete particles a scaling technique was introduced. This method involved scaling chamber/cone dimensions as well as particle size. The scaling empirical factor was introduced to account the possible number of particles to be generated.

Finally, the VCC CPT model was introduced. The cone was modeled by perfectly rigid walls. Some were cylindrical with a diameter d_c and the tip–conical with apex angle of 60°. The tip and the sleeve walls close to it retained the friction coefficient of the granular material, the rest were frictionless. The geometry of the numerical calibration chamber (VCC) was cylindrical, given by its height H and diameter D_{vcc}. All walls were frictionless. The CPT testing was design to (a) validate the empirical D_R-q_c-σ curves, (b) investigate chamber size and boundary type conditions and (c) reproduce the selected experimental tests.

6

HOMOGENEITY & SYMMETRY OF VCC CPT MODELS

6.1 INTRODUCTION

Granular materials are made up of grains being in contact and surrounding voids, which can be filled with water, air, etc. From the michromechanical point o view, that kind of material is highly discontinuous and inhomogeneous. These inhomogeneities can be smoothed by averaging micro - properties over a given volume. However, these averaged local properties are dependent on the size of the averaging volume. Different volumes will give different results, as long as the volume element is too small. As we increase the size of the averaging volume, the local properties will asymptotically reach some constant value. However, too large averaging volumes will result on too coarse an average value and on blurring of any inhomogeneity that we might be interested in. Typically, a size of the volume element near but above minimum needed for convergence gives the representative volume element (RVE) to be used for the mesoscopic description of stress and other local properties.

The granular material filling a CC is generally assumed to be homogeneous. However, this is an assumption that is rarely verified experimentally. It is believed that sand specimens, prepared by pluvial deposition in air or vacuum, using gravity mass or traveling spreaders give highly repeatable results and specimens of good, or at least acceptable, uniformity (Bellotti et al. [1982]). For DEM assemblies Jiang et al. [2003] proposed the multilayer with undercompaction method as an efficient technique for generating homogeneous specimens. The homogeneity was quantified by examination of planar void ratio.

In this chapter the mesoscopic homogeneity of VCC specimen before cone penetration is examined by means of measurement spheres (MS). MS is a default averaging volume of PFC^{3D} that allows to examine quantities such as coordination number (C_N), porosity (n), stress (σ) and strain rate (ϵ), etc. The optimal size of MS is explored by examining the changes of local averages with size of MS. The results can be seen in Figure 78. An asymptotic value on the averages micro–properties was observed for measurement spheres with radius of above 0.05 m ($\sim d_{50}$). Therefore, that size of the MS was treated as a RVE. For the scaled TS around 45 (± 4) particles enter into a MSs.

Therefore, to examine specimen homogeneity, MS of such size are distributed all over the specimens in six horizontal layers. Figure 79 illustrates the distribution plan of the MS. The position of each MS is defined by three spatial variables including azimuth angle Θ, normalized radial distance ($d_r = \frac{r_i}{R_{CC}}$) and normalized vertical distance ($d_z = \frac{z_i}{H_{CC}}$). A graphical definition of these variables is given in Figure 80. The post–processing required by the homogeneity study is considerable, therefore only three representative VCC CPT tests models (T16, T20 and T163), at different density (75 and 90%) and having suffered a different initial stress path (isotropic and anisotropic), were selected for detailed homogeneity examination. The specifics of these models can be read from Table 18.

Both the cone and the calibration chamber have cylindrical symmetry. Therefore, it might be expected that the outcomes of the problem will remain indifferent to the enforcement of such symmetry into the model by means, for instance, of frictionless radial walls. Such walls limit the circumferential motion of DEM particles, a motion that symmetry reasons would anyway suggest as being negligible. In fact the issue is somewhat more complex, since the symmetry of the process by which the VCC is filled is harder to gauge (Arroyo et al. [2011]). To reduce the time required for each simulation the possibility to include in the model only part of the cylindrical chamber (half, quarter, etc.) seems attractive.

Cylindrical symmetry of the specimen was examined by analyzing normalized porosity ($\frac{n_{MS}}{n_0}$), coordination number (C_N) and stress variation (σ_r, σ_Θ and σ_z) for three different models with the same density (see Table 18). The full, half and quarter models of VCC were examined for symmetry. Also in this analysis, the MS were incorporated to measure local properties. The distribution of MS in these three models can be seen in Figure 81.

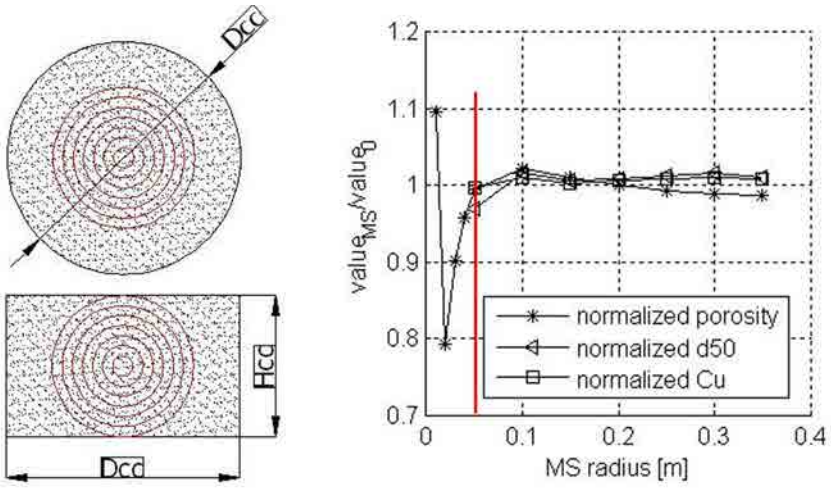

(a) (b)

Figure 78: Measurement Spheres: (a) employed to explore MS optimal size, (b) effect of MS size on local normalized properties–T16

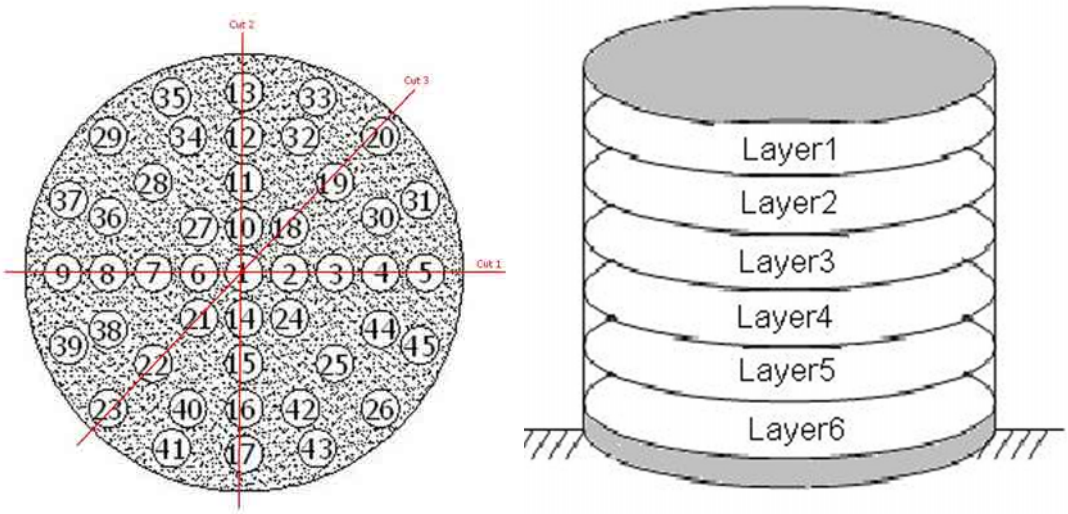

(a) (b)

Figure 79: (a) distribution of measurement spheres (MS) within the layer, (b) layer distribution within the specimen

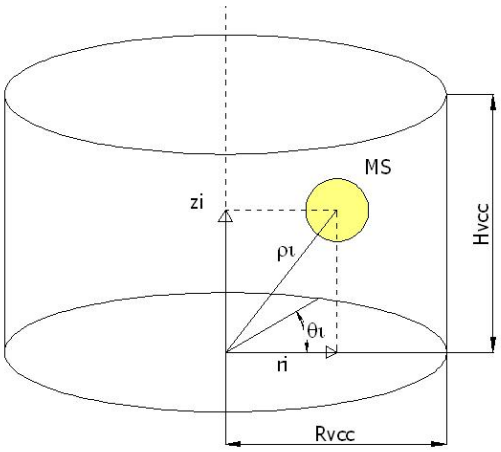

Figure 80: Spatial distribution of measurement spheres (MS)

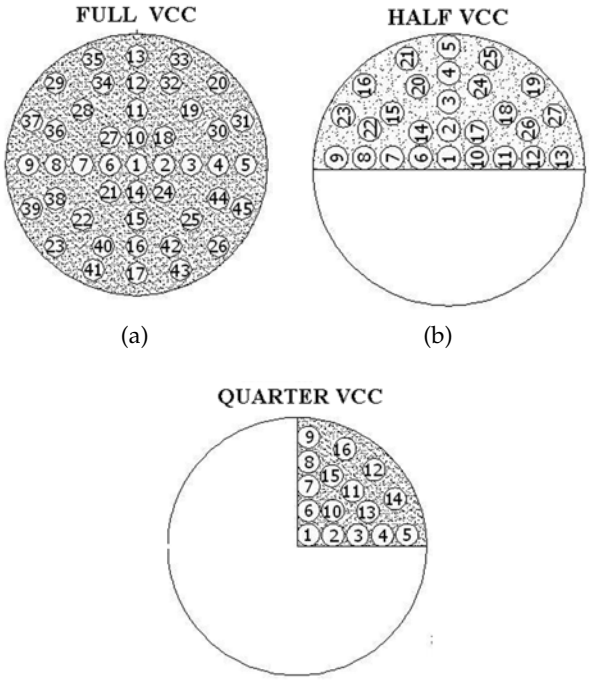

Figure 81: Distribution of MS in (a) full VCC, (b) half VCC and (c) quarter of VCC

Table 18: Models analyzed in this chapter

TEST ID	σ_{v0} [kPa]	σ_{h0} [kPa]	p_0 [kPa]	DR [%]	n_t $(= n_0)$ [-]	VCC	Analysis	Description
TEST16	100	100	100	75	0.4	full	homogeneity, symmetry	MediumIsoBC1Full
TEST20	100	100	100	90	0.38	full	homogeneity	DenseIsoBC1Full
TEST163	313	109.91	177.61	93.6	0.375	full	homogeneity	DenseKoBC1Full
TEST32	100	100	100	75	0.4	half	symmetry	MediumIsoBC1Half
TEST34	100	100	100	75	0.4	quarter	symmetry	MediumIsoBC1Quarter

6.2 EXAMINING HOMOGENEITY

Inhomogeneities were assessed in three ways:

1. observation of normal contact force networks developing between particles and their orientations–Section 6.2.1
2. examination of the mesoscopic values of n, C_N and σ using MS at different vertical and radial distances from the axis of symmetry and positioned at different angles–Section 6.2.2
3. contour plots of normalized parameters obtained by interpolation of all MS–evaluated values such as porosity (n), coordination number (C_N) and stresses (σ)–Section 6.2.3

All results are plotted for the layers presented in Figure 83 and MS (Figure 81a) distributions. Layer 1 is positioned at the top and layer 6 at the bottom of VCC. The effect of specimen size (chamber size effect) on the results will be examined in Chapter 9 while considering only quarter of VCC with various diameters, D_{vcc}.

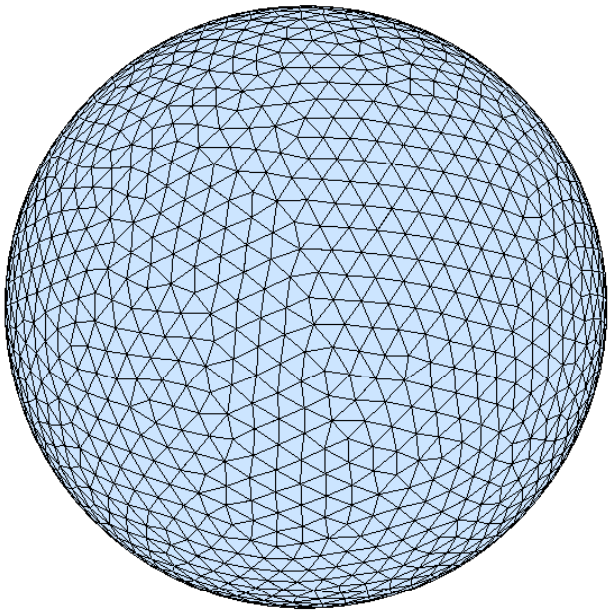

Figure 82: Spherical mesh used to plot contact point orientation and normal, tangential contact forces

6.2.1 *Contact force network, contact normal orientation and normal force magnitude*

The homogeneity of DEM models was initially assessed by visual observation of normal contact forces acting between contacting particles. For this analysis the specimen was divided into six horizontal layers of 0.1 m in thickness (Figure 83). The normal contact force examination was performed for three cases (T16, T20 and T163). Results for initial conditions (before cone penetration) can be seen in Figure 84 to Figure 87. The figures show only normal contact forces larger than the average value.

Looking at the normal contact force networks developing between contacting particles a visible difference between medium and dense specimens. For the medium–dense specimen (Figure 84), T16 ($D_R = 75\%$), we observed some kind of arching of normal contact forces (more visible in yz–plane (cut 2:Figure 87b) close to the radial wall and just above the bottom (layer 1). For the denser samples (Figure 85), T20 and T163, this kind of arching was not visible any more. Also, for isotropically compressed models a looser contact force network appeared close to the axis of the VCC. This was not observed for anisotropically compressed assembly. A possible reason for the appearance of these looser regions was that the bottom wall is fixed in the numerical simulations (not servo–controlled) and wall compression was performed only from the sides (through the radial wall) and the top (top wall). Moreover, for anisontropically compressed sample, the orientation of the contact forces ia in the direction of applied compression stress (vertical).

In DEM the fabric at the particle scale has most often been quantified by considering the contact normal orientations, contact normal force orientation. The spherical mesh used to plot contact point orientation and normal/tangential contact forces is shown in Figure 82.

The orientation of the contacts is shown in Figure 88. It can be observed clear difference between isotropically and anisotropically compressed sample. In the former there is no predominant orientation for which the number of contacts is more marked (Figure 88a and Figure 88b) while in latter the contacts are oriented vertically and only small number of contacts is oriented horizontally (Figure 88c). The figures 89 shows that medium specimen is developing less number of contacts than the very dense one. However, the difference between number of contacts in each layer is more visible for medium specimen than dense one. Test T16 ($D_R = 75\%$) developed around 3000 contacts in each direction at the top layer (Layer 1) and approximately 1000 contact less at the bottom layer (Layer 6). In dense and very dense models, T20 and T163, this difference is not so explicit. Moreover, the number of contacts increases with increasing confining pressure and relative density (Figure 89).

It can be observed that plotting the histograms based only on the information on the contact normal orientations cannot provide information on the magnitudes of the contact forces oriented in each direction. Hence, the histograms of the magnitude of contact normal forces and shear contact forces oriented in each direction can be viewed in Figures 90 and Figure 91, respectively.

It can be observed important differences between DEM material deposited under anisotropic and isotropic conditions. In the first the forces create the axisymmetric form about the vertical axes while for latter the fabrics appearing isotropic.

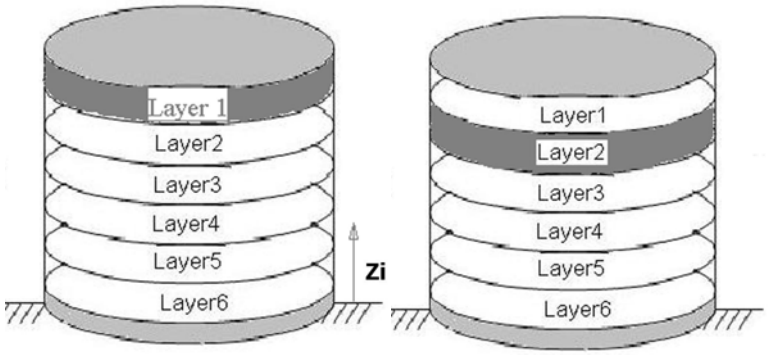

(a) layer 1 at $d_z = 0.85$ (b) layer 2 at $d_z = 0.71$

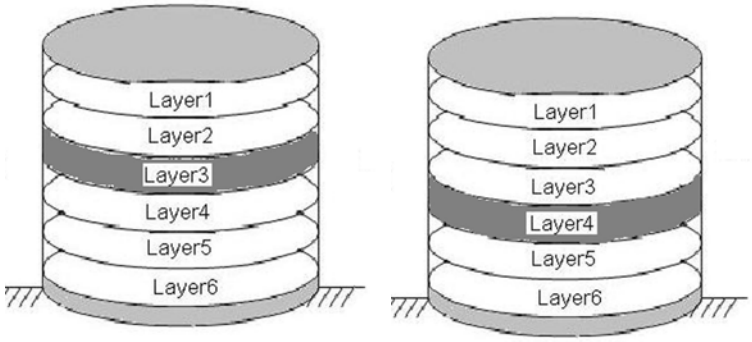

(c) layer 3 at $d_z = 0.57$ (d) layer 4 at $d_z = 0.42$

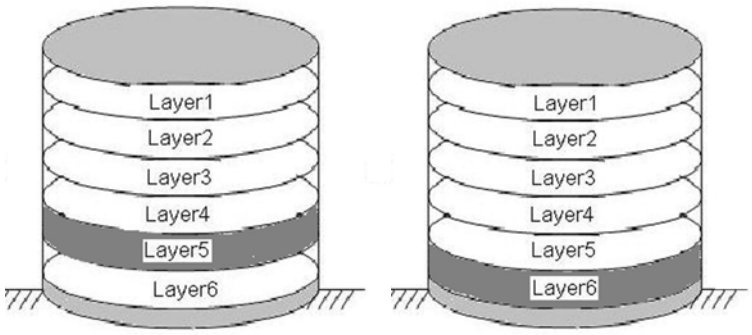

(e) layer 5 at $d_z = 0.28$ (f) layer 6 at $d_z = 0.14$

Figure 83: Layers of the analysis of contact force networks

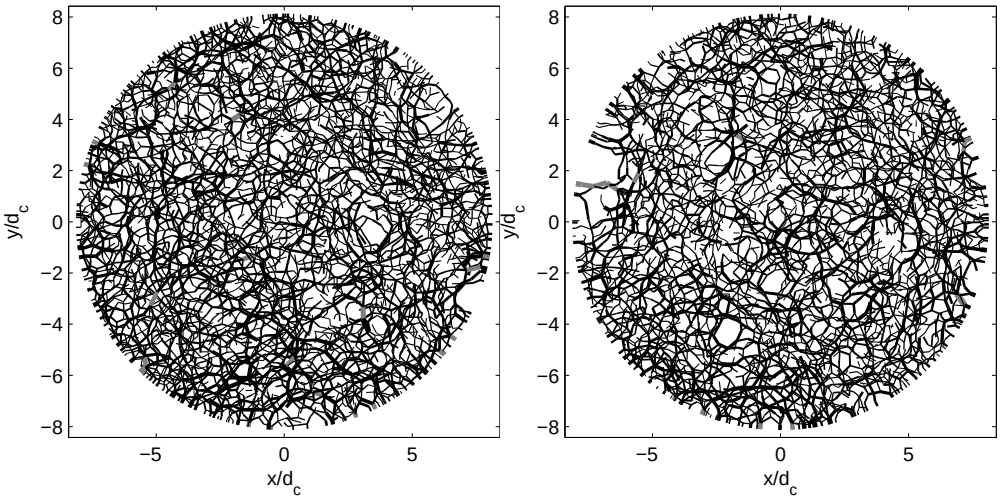

(a) layer 1 at $d_z = 0.85$

(b) layer 2 at $d_z = 0.71$

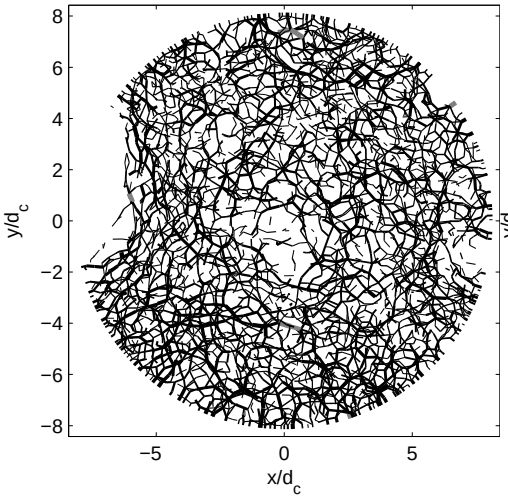

(c) layer 3 at $d_z = 0.57$

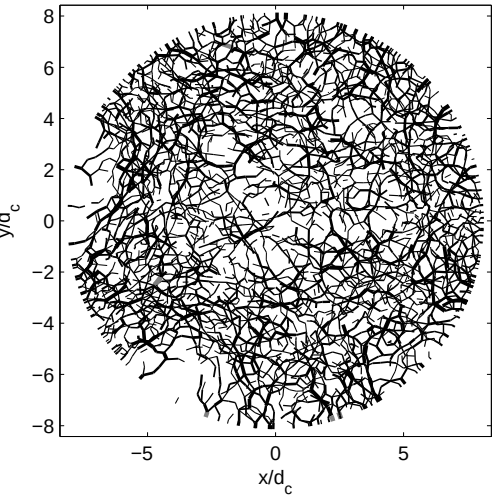

(d) layer 4 at $d_z = 0.42$

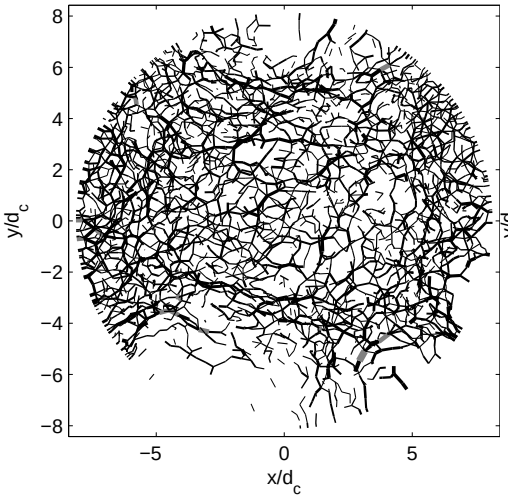

(e) layer 5 at $d_z = 0.28$

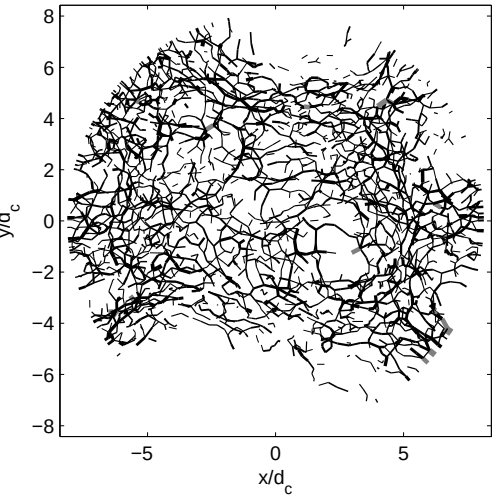

(f) layer 6 at $d_z = 0.14$

Figure 84: Contact force (only above–average) network for medium–dense, isotropically loaded assembly–T16

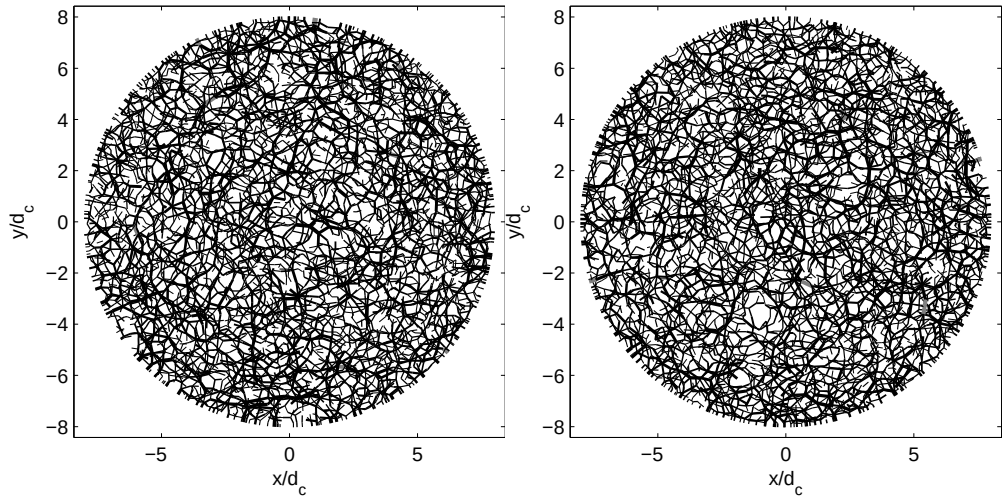

(a) layer 1 at $d_z = 0.85$ (b) layer 2 at $d_z = 0.71$

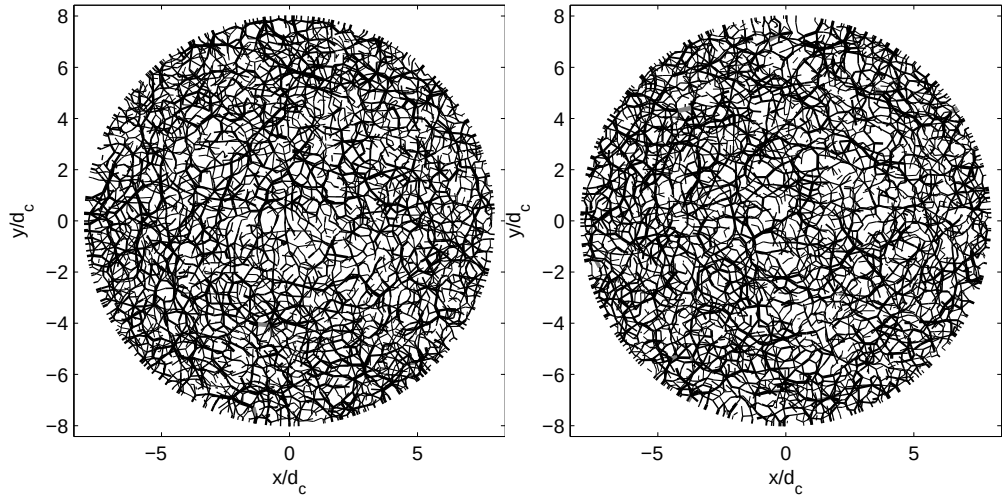

(c) layer 3 at $d_z = 0.57$ (d) layer 4 at $d_z = 0.42$

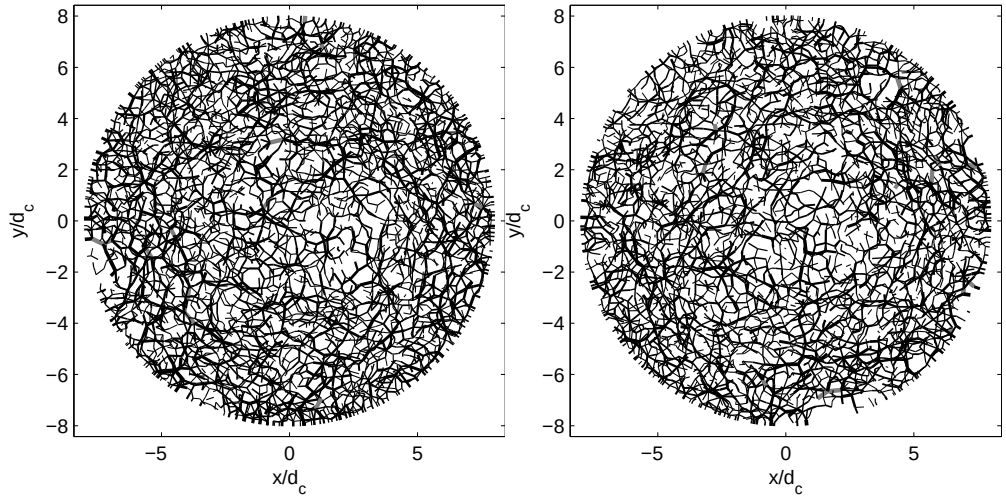

(e) layer 5 at $d_z = 0.28$ (f) layer 6 at $d_z = 0.14$

Figure 85: Contact force (only above–average) network for very dense, isotropically loaded assembly–T20

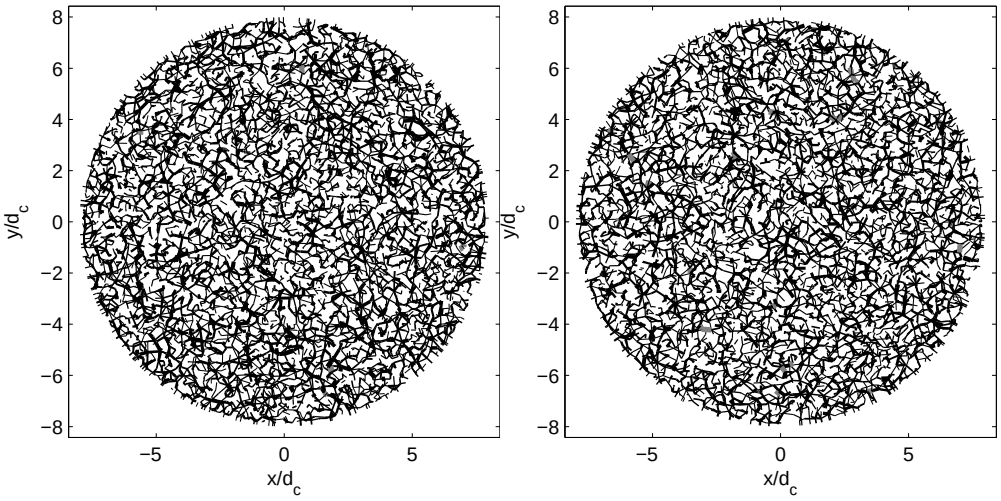

(a) layer 1 at $d_z = 0.85$

(b) layer 2 at $d_z = 0.71$

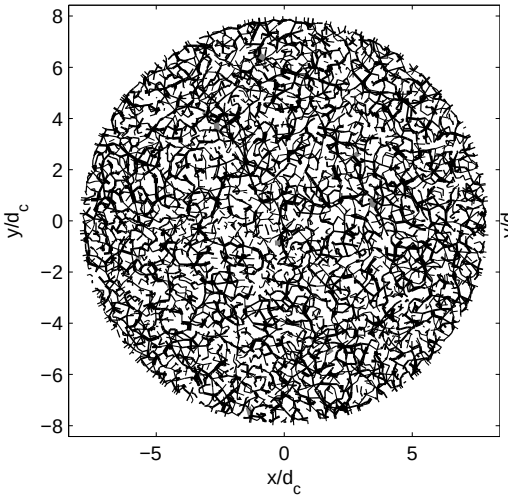

(c) layer 3 at $d_z = 0.57$

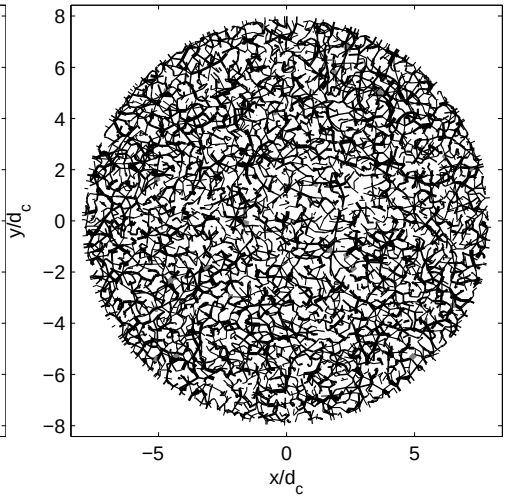

(d) layer 4 at $d_z = 0.42$

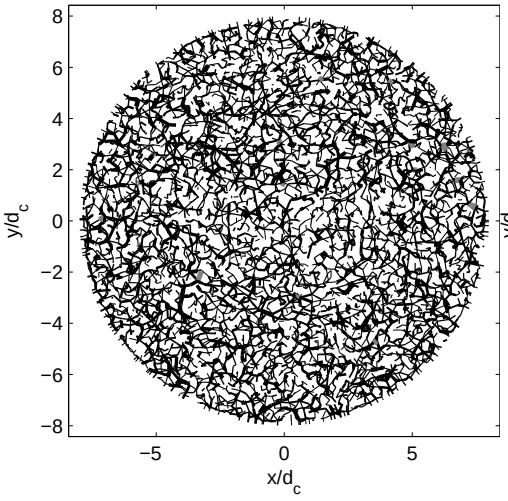

(e) layer 5 at $d_z = 0.28$

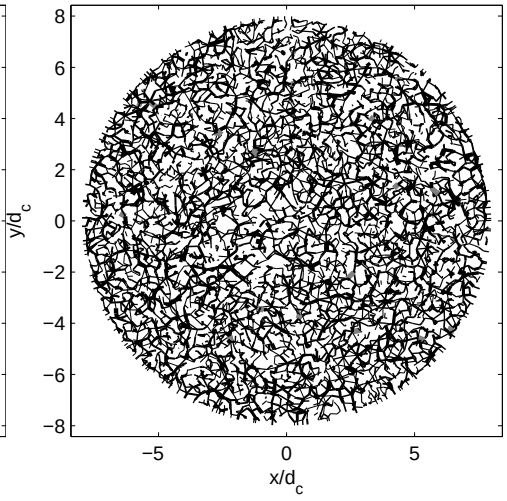

(f) layer 6 at $d_z = 0.14$

Figure 86: Contact force (only above–average) network for very dense, anisotropically loaded assembly–T163

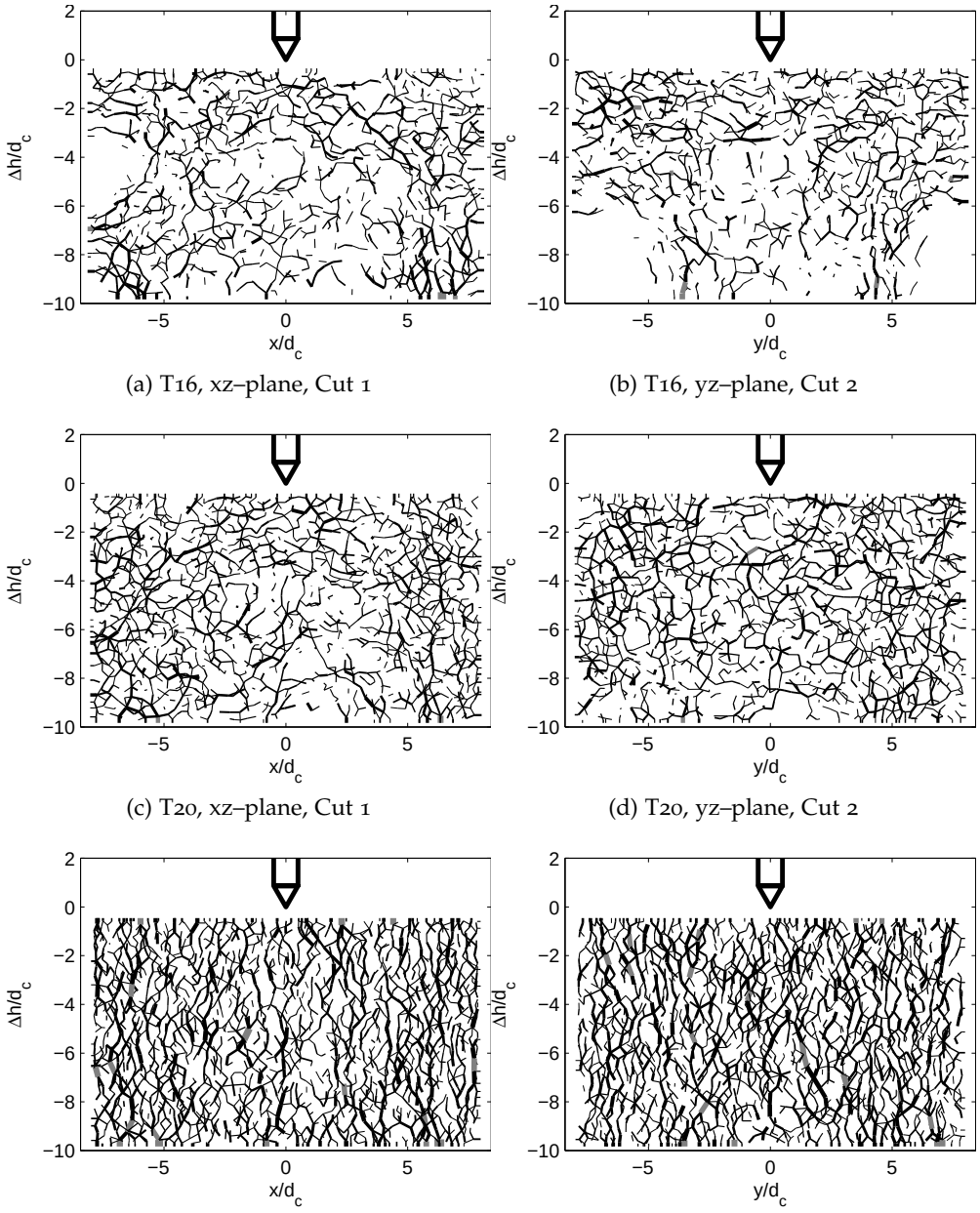

(a) T16, xz–plane, Cut 1

(b) T16, yz–plane, Cut 2

(c) T20, xz–plane, Cut 1

(d) T20, yz–plane, Cut 2

(e) T163, xz–plane, Cut 1

(f) T163, yz–plane, Cut 2

Figure 87: Section with contact force (only above–average) network for the isotropically loaded medium–dense (T16) and very dense (T20) assemblies and anisotropically loaded very dense (T163) assembly

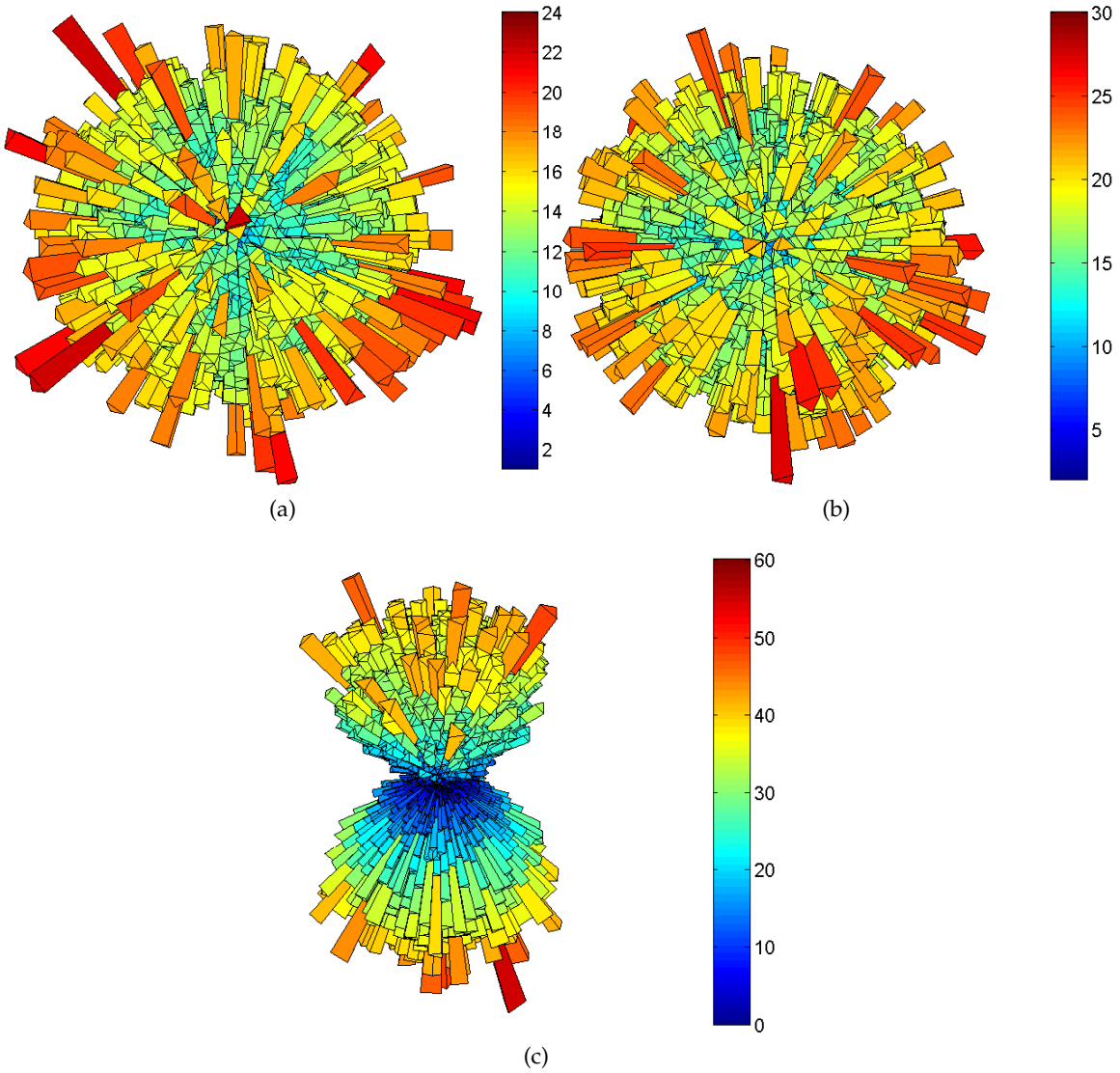

Figure 88: Contact normal orientation for isotropically consolidated sample and (a) medium/-dense (T16), (b) dense (T20) and anisotropic sample (c) very dense (T163) assemblies. Only contacts with normal contact force larger than mean value are shown.

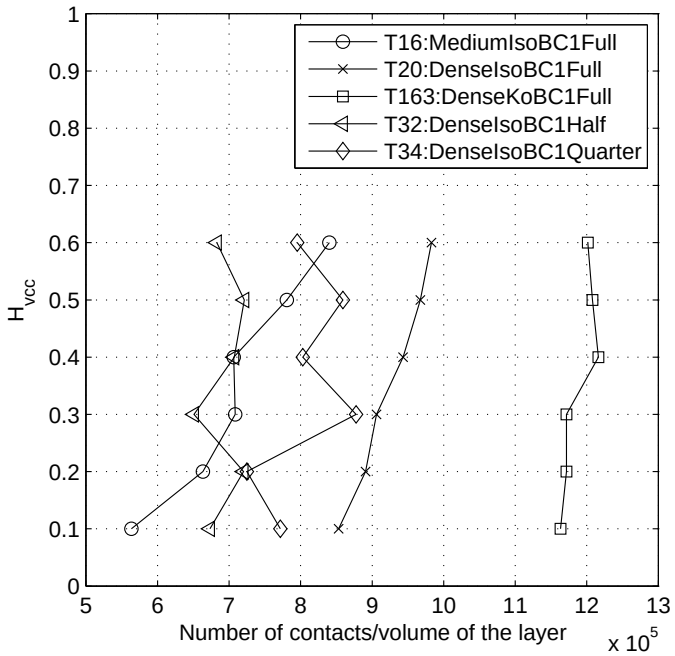

(a) for cf$\neq$ o

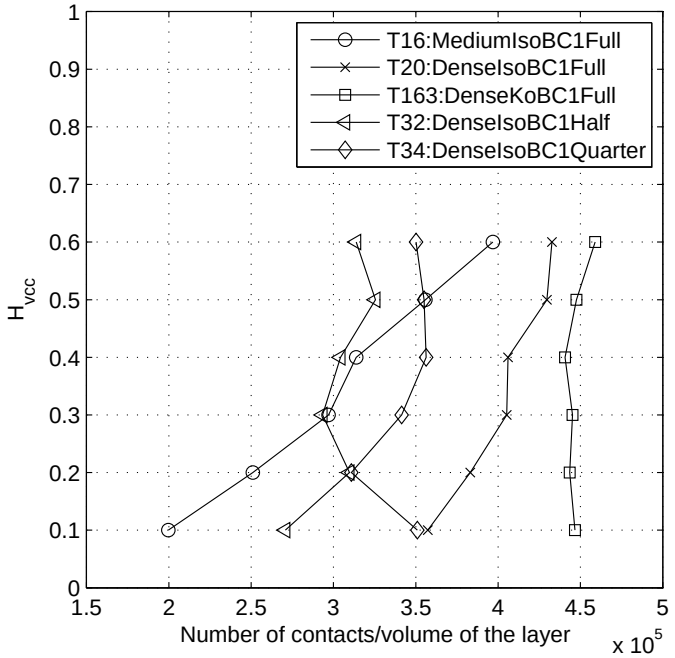

(b) for cf $\geqslant \overline{\text{cf}}$

Figure 89: Distribution of number of contacts with specimen normalized depth. cf–contact force, $\overline{\text{cf}}$–mean contact force

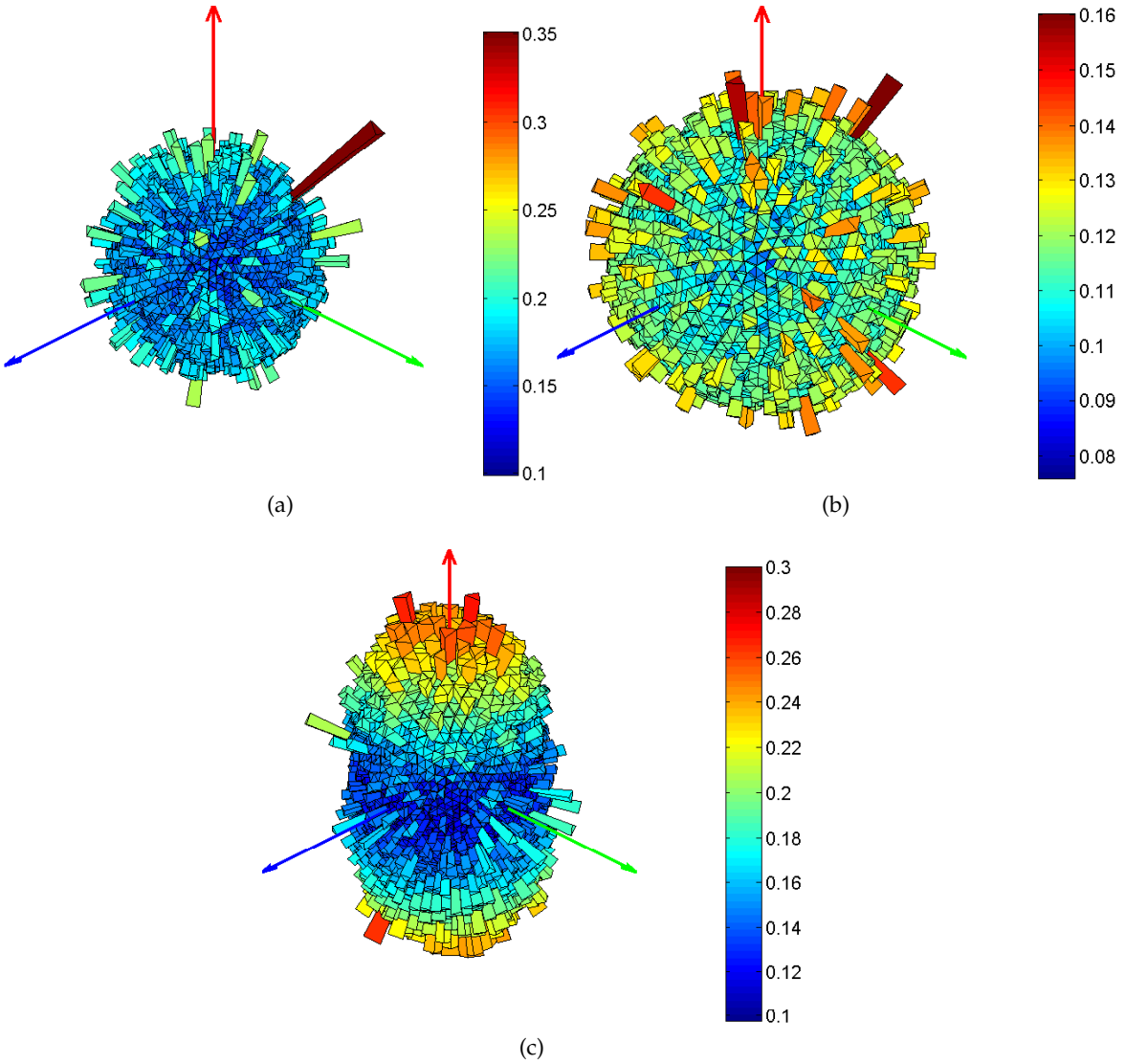

Figure 90: Histograms of the contact normal force magnitude (only above–average) for isotropically consolidated sample and (a) medium/dense (T16), (b) dense (T20) and anisotropic sample (c) very dense (T163) assemblies. Forces are shown in [kN].

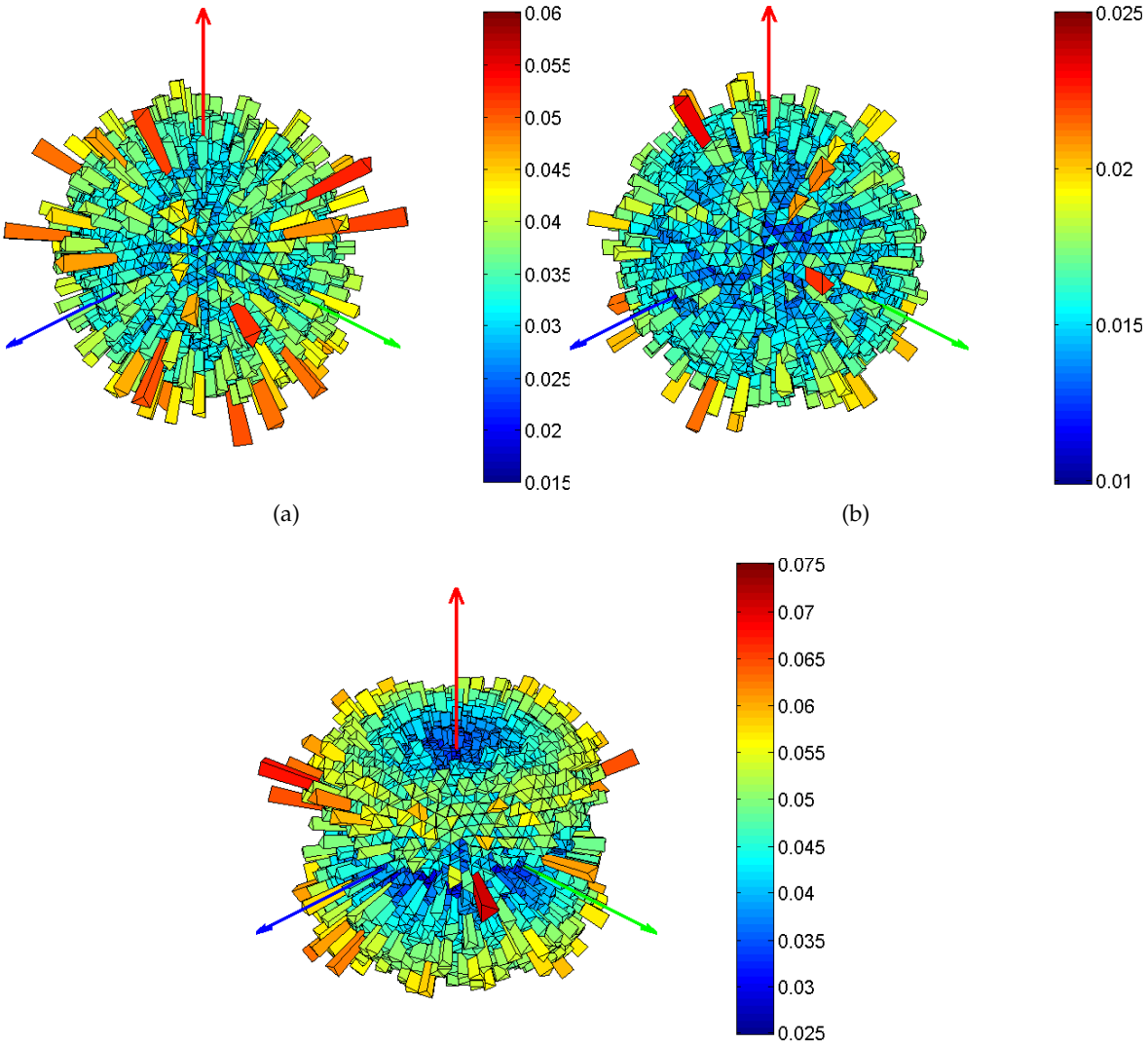

Figure 91: Histograms of the contact shear force magnitude (only above–average) for isotropically consolidated sample and (a) medium/dense (T16), (b) dense (T20) and anisotropic sample (c) very dense (T163) assemblies. Forces are shown in [kN].

6.2.2 *Mesoscopic variables at selected locations*

Measurement spheres (MS) provide mesoscopic values of different variables in locations distributed all over the VCC model. The MS is defined by three parameters: angle θ, and normalized distances d_r and d_z calculated as follow:

$$\begin{aligned} \theta &= \arctan(\frac{y}{x}) \\ d_r &= \frac{r_i}{R_{vcc}} \\ d_z &= \frac{z_i}{H_{vcc}} \end{aligned} \tag{6.1}$$

The definition of these parameters is illustrated in Figure 80.

In this section we examine the results obtained only at MSs. They include those positioned close to the radial wall with d_r = 0.8–0.85 (in Figure 79a, these are M5, MS31, MS20, MS33, M13, MS35, MS29, MS37, M9, MS39, MS23, MS41, M17,MS43, MS26, MS45) at different d_z values (corresponding to six horizontal layers). Also values from MS located on four vertical more examined, viz. **Cut 1** (θ = 0–180°),**Cut 2** (θ = 90–270°), **Cut 3** (θ = 45–225°) and **Cut 4** (θ = 135–315°). Finally, results from MS located at the specimen axis are also examined. All mentioned MSs and their positions can be viewed in Figure 81a and are also recalled in Table 19. In Table 20 mean values, standard deviation and coefficient of variation for the different variables (n, C_N, $\frac{\sigma_r}{p_0}$, $\frac{\sigma_\theta}{p_0}$ and $\frac{\sigma_z}{p_0}$) evaluated at different sets of measurement spheres are collected.

Table 19: MS included in analysis–Full Chamber: *AreaFactor*=1.0

Cut/zone	Measurement Sphere (MS)
Cut 1	5, 4, 3, 2, 1, 6, 7, 8, 9
Cut 2	13, 12, 11, 10, 1, 14, 15, 16, 17
Cut 3	20, 19, 18, 1, 21, 22, 23
Cut 4	29, 28, 27, 1, 24, 25, 26
close to radial wall	5, 9, 13, 17, 20, 23, 26, 29, 31, 33, 35, 37, 39, 41, 43, 45

6.2.2.1 *Porosity*

Figure 92a shows normalized porosity ($\frac{n}{n_0}$, n_0 is the target porosity used during specimen build–up: Table 18) plotted for MSs located close to the radial wall (d_r=0.8–0.85). Figures 93a, 94a and 95a show the distribution of $\frac{n}{n_0}$ in four different planes and averaged in six horizontal layers. Finally, Figure 96b shows the distribution of porosity with normalized VCC depth in the chamber axis.

It can be observed (Table 20) that porosity close to radial wall, in the four vertical cuts and in whole specimen seems to be somewhat below target one. However, the coefficient of variation is around 3(4)%. Looking at the distribution of porosity at the

VCC axis (Figure 96b) denser zones appear close to the top and bottom walls, while looser zones appear away from the walls. However, the average normalized porosity is close to the target value for all VCC–models analysed in this chapter. The C_v is within 2%.

6.2.2.2 *Coordination number*

Figure 92b shows the coordination number (C_N) plotted for MS located close to the radial wall (d_r=0.8–0.85). C_N lies between 0 and 6, by this measure the heterogeneity is more marked then by porosity. It can be also observed that for the four selected planes, C_N oscillates around 3 in medium isotropically compressed assembly, T16 (Figure 93b), 4 in dense isotropically compressed assembly, T20 (Figure 94b) and 5 in a very dense anisotropically compressed sample, T163 (Figure 95b). The variation of C_N is larger in the isotropically compressed assemblies, where it seems to increase near the radial wall. Moreover, Figure 96c shows also how C_N reduces while reaching the bottom of the VCC. The coefficient of variation reduces with the specimen density (clearly visible in Table 20).

6.2.2.3 *Stress*

The stress components normalized by the overall mean stress are plotted at the MSs located close to the radial wall (d_r=0.8–0.85) in Figure 92c ($\frac{\sigma_r}{p_0}$) and Figure 92d ($\frac{\sigma_z}{p_0}$). Moreover, figures 93c–93d, 94c–94d and 95c–95d show distribution of normalized stresses (σ_r and σ_z) evaluated at MSs located in the four selected planes. The stress distribution with VCC depth alongside the axis can be viewed in figures 96d and 96e).

Note that for isotropically compressed samples the p_0 normalized values of σ_z, σ_θ and σ_r shall be close to 1 for an homogeneous state of stress while for the anisotropically compressed assembly this normalized stresses should be $\approx$ 1.76, 0.61 and 0.61, respectively.

It can be appreciated, that stresses are more uniform for dense than for the medium/dense specimen. However, for isotropically compressed samples, the stresses are substantially smaller (by 10–50%) close to the chamber axis, whereas they are typically above target (by 10–40%) close to the radial wall. For anisotropically compressed sample a more uniform σ_r and σ_θ distribution is observed while σ_z has the same trend of smaller values close to the chamber axis and higher values near the radial wall. Again, it is clear that the isotropic compression process results in a much less uniform stress state alongside the chamber axis than anisotropic compression (see Table 20). The influence of the bottom wall is also visible.

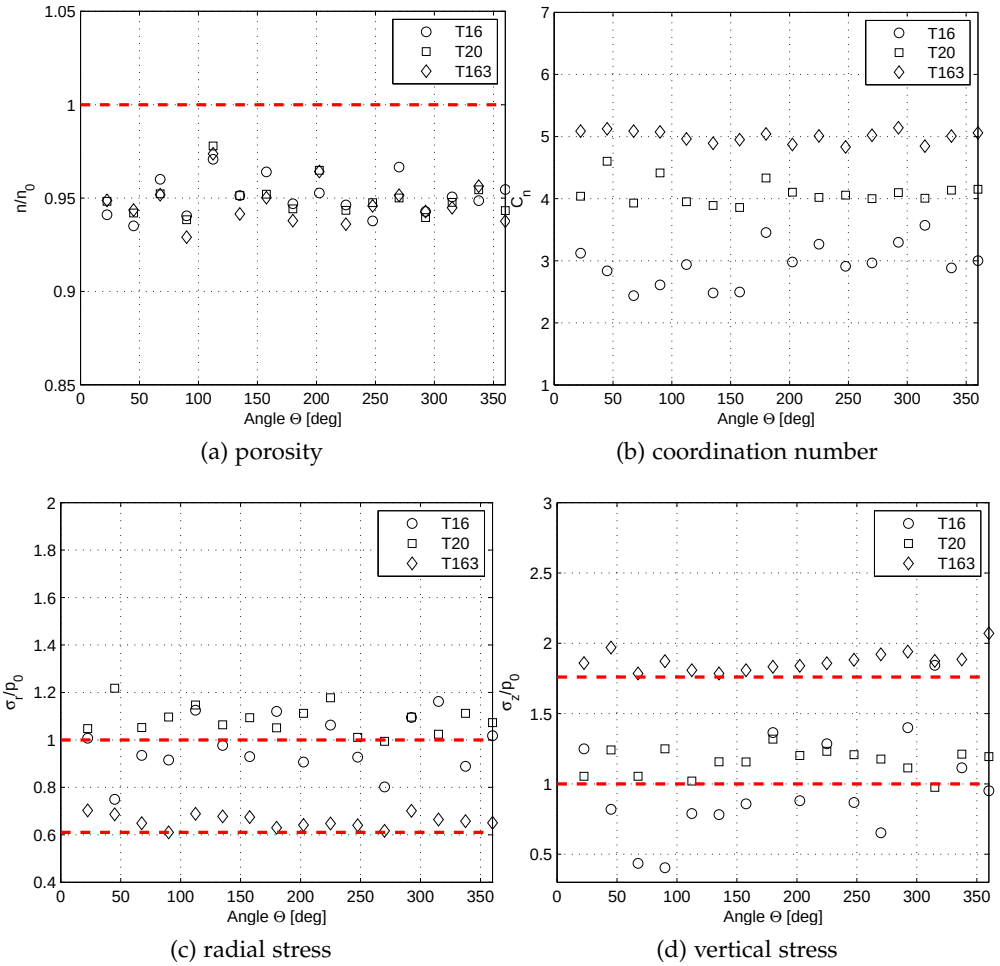

(a) porosity

(b) coordination number

(c) radial stress

(d) vertical stress

Figure 92: Plot of (a) normalized porosity, (b) coordination number, (c) normalized radial stress and (d) normalized vertical stress measured at initial stage in MS averaged with the depth and close to the radial wall for T16, T20 and T163

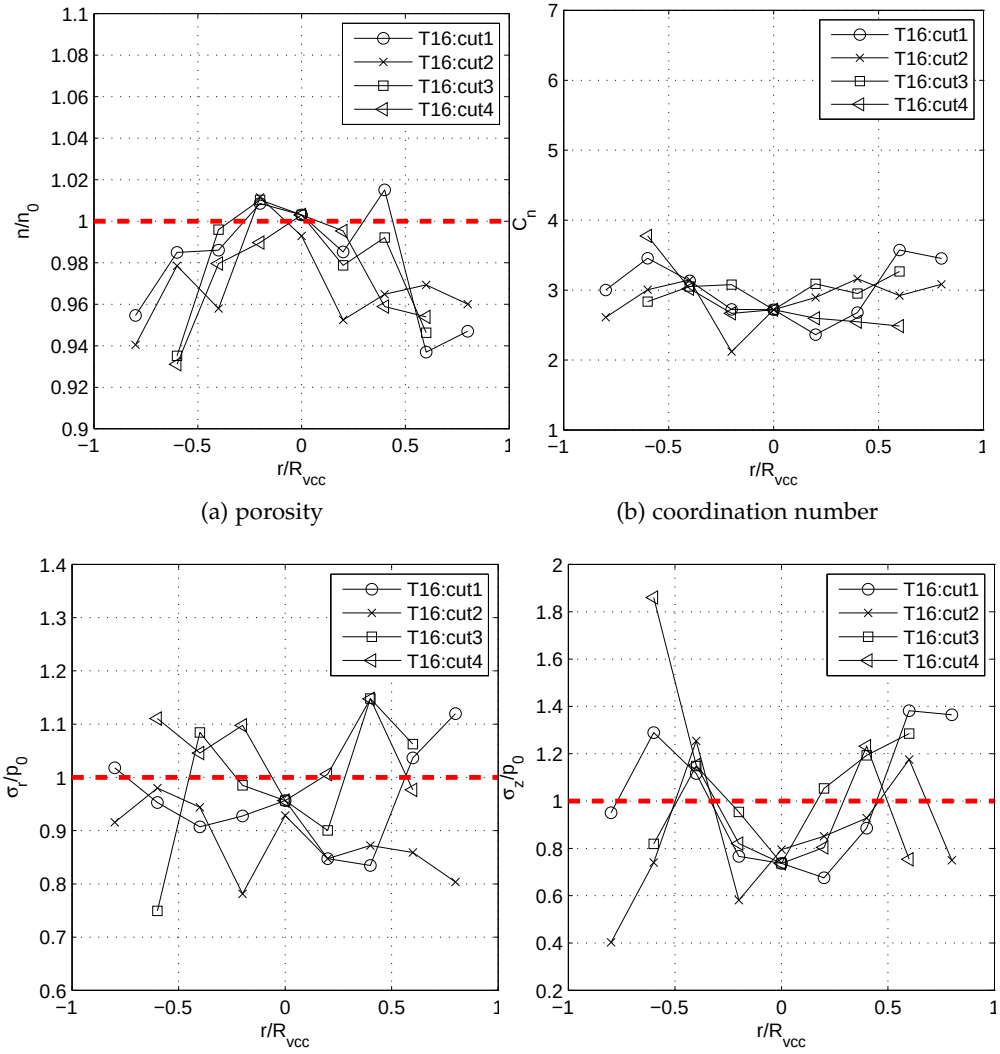

(a) porosity (b) coordination number

(c) radial stress (d) vertical stress

Figure 93: Plot of (a) normalized porosity, (b) coordination number, (c) normalized radial stress and (d) normalized vertical stress measured at initial stage in MS averaged with the depth and for four different cuts for medium–dense isotropically compressed assembly–T16:MediumIsoBc1

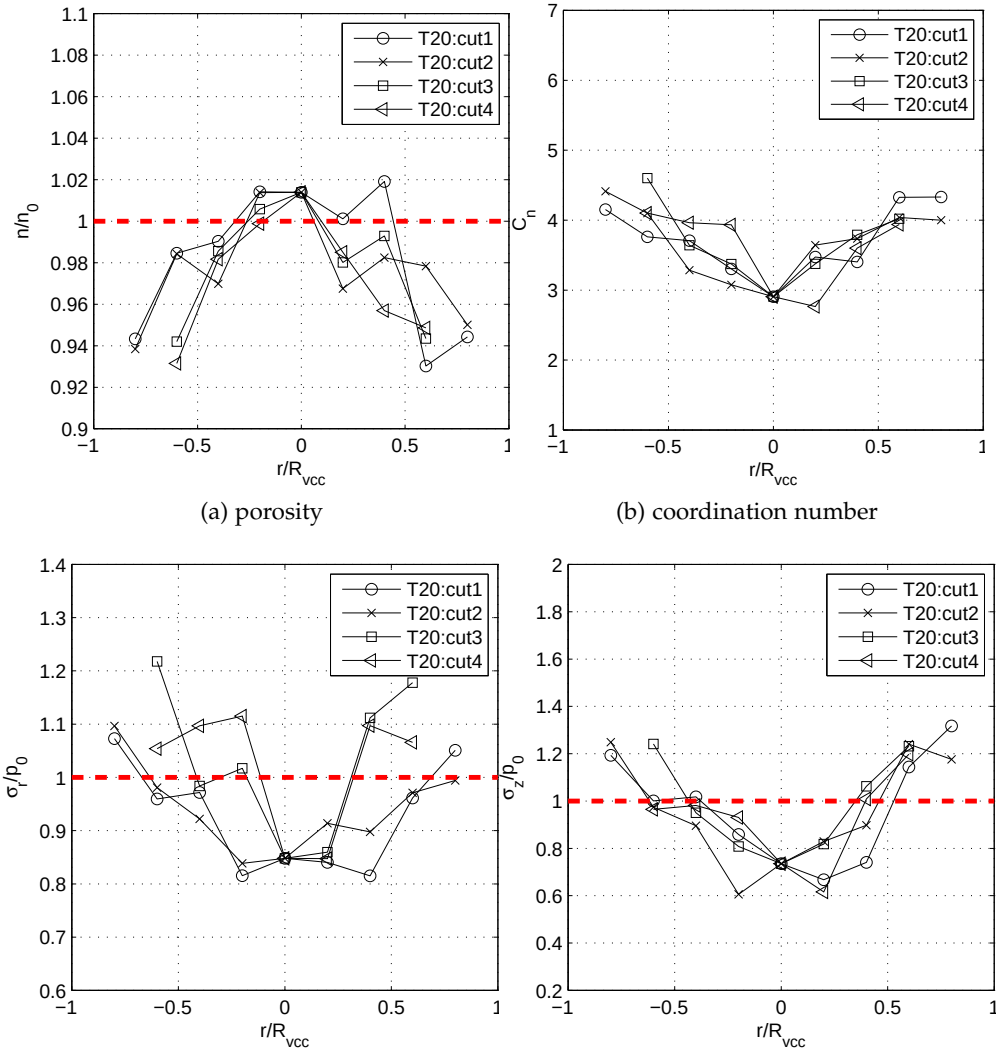

(a) porosity

(b) coordination number

(c) radial stress

(d) vertical stress

Figure 94: Plot of (a) normalized porosity, (b) coordination number, (c) normalized radial stress and (d) normalized vertical stress measured at initial stage in MS averaged with the depth and for four different cuts for dense isotropically compressed assembly–T20:DenseIsoBc1

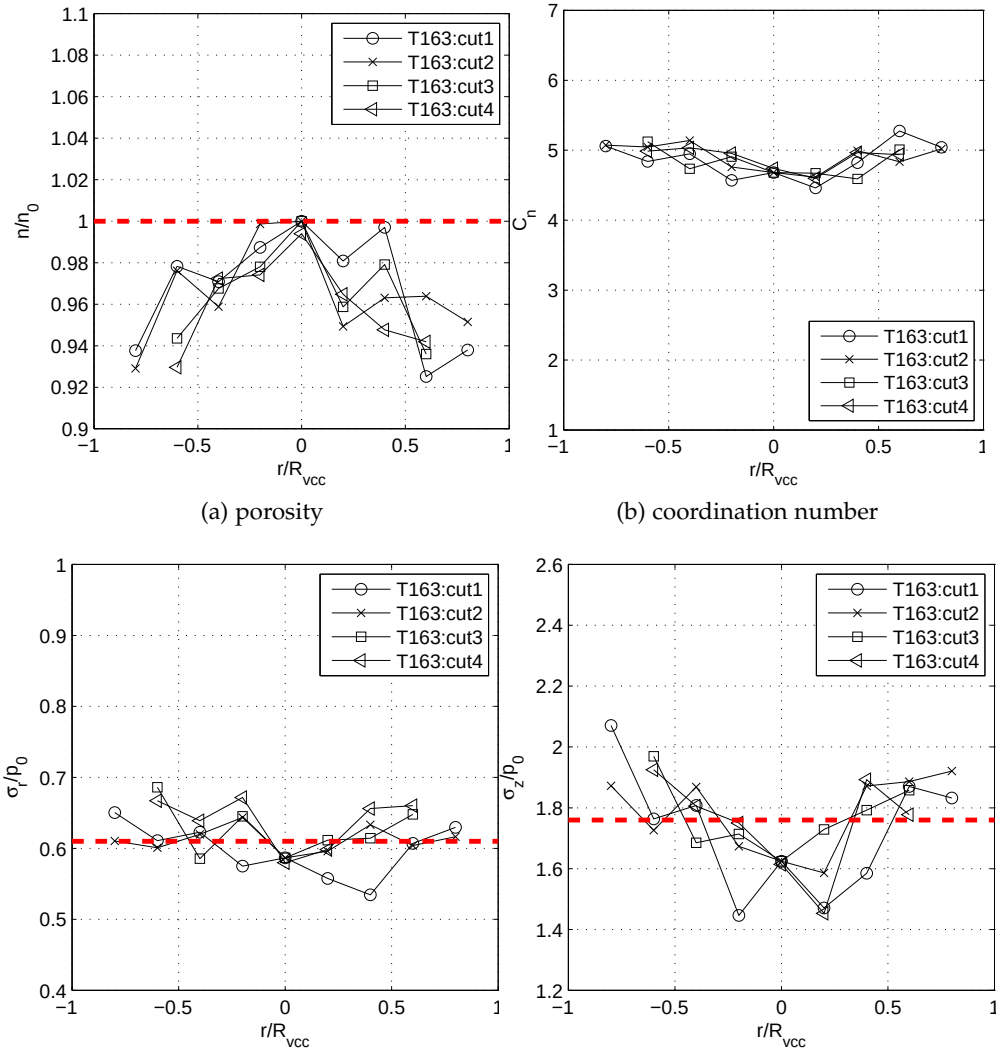

(a) porosity (b) coordination number

(c) radial stress (d) vertical stress

Figure 95: Plot of (a) normalized porosity, (b) coordination number, (c) normalized radial stress and (d) normalized vertical stress measured at initial stage in MS averaged with the depth and for four different cuts for dense anisotropically compressed assembly–T163:DenseKoBc1

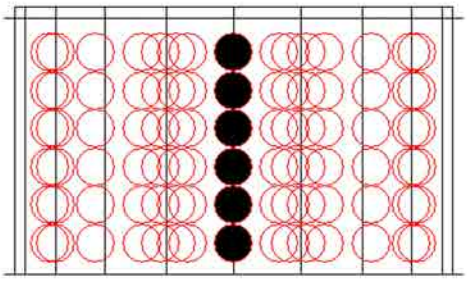

(a) position of MS

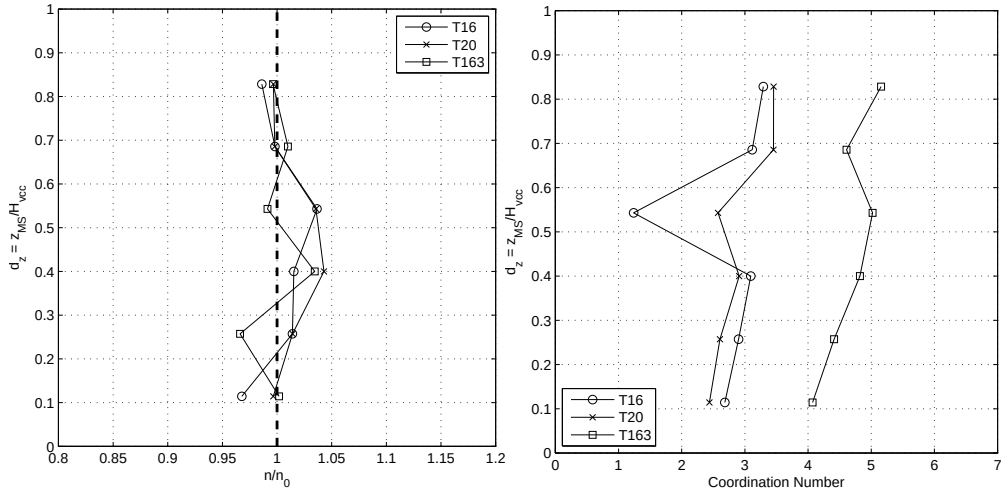

(b) $\frac{n}{n_0}$ (c) C_N

(d) $\frac{\sigma_{rr}}{p_0}$ (e) $\frac{\sigma_{zz}}{p_0}$

Figure 96: Distribution of variables with normalized depth of VCC for the MS positioned at the axis of the VCC for isotropically compressed medium–dense (T16), dense (T20) and anisotropically compressed dense (T163) assemblies

Table 20: Mean, standard deviation and coefficient of variation (ratio of the precedent) for the different variables (n, C_N, $\frac{\sigma_r}{p_0}$, $\frac{\sigma_\theta}{p_0}$ and $\frac{\sigma_z}{p_0}$) evaluated at different sets of measurement spheres

Tets ID	$\frac{n}{n0}$																				
	MS:radial wall			MS:Cut 1			MS:Cut 2			MS:Cut 3			MS:Cut 4			MS:axis			MS:whole VCC		
	$\widetilde{N}$	S	C_v	$\widetilde{N}$	S	C_v	$\widetilde{N}$	S	C_v	$\widetilde{N}$	S	C_v	$\widetilde{N}$	S	C_v	$\widetilde{N}$	S	C_v	$\widetilde{N}$	S	C_v
T163	0.96	0.03	0.03	0.98	0.03	0.03	0.98	0.03	0.03	0.98	0.03	0.03	0.97	0.03	0.03	1.01	0.02	0.02	0.97	0.03	0.03
T16	0.96	0.03	0.03	0.98	0.03	0.03	0.97	0.03	0.03	0.98	0.03	0.03	0.97	0.04	0.04	1.00	0.02	0.02	0.97	0.03	0.03
T20	0.95	0.03	0.03	0.98	0.03	0.03	0.98	0.03	0.03	0.98	0.03	0.03	0.97	0.03	0.03	1.01	0.02	0.02	0.97	0.03	0.03
	C_N																				
Test ID	$\widetilde{N}$	S	C_v	$\widetilde{N}$	S	C_v	$\widetilde{N}$	S	C_v	$\widetilde{N}$	S	C_v	$\widetilde{N}$	S	C_v	$\widetilde{N}$	S	C_v	$\widetilde{N}$	S	C_v
T163	5.0	0.37	0.07	4.86	0.34	0.07	4.92	0.43	0.08	4.82	0.38	0.07	4.89	0.34	0.07	4.68	0.40	0.08	4.91	0.35	0.07
T16	2.95	0.98	0.33	3.01	0.65	0.21	2.79	0.84	0.30	3.00	0.72	0.24	2.83	0.77	0.27	2.70	0.75	0.28	2.98	0.79	0.26
T20	4.10	0.52	0.13	3.71	0.55	0.15	3.69	0.51	0.14	3.67	0.57	0.15	2.83	0.77	0.27	2.90	0.45	0.15	3.84	0.54	0.14
	$\frac{\sigma_r}{p_0}$																				
Test ID	$\widetilde{N}$	S	C_v	$\widetilde{N}$	S	C_v	$\widetilde{N}$	S	C_v	$\widetilde{N}$	S	C_v	$\widetilde{N}$	S	C_v	$\widetilde{N}$	S	C_v	$\widetilde{N}$	S	C_v
T163	0.66	0.07	0.11	0.60	0.05	0.08	0.60	0.06	0.10	0.62	0.09	0.10	0.63	0.07	0.11	0.58	0.06	0.10	0.62	0.06	0.09
T16	0.98	0.52	0.53	0.95	0.32	0.34	0.91	0.50	0.55	0.98	0.39	0.39	1.03	0.33	0.32	0.96	0.30	0.31	0.98	0.40	0.41
T20	1.09	0.17	0.15	0.94	0.17	0.18	0.97	0.18	0.18	1.04	0.18	0.17	1.00	0.19	0.19	0.85	0.17	0.20	1.00	0.18	0.18
	$\frac{\sigma_\theta}{p_0}$																				
Test ID	$\widetilde{N}$	S	C_v	$\widetilde{N}$	S	C_v	$\widetilde{N}$	S	C_v	$\widetilde{N}$	S	C_v	$\widetilde{N}$	S	C_v	$\widetilde{N}$	S	C_v	$\widetilde{N}$	S	C_v
T163	0.65	0.07	0.11	0.64	0.06	0.09	0.64	0.06	0.09	0.60	0.05	0.08	0.61	0.06	0.09	0.60	0.04	0.07	0.63	0.06	0.09
T16	1.06	0.54	0.51	1.02	0.30	0.29	1.04	0.45	0.43	0.96	0.34	0.35	0.94	0.31	0.33	0.77	0.26	0.35	1.05	0.39	0.37
T20	1.12	0.19	0.17	1.05	0.19	0.18	1.06	0.20	0.19	0.94	0.20	0.21	0.92	0.20	0.22	0.83	0.17	0.20	1.04	0.21	0.20

Test ID	$\frac{\sigma_Z}{p_0}$																				
	$\widetilde{N}$	S	C_v	$\widetilde{N}$	S	C_v	$\widetilde{N}$	S	C_v	$\widetilde{N}$	S	C_v	$\widetilde{N}$	S	C_v	$\widetilde{N}$	S	C_v	$\widetilde{N}$	S	C_v
T163	1.87	0.22	0.12	1.72	0.18	0.10	1.78	0.18	0.10	1.77	0.18	0.10	1.75	0.20	0.11	1.62	0.12	0.07	1.79	0.18	0.10
T16	0.98	0.47	0.48	1.02	0.29	0.28	0.80	0.28	0.35	1.03	0.28	0.27	1.05	0.28	0.27	0.74	0.23	0.31	1.03	0.35	0.34
T20	1.16	0.16	0.14	0.96	0.15	0.16	0.96	0.15	0.16	0.98	0.14	0.14	0.92	0.13	0.14	0.73	0.13	0.18	0.92	0.13	0.14
$\widetilde{N}$-mean value, S-standard deviation, C_v-coefficient of variation																					

6.2.3 *Contour plots*

The homogeneity of mesoscopic MS–based values is perhaps best revealed by contour plots generated in MATLAB. All examined parameters were normalized by their material target value (except coordination number). Contour maps were generated for three specimens (T16, T20 and T163) using values at all the measurement spheres (MS) distributed all over the specimen in six horizontal layers. Note however, that the MSs were distributed in non regular manner. Hence, to be able to create contour plots a regular cylindrical grid had to be first generated. This was done by the *meshgrid* command as follow:

$$[\Theta, R, Z] = \mathtt{meshgrid}(\theta, r, z)$$

where: $\theta = 0 : \pi/36 : 2\pi$, $r = r_{min} : 0.05 : r_{max}$ and $z = z_{min} : 0.05 : z_{max}$; r_{max}, r_{min}, z_{max} and z_{min} are the extreme positions of the MS in the VCC. The graphical representation of the meshgrid as well as positions of MS are presented on Figure 97. In the next step, a corresponding Cartesian description was obtained using the following command:

$$[X, Y, Z] = \mathtt{pol2cart}(\Theta, R, Z)$$

The final step required the interpolation of the given data (n, σ, C_N, etc.) at the regular grid points. Data gridding and hypersurface fitting for 3-D data was done as follow:

$$\mathtt{Z{=}griddata3}(m_x, m_y, m_z, v, X, Y, Z, '\,\mathtt{method}');$$

where m_x, m_y and m_z are the position in x-,y- and z-direction of the MS, v is the data measured in the MS (n, σ, C_N, etc.), X,Y and Z are the Cartesian coordinates of the regular grid and *method* is either linear (Tesselation-based linear interpolation (default)) or nearest (nearest neighbor interpolation). The contour maps were generated to show distribution of the variables in horizontal layers and also in xz– and yz–planes by using *contourf* command. For more detailed description of the method refer to MATLab User guide.

6.2.3.1 *Porosity*

Figures 98, 99, 100 and 101 show a contour plot of normalized porosity ($\frac{n}{n_0}$) at initial stage. In all cases relatively denser zones appear close to the radial wall and looser zones close to the axis. These looser zones grow as we go from top to bottom of the VCC, such growth is more pronounced in the looser specimen (T16) (Figure 101a and Figure 101b). In dense assembly loose region starts approximately 0.2 m beneath top wall and spread towards bottom (Figure 101c) in xz–plane while in yz–plane it appears as a small region at the center of VCC away from the walls.

The variation range of $\frac{n}{n_0}$ for all cases is quite small and within $\pm 10\%$. It can be observed that, generally, in DEM models porosity obtained during the compression process is affected by the presence of walls which resulted in lower porosity close to

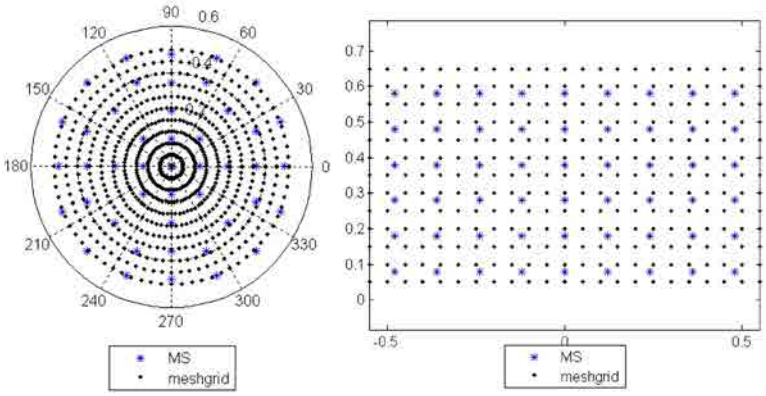

(a) (b)

Figure 97: Uniform meshgrid and distribution of MS (a) xy–plane and (b) xz/yz–plane

them and higher away from them (i.e. at axis of the VCC). These contour plots are in qualitative agreement with the contact force networks described in 6.2.1.

6.2.3.2 *Coordination number*

Figures 102, 103, 104 and 105 show contour plots of coordination number (C_N) just before CPT started. As expected, the number of contacts per ball is higher close to servo–control walls (top and radial walls) as shown in Figure 103 and 104. Dense and very dense assemblies generate more contacts (3.5–4.5 and 4.5–5.5) than medium assembly (< 4). As mentioned above when generating loose and medium specimens many floats may appear (particles with no contacts). These floats will then result in low coordination numbers (Figure 105b). When we recall the contact force network plot we will see that low C_N zones coincide with the zones with less than average contact forces (visible as a loose zones and/or white zones) in figures 84a, reff2 and 87b. Finally, it is clear from the plots that the scale of fluctuation of C_N is larger that of normalized porosity.

6.2.3.3 *Stresses*

Figures 106, 107, 108 and 109 show contour plots of normalized radial stress ($\frac{\sigma_r}{p_0}$), figures 110, 111, 112 113 show normalized circumferential stress ($\frac{\sigma_\theta}{p_0}$) and figures 114, 115, 116 and 113 show normalized vertical stress ($\frac{\sigma_z}{p_0}$) at initial stage, before cone penetration.

Remember that the reference values for an ideally homogeneously stressed assembly are 1 for all stresses in the isotropically compressed cases whereas, for the anisotropically compressed case, they are 1.76, 0.61 and 0.61 for $\frac{\sigma_r}{p_0}$, $\frac{\sigma_\theta}{p_0}$ $\frac{\sigma_z}{p_0}$, respectively.

Looking at the stress distributions we observe that σ_z increases slightly with chamber depth while σ_r and σ_θ decrease with VCC depth. The difference between top and bottom layers is more visible for medium than for dense assemblies (figures 106f, 110f and 114f). These differences are caused by the forces acting between contacting particles and these stress contours are in agreement with the normal contact forces plots presented above.

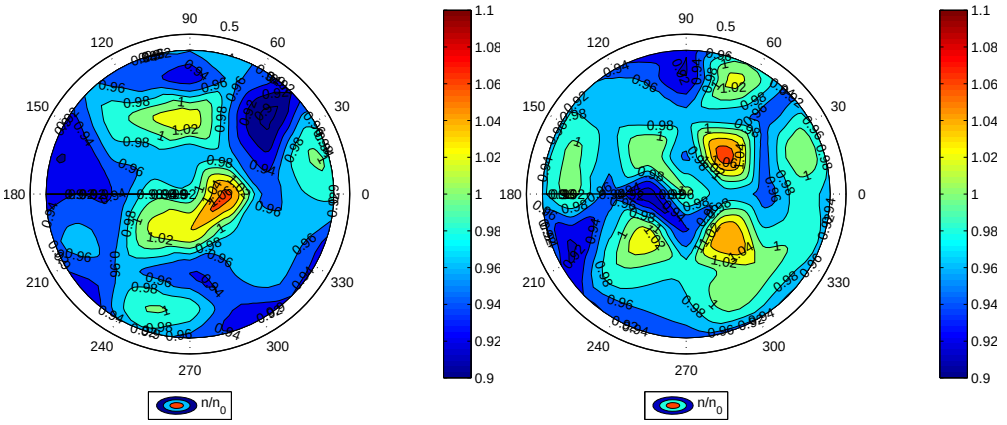

(a) layer 1 at $d_z = 0.85$ (b) layer 2 at $d_z = 0.71$

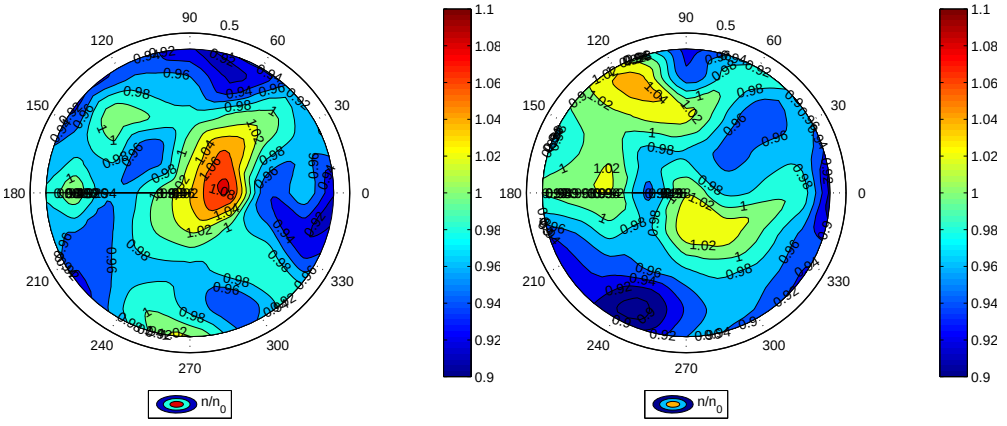

(c) layer 3 at $d_z = 0.57$ (d) layer 4 at $d_z = 0.42$

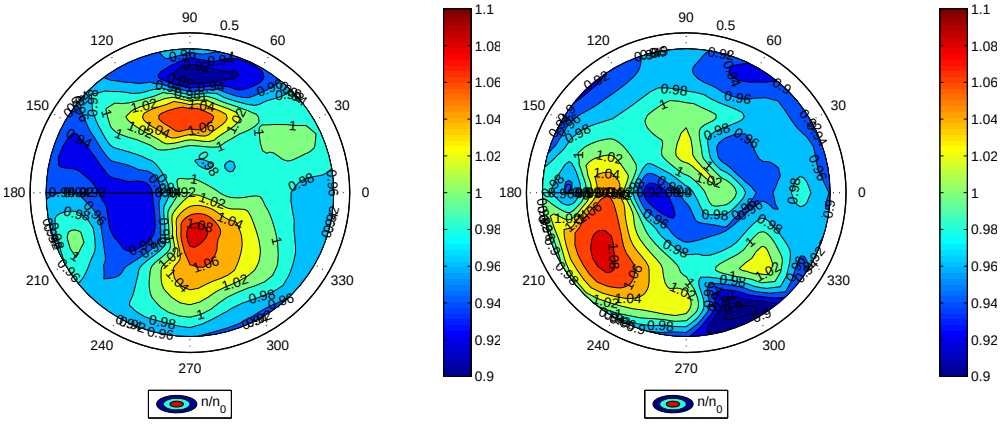

(e) layer 5 at $d_z = 0.28$ (f) layer 6 at $d_z = 0.14$

Figure 98: Contour plot of normalized porosity ($\frac{n}{n_0}$) measured at initial stage for medium–dense isotropically compressed specimen–T16 ($\sigma_z = \sigma_h = 100$kPa and $D_R = 75\%$)

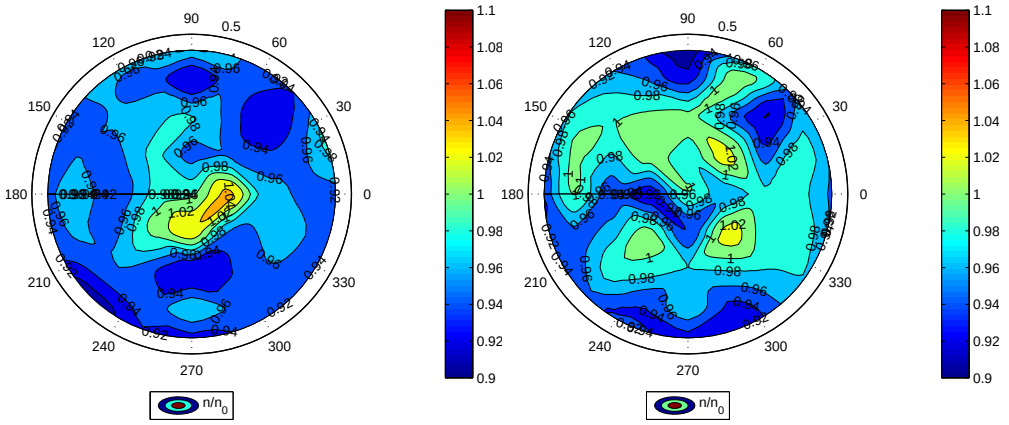

(a) layer 1 at $d_z = 0.85$ (b) layer 2 at $d_z = 0.71$

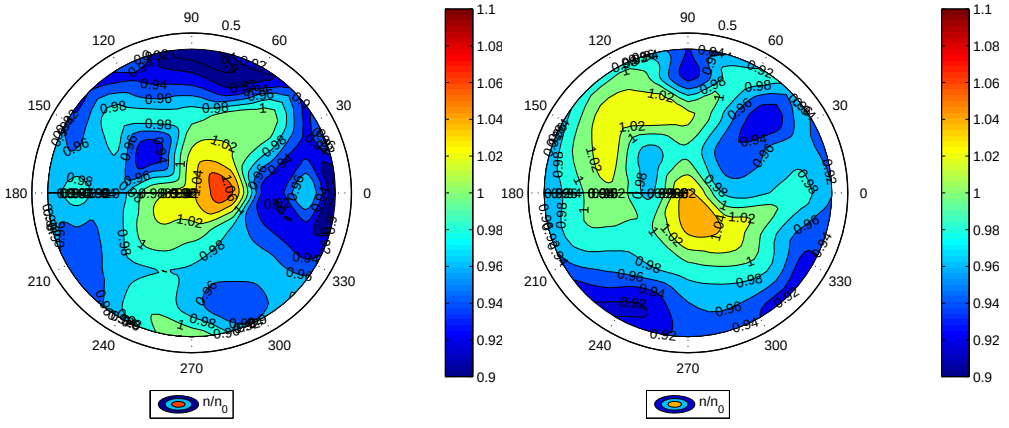

(c) layer 3 at $d_z = 0.57$ (d) layer 4 at $d_z = 0.42$

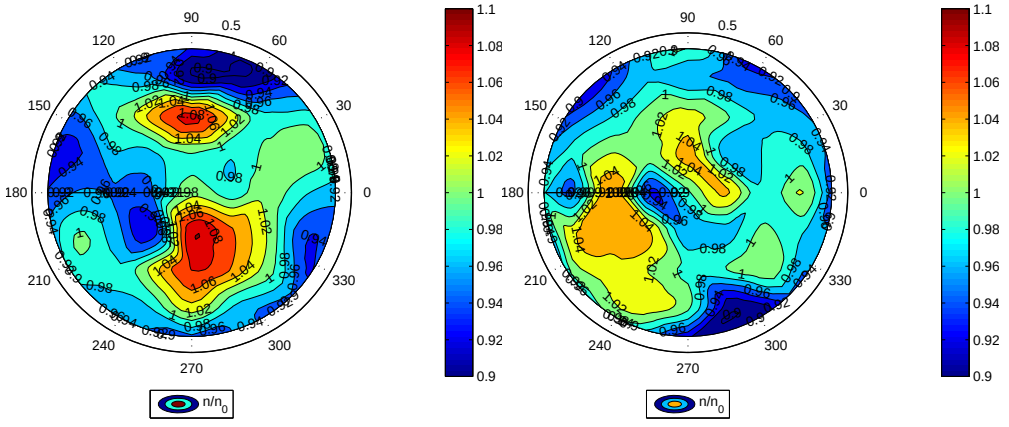

(e) layer 5 at $d_z = 0.28$ (f) layer 6 at $d_z = 0.14$

Figure 99: Contour plot of normalized porosity ($\frac{n}{n_0}$) measured at initial stage for dense isotropically compressed specimen–T20 ($\sigma_z = \sigma_h = 100$kPa and $D_R = 90\%$)

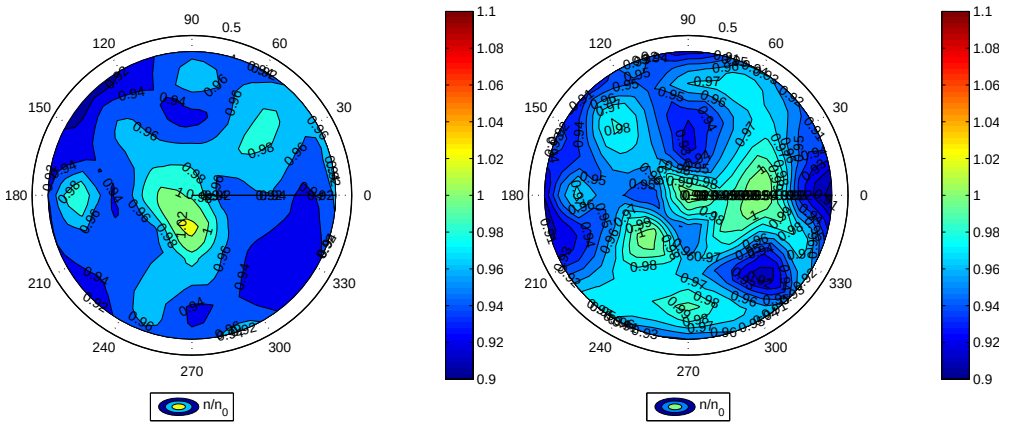

(a) layer 1 at $d_z = 0.85$ (b) layer 2 at $d_z = 0.71$

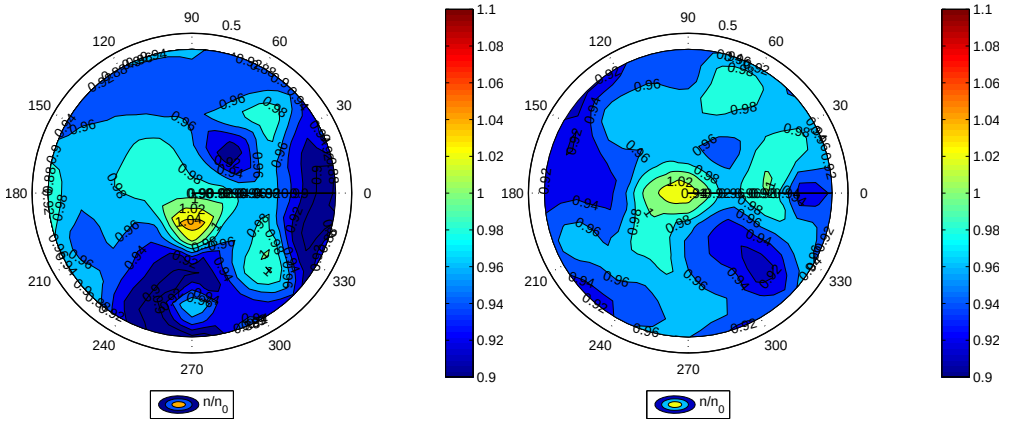

(c) layer 3 at $d_z = 0.57$ (d) layer 4 at $d_z = 0.42$

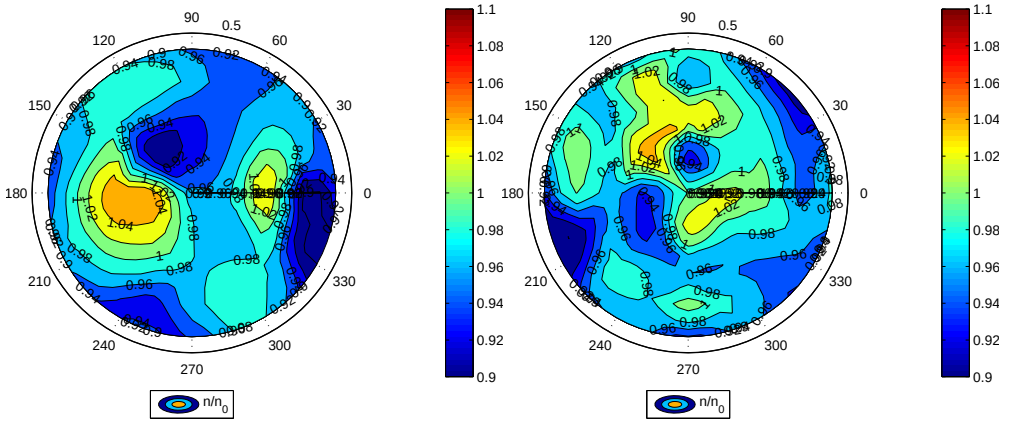

(e) layer 5 at $d_z = 0.28$ (f) layer 6 at $d_z = 0.14$

Figure 100: Contour plot of normalized porosity ($\frac{n}{n_0}$) measured at initial stage for anisotropically compressed dense specimen–T163 ($\sigma_z = 313$ kPa, $\sigma_h = 109.91$ kPa and $D_R = 93.6\%$)

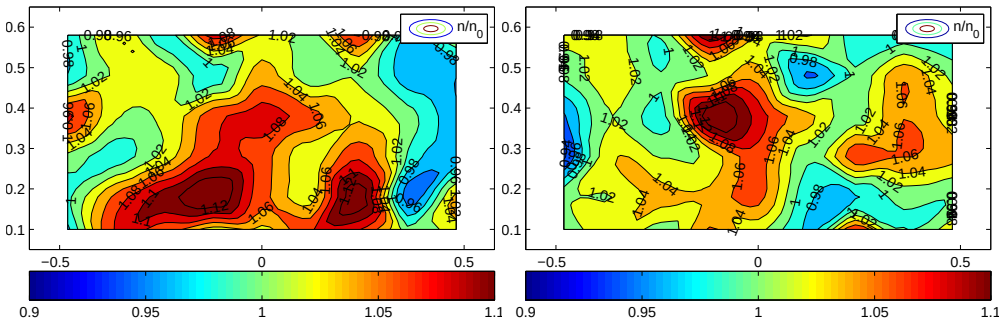

(a) T16, xz–plane, Cut 1

(b) T16, yz–plane, Cut 2

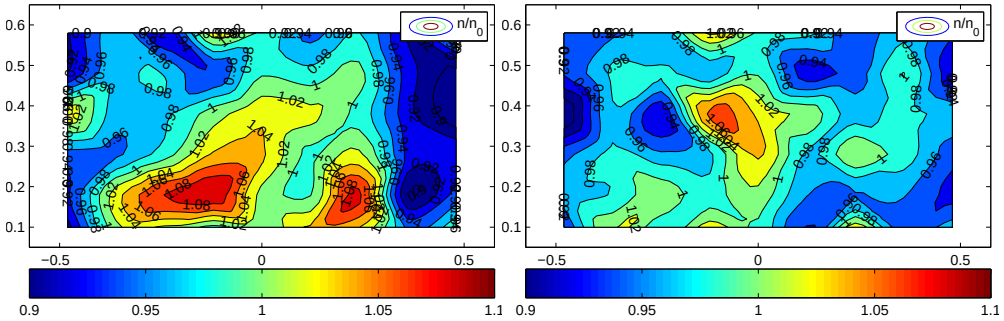

(c) T20, xz–plane, Cut 1

(d) T20, yz–plane, Cut 2

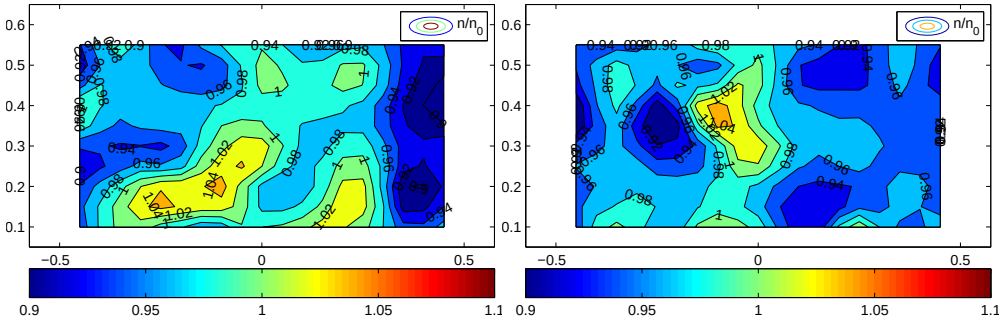

(e) T163, xz–plane, Cut 1

(f) T163, yz–plane, Cut 2

Figure 101: Contour plot of normalized porosity ($\frac{n}{n_0}$) at initial stage for isotropically compressed medium–dense (T16) and dense (T20) and anisotropically compressed dense (T163) assemblies

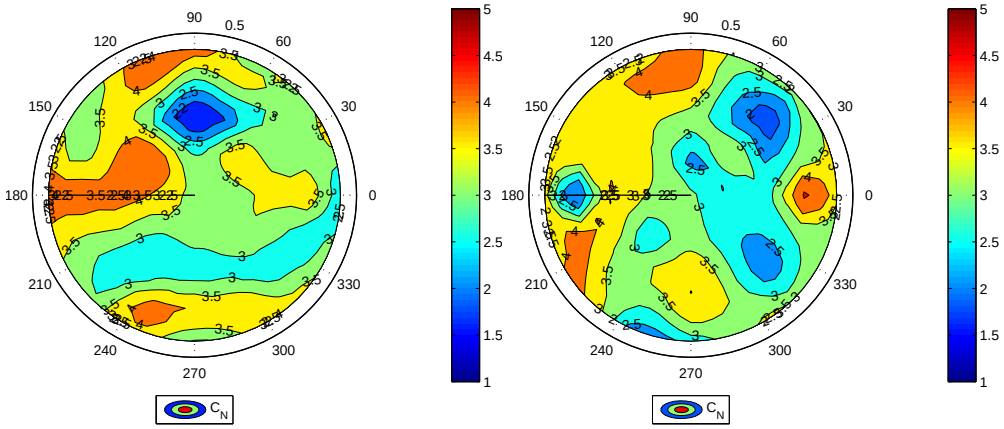

(a) layer 1 at $d_z = 0.85$ (b) layer 2 at $d_z = 0.71$

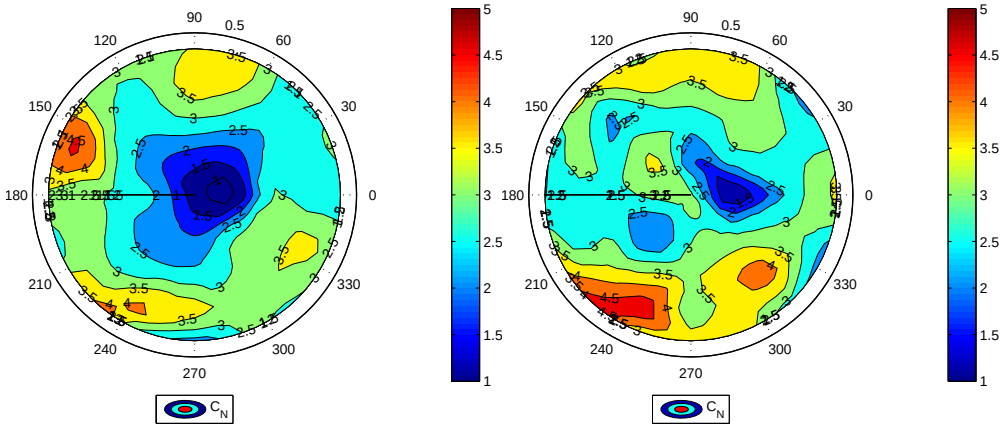

(c) layer 3 at $d_z = 0.57$ (d) layer 4 at $d_z = 0.42$

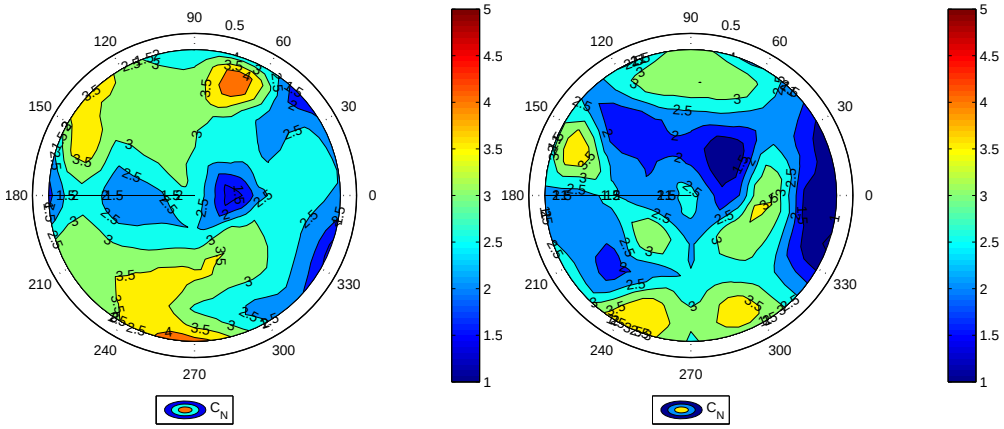

(e) layer 5 at $d_z = 0.28$ (f) layer 6 at $d_z = 0.14$

Figure 102: Contour plot of coordination number (C_N) measured at initial stage for isotropically compressed medium–dense specimen–T16 ($\sigma_z = \sigma_h = 100$kPa and $D_R = 75\%$)

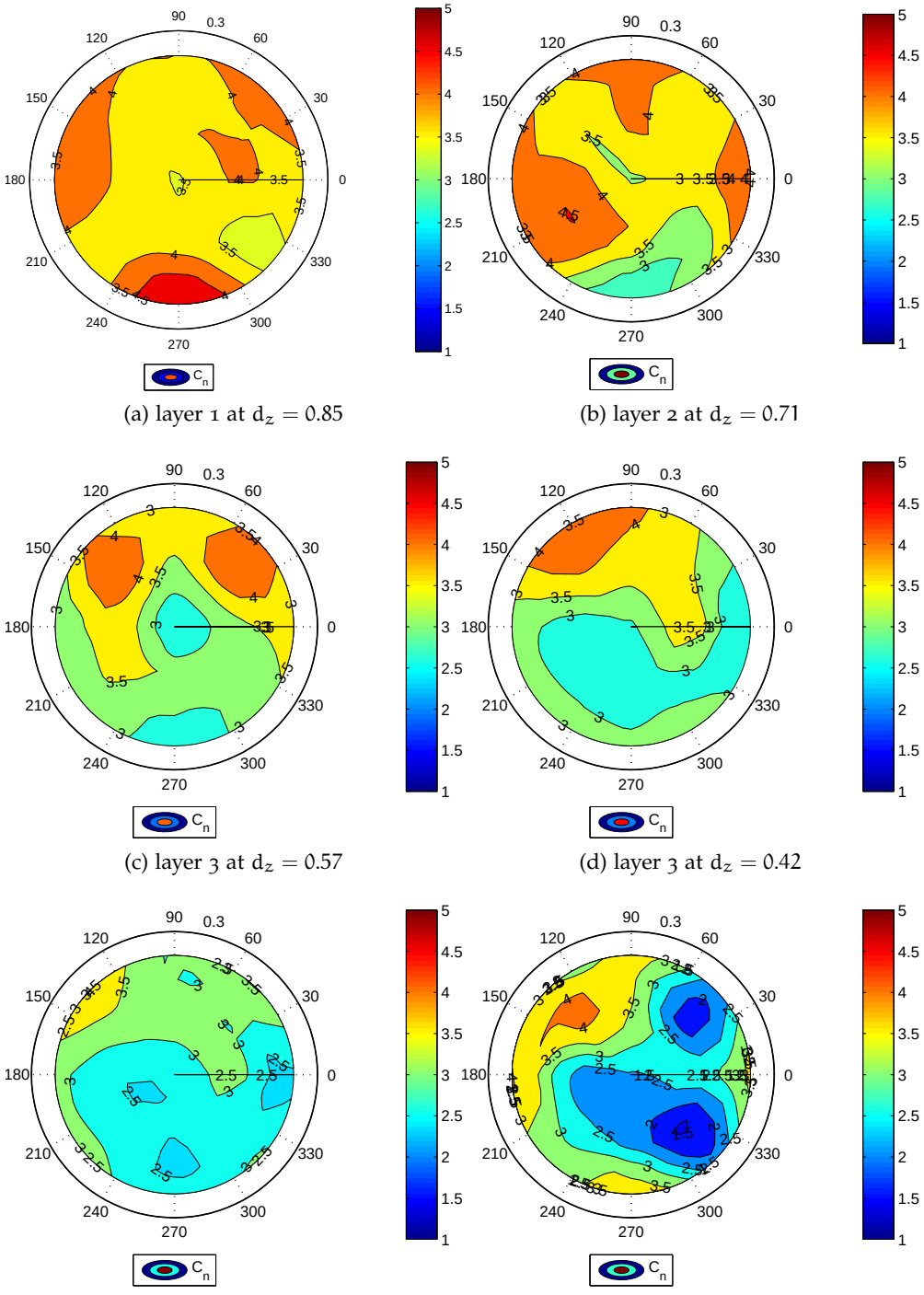

(a) layer 1 at $d_z = 0.85$

(b) layer 2 at $d_z = 0.71$

(c) layer 3 at $d_z = 0.57$

(d) layer 3 at $d_z = 0.42$

(e) layer 5 at $d_z = 0.28$

(f) layer 6 at $d_z = 0.14$

Figure 103: Contour plot of coordination number (C_N) measured at initial stage for isotropically compressed dense specimen–T20 ($\sigma_z = \sigma_h = 100$kPa and $D_R = 90\%$)

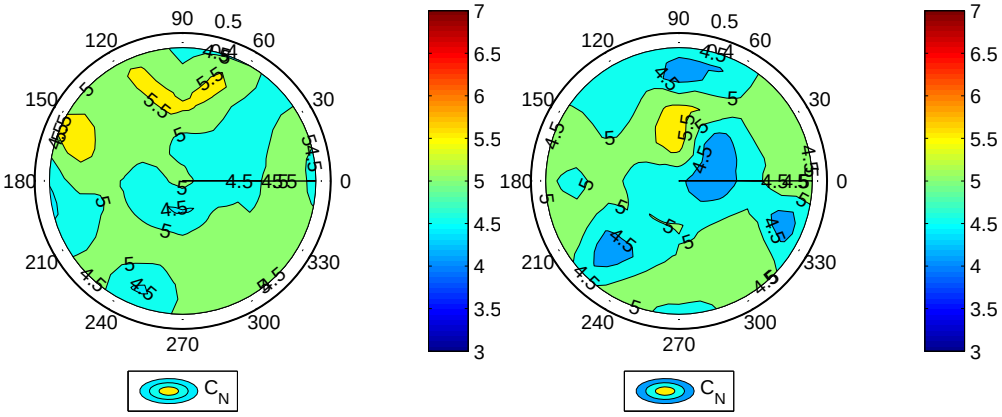

(a) layer 1 at $d_z = 0.85$ (b) layer 2 at $d_z = 0.71$

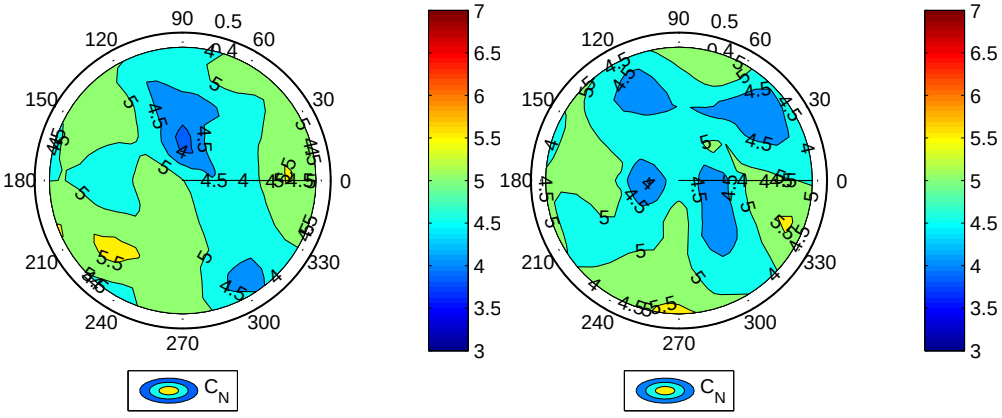

(c) layer 3 at $d_z = 0.57$ (d) layer 4 at $d_z = 0.42$

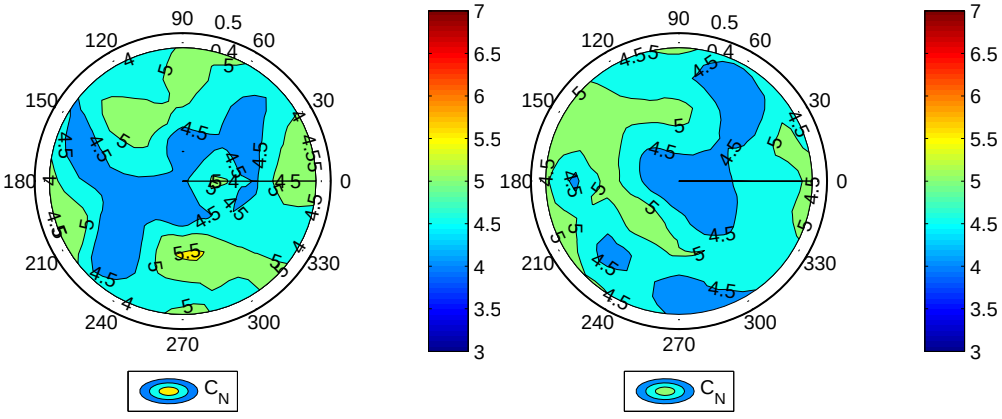

(e) layer 5 at $d_z = 0.28$ (f) layer 6 at $d_z = 0.14$

Figure 104: Contour plot of coordination number (C_N) measured at initial stage for anisotropically compressed dense specimen–T163 ($\sigma_z = 313$ kPa, $\sigma_h = 109.91$ kPa and $D_R = 93.6\%$)

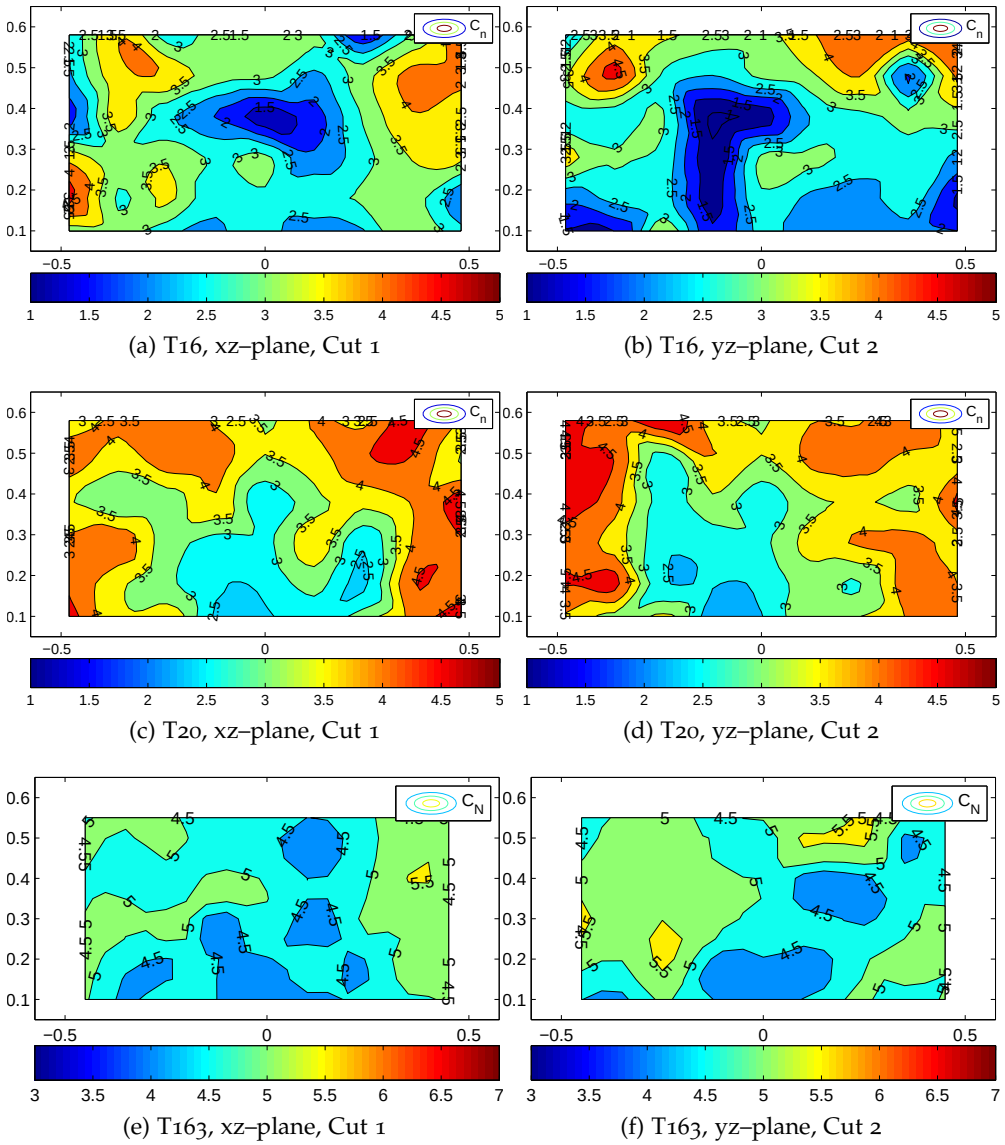

(a) T16, xz–plane, Cut 1

(b) T16, yz–plane, Cut 2

(c) T20, xz–plane, Cut 1

(d) T20, yz–plane, Cut 2

(e) T163, xz–plane, Cut 1

(f) T163, yz–plane, Cut 2

Figure 105: Contour plot of coordination number (C_N) at initial stage for isotropically compressed medium–dense (T16) and dense (T20) and anisotropically compressed dense (T163) assemblies

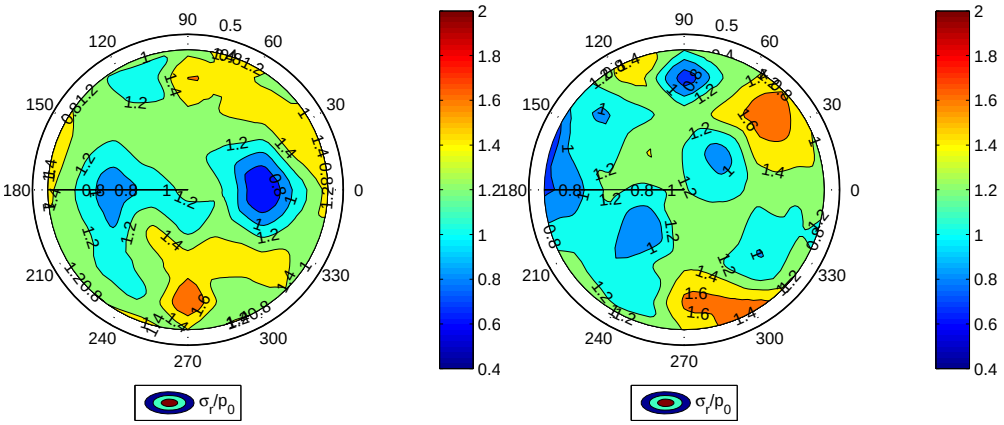

(a) layer 1 at $d_z = 0.85$ (b) layer 2 at $d_z = 0.71$

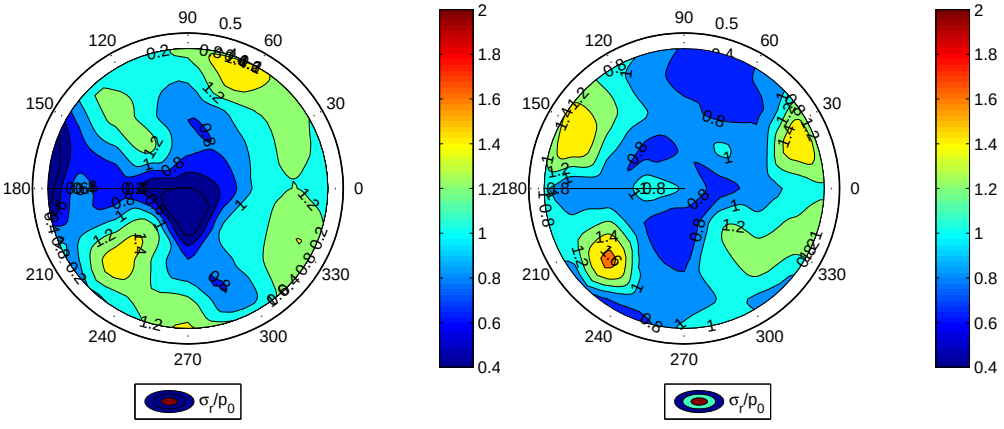

(c) layer 3 at $d_z = 0.57$ (d) layer 4 at $d_z = 0.42$

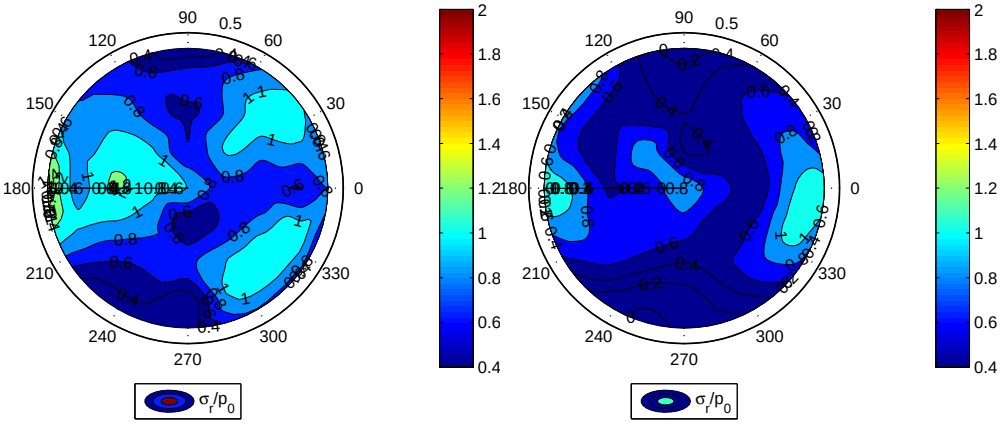

(e) layer 5 at $d_z = 0.28$ (f) layer 6 at $d_z = 0.14$

Figure 106: Contour plot of normalized radial stress ($\frac{\sigma_r}{p_0}$) measured at initial stage for isotropically compressed medium–dense specimen–T16 ($\sigma_z = \sigma_h = 100$kPa and $D_R = 75\%$)

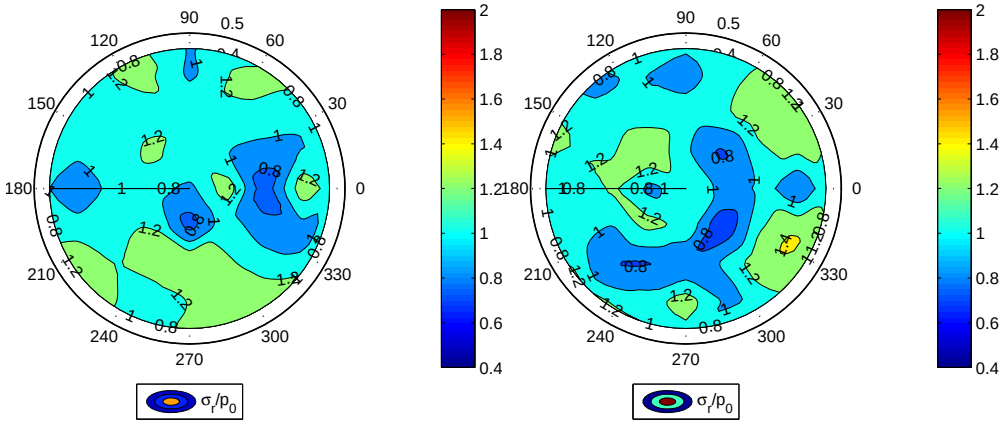

(a) layer 1 at $d_z = 0.85$ (b) layer 2 at $d_z = 0.71$

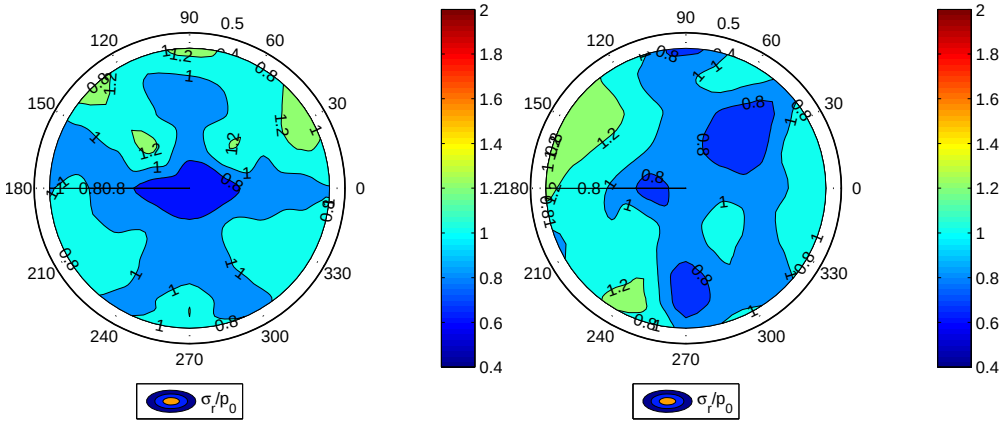

(c) layer 3 at $d_z = 0.57$ (d) layer 4 at $d_z = 0.42$

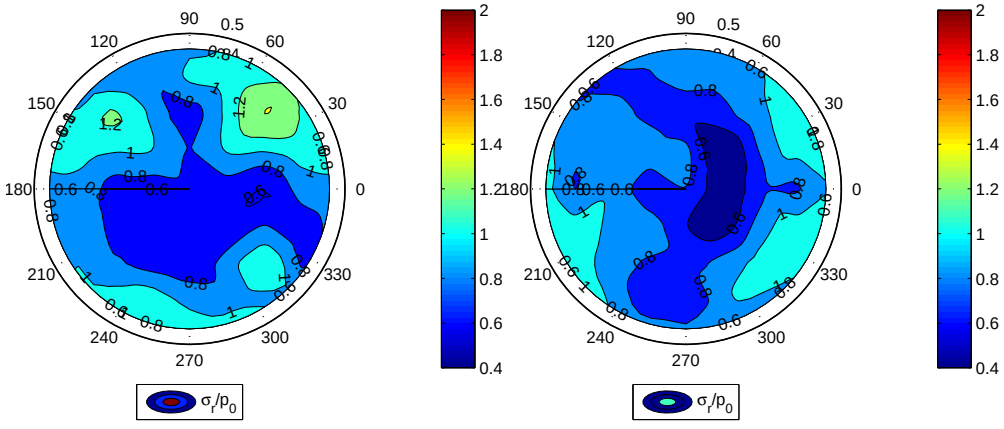

(e) layer 5 at $d_z = 0.28$ (f) layer 6 at $d_z = 0.14$

Figure 107: Contour plot of normalized radial stress ($\frac{\sigma_r}{p_0}$) measured at initial stage for isotropically compressed dense specimen–T20 ($\sigma_z = \sigma_h = 100$kPa and $D_R = 90\%$)

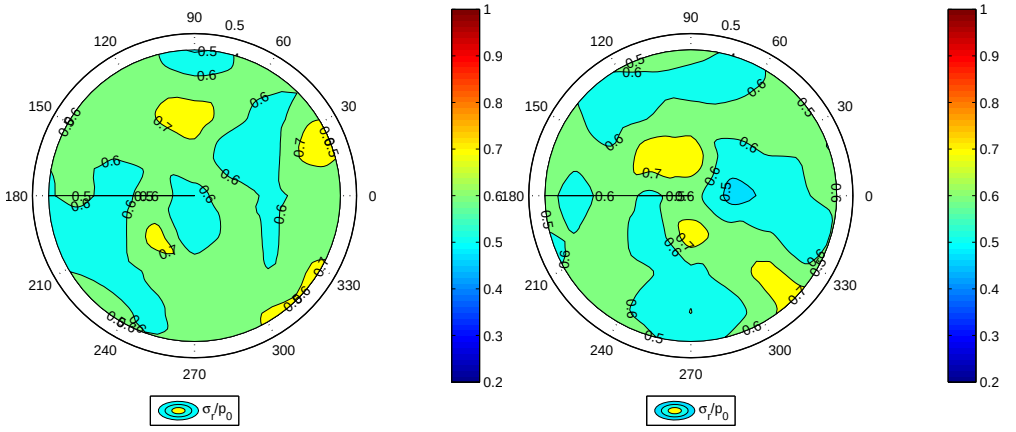

(a) layer 1 at $d_z = 0.85$ (b) layer 2 at $d_z = 0.71$

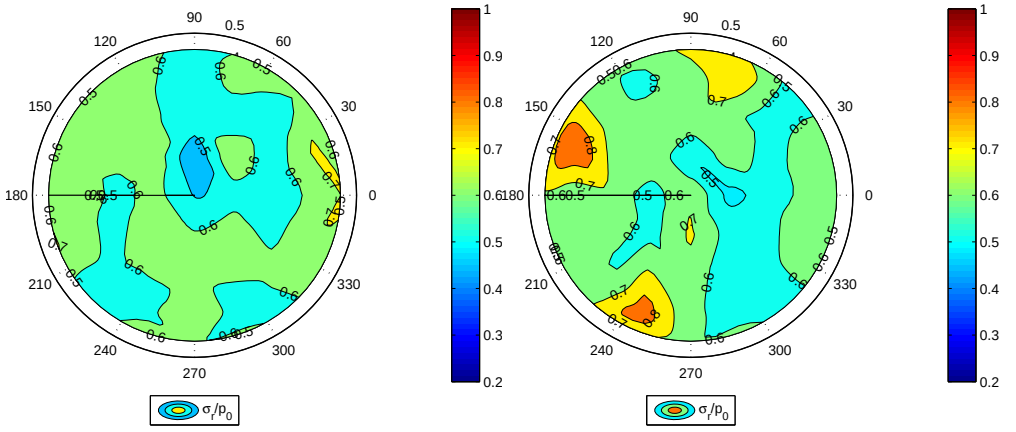

(c) layer 3 at $d_z = 0.57$ (d) layer 4 at $d_z = 0.42$

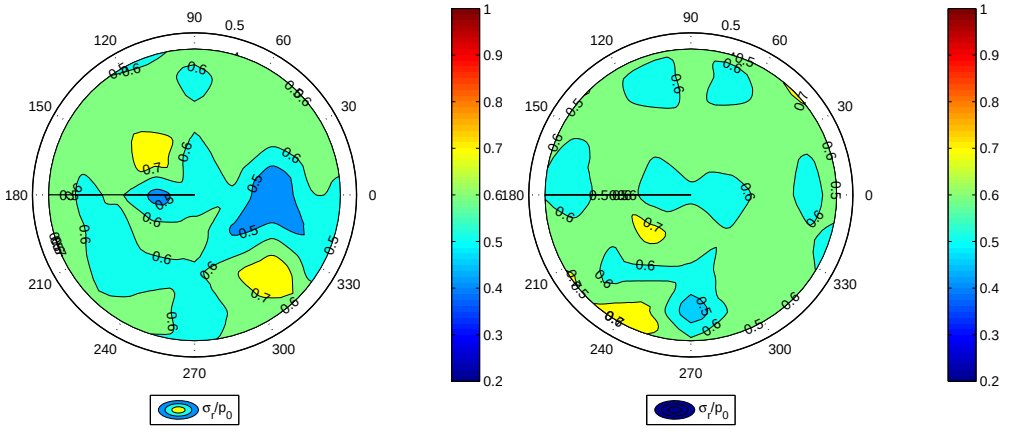

(e) layer 5 at $d_z = 0.28$ (f) layer 6 at $d_z = 0.14$

Figure 108: Contour plot of normalized radial stress ($\frac{\sigma_r}{p_0}$) measured at initial stage for anisotropically compressed dense specimen–T163 ($\sigma_z = 313$ kPa, $\sigma_h = 109.91$ kPa and $D_R = 93.6\%$)

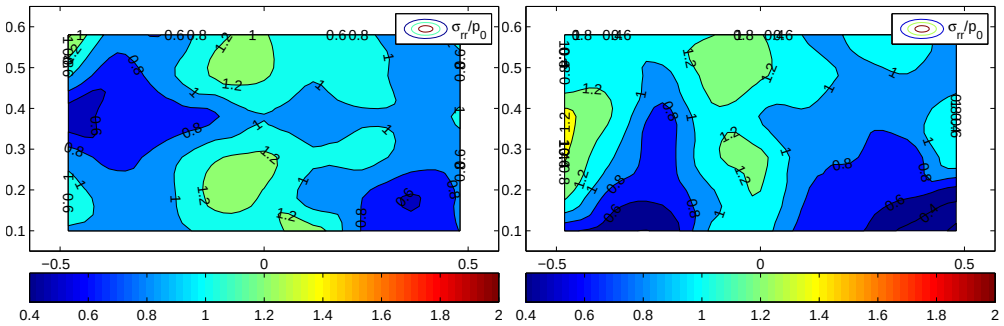

(a) T16, xz–plane, cut 1 (b) T16, yz–plane, cut 2

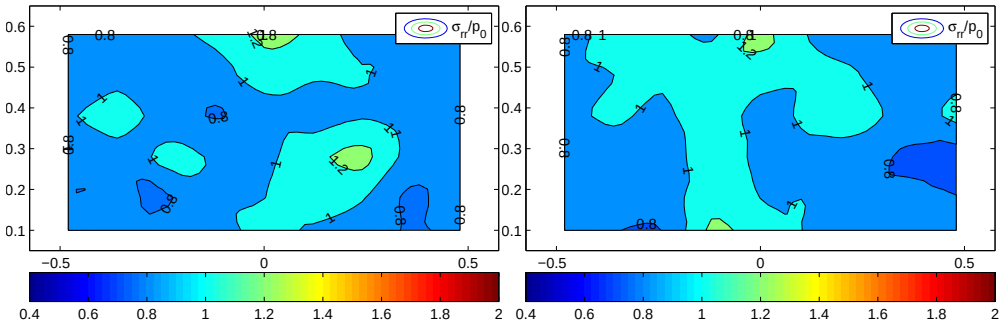

(c) T20, xz–plane, cut 1 (d) T20, yz–plane, cut 2

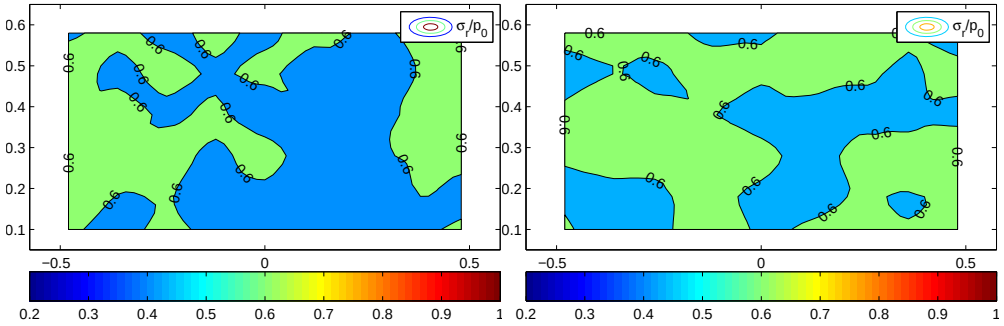

(e) T163, xz–plane, cut 1 (f) T163, yz–plane, cut 2

Figure 109: Contour plot of normalized radial stress ($\frac{\sigma_r}{p_0}$) at initial stage for isotropically compressed medium–dense (T16) and dense (T20) and anisotropically compressed dense (T163) assemblies

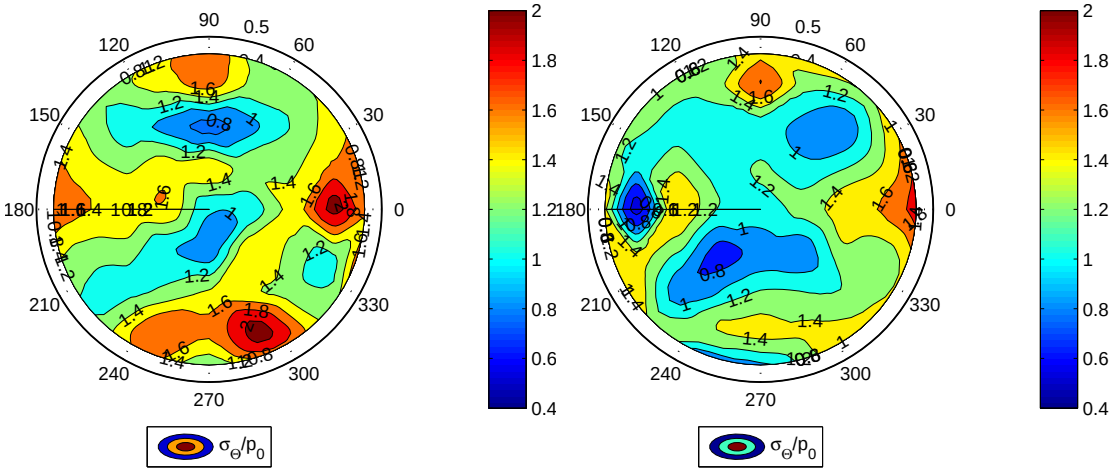

(a) layer 1 at $d_z = 0.85$ (b) layer 2 at $d_z = 0.71$

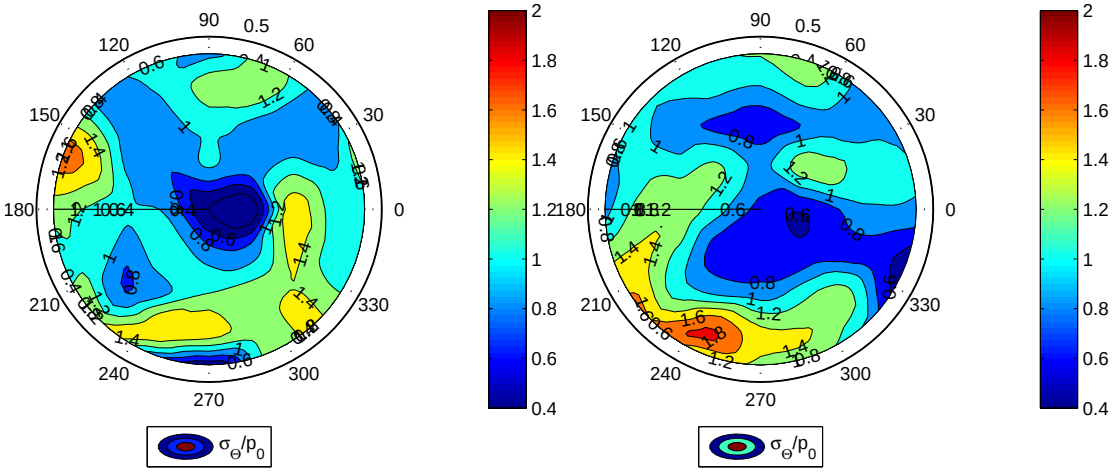

(c) layer 3 at $d_z = 0.57$ (d) layer 4 at $d_z = 0.42$

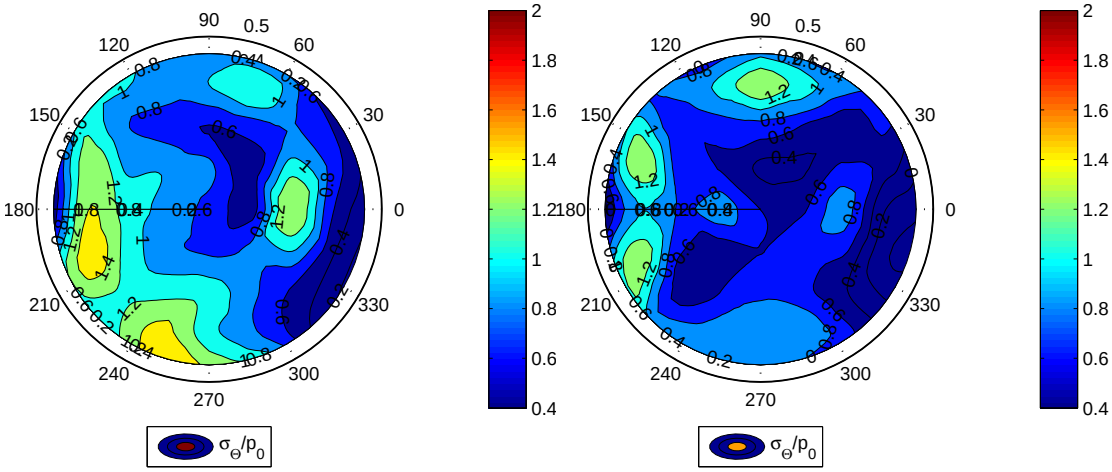

(e) layer 5 at $d_z = 0.28$ (f) layer 6 at $d_z = 0.14$

Figure 110: Contour plot of normalized circumferential stress ($\frac{\sigma_\theta}{p_0}$) measured at initial stage for isotropically compressed medium–dense specimen–T16 ($\sigma_z = \sigma_h = 100$kPa and $D_R = 75\%$)

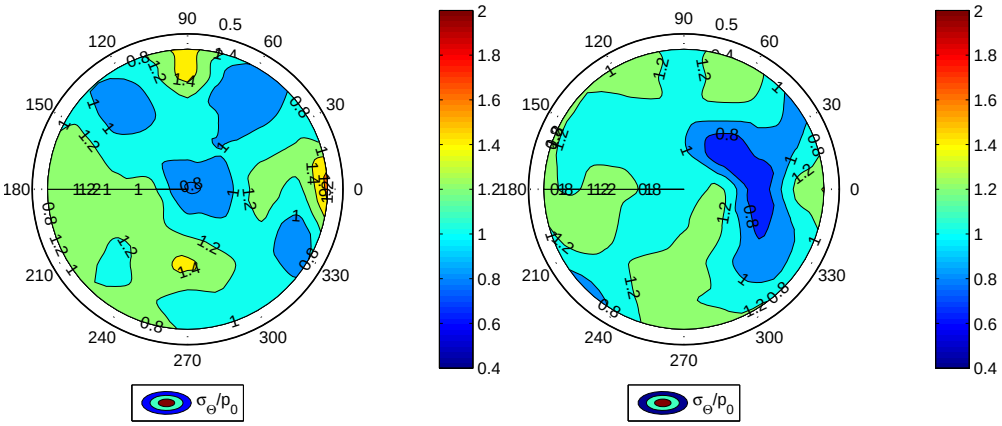

(a) layer 1 at $d_z = 0.85$ (b) layer 2 at $d_z = 0.71$

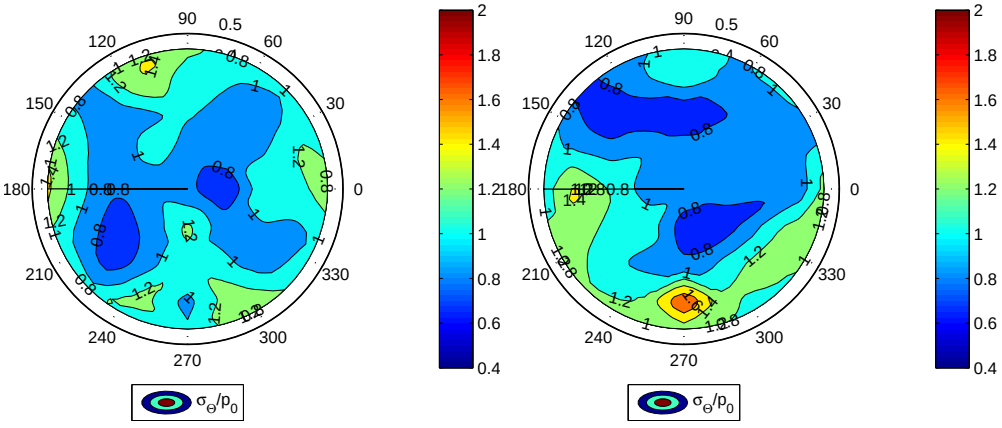

(c) layer 3 at $d_z = 0.57$ (d) layer 4 at $d_z = 0.42$

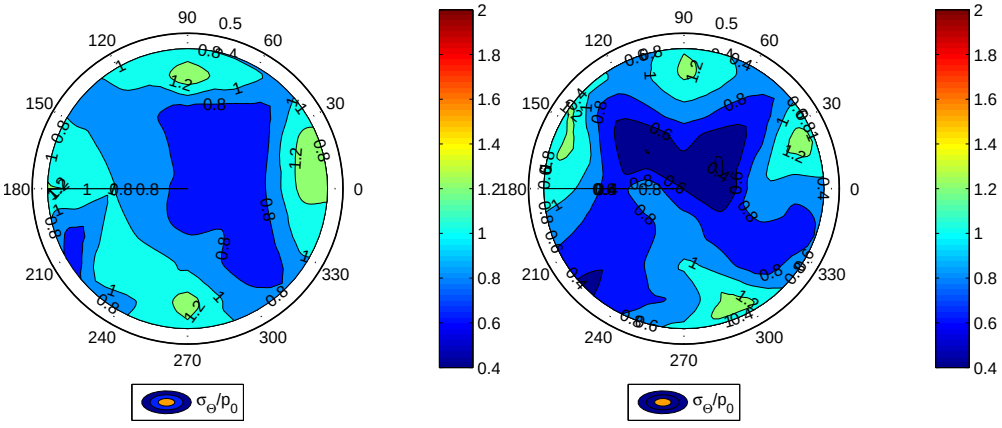

(e) layer 5 at $d_z = 0.28$ (f) layer 6 at $d_z = 0.14$

Figure 111: Contour plot of normalized circumferential stress ($\frac{\sigma_\theta}{p_0}$) measured at initial stage for isotropically compressed dense specimen–T20 ($\sigma_z = \sigma_h = 100$kPa and $D_R = 90\%$)

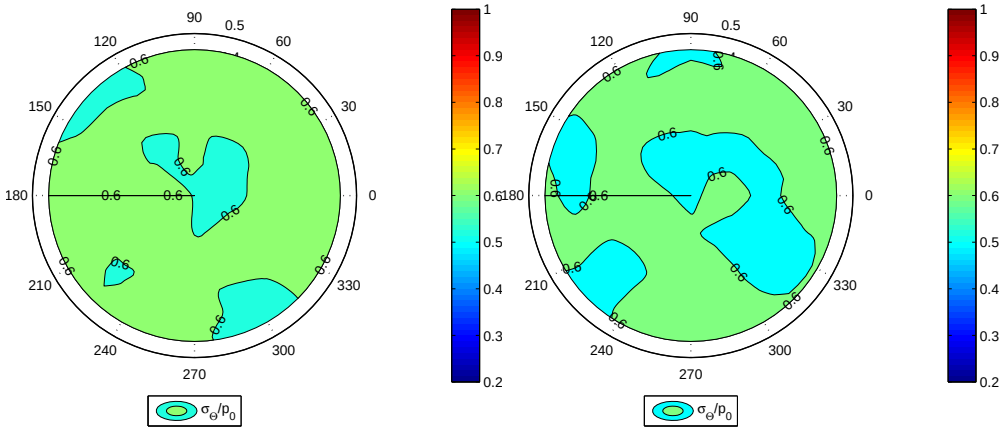

(a) layer 1 at $d_z = 0.85$ (b) layer 2 at $d_z = 0.71$

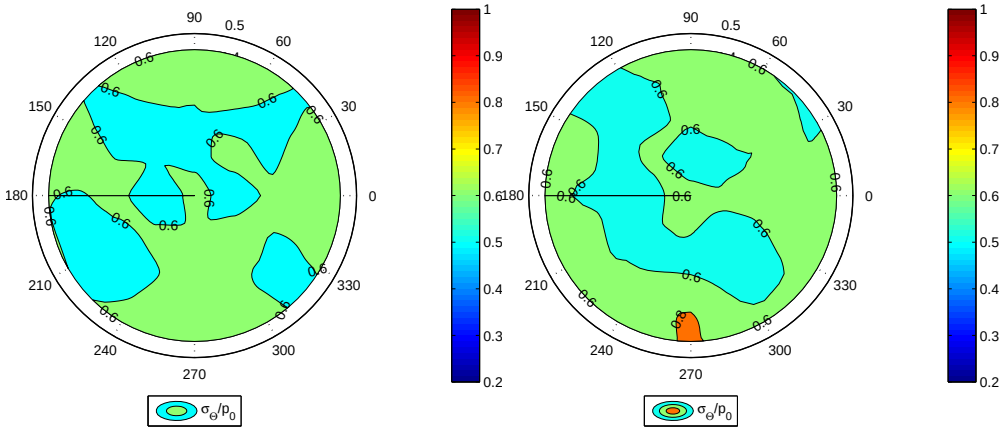

(c) layer 3 at $d_z = 0.57$ (d) layer 4 at $d_z = 0.42$

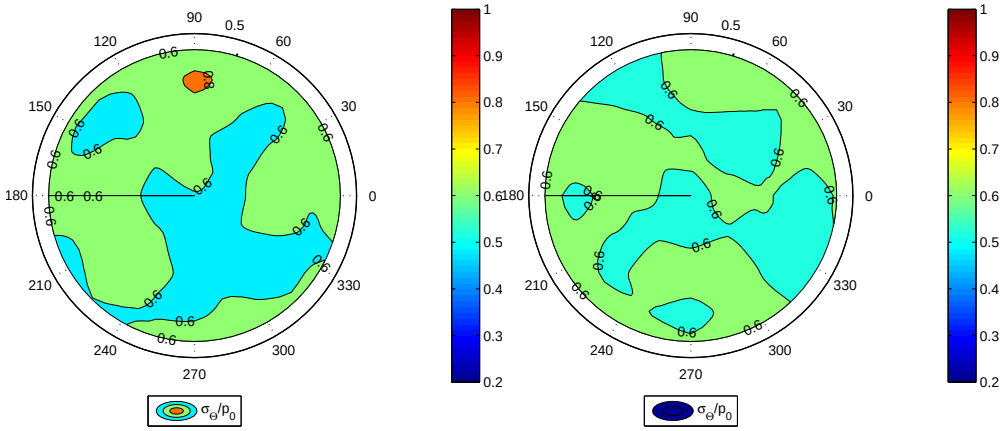

(e) layer 5 at $d_z = 0.28$ (f) layer 6 at $d_z = 0.14$

Figure 112: Contour plot of normalized circumferential stress ($\frac{\sigma_\theta}{p_0}$) measured at initial stage for anisotropically compressed dense specimen–T163 ($\sigma_z = 313$ kPa, $\sigma_h = 109.91$ kPa and $D_R = 93.6\%$)

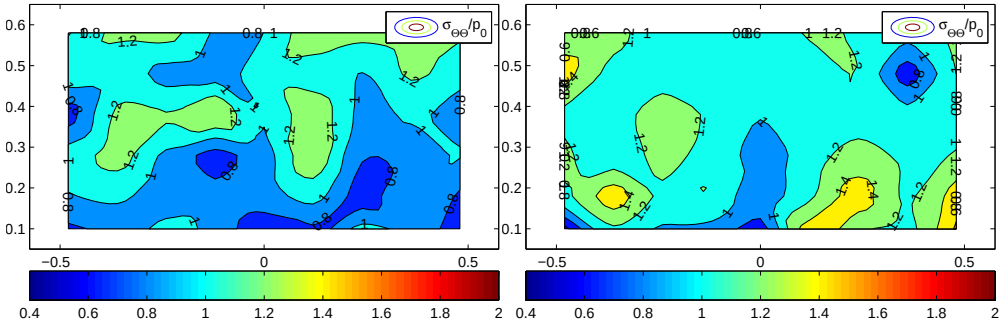

(a) T16, xz–plane, cut 1

(b) T16, yz–plane, cut 2

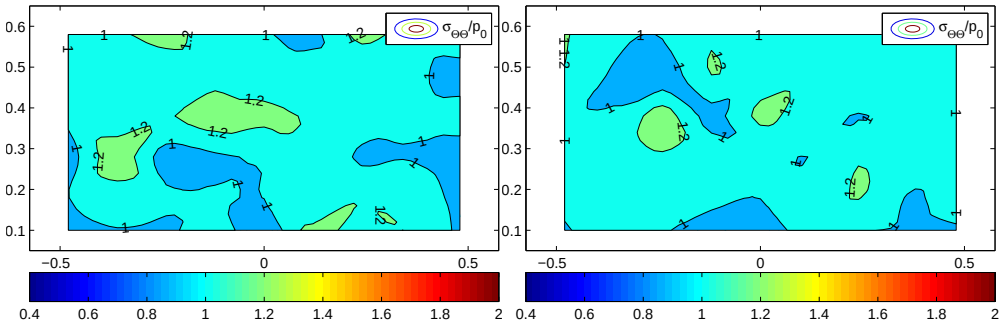

(c) T20, xz–plane, cut 1

(d) T20, yz–plane, cut 2

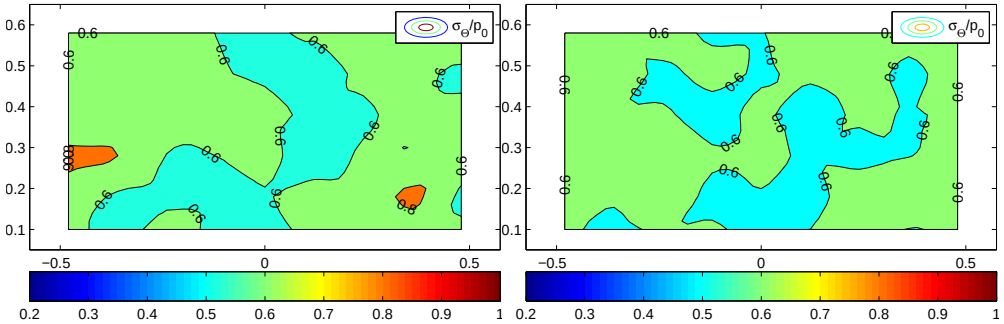

(e) T163, xz–plane, cut 1

(f) T163, yz–plane, cut 2

Figure 113: Contour plot of normalized circumferential stress ($\frac{\sigma_\theta}{p_0}$) at initial stage for isotropically compressed medium–dense (T16), dense (T20) and anisotropically compressed dense (T163) assemblies

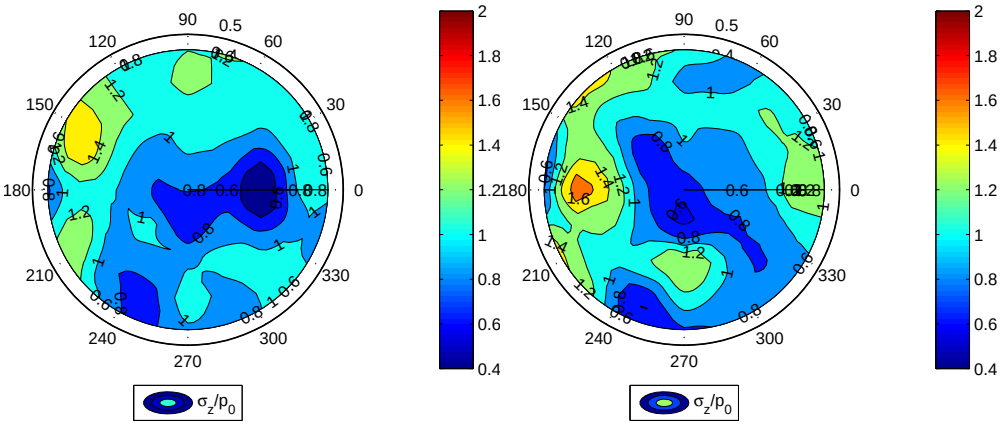

(a) layer 1 at $d_z = 0.85$ (b) layer 2 at $d_z = 0.71$

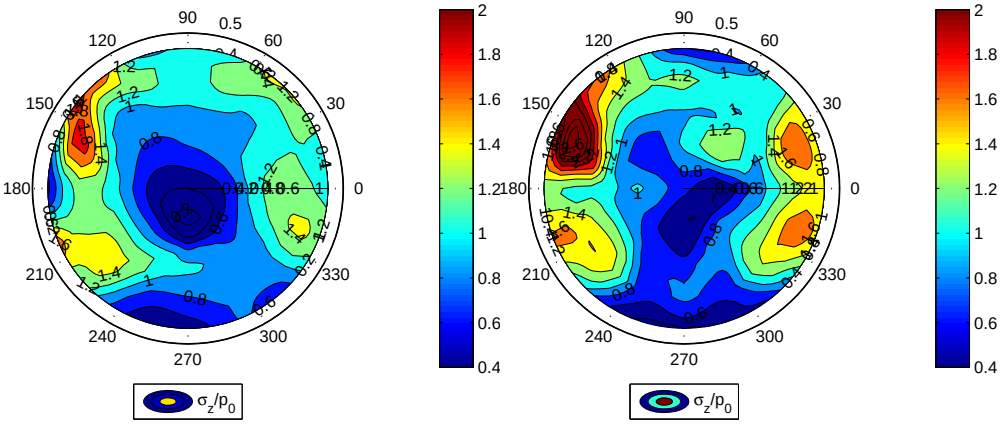

(c) layer 3 at $d_z = 0.57$ (d) layer 4 at $d_z = 0.42$

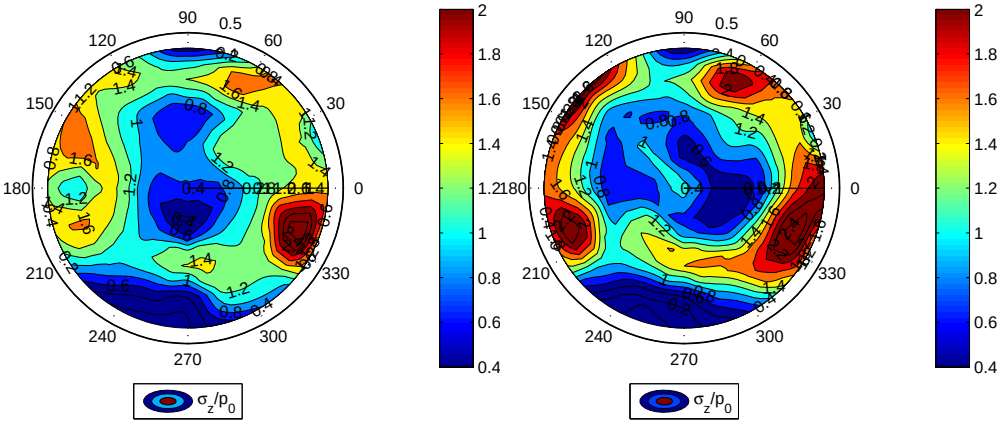

(e) layer 5 at $d_z = 0.28$ (f) layer 6 at $d_z = 0.14$

Figure 114: Contour plot of normalized vertical stress ($\frac{\sigma_z}{p_0}$) measured at initial stage for isotropically compressed medium–dense specimen–T16 ($\sigma_z = \sigma_h = 100$kPa and $D_R = 75\%$)

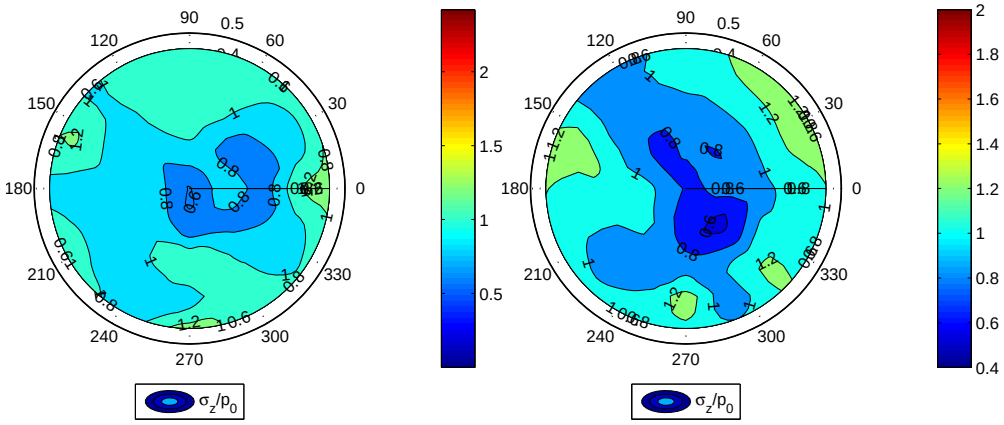

(a) layer 1 at $d_z = 0.85$ (b) layer 2 at $d_z = 0.71$

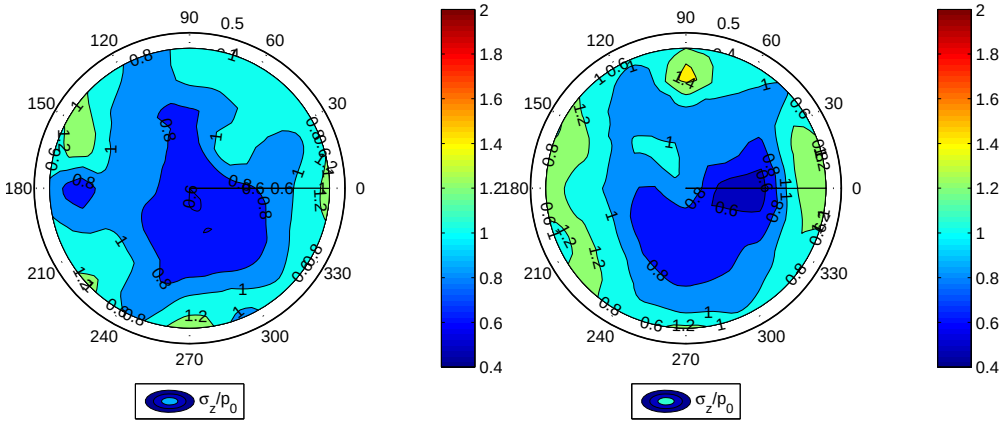

(c) layer 3 at $d_z = 0.57$ (d) layer 4 at $d_z = 0.42$

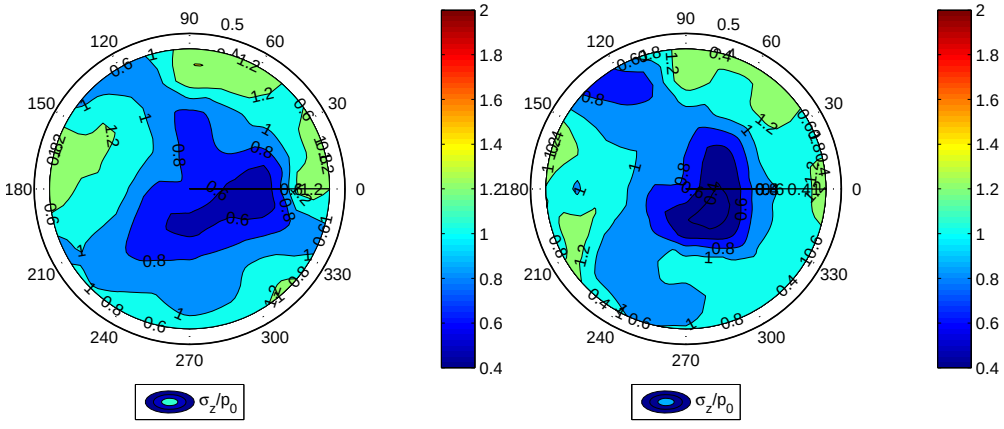

(e) layer 5 at $d_z = 0.28$ (f) layer 6 at $d_z = 0.14$

Figure 115: Contour plot of normalized vertical stress ($\frac{\sigma_z}{p_0}$) measured at initial stage for isotropically compressed dense specimen–T20 ($\sigma_z = \sigma_h = 100$kPa and $D_R = 90\%$)

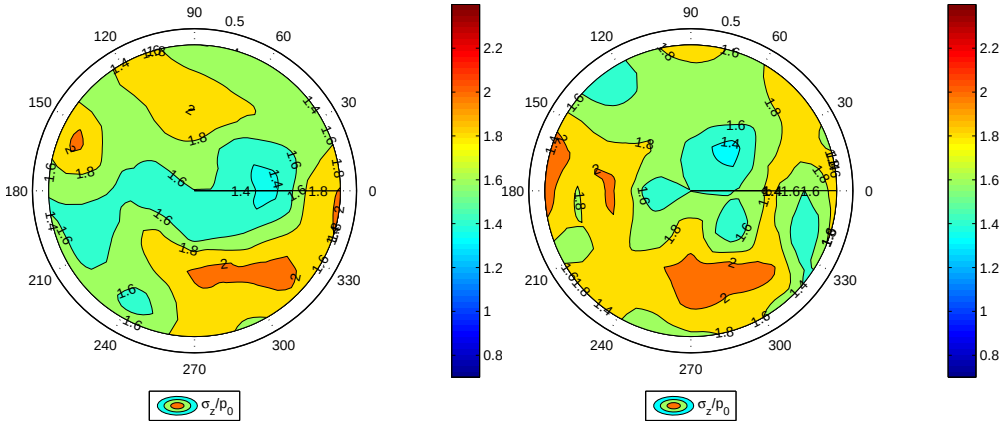

(a) layer 1 at $d_z = 0.85$ (b) layer 2 at $d_z = 0.71$

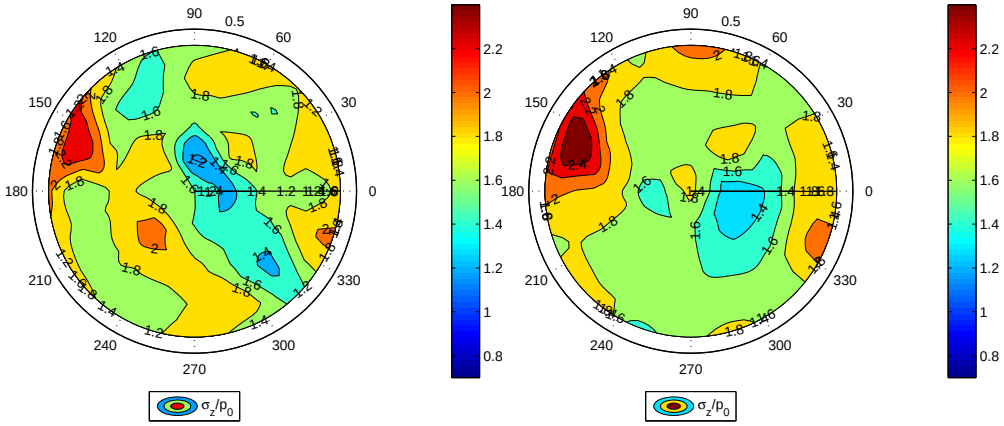

(c) layer 3 at $d_z = 0.57$ (d) layer 4 at $d_z = 0.42$

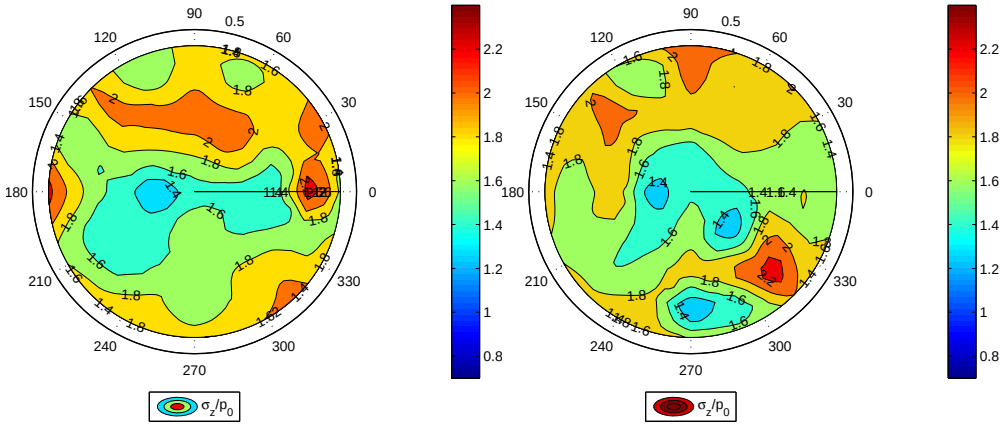

(e) layer 5 at $d_z = 0.28$ (f) layer 6 at $d_z = 0.14$

Figure 116: Contour plot of normalized vertical stress ($\frac{\sigma_z}{p_0}$) measured at initial stage for anisotropically compressed dense specimen–T163 ($\sigma_z = 313$ kPa, $\sigma_h = 109.91$ kPa and $D_R = 93.6\%$)

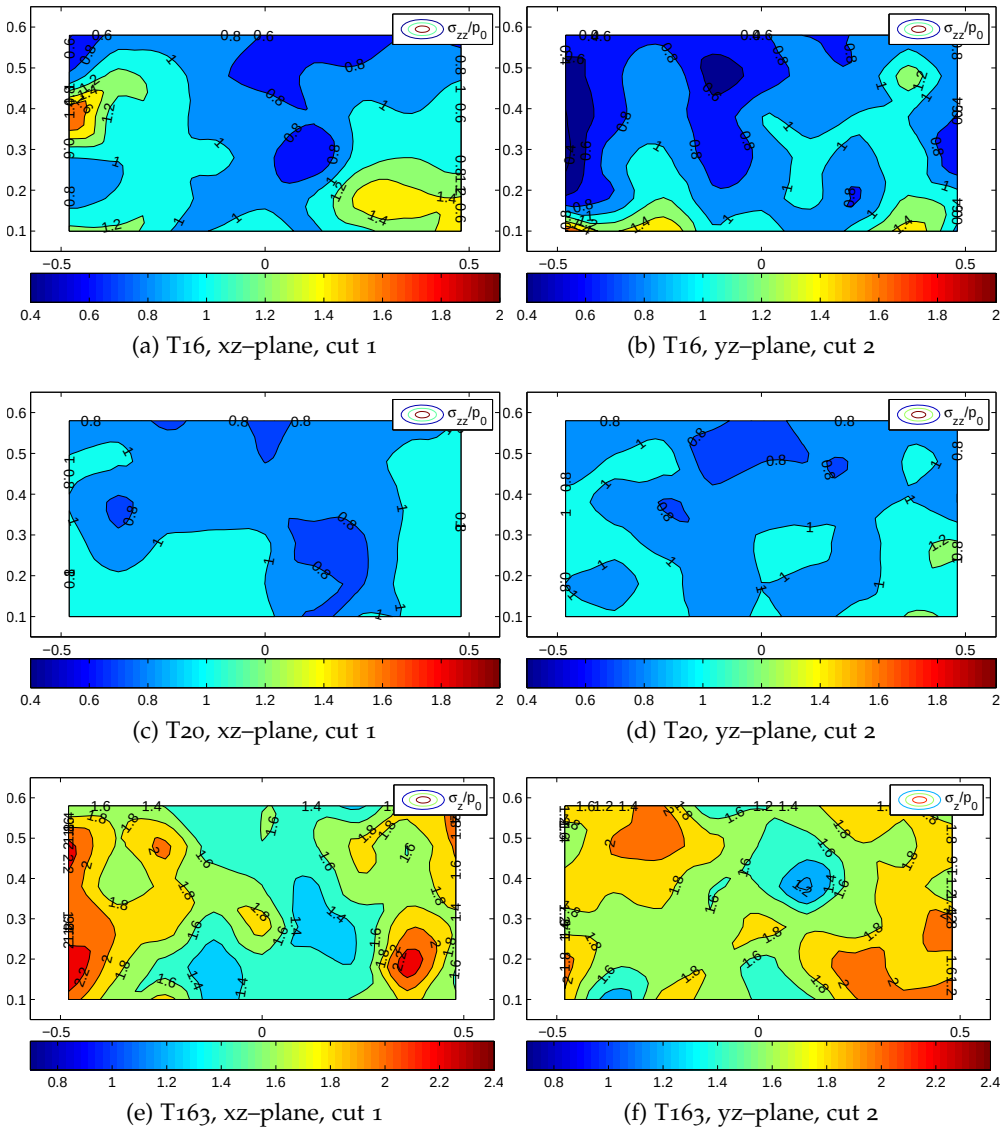

(a) T16, xz–plane, cut 1

(b) T16, yz–plane, cut 2

(c) T20, xz–plane, cut 1

(d) T20, yz–plane, cut 2

(e) T163, xz–plane, cut 1

(f) T163, yz–plane, cut 2

Figure 117: Contour plot of normalized vertical stress ($\frac{\sigma_z}{p_0}$) at initial stage for isotropically compressed medium–dense (T16) and dense (T20) and anisotropically compressed dense (T163) assemblies

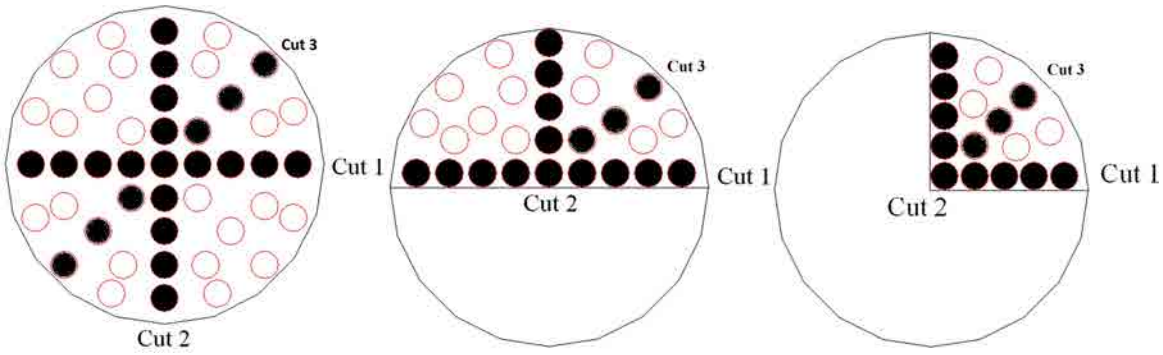

(a) xz–plane, Cut 1 (b) yz–plane, Cut 2 (c) rθ–plane, Cut 3

Figure 118: Planes (cuts) analyzed

6.3 EXAMINING SYMMETRY

The effect of rigid–wall enforced symmetry of the specimens was examined by analyzing ($\frac{n_{MS}}{n_0}$),(C_N) and $\frac{\sigma_{ii}}{p_0}$ for three cases with different horizontal section (full circle, half and quarter) but prepared at the same initial relative density (D_R = 75%) and stress state (p_0=100 kPa). Table 18 lists the tests included in this study. The analysis, similar to homogeneity study, was performed in three stages: (i) contact force network examination, (ii) distribution of MS–based mesoscopic variables within the specimen and (iii) contour plot analysis. To simplify the analysis and hence to reduce number of figures, only one horizontal layer with $d_z = 0.57$ (Layer 3) was chosen for examination. This layer is far from the top and the bottom walls hence, it is presumably less influenced by them. All planes (Cuts) analyzed in this study are shown in Figure 118.

6.3.1 *Contact force network, contact normal orientation and normal force magnitude*

Figures 119 and 120 present the contact force networks developed after isotropic compression in layer 3 for full (T16), half (T32) and quarter (T34) of VCC. It can be observed that in xy–plane half and quarter chamber models seem to be more homogeneous than the full VCC. While comparing distribution of contact force networks in xz–and yz–planes (Figure 120) we observe loose zones close to the fixed (not servo–controlled) walls, i.e. (i) those enforcing model symmetry and (ii) the bottom wall. It must be pointed out that only contact forces larger than $\overline{F}+2\sigma$[1] are shown in the figures.

The only difference in contact normal orientation is the maximum number of contacts in a given direction. Hence, in full chamber the maximum number of contact observed is of 24, in half chamber–14 and in the quarter of chamber–10. This is shown in Figure 121. In all chambers there are no preferred directions. Histograms of the contact normal and shear force magnitudes are shown in Figure 122 and Figure 123 respectvely. It can be observed a similar fabric ellipsoid that has a spherical symmetry. The contact force seems to be similar in all three cases. However, in the half and quarter of VCC some peak forces are observed.

1 σ is a standard deviation

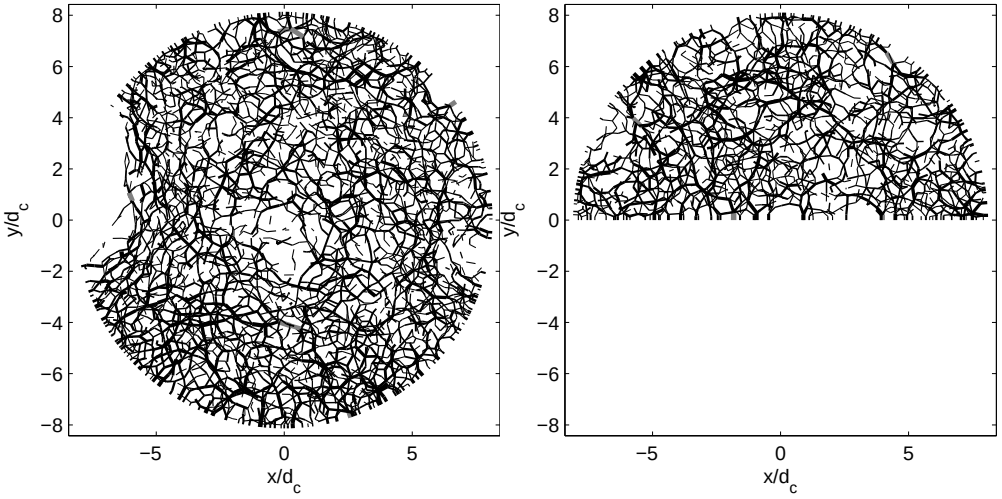

(a) full VCC, xy–plane, T16

(b) half VCC, xy–plane, T32

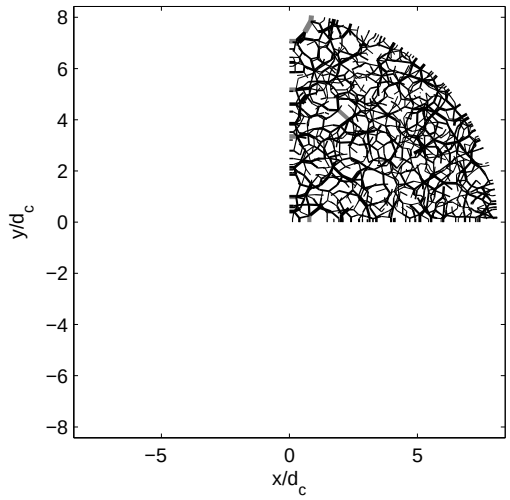

(c) quarter VCC, xy–plane, T34

Figure 119: Contact force network for layer 3 (d_z = 0.57) and D_R=75%

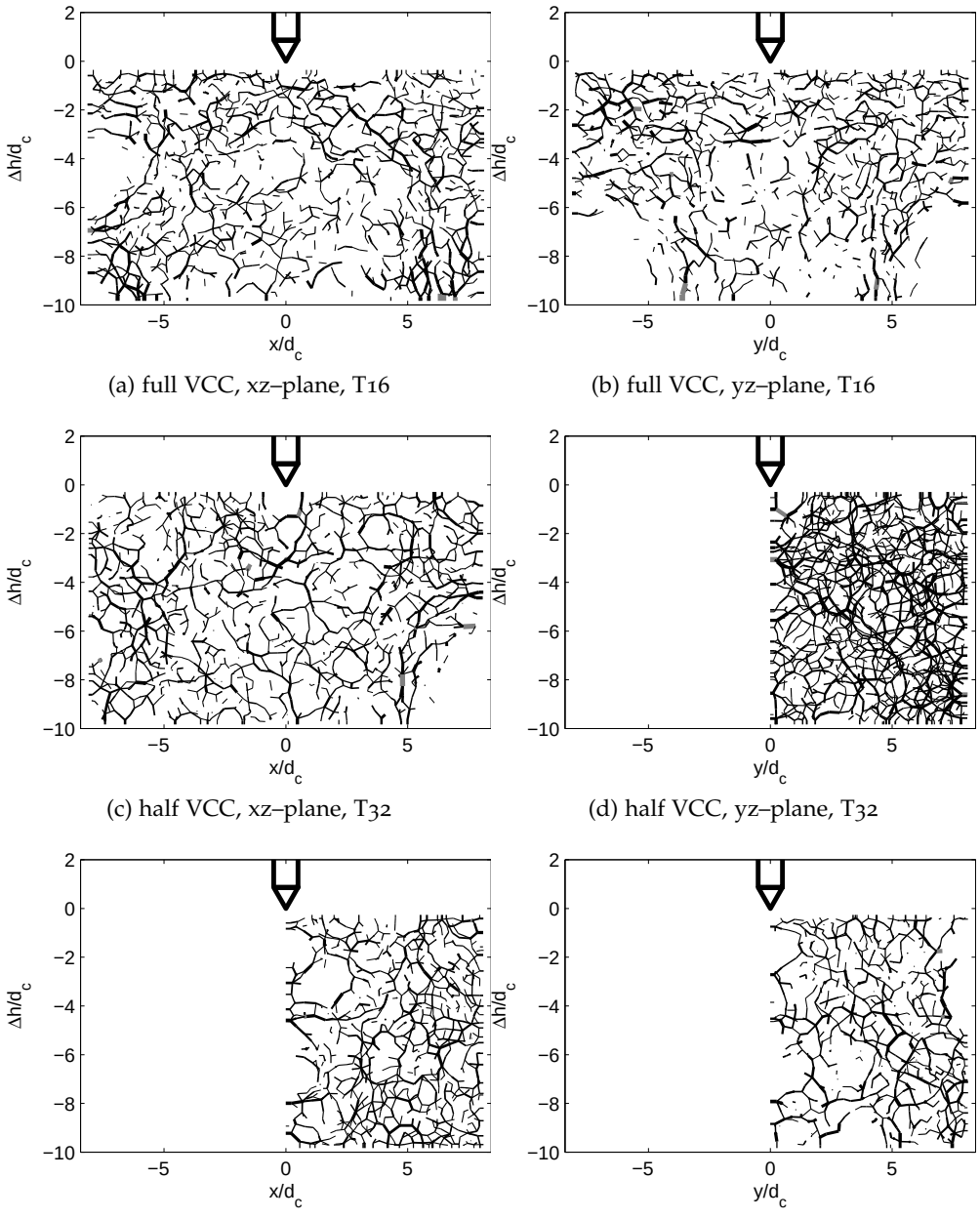

(a) full VCC, xz–plane, T16

(b) full VCC, yz–plane, T16

(c) half VCC, xz–plane, T32

(d) half VCC, yz–plane, T32

(e) quarter VCC, xz–plane, T34

(f) quarter VCC, yz–plane, T34

Figure 120: Contact force network in xz– and yz–plane and assemblies with D_R=75%

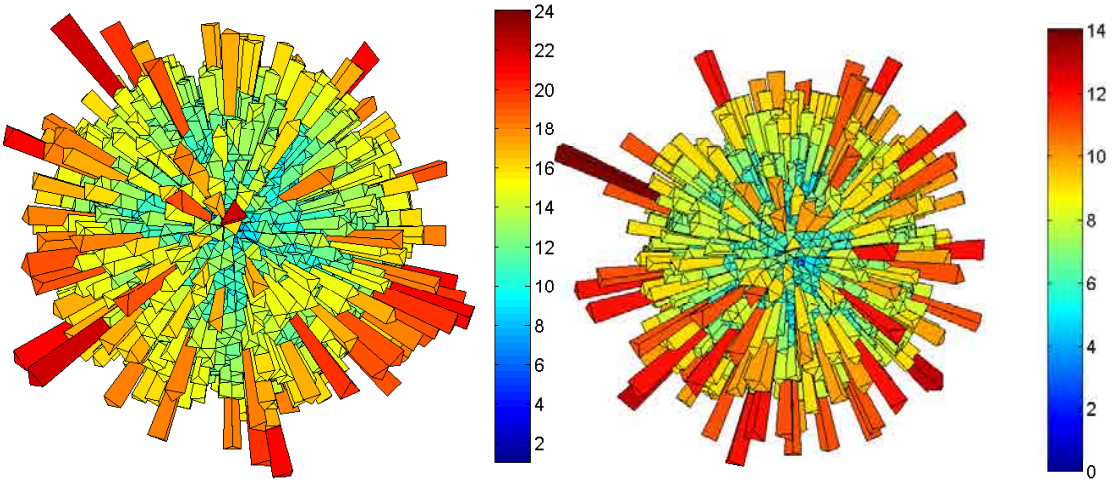

(a) full VCC, T16

(b) half VCC, T32

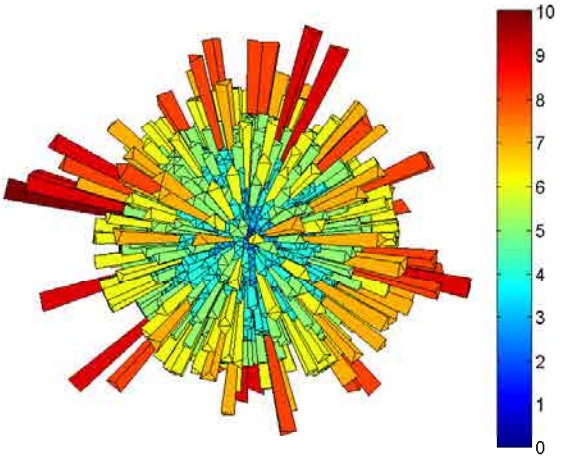

(c) quarter VCC, T34

Figure 121: Contact orientation for (a) T16, F–AreaFactor=1, (b) T32, H–AreaFactor=0.5 and (b) T34, Q–AreaFactor=0.25

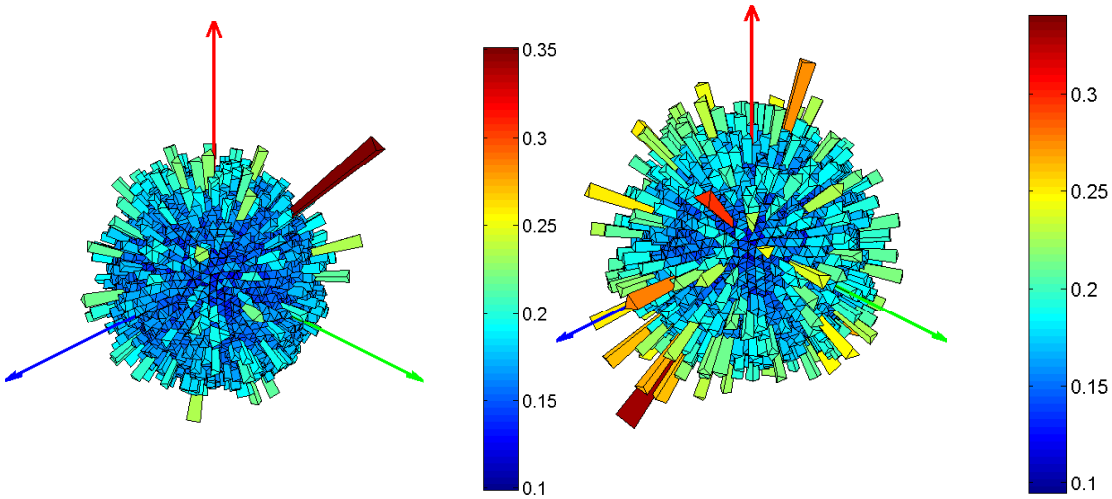

(a) full VCC, T16

(b) half VCC, T32

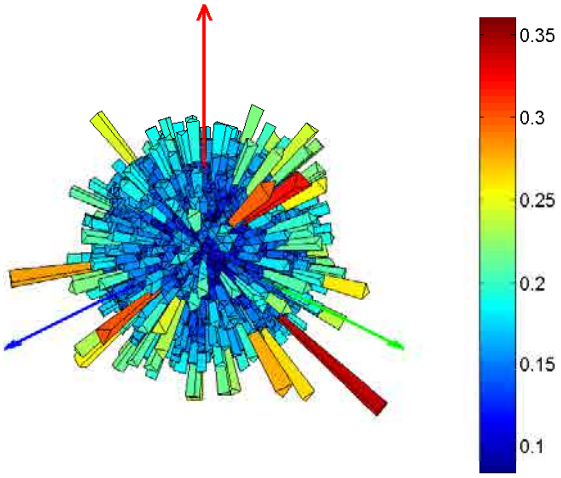

(c) quarter VCC, T34

Figure 122: Histograms of the contact normal force magnitude in (a) full chamber–model (T16), (b) half chamber–model (T32) and (c) quarter chamber–model (T34)

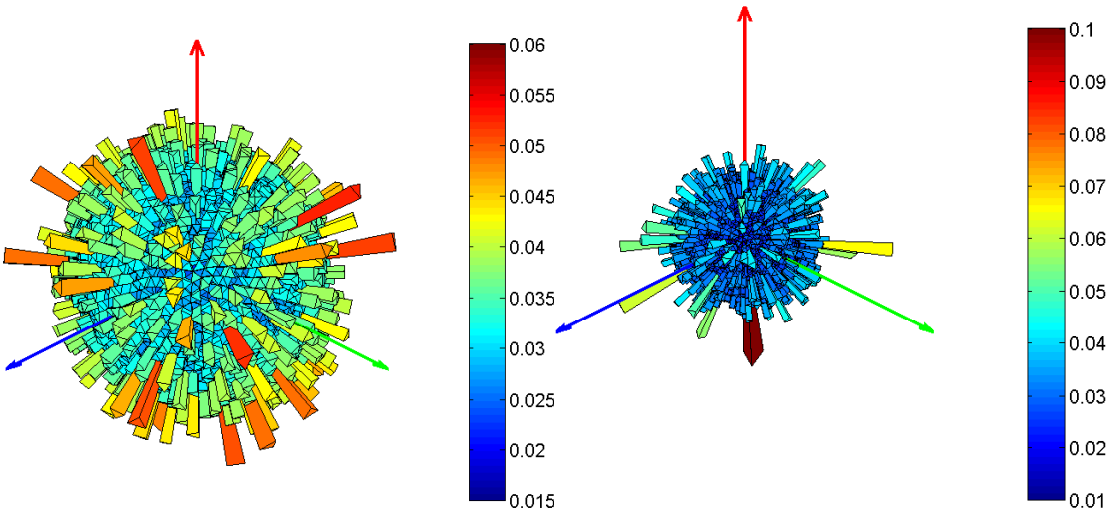

(a) full VCC, T16

(b) half VCC, T32

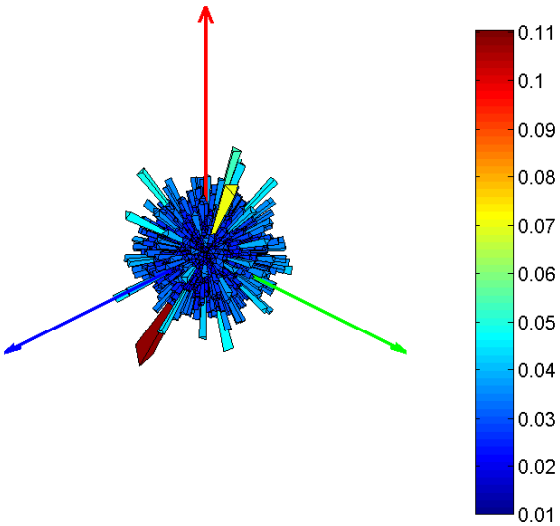

(c) quarter VCC, T34

Figure 123: Histograms of the contact tangential force magnitude in (a) full chamber–model (T16), (b) half chamber–model (T32) and (c) quarter chamber–model (T34)

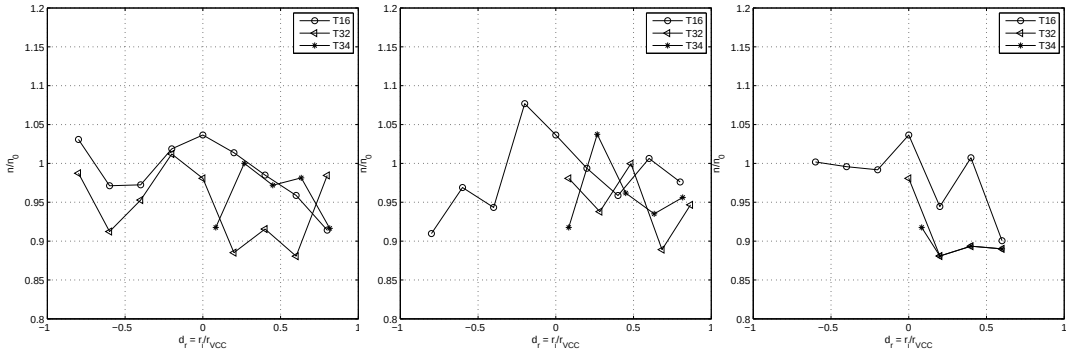

(a) xz–plane, Cut 1 (b) yz–plane, Cut 2 (c) rθ–plane, Cut 3

Figure 124: Comparison of normalized porosity ($\frac{n}{n_0}$) measured at initial stage in Layer 3 (d_z = 0.57) and for three models, T16, T32 and T34

6.3.2 *Mesoscopic variables at selected locations*

6.3.2.1 *Porosity*

Figure 124 shows the distribution of normalized porosity ($\frac{n}{n_0}$) in MS (on three different planes, see Figure 118), plotted for three models. Moreover, Figure 129a shows distribution of $\frac{n}{n_0}$ with height of VCC for MS positioned at the axis of VCC.

The distribution of porosity is inhomogeneous, however the maximum difference between target and actual value is smaller than 12%. Moreover, in Cut 3, the porosity plot is similar for both the half and quarter VCC models. Examining porosity with VCC depth, we can see that at the top of VCC (close to servo–controlled wall) all models start with the similar value of $\frac{n}{n_0}$. Below that, for half and quarter models the values oscillate between denser and looser zones. Close to the bottom wall (not servo–controlled) an increase in porosity is observed (loose zone). For the full chamber, top and bottom layers are denser than the zone between them.

The averaged normalized porosity evaluated at different sets of measurement spheres show similar trend for three different VCC–models. In all sets of MS the value of mean normalized porosity is always below the target one. The coefficient of variation is in range of 3–5%. This can be viewed in details in Table 21. Hence, in the averaged level we can say that symmetry is maintained.

6.3.2.2 *Coordination number*

Figure 125 shows the distributions of coordination number (C_N) in MS within the three selected planes (Figure 118) plotted for the three differently sized models. Moreover, Figure 129b shows distribution of C_N with height of VCC in the MS positioned at the axis of VCC. Similar to the porosity plots, the C_N distribution in selected planes (cuts) is not homogeneous. However, the symmetry enforcing walls do not seems to increase this effect. The similar scale of the variability in all cases is particularly noticeable at the chamber axis (Figure 129b). The C_N plot is similar for both half and quarter chambers in Cut 3.

Table 21 shows the mean value, standard deviation and coefficient of uniformity evaluated at the different sets of measurement spheres. It can be observed, that even

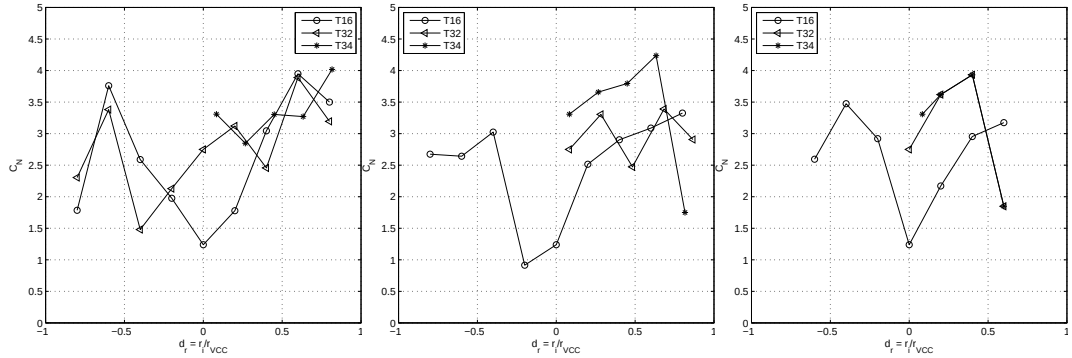

(a) xz–plane, Cut 1 (b) yz–plane, Cut 2 (c) rθ–plane, Cut 3

Figure 125: Comparison of coordination number (C_N) measured at initial stage in Layer 3 (d_z = 0.57) and for three models, T16, T32 and T34

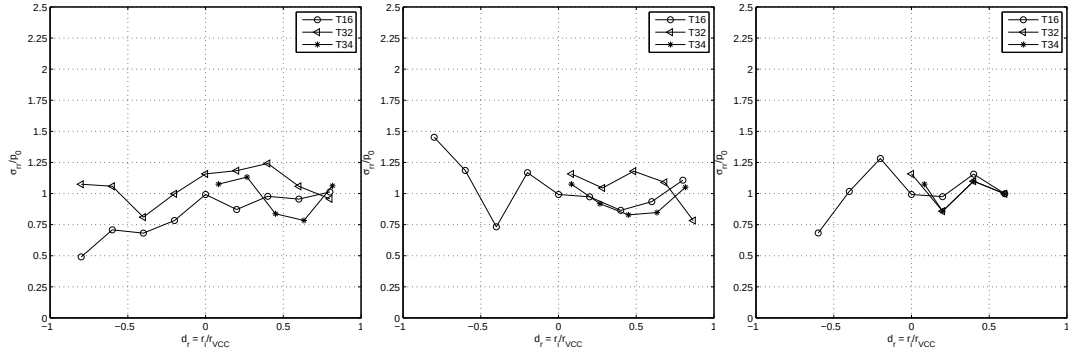

(a) xz–plane, Cut 1 (b) yz–plane, Cut 2 (c) rθ–plane, Cut 3

Figure 126: Comparison of normalized radial stress ($\frac{\sigma_{rr}}{p_0}$) measured at initial stage in Layer 3 (d_z = 0.57) and for three models, T16, T32 and T34

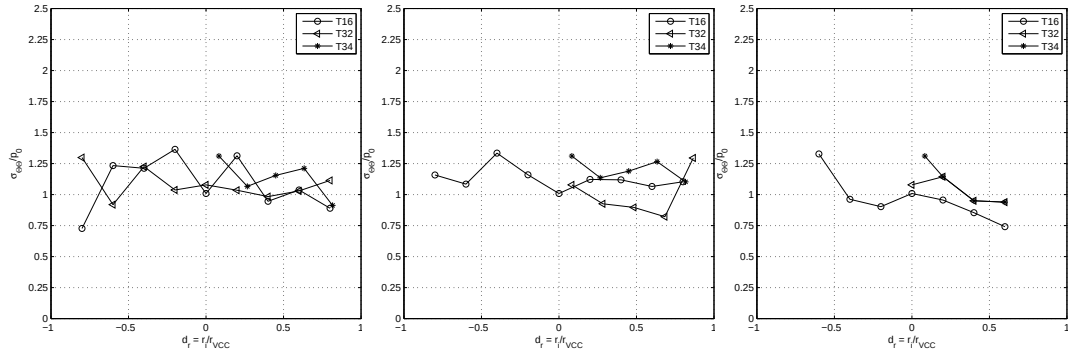

(a) xz–plane, Cut 1 (b) yz–plane, Cut 2 (c) rθ–plane, Cut 3

Figure 127: Comparison of normalized circumferential stress ($\frac{\sigma_\theta}{p_0}$) measured at initial stage in Layer 3 (d_z = 0.57) and for three models, T16, T32 and T34

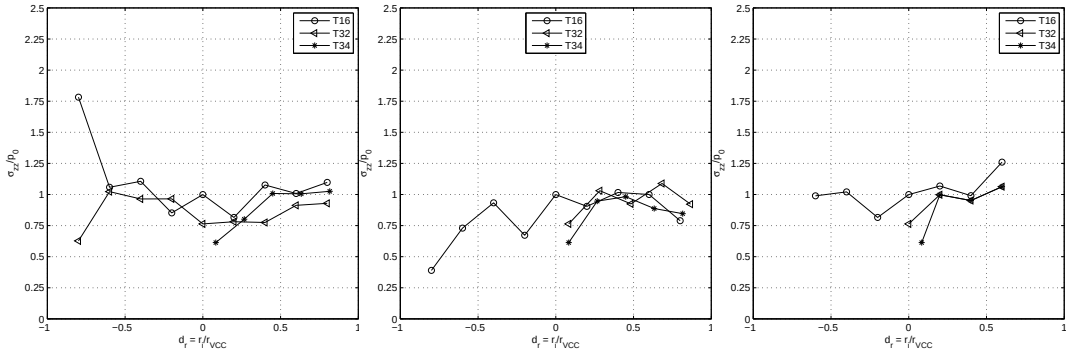

(a) xz–plane, Cut 1 (b) yz–plane, Cut 2 (c) rθ–plane, Cut 3

Figure 128: Comparison of normalized vertical stress ($\frac{\sigma_z}{p_0}$) measured at initial stage in Layer 3 ($d_z = 0.57$) and for three models, T16, T32 and T34

though the mean values are quite similar for different sizes of VCC–models, the coefficient of uniformity is quite large and range between 20 and 59% (for quarter VCC at the axis).

6.3.2.3 *Stress*

Figure 126, Figure 127 and Figure 128 show the distribution of normalized σ_r, σ_θ and σ_z in MS within three different planes (Figure 118) plotted for the three models. Moreover, figures 129c, 129d and 129e show the distribution of normalized stress components with height of VCC in the MS positioned at the axis of the VCC (marked as MS1 in Figure 81). It can be observed in this last plot, that the normalized σ_r, σ_θ and σ_z oscillate around the reference value of 1. The oscillation is more intense for the smaller model (quarter chamber) than for the larger ones. However, the stress distributions in Cut 3 are similar for half and quarter chamber models. The influence of the radial boundary seems higher for the full chamber model.

Looking at the average normalized stress evaluated at the different sets of measurement spheres (Table 21) we observed that these stresses are stresses are quite under below the target value for the MS at the axis of VCC–models (mode pronounced for the quarter VCC–model). Moreover, the coefficient of variation increases with increasing size of the VCC–models (large models are prone to inhomogeneities).

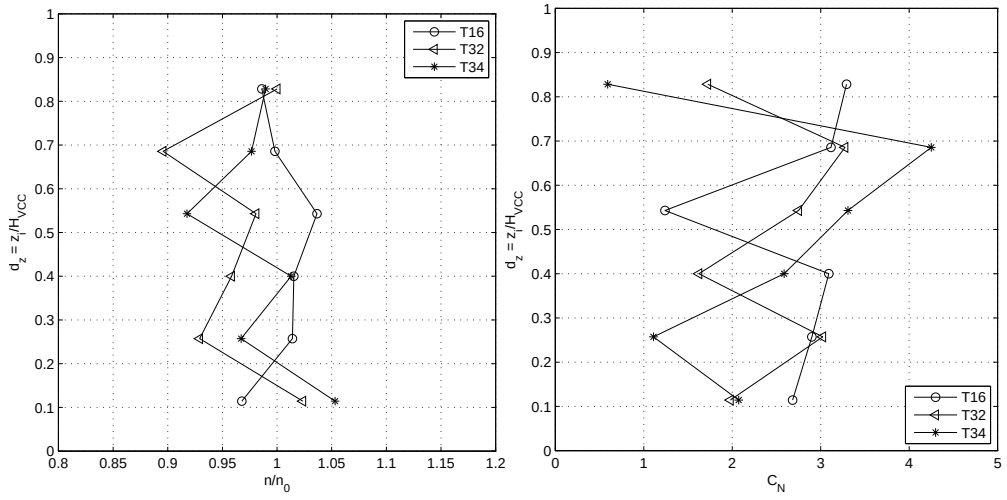

(a) $\frac{n}{n_0}$ (b) C_N

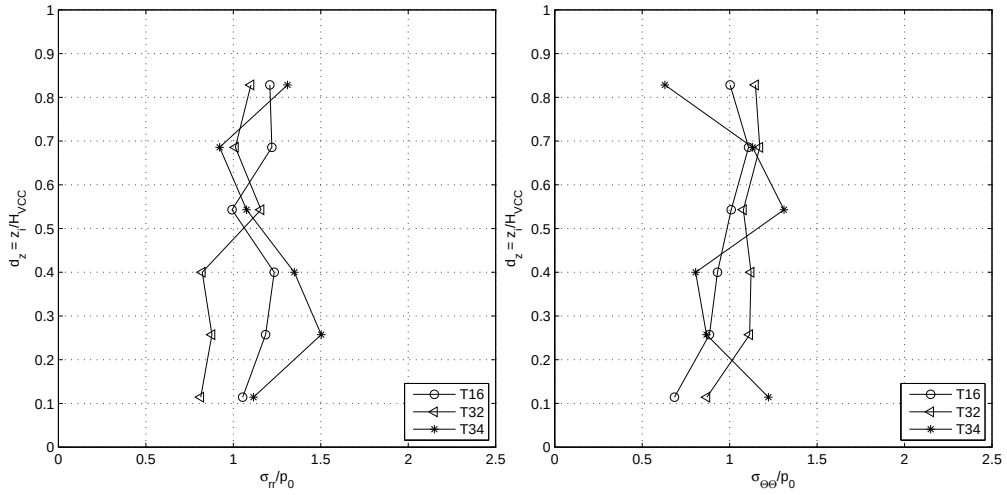

(c) $\frac{\sigma_r}{p_0}$ (d) $\frac{\sigma_\theta}{p_0}$

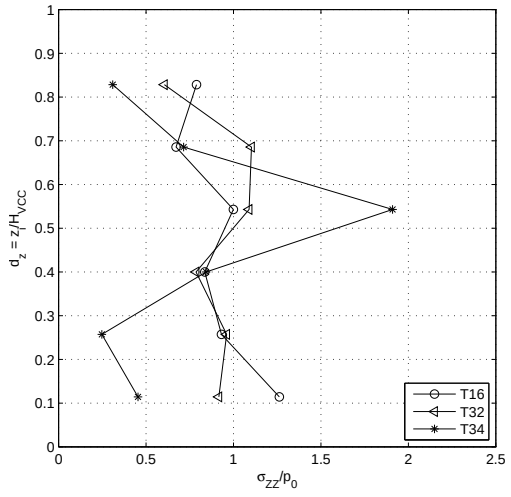

(e) $\frac{\sigma_z}{p_0}$

Figure 129: Distribution of measured variables with depth of VCC and for MS positioned at $d_r = 0$ (axis of symmetry) for AreaFactor=1–T16, T32–AreaFactor=0.5 and T34–AreaFactor=0.25

Table 21: Mean, standard deviation and coefficient of variation (ratio of the precedent) for the different variables (n, C_N, $\frac{\sigma_r}{p_0}$, $\frac{\sigma_\theta}{p_0}$ and $\frac{\sigma_z}{p_0}$) evaluated at different sets of measurement spheres

Tets ID	$\frac{n}{n0}$																	
	MS:radial wall			MS:Cut 1			MS:Cut 2			MS:Cut 3			MS:axis			MS:whole VCC		
	$\widetilde{N}$	S	C_v	$\widetilde{N}$	S	C_v	$\widetilde{N}$	S	C_v	$\widetilde{N}$	S	C_v	$\widetilde{N}$	S	C_v	$\widetilde{N}$	S	C_v
T16	0.96	0.03	0.03	0.98	0.03	0.03	0.97	0.03	0.03	0.98	0.03	0.03	0.97	0.04	0.04	0.97	0.03	0.03
T32	0.95	0.03	0.03	0.96	0.04	0.04	0.97	0.05	0.05	0.95	0.04	0.04	0.96	0.05	0.05	0.95	0.03	0.03
T34	0.94	0.03	0.03	0.97	0.03	0.03	0.96	0.04	0.04	0.96	0.03	0.03	0.98	0.04	0.04	0.96	0.03	0.03
	C_N																	
Test ID	$\widetilde{N}$	S	C_v	$\widetilde{N}$	S	C_v	$\widetilde{N}$	S	C_v	$\widetilde{N}$	S	C_v	$\widetilde{N}$	S	C_v	$\widetilde{N}$	S	C_v
T16	2.95	0.98	0.33	3.01	0.65	0.21	2.79	0.84	0.30	3.00	0.72	0.24	2.83	0.77	0.27	2.98	0.79	0.26
T32	2.73	0.70	0.25	2.74	0.57	0.21	2.90	0.69	0.24	2.80	0.79	0.28	2.40	0.70	0.29	2.90	0.66	0.23
T34	3.47	0.71	0.20	3.07	0.64	0.21	3.04	1.01	0.33	3.34	0.69	0.21	2.31	1.36	0.59	3.37	0.67	0.20
	$\frac{\sigma_r}{p_0}$																	
Test ID	$\widetilde{N}$	S	C_v	$\widetilde{N}$	S	C_v	$\widetilde{N}$	S	C_v	$\widetilde{N}$	S	C_v	$\widetilde{N}$	S	C_v	$\widetilde{N}$	S	C_v
T16	0.98	0.52	0.53	0.95	0.32	0.34	0.91	0.50	0.55	0.98	0.39	0.39	0.96	0.30	0.31	0.98	0.40	0.41
T32	1.03	0.27	0.26	0.90	0.29	0.32	1.03	0.31	0.30	0.98	0.33	0.34	0.86	0.38	0.44	1.00	0.28	0.28
T34	1.13	0.22	0.19	0.91	0.20	0.22	1.09	0.31	0.28	1.02	0.24	0.23	0.77	0.45	0.58	0.97	0.25	0.29
	$\frac{\sigma_\theta}{p_0}$																	
Test ID	$\widetilde{N}$	S	C_v	$\widetilde{N}$	S	C_v	$\widetilde{N}$	S	C_v	$\widetilde{N}$	S	C_v	$\widetilde{N}$	S	C_v	$\widetilde{N}$	S	C_v
T16	1.06	0.54	0.51	1.02	0.30	0.29	1.04	0.45	0.43	0.96	0.34	0.35	0.77	0.26	0.35	1.05	0.39	0.37
T32	1.05	0.30	0.29	1.06	0.30	0.28	1.00	0.25	0.25	0.97	0.36	0.37	0.77	0.32	0.41	1.07	0.28	0.26
T34	1.07	0.25	0.23	1.00	0.25	0.25	0.79	0.20	0.25	1.00	0.24	0.24	0.72	0.39	0.54	0.96	0.30	0.31

Test ID	$\frac{\sigma_z}{p_0}$																	
	$\widetilde{N}$	S	C_v	$\widetilde{N}$	S	C_v	$\widetilde{N}$	S	C_v	$\widetilde{N}$	S	C_v	$\widetilde{N}$	S	C_v	$\widetilde{N}$	S	C_v
T16	0.98	0.47	0.48	1.02	0.29	0.28	0.80	0.28	0.35	1.05	0.28	0.27	0.74	0.23	0.31	1.03	0.35	0.34
T32	0.99	0.24	0.24	0.84	0.26	0.31	0.94	0.23	0.24	0.99	0.25	0.25	0.73	0.22	0.30	1.01	0.22	0.22
T34	1.14	0.22	0.19	0.90	0.21	0.23	0.86	0.20	0.23	1.01	0.18	0.18	0.63	0.13	0.21	0.90	0.24	0.27
$\widetilde{N}$-mean value, S-standard deviation, C_v-coefficient of variation																		

6.3.3 *Contour plots*

6.3.3.1 *Porosity*

Figure 130 present contour plots of normalized porosity for the three mentioned cases alongside the xy (layer 3 ($d_z = 0.57$)), xz–(Cut 1) and yz–planes (Cut 2). The basic difference between these three models is that half (Figure 130b) and quarter (Figure 130c) VCC–models are more dense (Figure 130c) than the full chamber model (Figure 130a). This is clearly visible while looking at the porosity distribution in xz– and yz–planes. It can be observed that in half and quarter of chamber the regions more dense are those close to the servo–control wall (radial wall) and not close to walls forcing specimen symmetry (Figure 130i). The explanation for that is the isotropic compression method employed in model construction, which is enforced only by the radial and top wall.

6.3.3.2 *Coordination number*

Figure 131 present contour plots of coordination number for the three mentioned cases alongside the xy (layer 3 ($d_z = 0.57$)), xz–(Cut 1) and yz–planes (Cut 2). The distribution of C_N is similar for full and half chambers. For the quarter model, the value of C_N is higher than in two previous cases. For example, the lowest value observed in the VCC is equal to 1 for the full and half cases and 2.6 for the quarter of VCC. When we look at the C_N distribution with VCC height in xz– and yz–planes we observed similar behavior in all cases. The lowest values are in the zone where penetration takes place (center of the VCC) and higher close to radial wall. This is in agreement with the porosity distribution.

6.3.3.3 *Stresses*

Figure 132, 133 and 134 present contour plots of normalized radial, circumferential and vertical stresses, respectively, for three mentioned cases (plotted in layer 3 ($d_z = 0.57$)) and xz– (Cut 1) and yz–planes (Cut 2). In general, we can say that the stress distributions are similar for all three cases. There are some zones that either below or above the reference stress values. The lowest values of σ_r, σ_θ are observed close to bottom–radial and bottom walls, while for the case of σ_z–close to the top/radial wall.

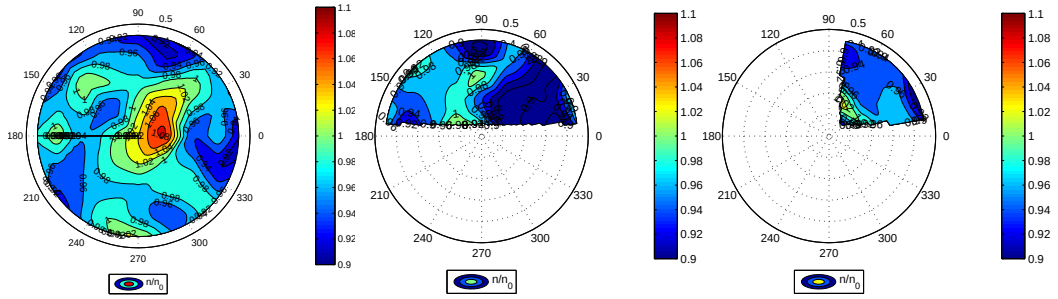

(a) xy–plane, T16 (b) xy–plane, T32 (c) xy–plane, T34

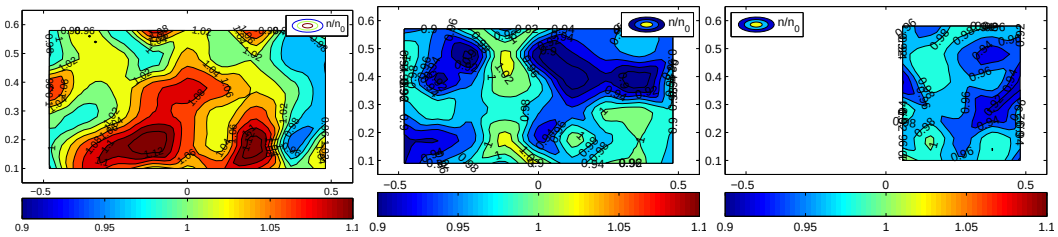

(d) xz–plane, T16 (e) xz–plane, T32 (f) xz–plane, T34

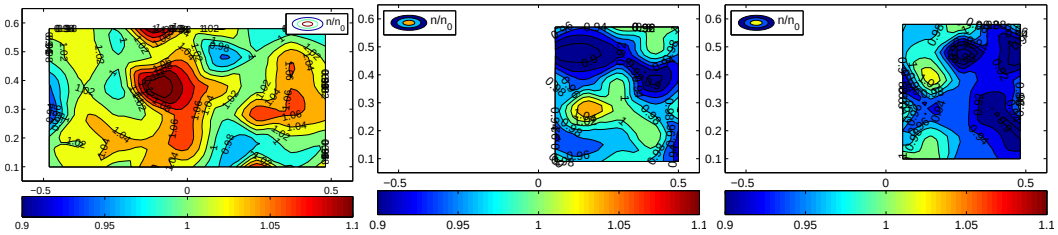

(g) yz–plane, T16 (h) yz–plane, T32 (i) yz–plane, T34

Figure 130: Normalized porosity ($\frac{n}{n_0}$) in xy–, xz– and yz–plane (Cut 1, 2 and 3), D_R=75%, $\sigma_v = \sigma_h = 100$ kPa for full VCC (AreaFactor=1)–T16; half VCC (AreaFactor=0.5)–T32 and quarter VCC (AreaFactor=0.25)–T34

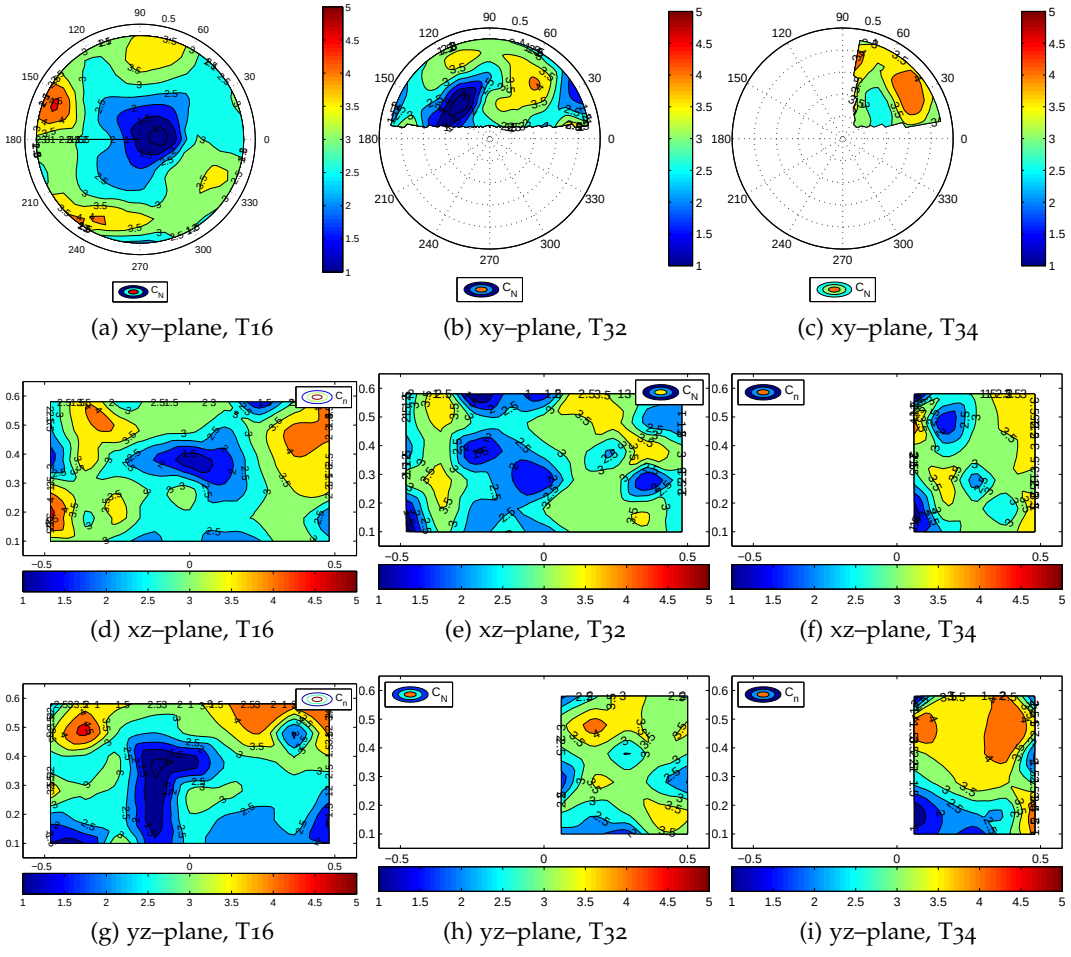

(a) xy–plane, T16 (b) xy–plane, T32 (c) xy–plane, T34

(d) xz–plane, T16 (e) xz–plane, T32 (f) xz–plane, T34

(g) yz–plane, T16 (h) yz–plane, T32 (i) yz–plane, T34

Figure 131: Coordination number (C_N) in xy–, xz– and yz–plane (Cut 1, 2 and 3), D_R=75%, $\sigma_v = \sigma_h = 100$ kPa for full VCC (AreaFactor=1)–T16; half VCC (AreaFactor=0.5)–T32 and quarter VCC (AreaFactor=0.25)–T34

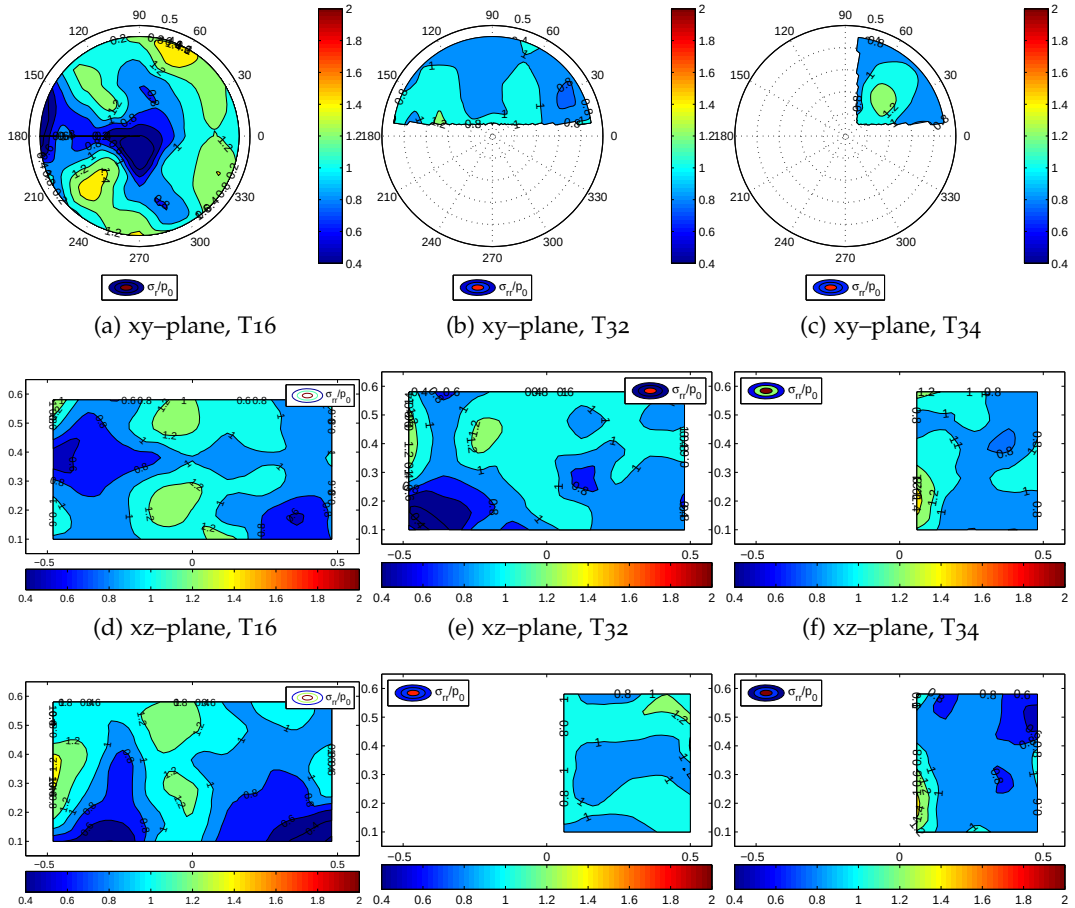

(a) xy–plane, T16 (b) xy–plane, T32 (c) xy–plane, T34

(d) xz–plane, T16 (e) xz–plane, T32 (f) xz–plane, T34

(g) yz–plane, T16 (h) yz–plane, T32 (i) yz–plane, T34

Figure 132: Normalized radial stress ($\frac{\sigma_r}{p_0}$) in xy–, xz– and yz–plane (Cut 1, 2 and 3), $D_R = 75\%$, $\sigma_v = \sigma_h = 100$ kPa for full VCC (AreaFactor=1)–T16; half VCC (AreaFactor=0.5)–T32 and quarter VCC (AreaFactor=0.25)–T34

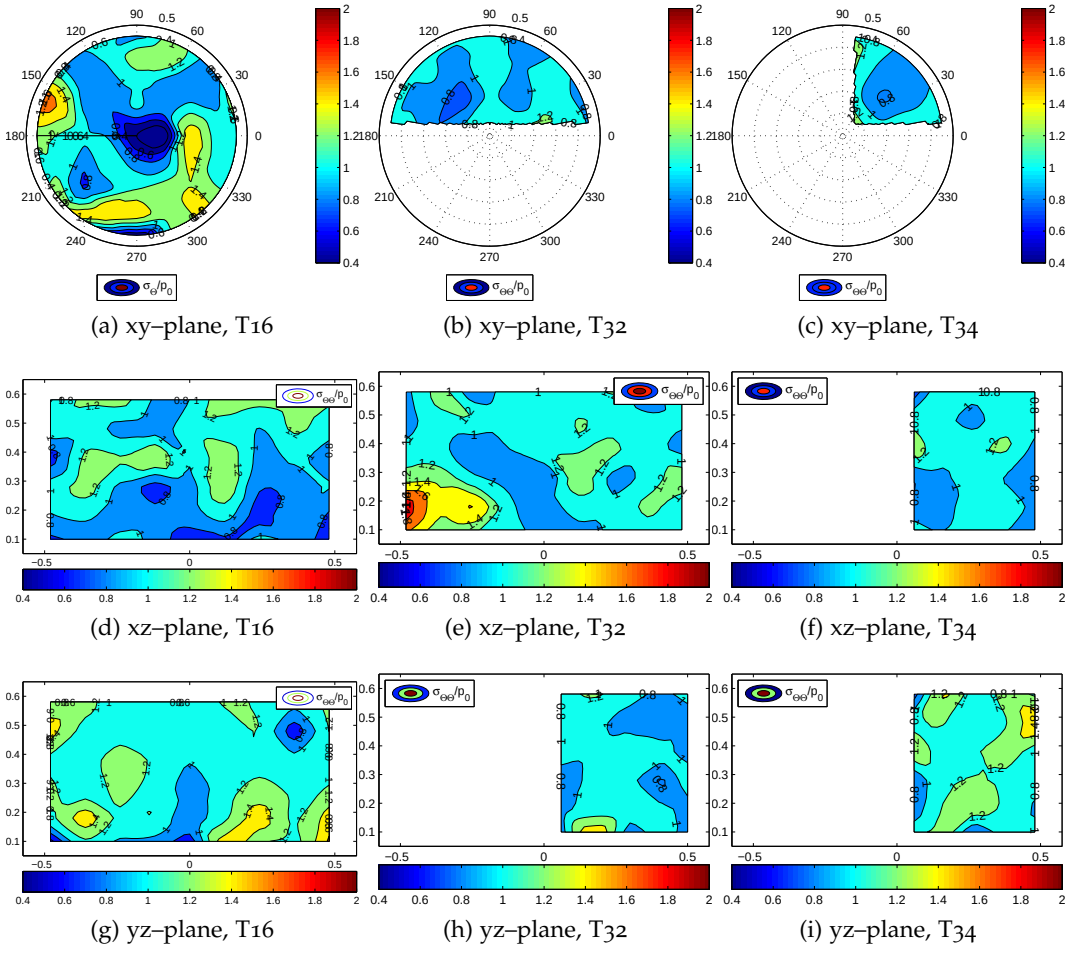

(a) xy–plane, T16 (b) xy–plane, T32 (c) xy–plane, T34

(d) xz–plane, T16 (e) xz–plane, T32 (f) xz–plane, T34

(g) yz–plane, T16 (h) yz–plane, T32 (i) yz–plane, T34

Figure 133: Normalized circumferential stress ($\frac{\sigma_\theta}{p_0}$) in xy–, xz– and yz–plane (Cut 1, 2 and 3), $D_R = 75\%$, $\sigma_v = \sigma_h = 100$ kPa for full VCC (AreaFactor=1)–T16; half VCC (AreaFactor=0.5)–T32 and quarter VCC (AreaFactor=0.25)–T34

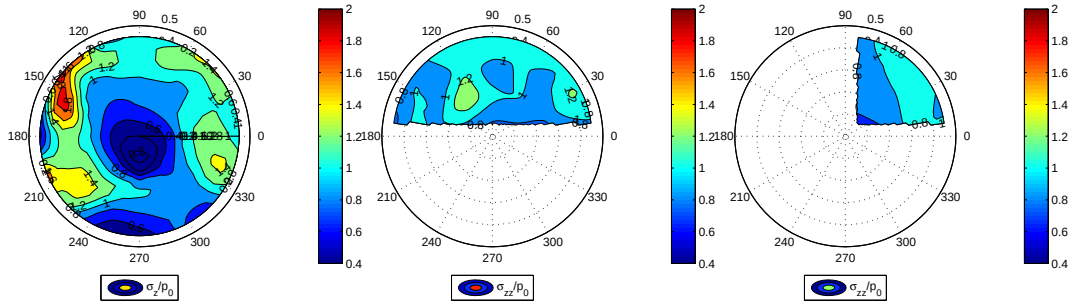

(a) xy–plane, T16 (b) xy–plane, T32 (c) xy–plane, T34

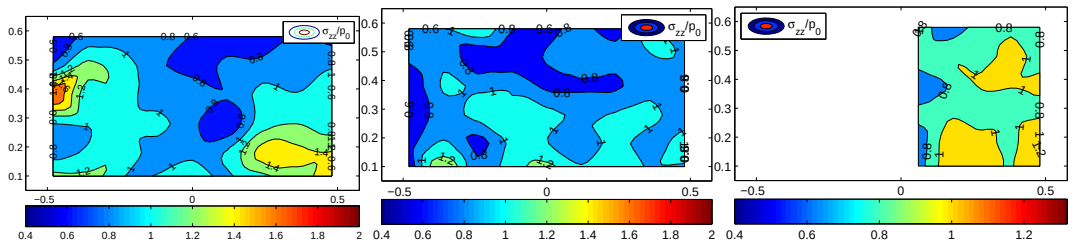

(d) xz–plane, T16 (e) xz–plane, T32 (f) xz–plane, T34

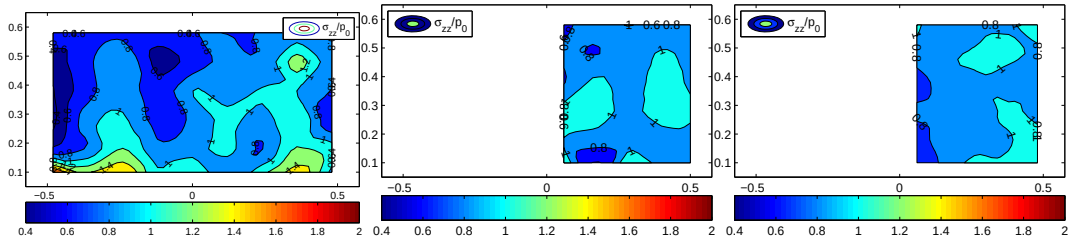

(g) yz–plane, T16 (h) yz–plane, T32 (i) yz–plane, T34

Figure 134: Normalized vertical stress ($\frac{\sigma_z}{p_0}$) in xy–, xz– and yz–plane (Cut 1, 2 and 3), $D_R = 75\%$, $\sigma_v = \sigma_h = 100$ kPa for full VCC (AreaFactor=1)–T16; half VCC (AreaFactor=0.5)–T32 and quarter VCC (AreaFactor=0.25)–T34

6.4 SUMMARY

In this chapter we presented a study on the homogeneity of VCC specimens, formed at different densities and under different stress regimes (isotropic and anisotropic). We did also examine the no sequences for specimen homogeneity of enforcing symmetry by introducing rigid walls along the radius. The analysis was performed by using measurement spheres (MS) as REV distributed all over the specimen. The study was performed at two levels, micro (contact force network and contact orientation) and meso–level (porosity, coordination number and stresses).

The initial state of the DEM VCC model reveals itself as somewhat inhomogeneous. Significant fluctuations of parameters such as porosity, coordination number and stress components do appear at the meso–level. Moreover, such fluctuations do not maintain cylindrical symmetry, and their distribution is clearly affected by symmetry-enforcing radial walls. The magnitude of differences between mesoscopic values (porosity, stress) and the reference value was higher for stress than for porosity. Moreover, the effect of rigid wall was also observed that resulted in either increased stress and density (servo-controlled wall) or decreased stress and density (fixed wall). One possible way to minimize this problem would be the inclusion of specifically designed boundary conditions (e.g. membrane like walls as described by O'Sullivan [2011b]) and/or use also the symmetry enforcing walls into the compression process.

The influence of homogeneity and model symmetry on the macro response (q_c and f_s) of the VCC CPT models is investigated in the next chapter (Chapter 7).

7

THE MACRO RESPONSE OF VCC CPT MODELS

7.1 INTRODUCTION

This chapter describes a series of simulated cone penetration tests in a discrete material representing Ticino sand under different initial conditions (stress history, relative density, method of consolidation) and subject to different boundary conditions (BC1 and BC3). The VCC CPT models are prepared as described in Chapter 5. The macro response of the DEM models are examined through their cone tip resistance (q_c) and, in some cases, shaft resistance (f_s) measurements. The cone resistance is calculated based on the vertical forces acting on the face of cone and projected area of the cone. The shaft resistance is obtained from the shear force acting along the side of the penetrometer. Several test series are employed to examine several issues related to the penetration process. A validation against existing q_c-D_R-σ relationships is performed. Moreover, direct comparisons (one-to-one) between numerical and physical calibration chamber results are also given. The changes in measured shaft resistance are analyzed in terms of initial conditions (p_0, D_R and BC), size and position of the measuring sleeve and shaft friction.

7.2 SIMULATION PROGRAM

The main conditions relevant to the numerical tests presented here are collected in Table 22 at the end of this chapter. The simulation program employs four models (1-4) and is organized into seven test series (A-G). Models used in this analysis differ either in chamber size and/or cone size depending on the topic that is investigated. Hence, model 1 incorporates full-sized chamber ($D_{VCC} = 1.2$ and $H_{VCC} = 0.7$ m) and cone with diameter (d_c) of 71.2 mm ('default DEM cone'). Model 2 consists of a VCC with diameter of 1.2 m (full-sized chamber) but variable cone diameters ($71.2 - 213.6$ mm). Model 3 uses a half-sized VCC with diameter of 1.2 m and default DEM cone. The last one, model 4, uses a quarter of chamber with different diameters ($D_{VCC} = 0.4 - 2.4$m) and the defaults DEM cone. Each model is then applied into one or more test series.

Model 1 is used in two main test series (A & B) that differ in the stress system applied during the consolidation stage (ConStage). Test series **A** consist of eight tests performed at two relative densities of 75% and 90% with initial isotropic stresses ranging from 60-400 kPa and performed under BC1 boundary conditions. Results from these tests are compared with the empirical q_c-D_R-σ relationship (Eq. 3.7) proposed by Jamiolkowski et al. [1988] (details in Chapter 3). Series **B** consist of nine tests performed on a material with D_R approximately $94 \mp 3\%$ at different stress states resulting from anisotropic consolidation (K_0-conditions) under two different boundary conditions (BC1 & BC3) and for both normally consolidated and overconsolidated assemblies. It these case, numerical results are compared with experimental tests from the ENEL/ISMES database performed at similar conditions.

As mentioned previously (Chapter 5), present computational capabilities make impossible to represent all individual sand grains as discrete elements, scaling and fine truncation are therefore necessary. To compare the results of the main test series with the actual CC tests, it is necessary to perform additional analyses to check on the effects of the various hypotheses adopted. Hence:

SERIE C explores the effect of a variable cone diameter on the results;

SERIE D examines the possibility of exploiting the apparent symmetries of the test configuration. This series employed models of a half chamber and a quarter chamber, as indicated in the table;

SERIE E is a complementary test series to **A** for $D_R \approx 60\%$ but performed using half - chamber models;

SERIE F is aimed, using quarter - chamber models, to evaluate calibration chamber size effects;

SERIE G is performed to compare DEM results with results from physical CC for different R_d ratios and on material with $D_R \approx 94\%$ at stresses resulted from 1D-compression and under either BC1 or BC3 boundary conditions. In this serie only quarter of chamber was used.

The results of series C, D and F are used to support the interpretation of of Series A and facilitate their comparison with the CC experimental results.

7.3 TIP RESISTANCE: RAW RESULTS AND POST-PROCESSING

7.3.1 *Cone tip penetration curves*

The cone penetration point resistance curves recorded for tests series A are collected in Figure 135, for test series B in Figure 136, for test series C in Figure 137, for test series D in Figure 138, for test series E inFigure 139, for test series F in Figure 140 and for test series G in Figure 141. It can be appreciated that, although the penetration resistance curves order themselves as expected (increasing resistance with confining pressure and relative density-Figure 135-75 and 90 %, Figure 139-60 %) their graphs are very noisy, with large oscillations. This trend is in agreement with other DEM-CPT simulations (Huang and Ma [1994], Jiang et al. [2006b], Breul et al. [2009]). It is suspected that the main source of noise in the penetration curves is the reduced n_p ratio, since, as explained before, numerical constraints resulted in relatively few particles per cone diameter in the basic simulation-Model 1. Hence, a numerical experiment (series C) was specifically performed to check if this was the case. The results of this experiment, shown in Figure 137, are very convincing: as the ratio n_p between cone diameter (d_c) and mean grain size (d_{50}) increases the penetration curve smoothes visibly. At the largest n_p employed, of circa 8, the curve oscillations around the mean value have practically disappeared.

The results from test series C illustrate another phenomenon due to cone-to-chamber size effects. We observe an important reduction in tip resistance ($\approx$ 3 (75%)-3.5 (90%) times) caused by a reduction in R_d ratio (16.6-5.6). To dissipate such ambiguity it was needed to explore separately models with fixed relative cone-to-particle size (n_p),

but varying relative cone-to-chamber size (R_d). That exercise required, in principle, larger-sized chambers which were computationally expensive.

To limit the computational expense, it seemed logical to exploit the apparent symmetry of the problem. The results of Series D (Figure 138) shows comparison of penetration curves obtained for models with a variable plan section (*AreaFactor*) but similar initial conditions (σ, D_R, d_{50}). Despite the noisy response, the three models have a similar response. This similitude is even more apparent if the raw results are post-processed as explained below. The cone resistance discrepancy is less than 10% (assuming tests with AreaFactor equal 1 (full chamber) as a reference).

The Series F is then performed to explore chamber size effect by increasing diameter of VCC using model 4, hence using only a quarter of chamber. The results can be viewed in Figure 140. Again in this case the oscillations are significant and quantitative comparison difficult. Hence, the raw penetration curves required some post-processing.

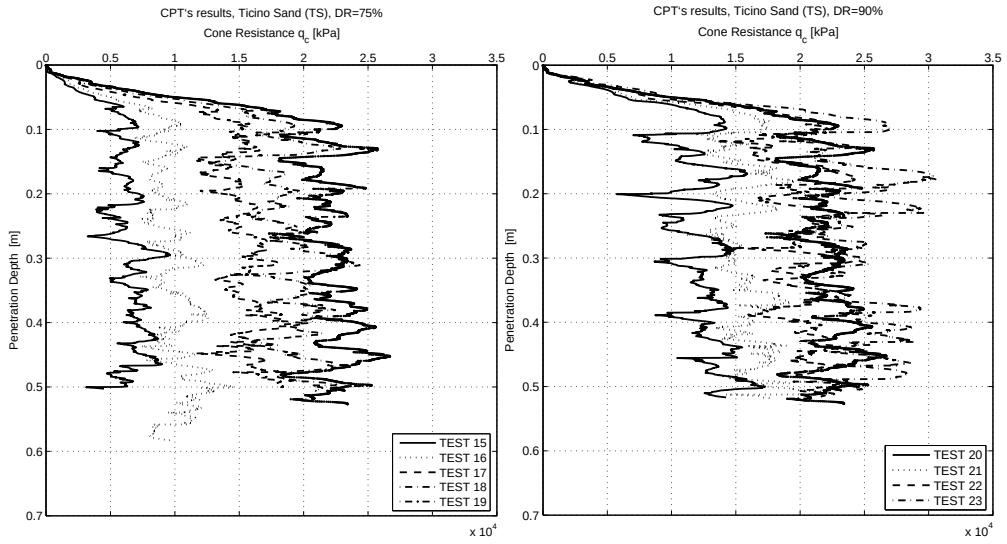

(a) $D_R = 75\%$ (b) $D_R = 90\%$

Figure 135: Raw cone penetration resistance curves for Model 1 Serie A for isotropic consolidation

7.3.2 *Post-processing method*

Since the oscillations appeared to be a noisy artifact of the scaled discrete material, it seemed then reasonable to filter them out. To do so, a steady state cone resistance was extracted from the raw penetration curves by fitting them to the following expression:

$$f(x) = a \cdot (1 - e^{-bx}) \tag{7.1}$$

where:

a, b=fitting parameters; a gives the asymptotic value of cone penetration; b gives the depth at which a certain % of cone penetration value is attained, through $X_{\%} = \frac{\ln(1/\%)}{b}$. Hence b is inversely related to the limit of shallow penetration;

y=q_c-cone resistance in [kPa]
x=h-penetration depth in [m]

A graphical example can be viewed in Figure 142. The steady state cone resistance is given by the parameter a of the curve-fit. The fitting parameters (a, b) and the value of the squared regression coefficient (R^2) for the curve-fit are collected in Table 23 for each particular test performed in this study. Results of the curve-fit for all tests are presented in Appendix H (Figure 337 to Figure 354).

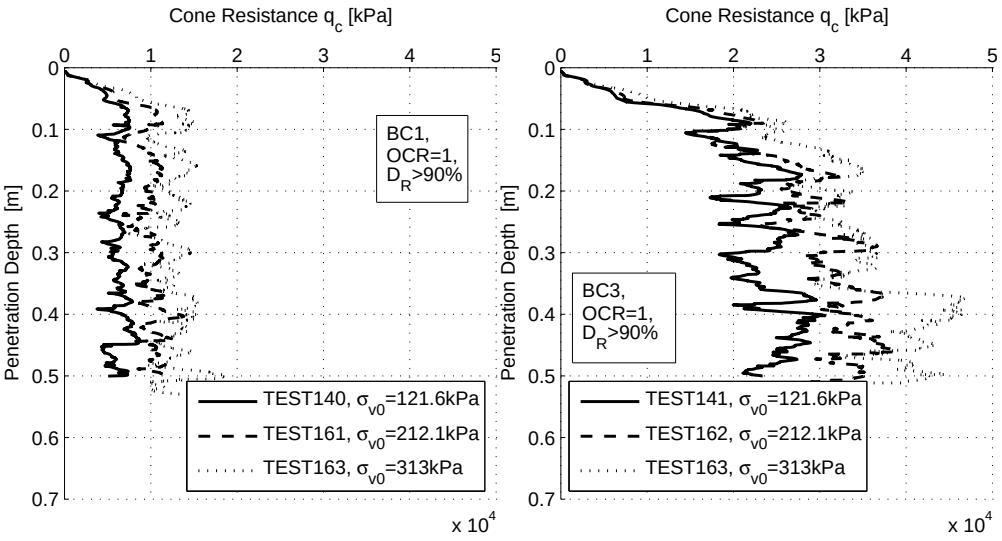

(a) BC1, OCR=1, $D_R = 93.9 - 96.8\%$ (b) BC3, OCR=1, $D_R = 93.9 - 96.8\%$

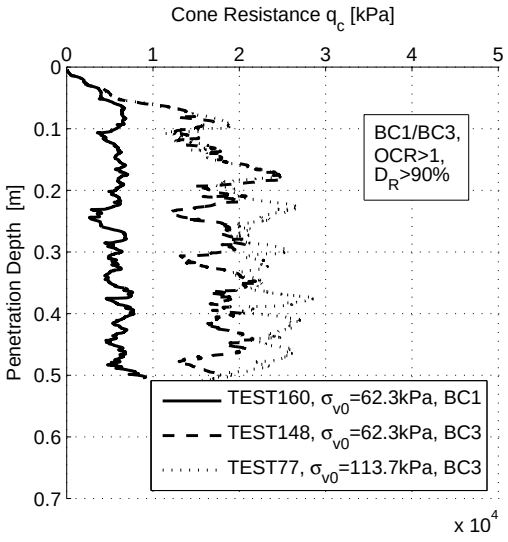

(c) BC1/BC3, OCR>1, $D_R = 90.8 - 93.4\%$

Figure 136: Raw cone penetration resistance curves for Model 1 Serie B for anisotropic consolidation

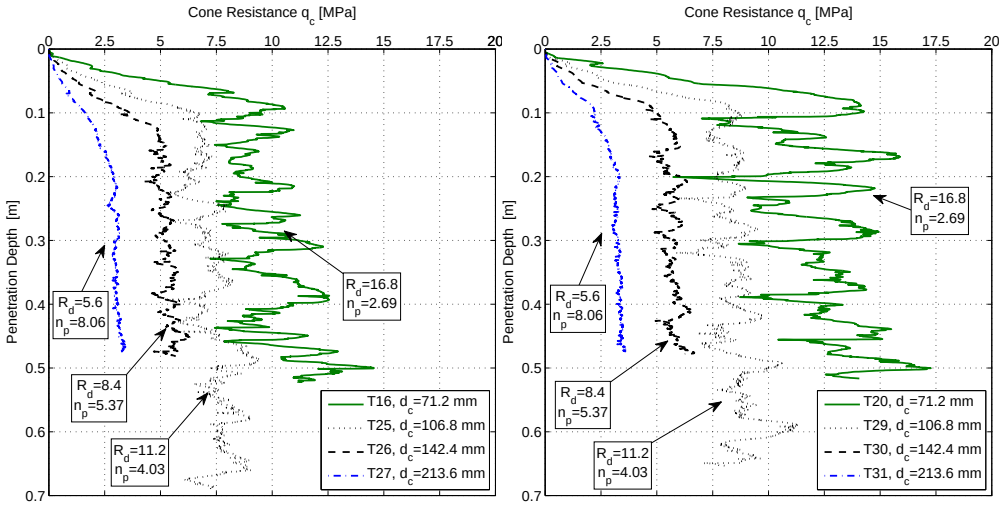

(a) $D_R = 75\%$ (b) $D_R = 90\%$

Figure 137: Raw cone penetration resistance curves for Model 2 Series C for isotropic consolidation and different cone sizes

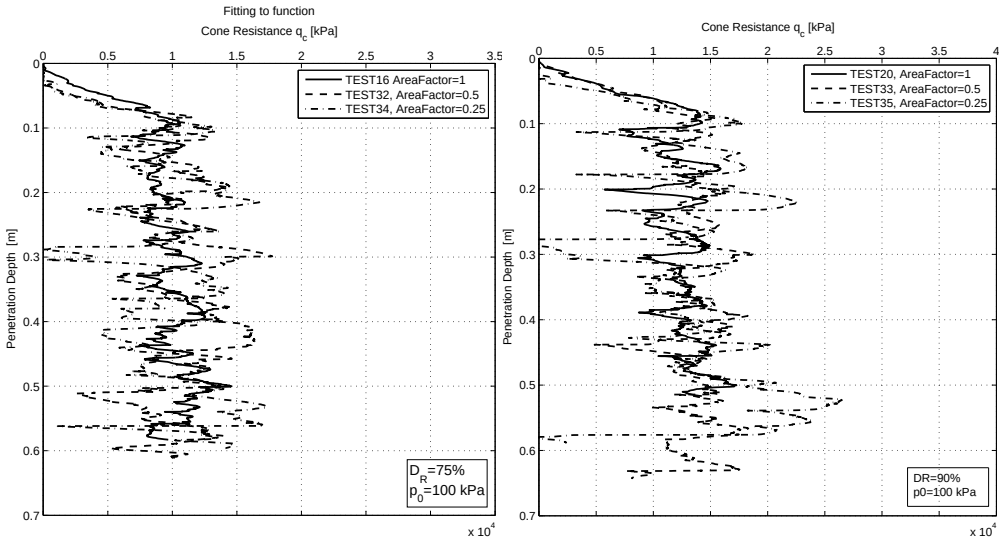

(a) $D_R = 75\%$ (b) $D_R = 90\%$

Figure 138: Raw cone penetration resistance curves for Model 4 Series D for isotropic consolidation and different AreaFactors

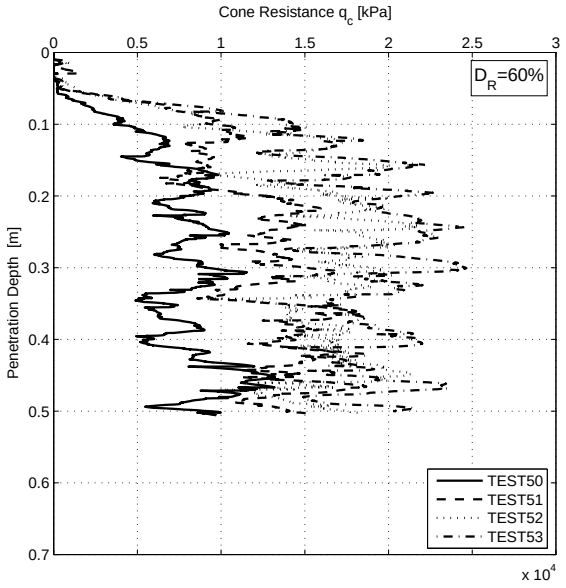

Figure 139: Raw cone penetration resistance curves for Model 3 Series E for isotropic consolidation and AreaFactor = 0.25, D_R = 60 [%]

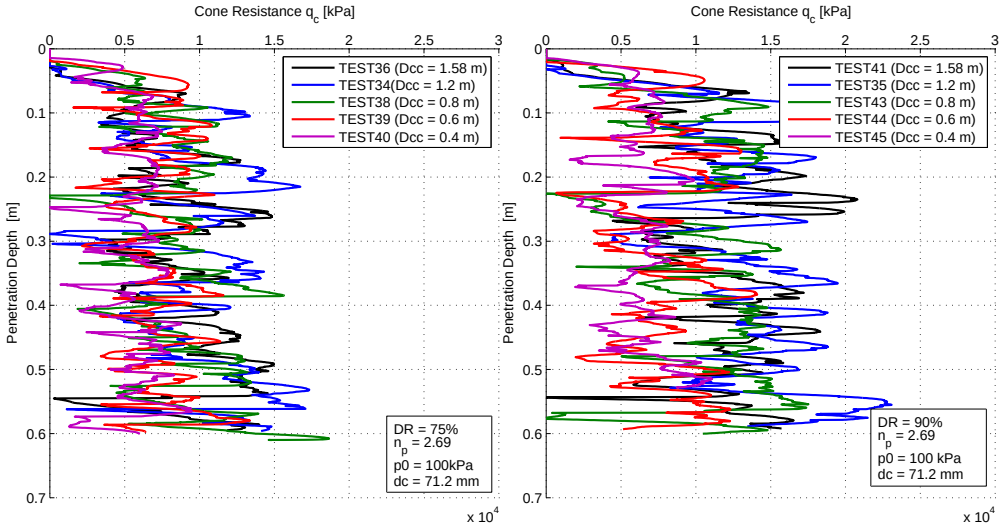

(a) $D_R = 75\%$ (b) $D_R = 90\%$

Figure 140: Raw cone penetration resistance curves for Model 4 Series F for isotropic consolidation and AreaFactor = 0.25

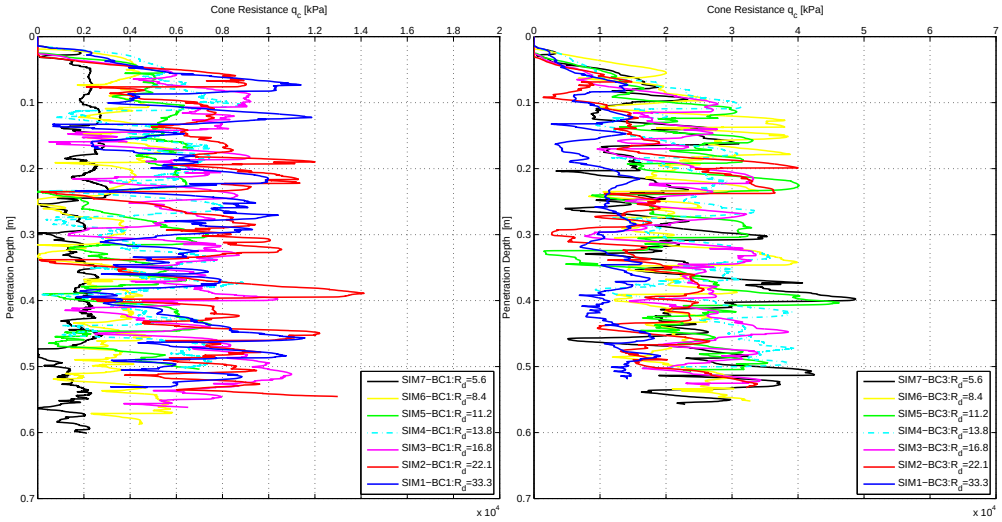

(a) BC1 (b) BC3

Figure 141: Raw cone penetration resistance curves for Model 4 Series G for non-isotropic consolidation and AreaFactor = 0.25, $D_R \approx 94$ [%]

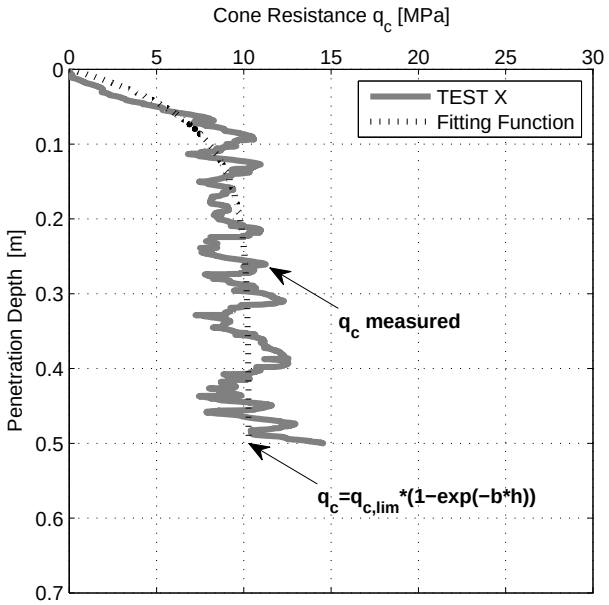

Figure 142: Post-processing method: definition of steady state

7.4 TIP RESISTANCE: COMPARISONS WITH PHYSICAL DATABASE

From all tests included in this study two series (A/C) are specially performed to validate the modeling results against empirical q_c-D_R-σ curves (Series A/C) whereas series B is designed to make one-to-one comparisons between DEM results and selected tests from the experimental ENEL/ISMES database.

The vast majority of the CC physical tests are performed using a 35.6 mm diameter cone (standard cone). As is mentioned in Chapter 3 in section 3.3 (*Problems & limitations of CC CPT testing*) the chamber and cone sizes have an important effects on the CPT results. That is why, for tests with boundary conditions of the BC1 type, Jamiolkowski et al. [2003] adopted a correction factor, CF, of the following form:

$$CF = A\,(D_R)^B \tag{7.2}$$

A graphical representation of correction factor, CF is shown on Figure 143c. The coefficients A and B are functions of relative density and relative chamber size, R_d. For relative densities above 60%, the influence of the relative chamber size is dominant, and the coefficients A and B can be expressed with good approximation as functions of R_d:

$$\begin{aligned} A &= 0.00009(R_d)^{2.02} \\ B &= -0.565\ln(R_d) + 2.59 \end{aligned} \tag{7.3}$$

A graphical representation of parameters A and B is illustrated in Figure 143a and Figure 143b, respectively. To be consistent with the CC database, the raw results of this study are then multiplied by factor CF to obtain a corrected value of tip resistance, $q_{c,cor}$. The raw $q_{c,lim}$ as well as CF and $q_{c,cor}$ obtained for all numerical tests are summarized in Table 23.

7.4.1 *Comparison with empirical curves*

The CC CPT database results had been summarized by several empirical relationships between corrected cone resistance q_c, relative density D_R and a stress measure σ'. Jamiolkowski et al. [2003], using results from CPT tests on normally and overconsolidated physical samples of Ticino sand, proposed the following Schmertmann-type empirical correlation:

$$q_c = C_0 \cdot p_a \left(\frac{\sigma'}{p_a}\right)^{C_1} \cdot e^{C_2 \cdot D_R} \tag{7.4}$$

where p_a is the atmospheric pressure ($\approx$ 100 kPa), D_R is a relative density [-] and σ' is a relevant effective stress measure. For normally consolidated Ticino sand, the correlation is established using vertical effective stress ($\sigma_v 0$), with $C_0 = 17.74$, $C_1 = 0.55$ and $C_2 = 2.90$. When results from both normally consolidated and overconsolidated Ticino sand were employed to establish the correlation, best results were obtained using mean effective stress (p_0) as the relevant stress measure, and C_0=23.19, C_1=0.56 and C_2=2.97. Note that the q_c that appears in eqn. 7.4 has been already corrected by chamber size effects using the correction factor, CF just discussed. After applying the same correction, the numerical results are then plotted in the q_c-D_R-σ_v plots that summarize these relations as done in Figure 144.

Figure 145 shows a direct comparison between numerical results and the values predicted by the empirical correlations. It appears that the q_c obtained in VCC system is well predicted by the previously established empirical correlation that uses p_0 as the relevant stress (Figure 145b), on the other hand the empirical correlation that used vertical stress systematically under predicts the numerical result.

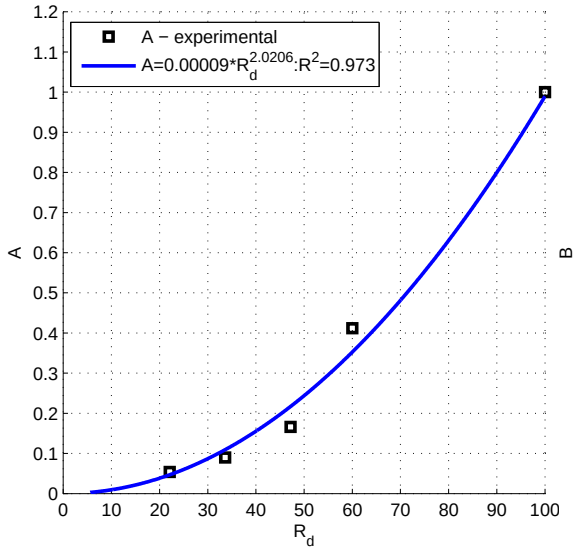

(a) A-parameter

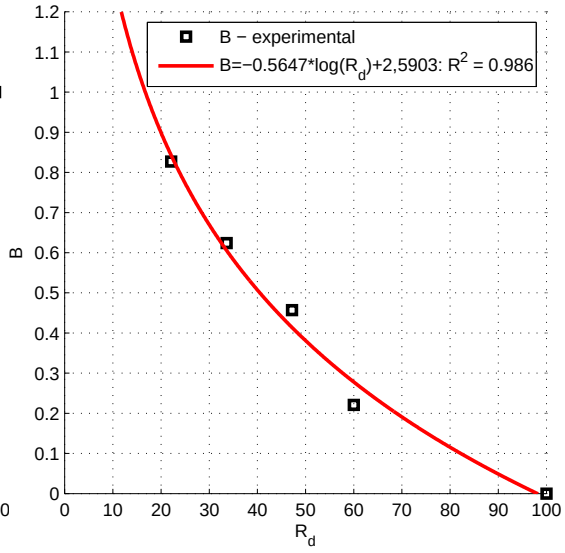

(b) B-parameter

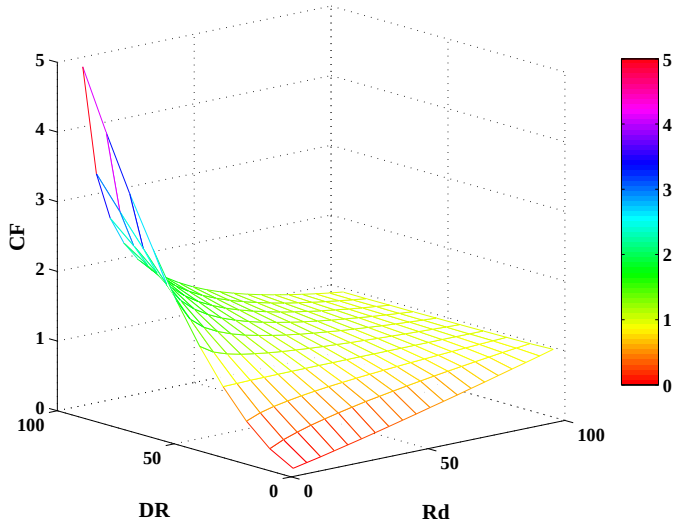

(c) $CF = f(D_R, R_d)$

Figure 143: The coefficients (a) A, (b) B and (c) the graphical interpretation of correction factor CF

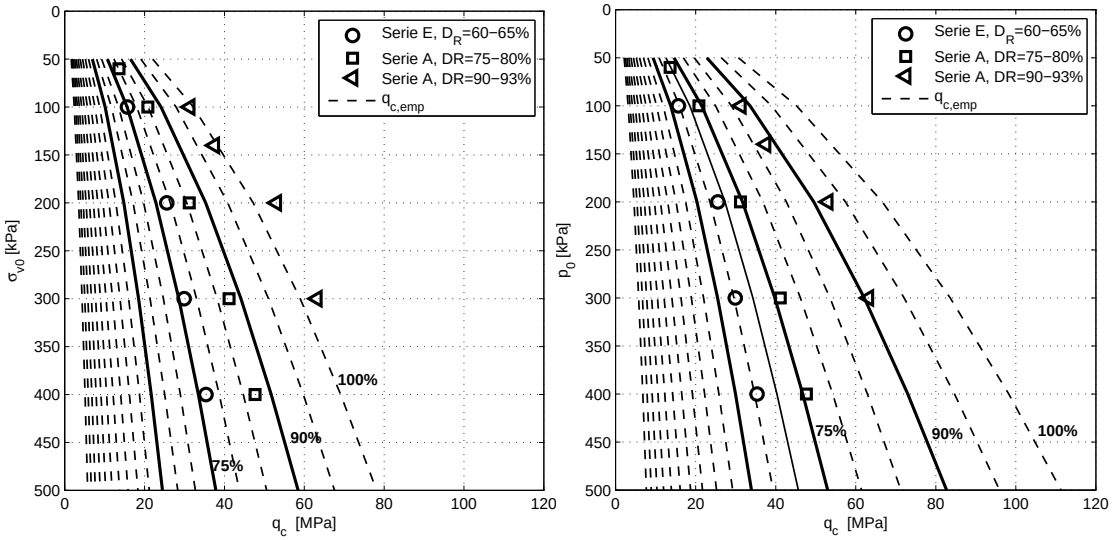

(a) $q_c = C_0 p_a \left(\frac{\sigma_{v0}}{p_a}\right)^{C_1} e^{C_2 D_R}$, C_0=17.74, C_1=0.55 (b) $q_c = C_0 p_a \left(\frac{p_0}{p_a}\right)^{C_1} e^{C_2 D_R}$, C_0=23.19, C_1=0.56, C_2=2.90 C_2=2.97

Figure 144: Cone resistance results plotted in D_R-q_c curves

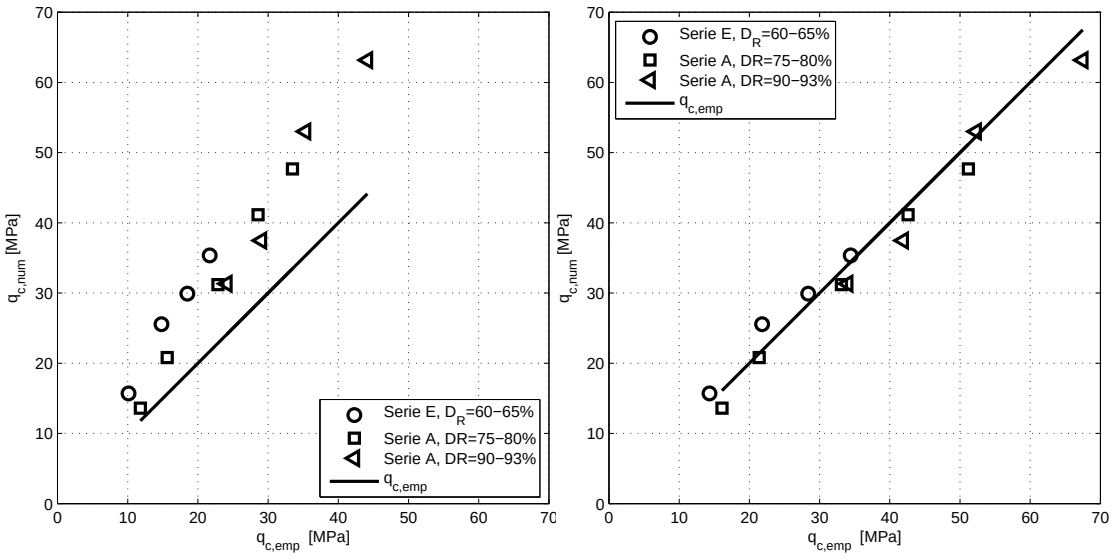

(a) $\sigma' = \sigma_v$ (b) $\sigma' = p_0$

Figure 145: Comparison of corrected cone resistance from isotropically confined DEM tests and the predictions of the empirical correlation obtained for Ticino sand Eqn. 7.4 (a) $\sigma' = \sigma_v$ and (b) $\sigma' = p_0$

7.4.2 *One-to-one comparisons with selected tests of the experimental database*

Simulations in series B (Table 22) correspond to CPT tests performed after anisotropic consolidation (K_0-conditions) in the VCC. These tests allow for a more direct comparison with physical CC results, including consolidation and penetration stages. The numerical tests in series B are prepared after normal consolidation to the given vertical stress (σ_v=62.3-313 kPa), share the same initial relative density range (90.8-96.8%), horizontal stress range (σ_v=38.05-109.9 kPa), boundary conditions (BC1 or BC3) and overconsolidation ratio that some tests made in the physical CC.

However, it should be noted that some differences remain. The most important one is that of CC and cone size. The VCC length has been shortened by a factor ≈ 2, the cone tip was multiplied by a factor 2. As explained in Chapter 5 this has a different effect according to the CC chamber BC. The results from tests under BC3 conditions can be compared directly with their physical counterparts, since, in principle, there is no calibration chamber size correction to be applied. On the other hand, tests under BC1 conditions need to be corrected for chamber size effects and that correction should be, in principle, different for the numerical tests (where R_d=16.8) and the physical tests (where R_d=33.7).

Also, the initial conditions of the numerical and physical tests are not strictly identical. Differences between a numerical test and its counterpart in relative density are within 2% whereas those in horizontal stress,before CPT, are slightly higher (within 26%, averaging 25%). This can be seen in Figure 146. It is possible and convenient to purge these effects with additional correction factors for either density and/or mean stress diffrence derived from expressions such as eqn. 7.4.

During the consolidation stage (e.g. Figure 147) the stress path is well reproduced, especially for low vertical stresses. For the highest σ_v ($\approx$ 313 kPa) the σ_r error is within 17% ($\approx$ 30 kPa). The reason of the increasing error in σ_r might be that no particle crushing is included in the numerical tests whereas some was observed in the physical tests. The influence of particle crushing on K_0 has been noted, for instance, by Mesri and Vardhanabhuti [2009]. During loading-unloading cycles, the DEM model recovered more deformation than the physical tests, showing less plastic behavior (Appendix H: Figure 349b and Figure 350b).

Figures 148-151 present one-to-one comparisons of numerical and experimental results for several paired tests. In all the comparative graphs just mentioned and for the numerical CPT tests we present (i) the raw, uncorrected, numerical data and (ii) the exponential curve-fit to these data. For the physical CPT tests we present the uncorrected raw data.

For similar initial conditions (σ and D_R) and BC3 boundary conditions the cone tip resistance (q_c) obtained numerically is very close to the experimental one (Figure 152a). The behavior of both normally consolidated and overconsolidated tests is similar. The difference between numerical and physical tests do increase somewhat with mean stress level (Figure 7.4.2) and can be explained by the small discrepancies of initial state shown in Figure 146 between corresponding numerical and physical tests. Note that the larger discrepancies between the experimental and numerical trends appear when the probe approaches the lower horizontal boundary. As mentioned before that boundary condition was differently implemented in the numerical experiments (fixed displacement at the bottom, constant stress at the top) and in the physical ones

(constant stress at the bottom, fixed displacement at the top). In chapter 9 the effect of this switch on the CPT result is thoroughly explored, here is enough to say that it does indeed explain the discrepancy noted here.

On the other hand, the results from the BC1 cases in the numerical model are well below their physical counter parts. Even after both numerical and empirical results are corrected for chamber size effects (152b) using empirical equations 7.2and 7.3 only a small improvement is observed. Several factors might explain this observation (a) the extrapolation of the empirical correction factor to a range of Rd below the one where it was originally established. (b) the effect of the relative discrepancy in initial D_R between physical and numerical results on the CF function (Figure 143) and (c) the effect of that initial error on the test response, even discounting that due to the size effect correction.

The first two factors-in essences, linked to the appropriateness of the CF formulation-cannot be addressed at this stage. But we can explore here the possible influence of the third factor i.e. the different initial states (porosity, relative density) using the following empirical results. For the sake of clarity the symbols with subindex **n** will reffer to numerical tests and with subindex **p** to physical tests. Hence, using expression propsed by Jamiolkowski et al. [2003] (A and B) and Houlsby and Hitchman [1988] (C) we obtained the following correction or comparison factors:

(A) initial density factor:

$$cf_{D_R}(\Delta D_R) = exp\left[C_1\left({D_R}^{(\mathbf{n})} - {D_R}^{(\mathbf{p})}\right)\right] \tag{7.5}$$

D_R [-], C_2=2.97

(B) initial mean stress factor:

$$cf_{p_0}(\Delta p_0) = \left(\frac{{p_0}^{(\mathbf{n})}}{{p_0}^{(\mathbf{p})}}\right)^{C_1} \tag{7.6}$$

p_0 [kPa], C_1=0.56

(C) initial horizontal stress factor

$$cf_{\sigma_h}(\Delta \sigma_h) = \left(\frac{{\sigma_h}^{(\mathbf{n})}}{{\sigma_h}^{(\mathbf{p})}}\right)^{0.6} \tag{7.7}$$

σ_h [kPa]

Since both calibration chamber sizes are different, each test will have its own chamber size effect correction factor (note that the chamber size effect correction factor is like a comparison factor between a chamber test and an ideal test in the field) from which we deduce a final chamber size difference comparison factor.

$$cf(\Delta R_d) = \frac{CF(R_d, D_R)^{(\mathbf{p})}}{CF(R_d, D_R)^{(\mathbf{n})}} \tag{7.8}$$

So now we have that in theory either

$$\left(\frac{{q_c}^{(\mathbf{n})}}{{q_c}^{(\mathbf{p})}}\right)_{raw} = cf_{R_d}(\Delta R_d) \cdot cf_{D_R}(\Delta D_R) \cdot cf_{p_0}(\Delta p_0) \tag{7.9}$$

or if horizontal stress effect is dominant

$$\left(\frac{q_c{}^{(n)}}{q_c{}^{(p)}}\right)_{raw} = cf_{R_d}(\Delta R_d) \cdot cf_{D_R}(\Delta D_R) \cdot cf_{\sigma_h}(\Delta\sigma_h) \tag{7.10}$$

The effect of changes in mean/horizontal stress, relative density and relative cone size is summarized in Table 24 and shown in Figure 154.

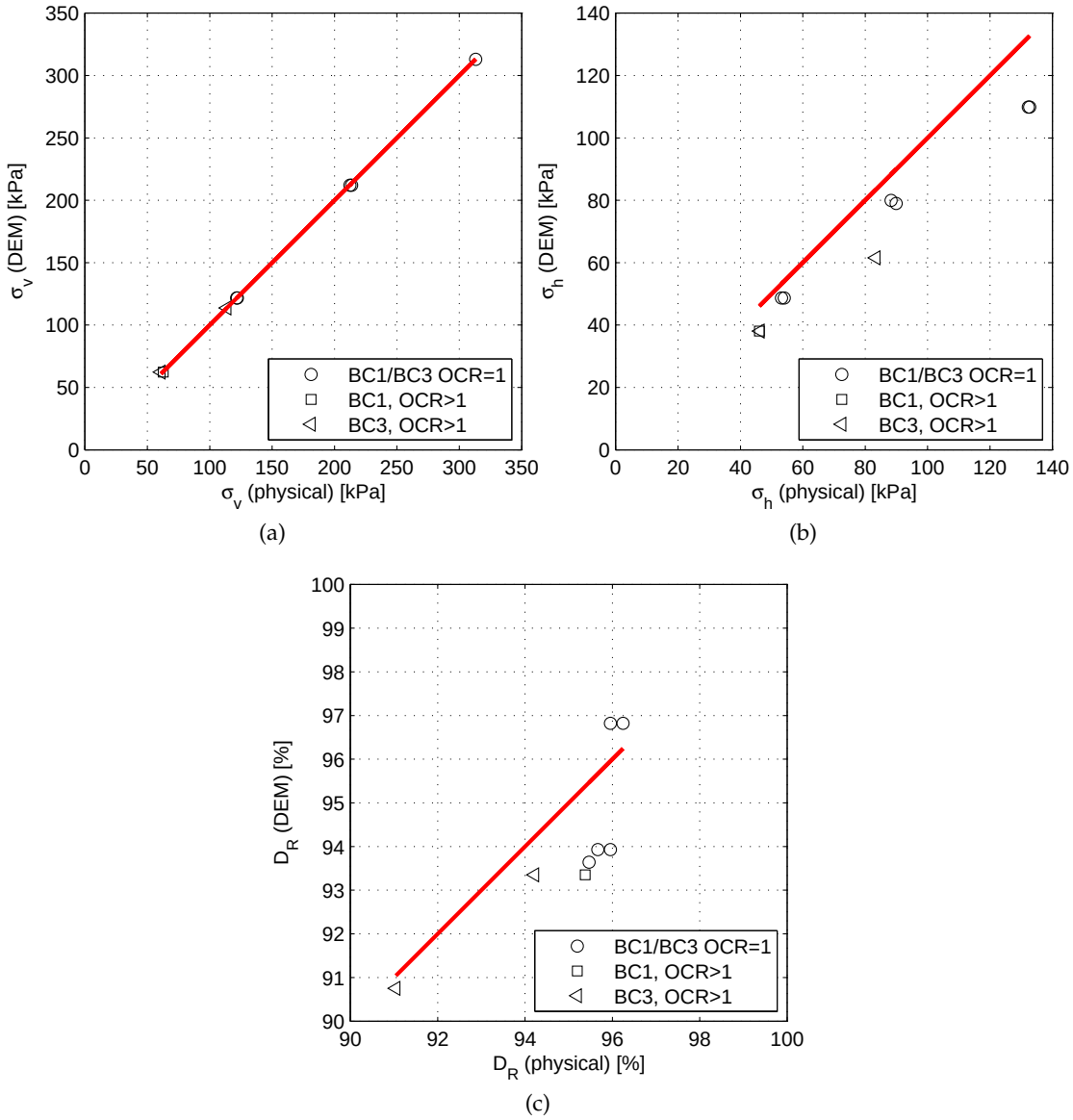

Figure 146: Comparison of vertical stresses, horizontal stresses and relative density at initial conditions between physical and numerical tests (Series B)

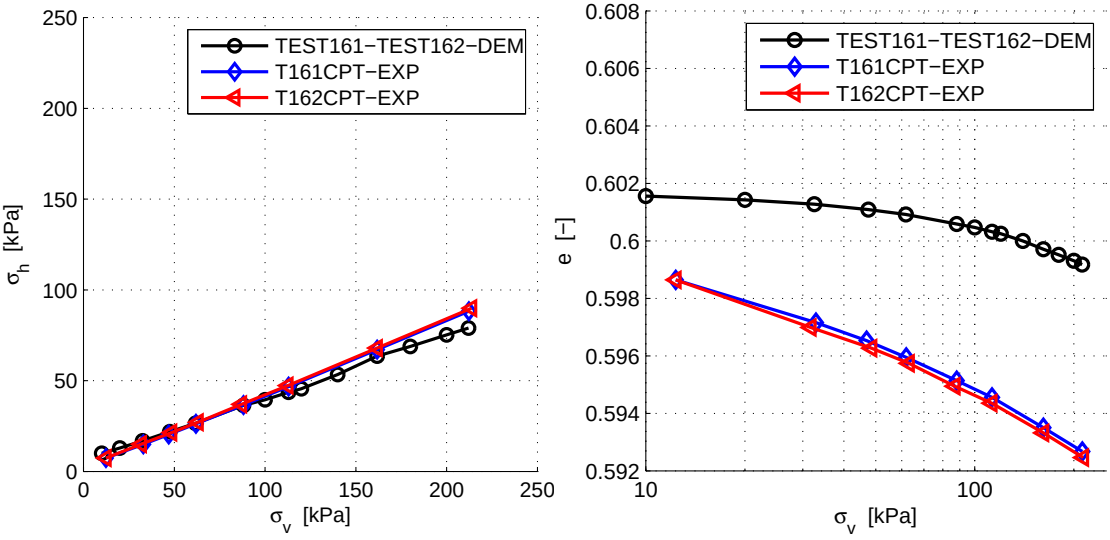

(a) consolidation stage: σ_v vs. σ_h (b) consolidation stage: e vs. σ_v

Figure 147: Comparison of numerical results with corresponding experimental tests: 1D compression test

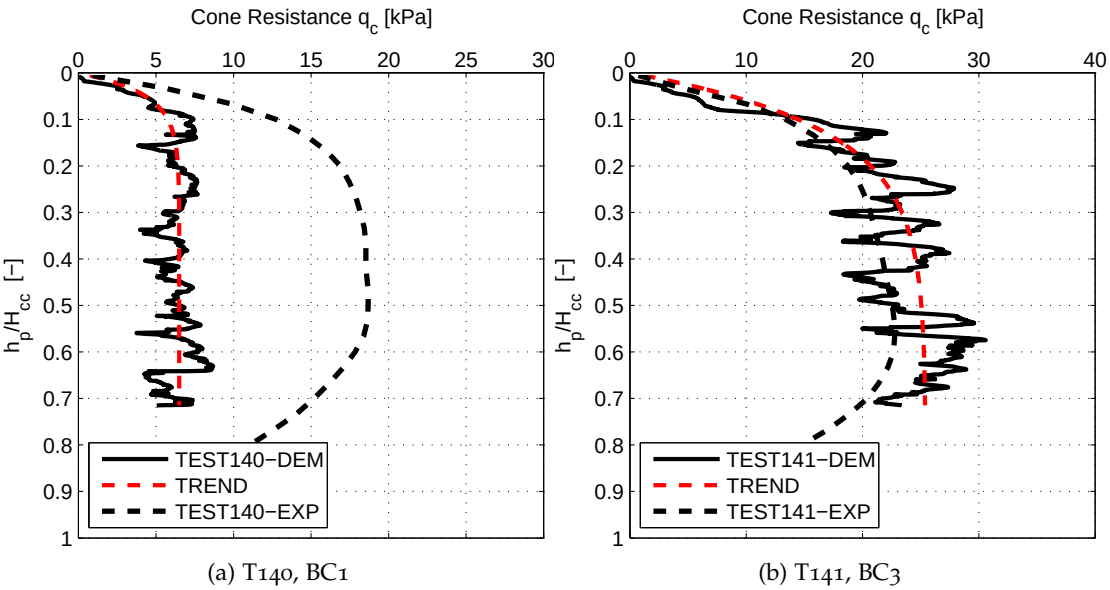

(a) T140, BC1 (b) T141, BC3

Figure 148: Comparison of raw experimental q_c with raw numerical fit curve; NUM/EXP: σ_v = 121.6 kPa, NUM:σ_r = 48.7 kPa, D_R = 93.9% EXP:σ_r = 54kPa and D_R = 95.5%

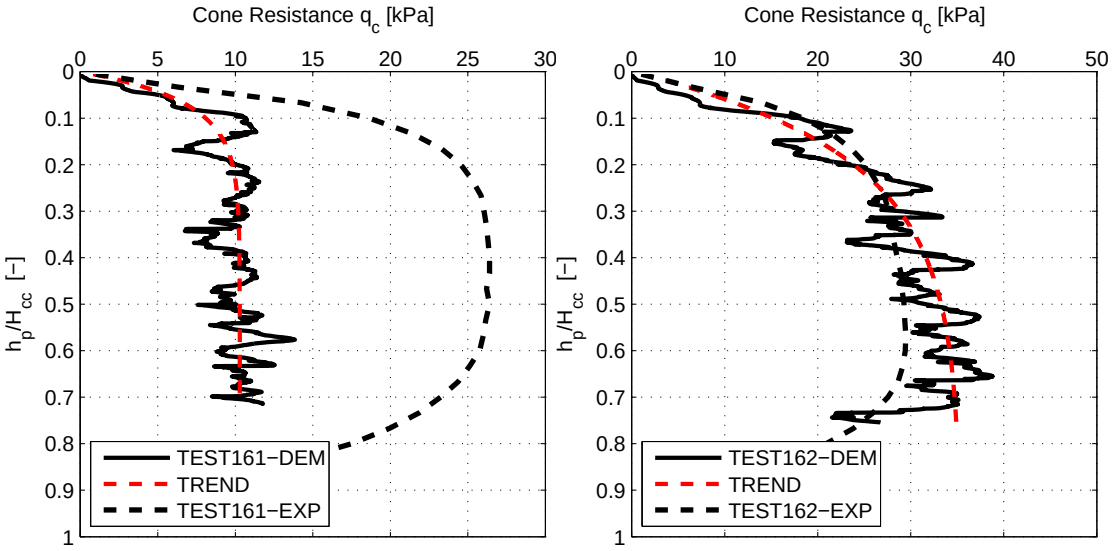

(a) T161, BC1 (b) T162, BC3

Figure 149: Comparison of raw experimental q_c with raw numerical fit curve; NUM/EXP: $\sigma_v = 212.6$ kPa, NUM:$\sigma_r = 78.7$ kPa, $D_R = 93.9\%$ EXP:$\sigma_r = 88.3$ kPa and $D_R = 95.9\%$

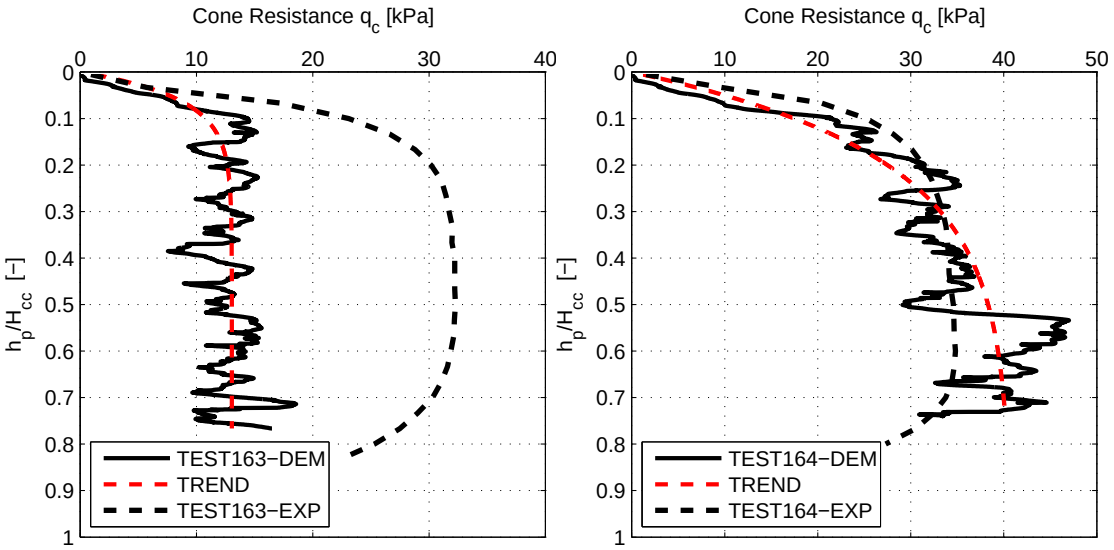

(a) T163, BC1 (b) T164, BC3

Figure 150: Comparison of raw experimental q_c with raw numerical fit curve; NUM/EXP: $\sigma_v = 313$ kPa, NUM:$\sigma_r = 109.91$ kPa, $D_R = 96.8\%$ EXP:$\sigma_r = 132.7$ kPa and $D_R = 96.2\%$

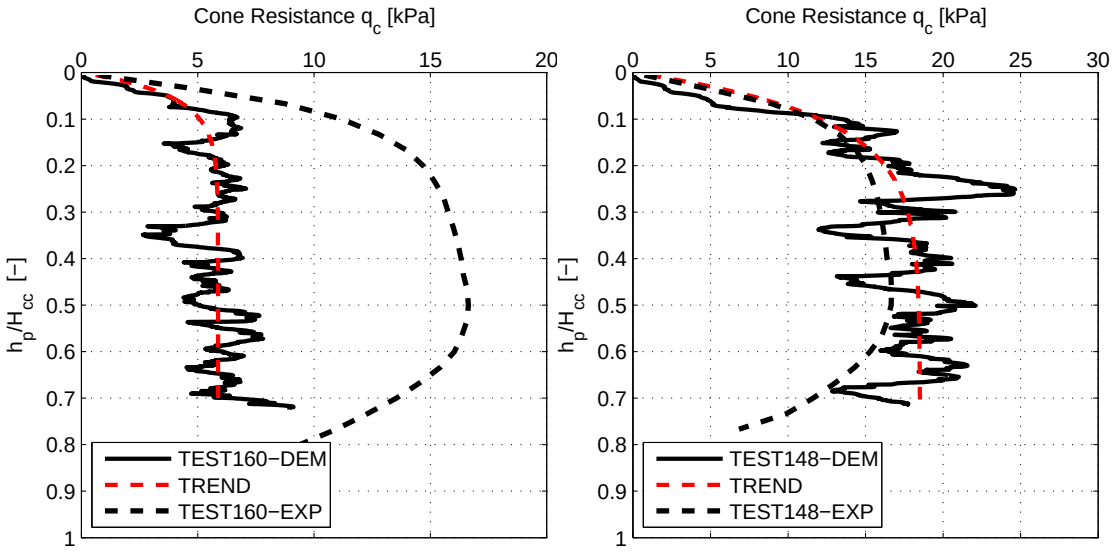

(a) T160, BC1, OCR=3.396

(b) T148, BC3, OCR=3.545

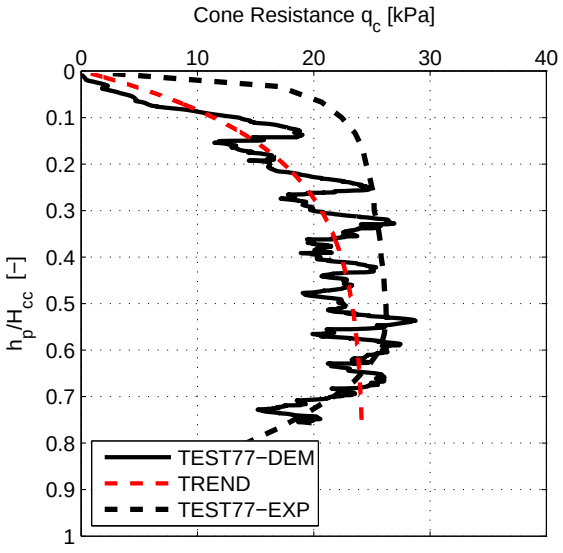

(c) T77, BC3, OCR=2.8

Figure 151: Comparison of raw experimental q_c with raw numerical fit curve

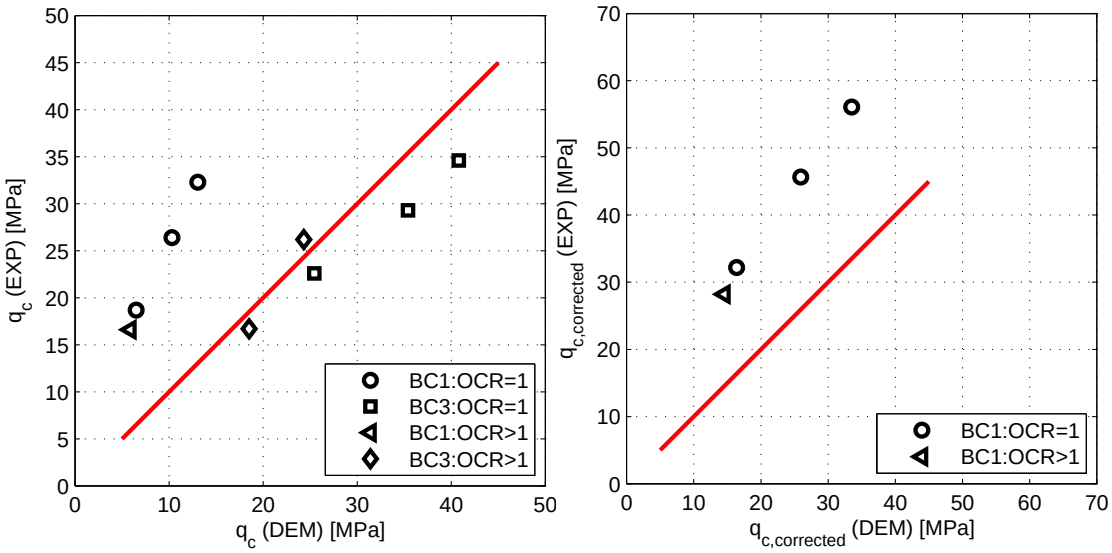

(a) raw results (b)

Figure 152: Comparison of (a) raw and (b) corrected cone resistance from non isotropically confined DEM tests and the experimental results performed in the physical CC in Ticino sand

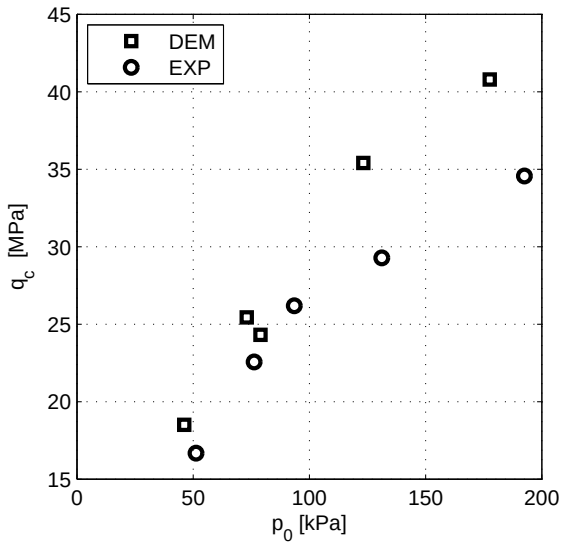

Figure 153: Changes in raw cone resistance from non isotropically confined DEM tests and the experimental results performed in the physical CC in Ticino sand with mean effective stress

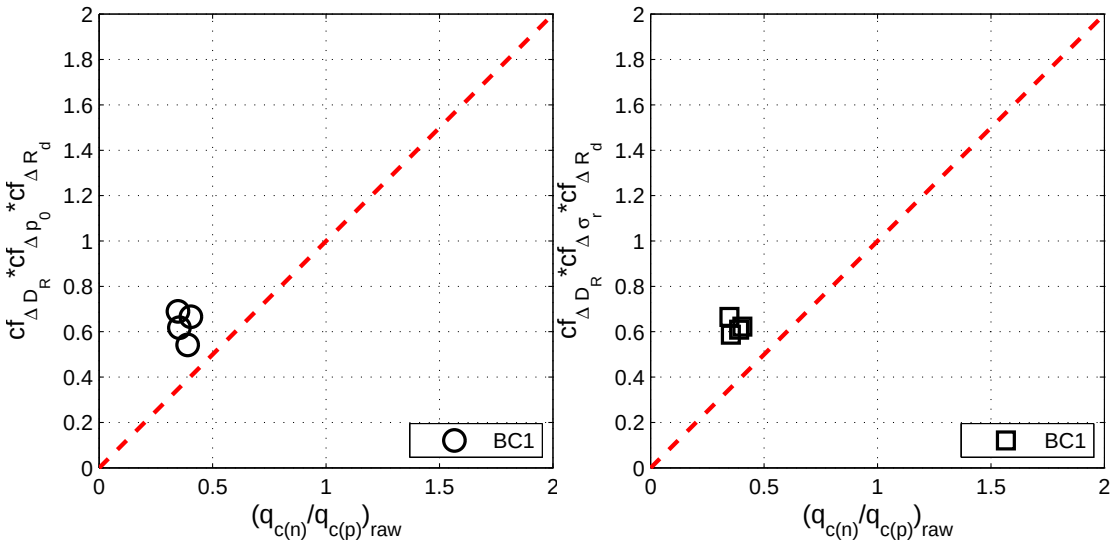

(a) (b)

Figure 154: Correction function combining (a) mean stress (p), (b) horizontal stress (σ_h) and relative density (D_R) and relative cone size (R_d) changes

Table 22: Summary of the simulation program

ID			VCC			ConStage			Type		
Model	Series	Tests	d_c	D_{cc}	H_{cc}	σ_{v0}	σ_{h0}	D_R	BC	AreaFactor	OCR
[-]	[-]	[-]	[mm]	[mm]	[mm]	[kPa]	[kPa]	[%]	[-]	[-]	[-]
(1)	(2)	(3)	(4)	(5)	(6)	(7)	(8)	(9)	(10)	(11)	(12)
1	A	T15	72.1	1200	700	60	60	75.2	1	1	1
		T16				100	100	75.2			
		T17				200	200	76.8			
		T18				300	300	77.6			
		T19				400	400	78.4			
		T20				100	100	90.7			
		T21				140	140	91.4			
		T22				200	200	92.2			
		T23				300	200	92.9			
	B	T140				121.6	48.69	93.9			
		T161				212.1	78.69	93.9			
		T163				313	109.91	96.8			
		T141				121.6	48.69	93.9	3		
		T162				212.1	78.69	93.9			
		T164				313	109.91	96.8			
		T160				62.3	38.05	93.4	1		3.396
		T148				62.3	38.05	93.4	3		3.545
		T77				113.7	61.55	90.8			2.8

2	C	T25	106.8		100	100	75.2	1		1	
		T26	142.4								
		T27	213.6								
		T29	106.8				90.7				
		T30	142.4								
		T31	213.6								
3	D/E	T32	72.1				76.0		0.5		
		T33					90.7				
	E	T50					61.3				
		T51			200	200	62.4				
		T52			300	300	64.6				
		T53			400	400	64.7				
4	D/F	T34			100	100	72.8		0.25		
		T35					86.1				
	F	T36		1580			72.8				
		T37		2400			72.0				
		T38		800			72.0				
		T39		600			73.6				
		T40		400			72.0				
		T41		1580			86.1				
		T42		2400			89.1				
		T43		800			89.9				
		T44		600			89.2				
		T45		400			86.9				

	G	SIM1-B1	71.2	2400	700	121.6	45.43	94.3			
		SIM2-B1		1580			46.41	94.2			
		SIM3-B1		1200			46.12	94.3			
		SIM4-B1		1000			45.52	94.0			
		SIM5-B1		800			44.26	94.2			
		SIM6-B1		600			45.19	94.6			
		SIM7-B1		400			42.70	92.8			
		SIM1-B3		2400			45.43	94.3	3		
		SIM2-B3		1580			46.41	94.2			
		SIM3-B3		1200			46.12	94.3			
		SIM4-B3		1000			45.52	94.0			
		SIM5-B3		800			44.26	94.2			
		SIM6-B3		600			45.19	94.6			
		SIM7-B3		400			42.70	92.8			
	H	SIM5-B1(b)		800			44.26	94.2	1		
		SIM5-B3(b)							3		

Table 23: Summary of the CPT results, numerical, experimental and empirical

ID									NUM	EXP
Model	Serie	Tets	$a=q_{c,lim}$	b	R^2	$q_{c,emp}$	$q_{c,exp}$	CF_{num}/CF_{exp}	$q_{c,cor}$	$q_{c,cor}$
[-]	[-]	[-]	[MPa]	[MPa]	[-]	[MPa]	[MPa]	[-]	[MPa]	[MPa]
(1)	(2)	(3)	(4)	(5)	(6)	(7)	(8)	(9)	(10)	(11)
1	A	T15	6.77	20	0.412	16.1	-	2.01/-	13.6	-
		T16	10.36	20	0.594	21.4	-	2.01/-	20.81	-
		T17	16.14	20	0.780	33.1	-	2.05/-	33.12	-
		T18	19.85	20	0.735	42.6	-	2.07/-	41.15	-
		T19	22.71	20	0.795	51.2	-	2.09/-	47.67	-
		T20	12.92	20	0.436	34	-	2.42/-	31.32	-
		T21	15.34	20	0.623	41.9	-	2.44/-	37.48	-
		T22	21.51	20	0.719	52.3	-	2.46/-	53.01	-
		T23	25.42	20	0.675	67.5	-	2.48/-	63.17	-
	B	T140	6.49	31	-	-	18.7	2.52/1.72	16.37	32.18
		T161	10.29	22	-	-	26.4	2.52/1.73	25.93	45.65
		T163	13.04	25	-	-	32.3	2.57/1.74	33.51	56.10
		T141	25.44	12	-	-	22.6	1.0/1.0	25.44	22.57
		T162	35.41	8	-	-	29.3	1.0/1.0	35.41	29.28
		T164	40.80	8	-	-	34.6	1.0/1.0	40.80	34.57
		T160	5.87	29	-	-	16.6	2.48/1.70	14.56	28.20
		T148	18.51	15	-	-	16.7	1.0/1.0	18.51	16.68
		T77	24.32	9	-	-	26.2	1.0/1.0	24.32	26.20

2	C	T25	7.72	11	0.780	21.4	-	2.37/-	18.30	-
		T26	5.73	9	0.888	21.4	-	2.68/-	15.32	-
		T27	3.42	7	0.934	21.4	-	3.17/-	10.86	-
		T29	8.82	14	0.739	34.0	-	2.98/-	26.31	-
		T30	6.22	11	0.859	34.0	-	3.47/-	21.58	-
		T31	3.67	8	0.946	34.0	-	4.30/-	15.78	-
3	D/E	T32	11.30	1	0.427	22.0	-	2.03/-	22.94	-
		T33	13.80	2	0.349	34.0	-	2.42/-	33.45	-
	E	T50	9.64	6.5	0.472	14.32	-	1.63/-	15.70	-
		T51	15.39	7	0.717	21.81	-	1.66/-	25.56	-
		T52	17.70	9	0.554	28.37	-	1.69/-	29.91	-
		T53	20.56	10	0.604	34.43	-	1.72/-	35.36	-
4	D/F	T34	10.60	1	0.188	20.0	-	1.94/-	20.61	-
		T35	14.80	2	0.100	29.7	-	2.30/-	34.07	-
	F	T36	9.97	8	0.469	20.0	-	1.74/-	17.34	-
		T37	9.16	10	0.612	19.5	-	1.46-	13.37	-
		T38	8.97	17	0.697	19.5	-	2.26/-	20.26	-
		T39	7.40	36	0.310	20.4	-	2.61/-	19.31	-
		T40	5.73	29	0.222	19.5	-	2.97/-	17.04	-
		T41	12.65	2	0.722	29.7	-	2.01/-	25.38	-
		T42	15.91	13	0.722	32.7	-	1.66/-	26.41	-
		T43	11.09	2	0.819	33.2	-	2.97/-	32.94	-
		T44	8.08	33	0.511	32.5	-	3.41/-	27.58	-

		T45	6.38	39	0.614	30.4	-	4.04/-	25.77	-
	G	SIM1-B1	6.52	32	-	31.4	-	1.71/-	11.15	-
		SIM2-B1	7.73	18	-	31.5	-	2.17/-	16.78	-
		SIM3-B1	6.35	25	-	31.4	-	2.51/-	15.95	-
		SIM4-B1	5.10	44	-	31.2	-	2.81/-	14.35	-
		SIM5-B1	4.59	32	-	31.0	-	3.13/-	14.38	-
		SIM6-B1	3.28	53	-	31.7	-	3.69/-	12.12	-
		SIM7-B1	1.92	44	-	29.7	-	3.59/-	6.91	-
		SIM1-B3	12.72	11	-	31.4	-	1.00/-	12.72	-
		SIM2-B3	21.19	11	-	31.5	-	1.00/-	21.19	-
		SIM3-B3	26.94	9	-	31.4	-	1.00/-	26.94	-
		SIM4-B3	29.63	8	-	31.2	-	1.00/-	39.63	-
		SIM5-B3	27.00	11	-	31.0	-	1.00/-	27.00	-
		SIM6-B3	23.05	23	-	31.7	-	1.00/-	23.05	-
		SIM7-B3	28.23	7	-	29.7	-	1.00/-	28.23	-
	H	SIM5-B1(b)	5.34	32	-	31.0	-	3.13/-	16.72	-
		SIM5-B3(b)	8.09	32	-	31.0	-	3.13/-	25.35	-

Table 24: Summary of the correction differences

TEST ID	$cf_{\Delta R_D}$	$cf_{\Delta D_R}$	$cf_{\Delta p_0}$	$cf_{\Delta \sigma_h}$	Eqn. 7.9 (r)	Eqn. 7.10 (r)	$\left(\frac{q_c{}^{(n)}}{q_c{}^{(p)}}\right)_{raw}$
T140	0.68	1.04	0.97	0.94	0.69	0.67	0.35
T161	0.69	0.95	0.83	0.93	0.54	0.61	0.39
T163	0.68	1.03	0.95	0.89	0.67	0.62	0.40
T140	0.69	0.96	0.94	0.89	0.62	0.59	0.35
(r) - right side of the mentioned equations							

7.5 SIDE RESISTANCE

Although it was not a primary objective of this thesis some results on side resistance were also obtained and are discussed here. Side resistance was calculated from the shear tangential force (F_s) acting along a section (called sleeve by analogy with the arrangement in physical tests) of the penetrometer shaft divided by the sleeve area (A_s).

$$f_s = \frac{F_s}{A_s} \tag{7.11}$$

The standard penetrometer used in the physical reference chamber (Jamiolkowski et al. [2003]) had a diameter of 35.6 mm and a corresponding cross-sectional area of A_c=10 cm^2. The friction sleeve area was A_s=150 cm^2 corresponding to a height of 134 mm. The cone tip and friction sleeve were separated by a 5 mm cylindrical section (h_x).

In the numerical model the tip angle is 60° but the cone diameter, d_c, is 71.2 mm (twice size of a standard cone tip). Three frictional sleeves are incorporated in the shaft. Their lengths are noted h_{s1}, h_{s2} and h_{s3}, with the number increasing with distance from the tip. The cone tip is always completely rough (i.e. the cone-particle contact has the same friction as a particle-particle contact) while shafts varies in friction. A section of the shaft just behind the cone tip, of length h_x, is frictionless and separates cone tip and the first sleeve.

The length of the second and third sleeves is always equal to 100 mm. The length of the first sleeve was set to three different values: (a) h_{s1}=100 mm which was the initial simulation default, (b) h_{s1}=134 mm-equal in length to that of the standard cone and (c) h_{s1}=67 mm which will give a sleeve equal in area to that of a typical cone. A summary of geometrical characteristics of the VCC, CPT and physical model are collected in Table 25.

The position of each sleeve (h_{si}, i=1,2,3) can be best tracked by the distance of its center (Figure 155) to the cone tip (z_i) normalized by the cone diameter (d_c):

$$h_{si} = \frac{z_i}{d_c} \tag{7.12}$$

The normalized position of each section, $\frac{z_i}{d_c}$, is collected in Table 26. Table 27 collects the results of series A, for which $h_{s1} = h_{s2} = h_{s3}$=100 mm. Additionally to Series A, sixteen extra CPT tests were performed expressly to examine various effects on side friction. The characteristics of these tests, organized on two separate series, are summarized on Table 28.

The first test series (NUM1) contains six tests for each calibration chamber boundary conditions, viz. BC1 and BC3 and had varying geometrical sleeve arrangements, as previously described. These tests are named in the following manner: T_hx_hs1_BC, where h_x is a separation length, h_{s1} is a height of the first sleeve and BC is a type of boundary conditions.

The second test series (NUM2) contained five tests in which different shaft frictions were applied. These tests with different shaft friction are named as follows. T_10_134_1_fri, where fri is a friction of the first shaft.

All these tests were performed under anisotropic stress conditions, directly analogous to those reigning in two physical tests reported by Baldi et al. [1986a] (T140e and

T141e), whose data are also collected in Table 28. Indeed, after normal consolidation to similar vertical stress as in the physical tests, the numerical tests have a similar initial relative density (93.9%) and horizontal stress (49 kPa) than the physical tests (93% and 53-54 kPa). Therefore a direct comparison is possible, bearing in mind the differences in chamber and cone size already commented.

An example of sleeve response is shown in Figure 156. The response is noisy, especially for the sleeve closest to the cone tip. As shown above for the cone-tip behavior such noise is a consequence of the scaled up particle size and should be filtered. Moreover, Butlanska et al. [2013a]] show that steady state values of macro responses such as cone tip resistance, can be easily identified by observing steady states of micro responses, such as particle- cone contact number. The same approach was followed here for sleeve friction and a steady state depth (h_{ss}) was chosen as the depth were sleeve-particle contacts stabilize around constant value (N_{ss}). Therefore, a representative friction was then obtained as the average value recorded below that depth. Typically that happened slightly after the whole sleeve was inserted on the discrete media.

In most of the CPT tests performed an important reduction in shaft resistance with sleeve distance to the tip can be observed. It can be seen that for the shaft section just behind the cone tip (sleeve-1) the maximum resistance is registered. A similar effect was already noted in physical measurements by Campanella and Robertson [1981] who observed that shaft friction had a marked maximum behind the tip before stabilizing farther from the tip. DeJong and Frost [2002] used a multi-sleeve friction attachment for CPT to measure shaft resistance at different levels (167-1517 mm behind the cone tip). The sounding indicated no reduction in shaft friction (smooth shaft) between 4-35d_c behind the cone tip. However, the readings were lower than the sleeve friction measured at the standard location (i.e. near the cone tip), once again indicating the presence of a high or peak friction zone just behind the cone tip that decreased and stabilized up above the shaft. This is compatible with the results of the numerical simulations here presented, since the centroid of the third shaft is still only between 4 to 5 diameters behind the cone tip.

7.5.1 *Effect of initial state: stress state and relative density*

Figure 157 shows changes in f_S measured for initial isotropic stresses ranging from 60 to 400 kPa and $D_R = 75\%$ (Series A). It can be observed that, for every segment, f_s follows the similar trends as the cone tip resistance; steady state f_{si} increases with confining pressure and to a lesser degree, with relative density (Figure 158 and Figure 159). In fact, the effect of initial relative density diminishes with sleeve distance up the shaft and this is coherent with the creation of a remoulded steady state around the cone shaft. Moreover, f_s-curves at sections 2 and 3 have a similar pattern and are much less noisy that those corresponding to section 1 (σ reduces). The values of sleeve resistance, steady state depth and number of steady state sleeve-particle contacts are collected in Table 27. It can be observed, that steady state depth of corresponding sleeve is independent on initial stress and relative density and is reached in average at 180 mm (2.5d_c), 280 mm (3.9d_c) and 380 mm (5.3d_c) above the cone tip for sleeve 1, 2 and 3, respectively. Moreover, Figure 160 shows changes in mobilized shaft friction, with relative density and initial stress state.

7.5.2 *Effect of sleeve size and position*

In the simulations on series NUM1 three different first sleeve lengths were used; 67, 100 and 134 mm. An important increase in side response with shaft size is observed under BC3, on the contrary the effect of sleeve size is not that clear for BC1 (Table 29). It can also be observed that the steady state depth (hss), at which the number of elements in contact with the sleeve stabilizes increases with sleeve size. For example for the sleeve-1 the average hs1 is reached at 145 mm (2dc), 180 mm (2.5dc) and 220 mm (3dc) above the cone tip for sleeve height equal to 67 mm, 100 mm and 134 mm, respectively. For the second (third) sleeve the steady state is reached at 3.3dc (4.9dc), 3.9dc (5.3dc) and 4.7dc (5.9dc) for 67-, 100- and 134- mm sleeve. In general, the steady state is reached around 19 mm above the depth of completely submerged sleeve. Figure 161 shows the numerical/physical comparison of normalized shaft resistance with with normalized position of the centroid of corresponding sleeves.

Two effects are noted from the inclusion of an intermediate frictionless sleeve just behind the tip. Figures 162a and 162c show that when the first sleeve is located directly behind the cone tip its friction response shows a quite large peaks and troughs. The oscillation amplitude reduces if we incorporate the separation element between the cone tip and the shaft (Figures 162b and 162d). Apart from this, inspection of Table 29 shows that pushing back sleeve 1 always result in a friction measurement in that sleeve that is closer to those of sleeves 2 and 3. This might be related to the reduction in stresses caused by the shape of the high stress field located around the cone tip.

7.5.3 *Effect of radial boundary conditions*

Two types of radial boundary conditions were applied, viz. BC1 (σ_r=const. and σ_z=const) and BC3 (σ_z=const. and ϵ_r=0). Figure 162 shows the example of shaft resitance (1, 2 and 3) measured for different radial boundary conditions. It can be observed that no radial displacement conditions (BC3) led to mush higher steady state shaft resistance than constant stress boundary conditions (BC1). Moreover, the existance of an intermediate frictionless sleeve just behind the tip and size of the shaft also affects the shaft readings. Hence, for $h_x = 0$ the average (mean value taken from test with different shaft sizes but similar radial boundary conditions) f_{si} measured under BC3 conditions is 10, 42 and 44 greater than steady state f_si measured under BC1 for shaft 1, 2 and 3, respectively. For $h_x = 10$ the average f_{si} measured under BC3 conditions is 20, 47 and 55 greater than steady state f_si measured under BC1 for shaft 1, 2 and 3, respectively. This changes in shaft resistance might be explained by high stress gradient located around the cone tip, which includes a bulb of radial stresses in the vicinity of the cone, reaching a maximum close to the tip and decreasing up the shaft. Such a radial stress bulb has been indeed obtained by mesoscopic analysis of the discrete element simulations (Butlanska et al. [2013c]). More details about effect of boundary conditions on the CPT results may be found in Chapter 8.

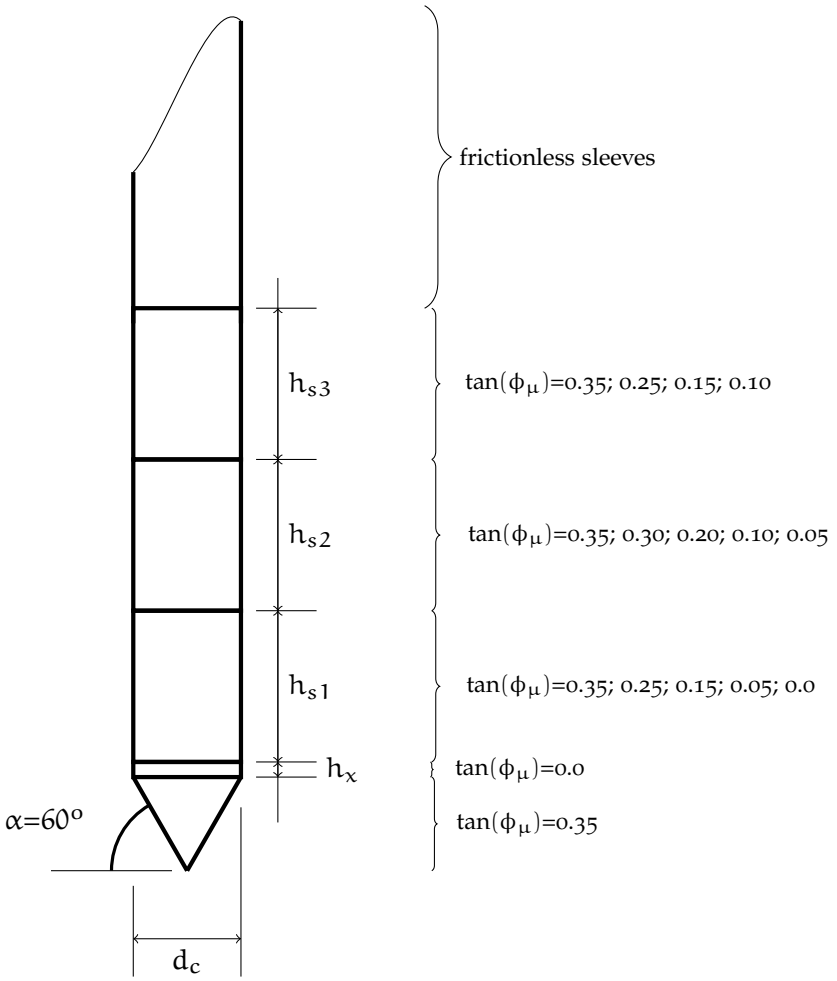

Figure 155: Position of each sleeve section

7.5.4 *Effect of shaft friction*

The effect of the shaft roughness was examined on T_10_134_1 test by comparing (a) the measured shaft resistances with corresponding shaft friction and (b) applied shaft friction with mobilzed shaft friction. The mobilized shaft friction was caluclated as:

$$\tan(\phi_m) = \frac{f_{si}}{\sigma_c} \tag{7.13}$$

where f_{si} is a measured shaft resistance and σ_c is horizontal stress acting at the corresponding section.

Figure 163a shows the relationship between sleeve resistance and friction coefficient between device and the spherical particles. The sleeve response increases as the sleeve roughness (texture) increases. Similar trend was observed by Frost et al. [2013] while using cyclic multi-piezo-friction sleeve for liquefaction assessment. Figure 163b shows the comparison between $\tan(\phi_\mu)$ and $\tan(\phi_m)$, measured at the corresponding sleeve element.

Table 25: Summary of geometrical characteristic of CC

Dimensions	D	H	d_c	h_x	h_{s1}	h_{s2}	h_{s3}
Units	[mm]						
Physical CC	1200	1500	35.7	5	134	-	-
Numerical VCC	1200	700	71.2	0;10	67;100;134	100	100

Table 26: Summary of position of each sleeve

		h_x=0			h_x=10		
	shaft 1	67	100	134	67	100	134
	z1	1.34	1.57	1.81	1.48	1.70	1.95
shaft2	z2	2.51	2.97	3.45	2.65	3.12	3.59
shaft3	z3	3.92	4.38	4.86	4.06	4.52	4.99

Table 27: Results of Series A

Model		1								
Serie		A								
Test		T15	T16	T17	T18	T19	T20	T21	T22	T23
p_0	[kPa]	60	100	200	300	400	100	140	200	300
D_R	[%]	75.2	75.2	76.8	77.6	78.4	90.7	91.4	92.2	92.2
$a=q_{c,lim}$	[MPa]	6.44	10.36	16.14	19.85	22.71	12.92	15.34	21.51	25.42
f_{s1}	[kPa]	248.2	250.3	1409	2251	2823	427.8	1394	2324	3204
σ	[-]	147	107	410	604	555	132	413	469	637
CV	[%]	59	43	29	27	20	31	30	20	20
N_{ss1}	[-]	42	44	45	44	44	44	43	46	43
h_{ss1}	[mm]	179	185	179	179	178	181	183	176	180
f_{s2}	[kPa]	25.26	67.47	615.5	808.5	1536	78.3	402.5	770.9	1384
σ	[-]	14	17	222	259	259	14	123	285	246
CV	[-]	55	25	36	32	17	18	30	37	18
N_{ss2}	[-]	45	45	43	42	42	43	41	43	41
h_{ss2}	[mm]	278	283	278	282	280	278	283	280	282
f_{s3}	[kPa]	31.35	55.21	621.6	808.9	1390	57.25	297.0	493.7	1100
σ	[-]	14	20	171	204	267	15	110	255	215
CV	[-]	45	36	27	25	19	26	37	52	19
N_{ss3}	[-]	45	45	41	50	40	43	41	44	41
h_{ss3}	[mm]	378	385	379	378	380	378	382	380	381

Table 28: Test program

	TEST ID	BC	h_x [mm]	h_{s1} [mm]	σ_z [kPa]	σ_h [kPa]	D_R [%]	$\tan(\phi_{\mu,s1})$ [-]	$\tan(\phi_{\mu,s2})$ [-]	$\tan(\phi_{\mu,s3})$ [-]
EXP	T140e	1	5	134	121.6	54.1	92.62	-	-	-
	T141e	3			122.2	53.2	92.52	-	-	-
NUM1	T_0_67_1	1	0	67	121.6	48.69	93.9	0.35	0.35	0.35
	T_0_100_1			100						
	T_0_134_1			134						
	T_10_67_1		10	67						
	T_10_100_1			100						
	T_10_134_1			134						
	T_0_67_1	3	0	67						
	T_0_100_1			100						
	T_0_134_1			134						
	T_10_67_1		10	67						
	T_10_100_1			100						
	T_10_134_1			134						
NUM2	T_10_134_1_025	1	10	134				0.25	0.30	0.35
	T_10_134_1_015							0.15	0.20	0.25
	T_10_134_1_005							0.05	0.10	0.15
	T_10_134_1_000							0.00	0.05	0.10

Table 29: Results of Series NUM1

	BC1					
	h_x=0			h_x=10		
f_s \ Test ID	T_0_67_1	T_0_100_1	T_0_134_1	T_10_67_1	T_10_100_1	T_10_134_1
f_{s1} [kPa]	195.7	162.6	211.3	47.08	45.54	137.0
h_{ss1} [mm]	147	183	216	148	184	223
N_{ss} [-]	31	44	57	26	39	59
f_{s2} [kPa]	33.16	24.63	23.84	33.03	22.57	26.33
h_{ss2} [mm]	225	282	323	247	279	328
N_{ss} [-]	43	44	45	45	44	43
f_{s3} [kPa]	24.32	20.91	21.65	19.26	18.49	25.33
h_{ss3} [mm]	351	383	430	354	387	425
N_{ss} [-]	45	43	44	44	43	44

	BC3					
	h_x=0			h_x=10		
f_s \ Test ID	T_0_67_3	T_0_100_3	T_0_134_3	T_10_67_3	T_10_100_1	T_10_134_1
f_{s1} [kPa]	1582	1818	2373	769	1215	2823
h_{ss1} [mm]	145	178	216	142	176	225
N_{ss} [-]	33	45	56	28	41	60
f_{s2} [kPa]	1227	1115	1115	1345	1197	1307
h_{ss2} [mm]	243	278	366	247	280	328
N_{ss} [-]	43	42	42	43	46	43
f_{s3} [kPa]	1005	993.4	987.4	1213	988.4	1271
h_{ss3} [mm]	352	378	410	341	377	428
N_{ss} [-]	43	42	42	44	46	45

Table 30: Effect of sleeve friction

NUM1	Test ID	T_10_134_1				
		sleeve-1				
$\tan(\phi_\mu)$		0.35	0.25	0.15	0.05	0.00
f_{s1}	[kPa]	137.0	56.5	18.9	8.6	0.25
N_{ss1}	[-]	59	50	53	50	50
h_{ss1}	[mm]	223	182	210	216	217
		sleeve-2				
$\tan(\phi_\mu)$		0.35	0.30	0.20	0.10	0.05
f_{s2}	[kPa]	26.3	30.2	18.5	8.9	4.6
N_{ss2}	[-]	43	43	45	43	45
h_{ss2}	[mm]	328	322	311	318	316
		sleeve-3				
$\tan(\phi_\mu)$		0.35	0.25	0.15	0.10	
f_{s3}	[kPa]	25.0	21.0	12.3	6.8	
N_{ss3}	[-]	44	43	44	45	
h_{ss3}	[mm]	424	419	418	417	

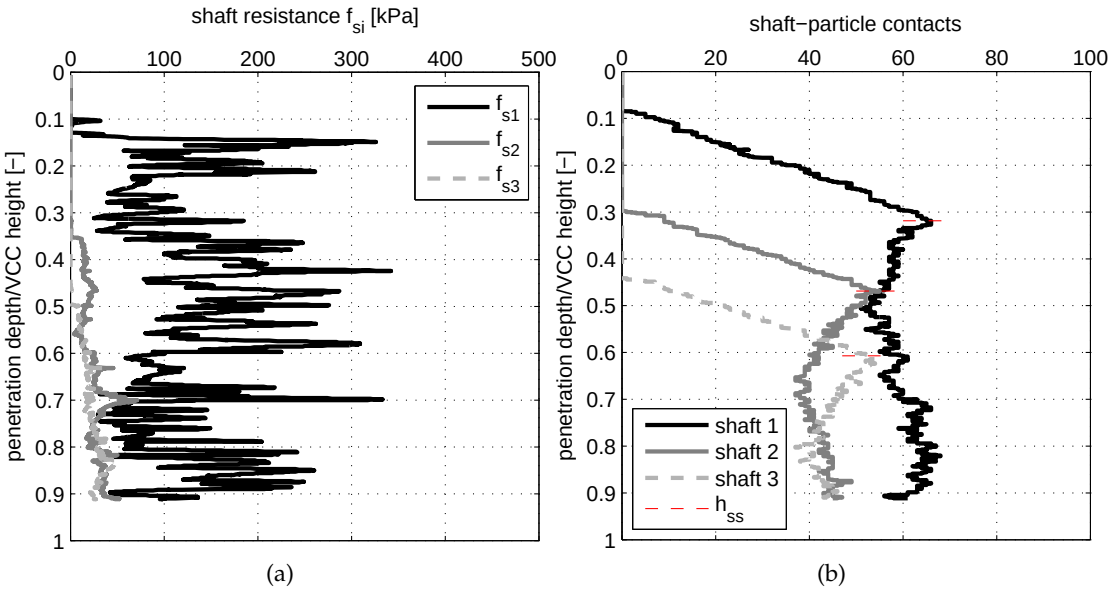

Figure 156: Example of (a) raw shaft resistance curves and (b) selecting the position of the steady state depth

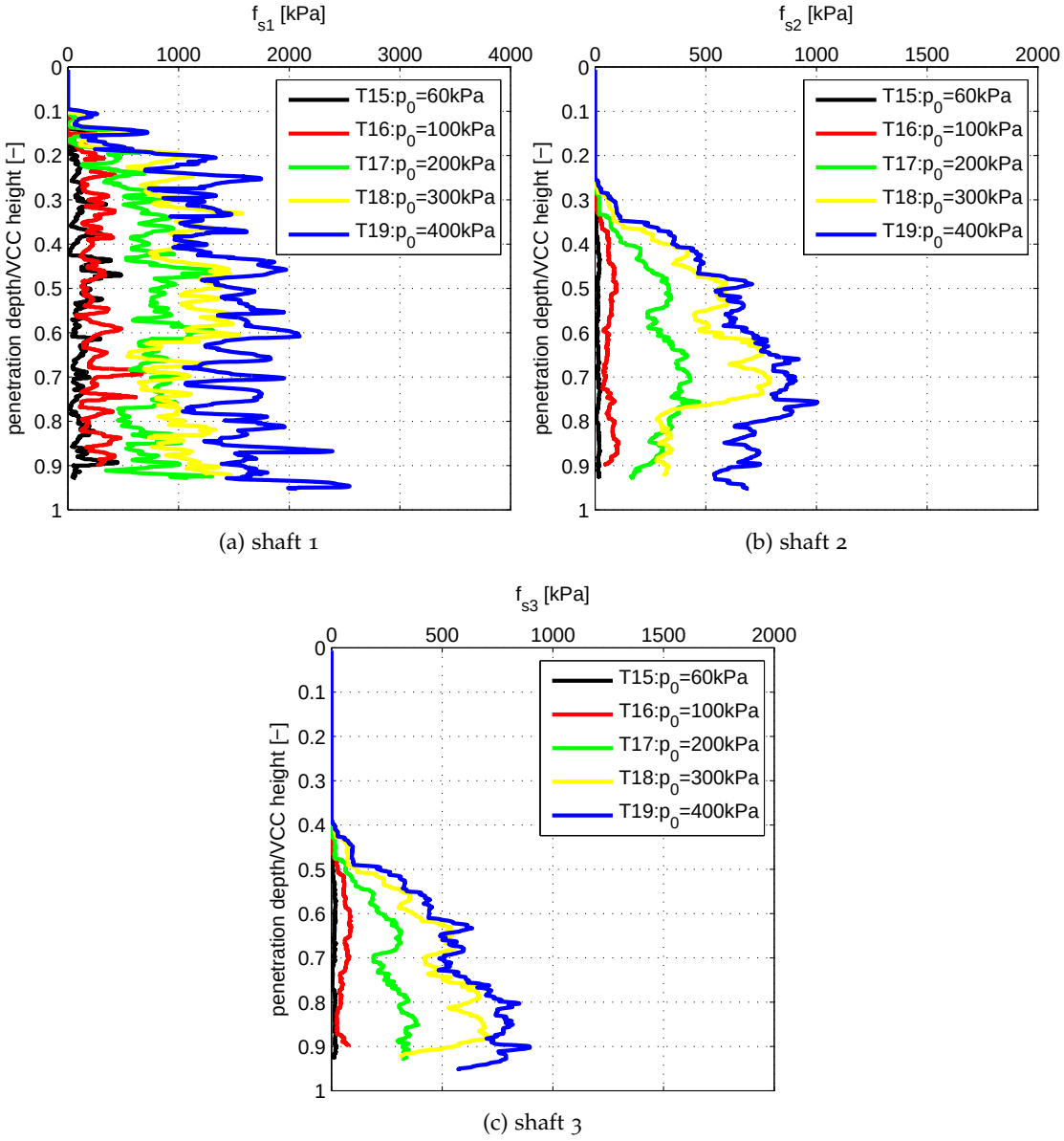

(a) shaft 1

(b) shaft 2

(c) shaft 3

Figure 157: Raw shaft resistance curves for Model 1 Series A for isotropic consolidation and D_R=75 %

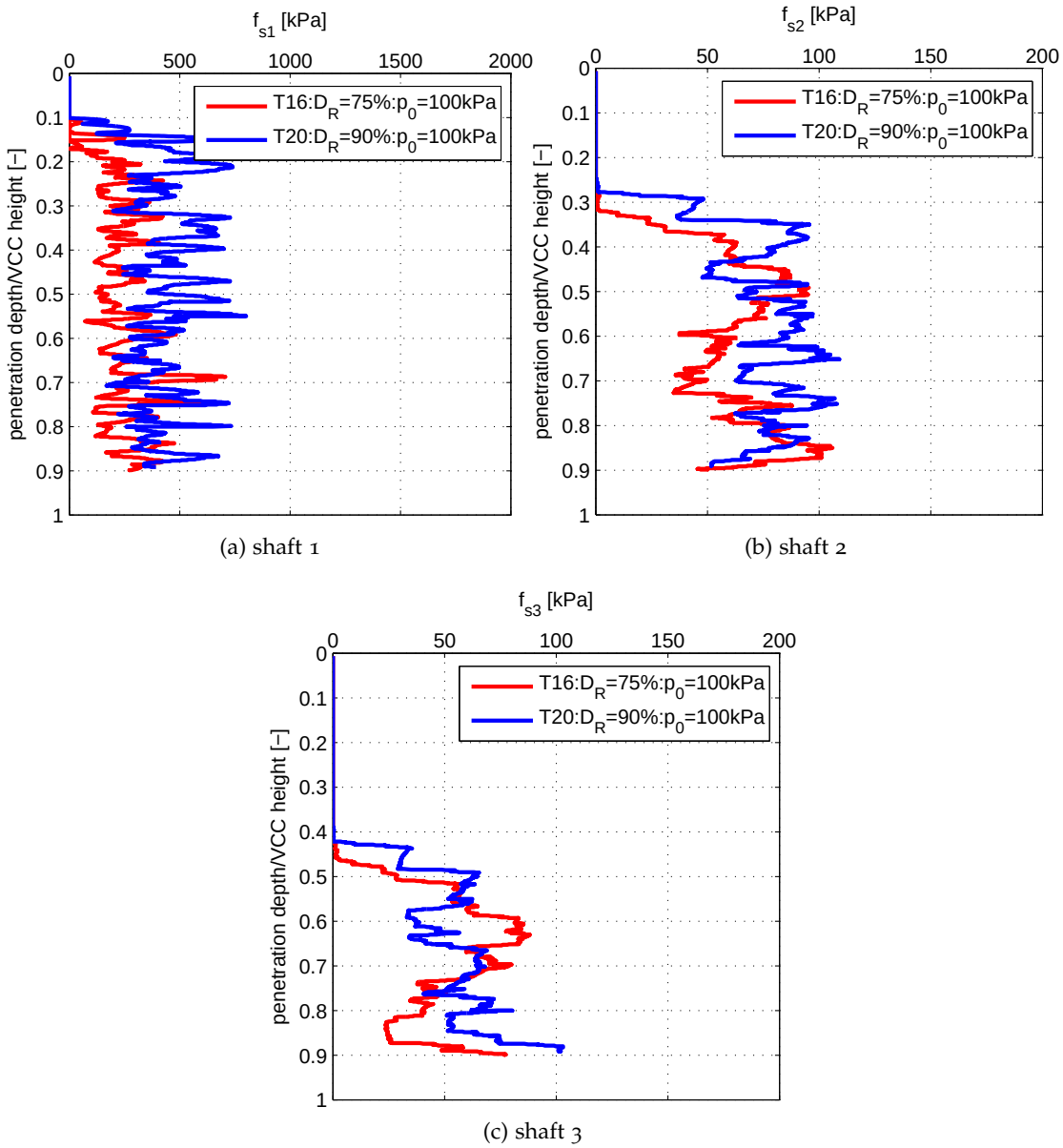

(a) shaft 1

(b) shaft 2

(c) shaft 3

Figure 158: Changes of shaft resistance with relative density D_R = 75 and 90 % (a) shaft 1 (b) shaft 2 and (c) shaft 3

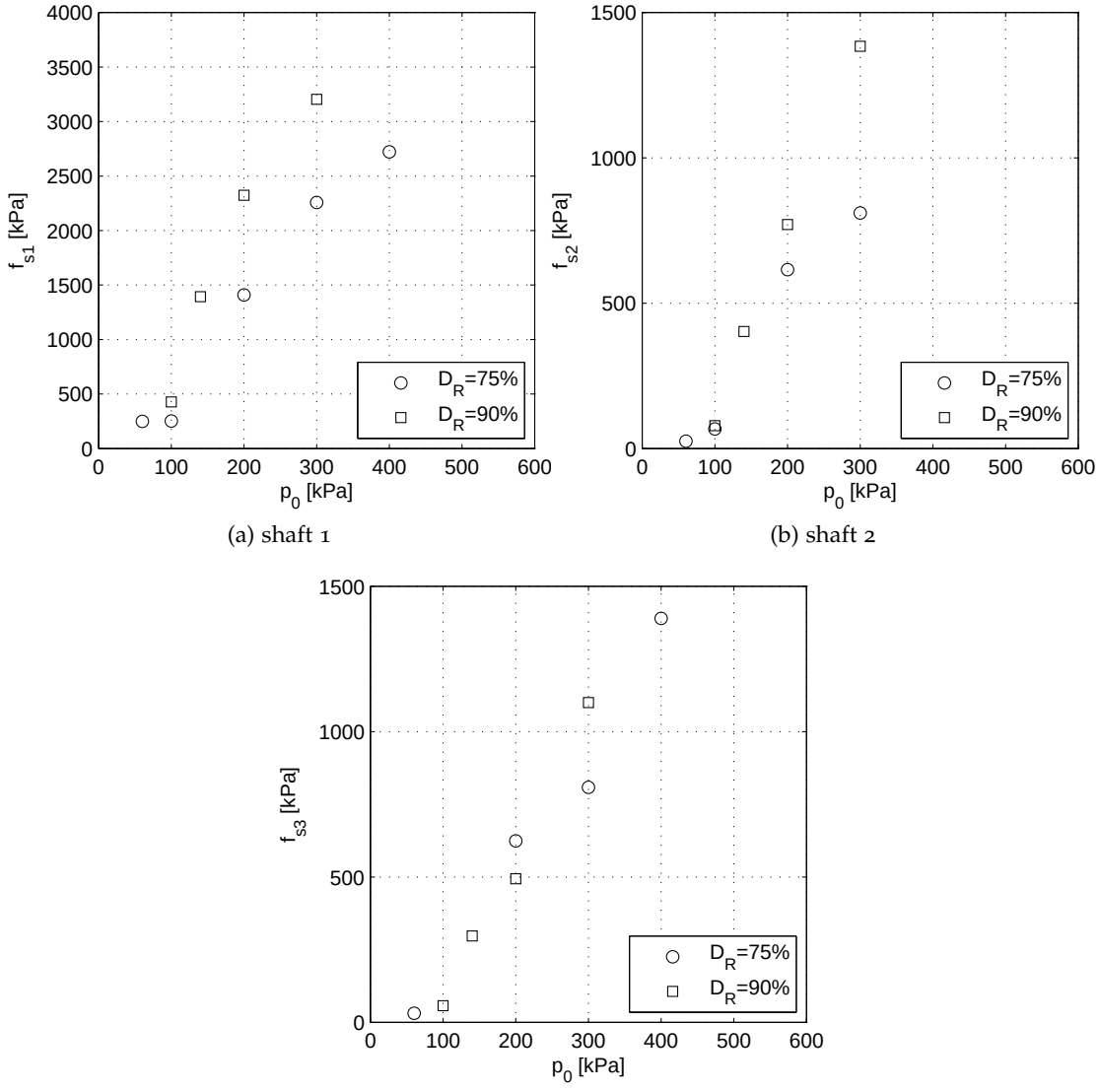

(a) shaft 1

(b) shaft 2

(c) shaft 3

Figure 159: Changes of shaft resistance, f_s, with relative density and initial stress state (Series A, BC1)

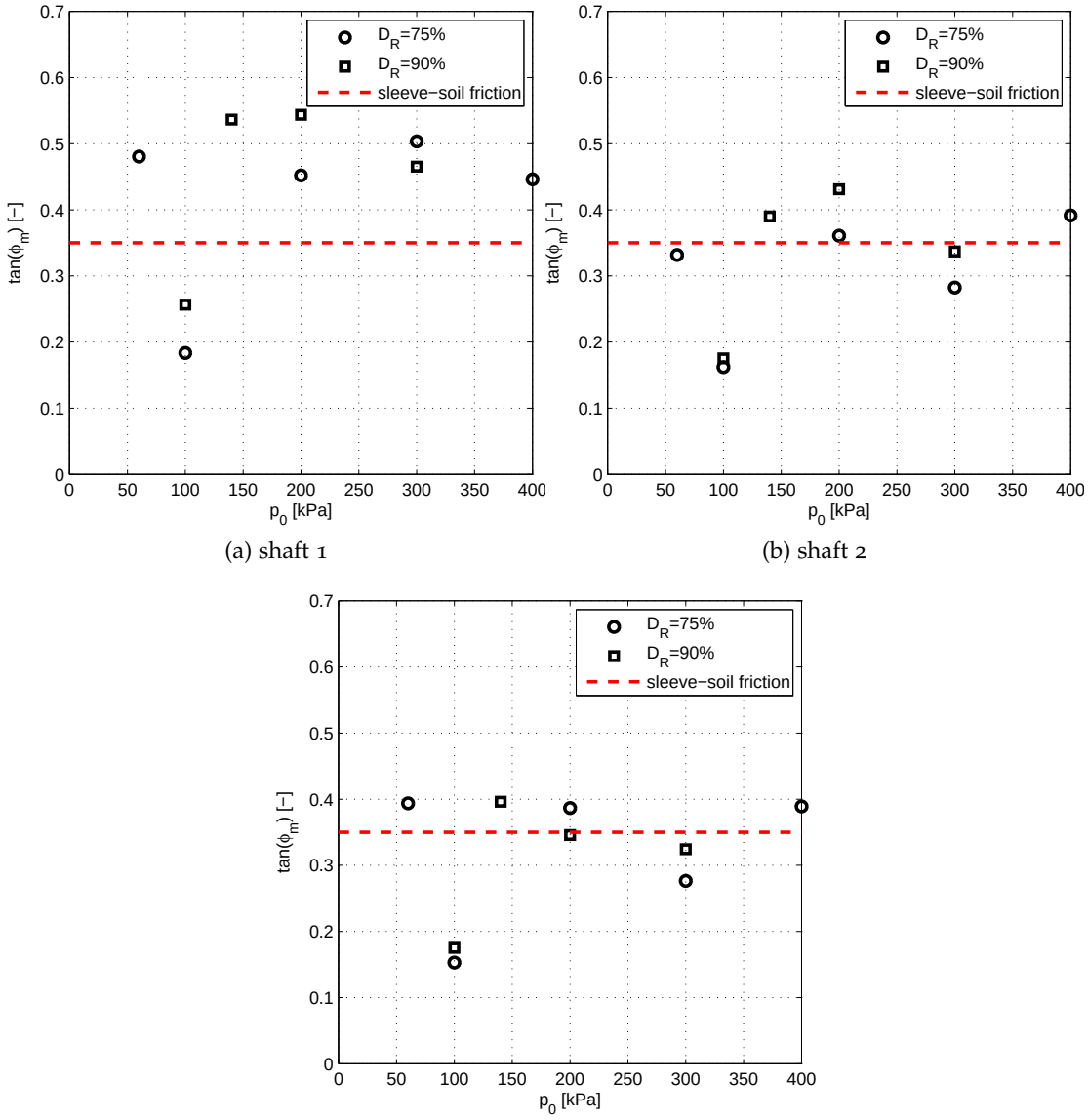

(a) shaft 1

(b) shaft 2

(c) shaft 3

Figure 160: Changes in mobilized shaft friction, with relative density and initial stress state (Series A, BC1)

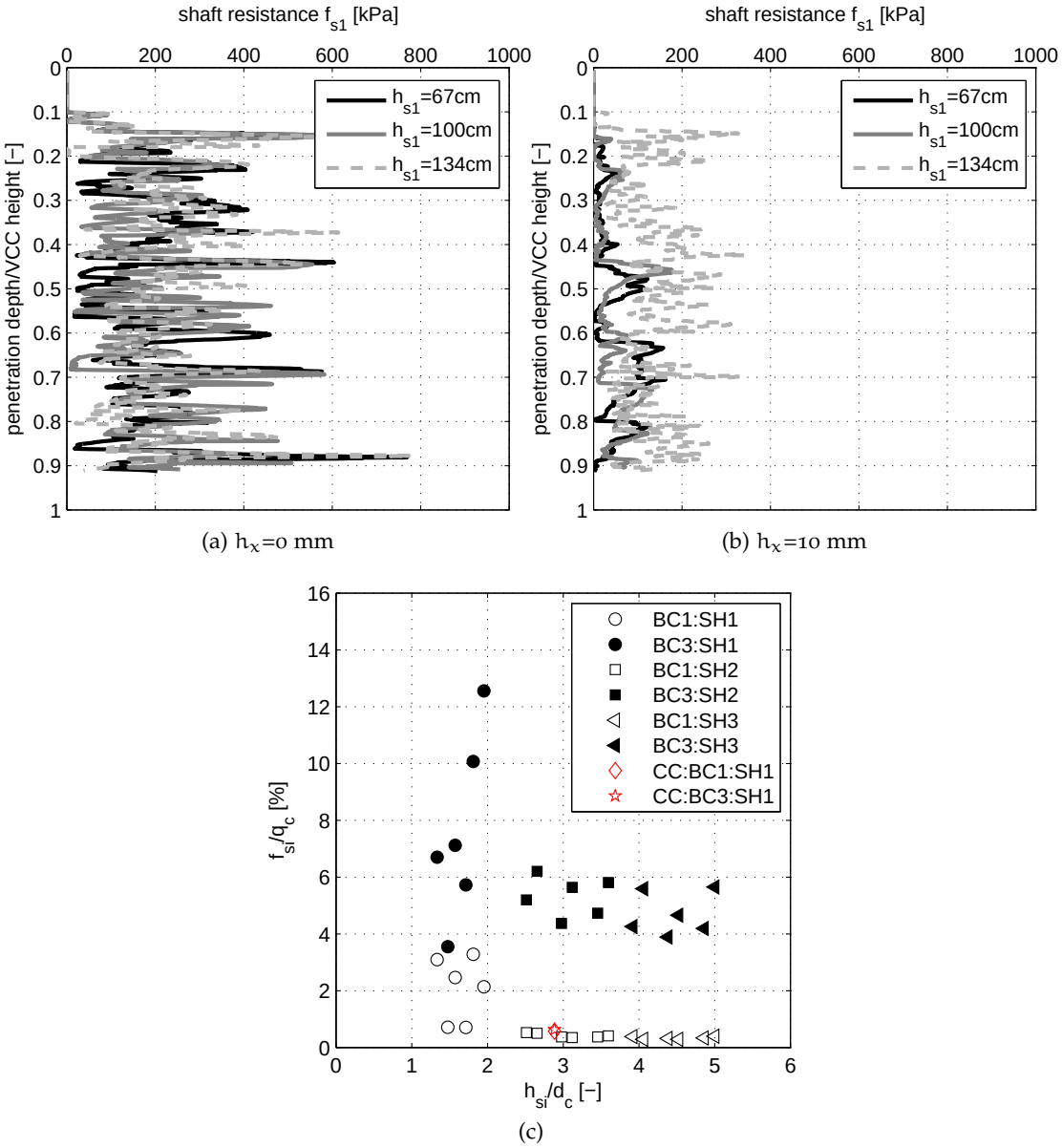

Figure 161: Changes in normalized shaft resistance, $\frac{f_s}{q_c}$, with normalized position of the centroid of corresponding sleeves (NUM2 test series)

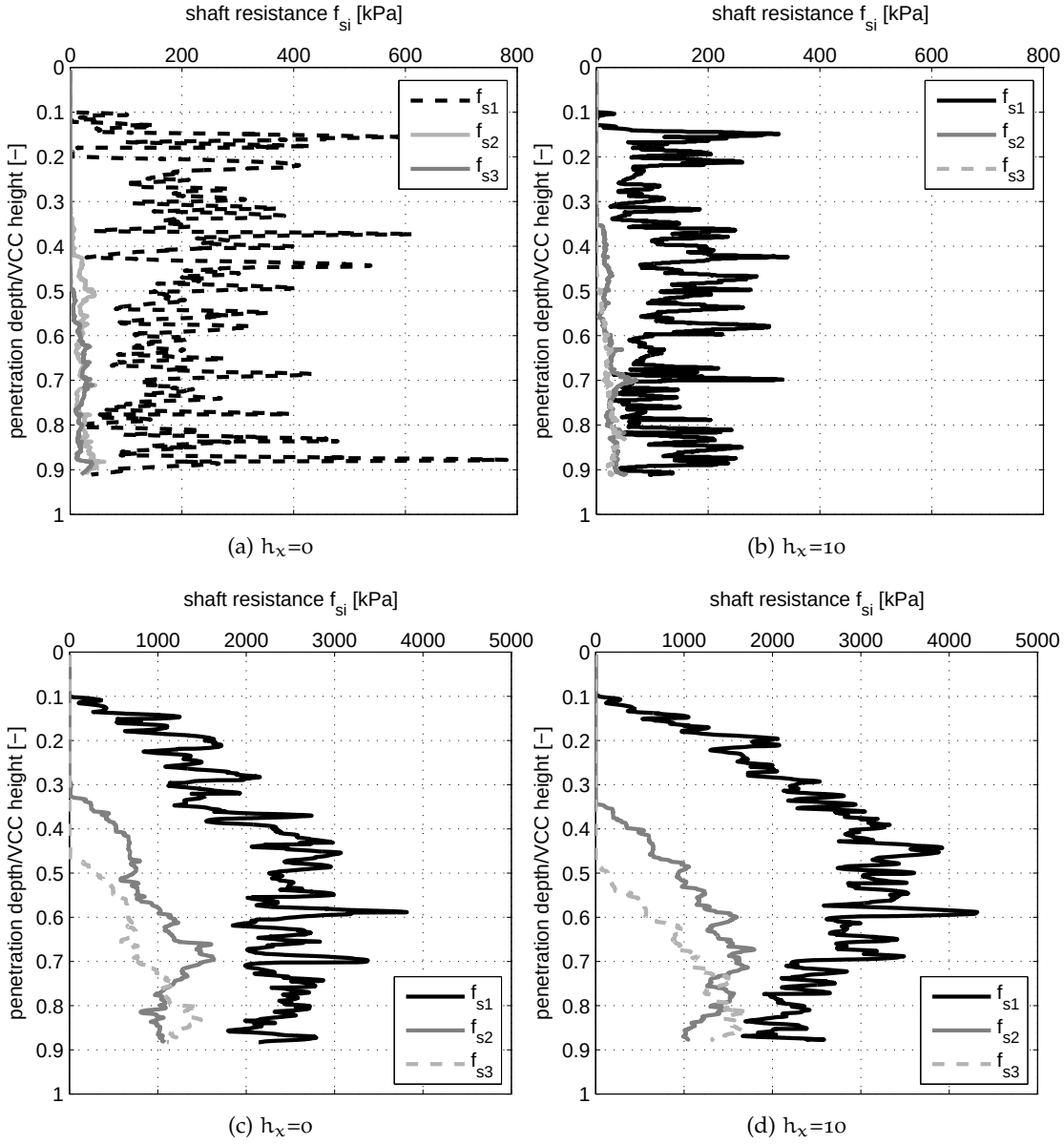

(a) h_x=0 (b) h_x=10

(c) h_x=0 (d) h_x=10

Figure 162: Example of sleeve resistance under (a)-(b) BC1 and (c)-(b) BC3 boundary conditions

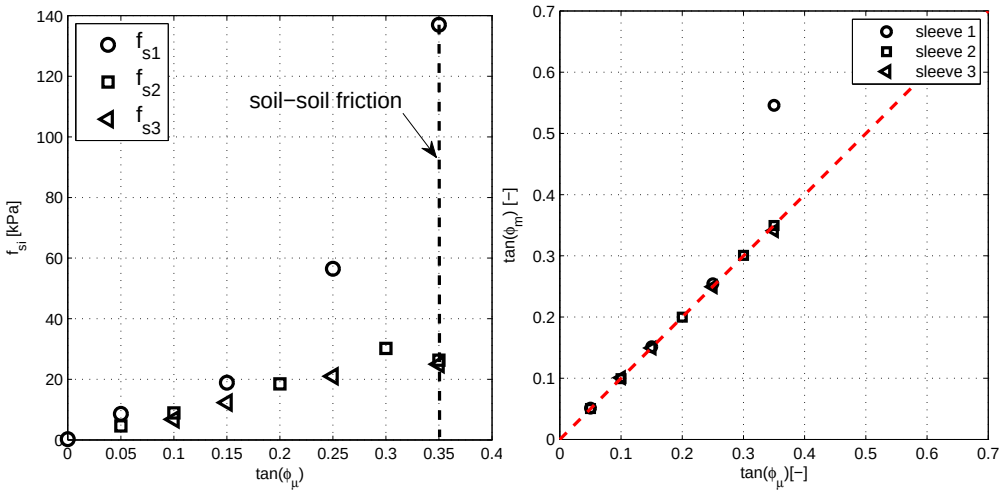

(a) (b)

Figure 163: Effect of sleeve texture on measured resistance measured mobilized friction

7.6 SUMMARY

In this chapter a series of simulated cone penetration tests in a discrete material representing Ticino sand under different initial conditions (stress history, relative density, method of consolidation) and subjected to different boundary conditions (BC1 ad BC3) were described. The results were examined through the cone tip resistance and side shaft resistance. Many issues related to the penetration process were investigated. These are some of the findings:

- the penetration resistance curves ordered themselves as expected via. increasing resistance with confining pressure and relative density;
- the penetration curves show two clearly marked phases: the cone tip resistance initially increases and then oscillates around a constant valus, in what can be seen as a macroscopic steady state zone;
- the steady state was defined by fitting the curves to an exponential function to extract steady state cone resistance, $q_{c,lim}$;
- the $q_{c,lim}$ (from test series A, E and F) results compared with the predictions of pre-established D_R-q_c-σ correlation and best results were obtained using mean effective stress (p_0) as the relevant stress measure;
- the $q_{c,lim}$ results from tests series B compared directly with the physical tests showed a good agreement for the tests under no-radial strain conditions (BC3). On the other hand, the results from the BC1 cases in the numerical model are well below their physical counter parts. The difference between numerical and physical tests is not explained by the small discrepancies of initial state before CPT. One possible explanation for the observed discrepancy is that the chamber size effect correction factor applied had not been calibrated for the range of chamber/cone ratios in which the numerical chambers operate.
- Sleeve resistance results showed that: (a) the resistance increases with initial stress and relative density, (b) the sleeve closest to the cone tip generally records a larger resistance than those located above the shaft, (c) the mechanism of shaft resistance is very much affected by the radial boundary conditions; stress control (BC1) results in force relaxation along the shaft whereas radial displacement fixity (BC3) favors large forces acting on the shaft. Moreover, the results obtained were similar to the experimental observations.